PATIENT SPECIFIC 3D FINITE ELEMENT MODELLING, ANALYSIS AND VERIFICATION OF DENTAL IMPLANT NAVIGATION AND INSERTION SYSTEM

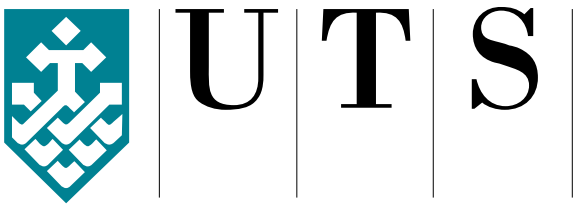

Valerio Taraschi

School of Mathematical and Physical Sciences

University of Technology - Sydney

This dissertation is submitted for the degree of

Doctor of Philosophy

August 2016

Declaration

This thesis is the result of a research candidature conducted jointly with another University as part of a collaborative Doctoral degree. I certify that the work in this thesis has not previously been submitted for a degree nor has it been submitted as part of requirements for a degree except as part of the collaborative doctoral degree and/or fully acknowledged within the text.

I also certify that the thesis has been written by me. Any help that I have received in my research work and the preparation of the thesis itself has been acknowledged. In addition, I certify that all information sources and literature used are indicated in the thesis.

Valerio Taraschi

August 2016

Acknowledgements

First and foremost I would like to express my gratitude to my supervisor Professor Besim Ben-Nissan, for sharing his immense and passionate knowledge with me during this research work, for guiding my professional growth in the last years and for his enlightening friendship.
I would also like to thank my co-supervisor Professor Bruce Milthorpe for directing this long research journey with wisdom regardless of his numerous commitments.

A special acknowledgement goes to BresMedical's General Management for their contribution to this research by allocating resources in assisting with the development of the navigation system. In particular, I would like to express my gratitude to the technical work of Daniele Giunchi, Waldemar Rostek, Soong Vongbunyong, Chris Dodson, Mel McNair and Mark Helou and to the significant support offered by Kevin Cullen, Tracy Rix and Marcos Perez.
For their remarkable clinical contribution in assisting with the design of the navigation system, for performing Clinical Trials and for making software packages available to this research I would also like to acknowledge Dr Gerardo Pellegrino and Professor Marchetti from University of Bologna.

I would like to thank my supporting and lovely wife Sarah for making my life better and more meaningful every day.
Last but not least, thanks to my always caring now asleep mother and father and my sisters who have always encouraged me from Italy.

Abstract

The use of a biomechanically correct finite element model (FEM) for simulating the behaviour of the human mandible during functional movements can be improved by including patient-specific anatomical data and real bone density data derived from a tomographic scan.

A model produced through this approach could be more realistic than the ones reported in literature over the last decades which lack subject-specificity in terms of morphological features and local material properties. Most of the published models over-constrain the mandible and do not include the action of facial muscles leading to what this study proves being simplistic or even erroneous interpretations of crucial implant osseointegration processes.

By interpreting tomographic data, in this research work the author developed advanced FEMs of the human mandible applied to realistic clinical scenarios and which can therefore be used to guide treatment plans.

Finite element simulations were also created to validate the design and the mechanical stability of a dimensionally reduced implant-supported patient reference tool used with an innovative and minimally invasive image-guided surgery system.

The author developed such novel navigation system for oral implantology to allow surgical approaches which otherwise could be not pursued using traditional techniques. This task required the design and prototype of software and hardware components which are now being clinically tested.

This thesis shows the application of the navigation system to the insertion of long angled implants for posterior support of full-arch prostheses. From the results of the FEM and by taking into account the micro-motions of the inserts generated by the full set of muscular

forces acting on a mandible in mechanical equilibrium under functional loading, this configuration showed superior osseointegration potential as opposed to what is reported in literature.

The author also applied the FEM to evaluate the osseointegration potential of implants with deep cortical anchorage, as opposed to shorter mono-cortical implants.

Moreover, a novel procedure for their safe insertion was designed by combining the benefits of ultrasonic bone socketing (piezoelectric osteotomy) with the dynamic guidance offered by the developed navigation system.

In force of its clinical potential, the surgical approach proposed in this study is currently being validated through in vivo trials approved by the independent ethical committee of University of Bologna. Preliminary results from Clinical Trials, as presented in this work, reported an average accuracy for implant insertion of 0.90+/-0.07 mm.

It is reasonable to state that the ultimate conclusion of this investigation is that the developed image-guided surgery system can be used safely and for significant outcomes on a routine basis for orthodontic or maxillofacial surgical procedures.

On the other hand the simulation designed to investigate its safe use on a patient is potentially suitable to determine the impact of patient-specific treatment procedures for ideal prosthetic restorations and to simulate the behaviour of other implantable components.

Table of contents

List of figures

List of tables

Chapter 1

Introduction

This research work presents a finite element model (FEM) of the human mandible validating an image-guided surgery system for clinical applications. The model is based on a computed tomography scan of the jaw performed on a living subject. This gives to the study the realistic attribute of being subject-specific. It was designed to be biomechanically valid and to reproduce the most realistic scenarios of constraints and forces during functional movements in an attempt to simulate the impact on a patient of a new image-guided surgery systems and implant insertion techniques developed for and utilised by BresMedical Pty Ltd (Ingleburn, Australia).

Through advanced modelling and clinically relevant applications, like subject-specific material mapping of the bone mineral densities and generation of a dedicated software for intra-surgical navigation, the developed technology is envisaged to become a functional tool for clinical diagnosis and planning treatments in maxillofacial surgery and dentistry.

The part of the project relative to the development of a surgical navigation system is industry based. For this reason, due to its commercial sensitivity, publication of this research in journals has been curtailed by the company while the research is still in progress.

1.1 Mandibular model

The major aim of this research study is to develop an innovative navigation system for dentists and oral maxillofacial surgeons and the clinical application of a patient-matched biomechanical model of a human mandible based on specific patient's tomography scan and its analysis via the Finite Element Method.

Mandibular modelling and finite element analysis with appropriate biomechanical considerations goes back to the early 1980s although earlier biomechanical considerations were initiated in the19th century.

A number of investigators like Barbanel (1975), Throckmorton (1985), Pruim (1980), Knoll (1977), Ben-Nissan (1987), Hart (1992), Choi (2005) have reported that there is a broad range of fundamental questions regarding the biomechanics of the mandible which need to be investigated: how strain and stress changes in the mandibular bone in response to the loss of teeth, mandibular distortion and reconstruction, endosseus dental implants and temporomandibular reconstruction; how the mandible changes its geometry and stiffness as a consequence of changes in functional loading, tooth loss, and temporomandibular joint degeneration.

According to the general biomechanical movements observed, there has been more than one approach to the problem of characterising a morphologically correct shape for mandibular bone and jaw musculature. All the approaches have to deal with the essential issue that stress is not directly and accurately measurable within the mandible by any clinical means.

1.2 Biomechanical Approach and FEA

Before finite element analysis several modelling techniques have been explored for modelling the biomechanical behaviour of the mandible: a free-body analysis (Hylander 1975), the use of photoelastic resin for modelling mandibular stresses (Lehman 1968; Ralph and Caputo 1975; Standlee 1977; Mongini 1979), holographic interferometry (as reported by Hussein & Rabie 2015) and an empirical assessment of stress distribution through in vivo

and in vitro strain gauge studies. In vivo strain gauges can give accurate localised measurements of strain on the surface of a structure, but the choice of surface locations is restricted due to potential interference with muscles, while strain cannot be measured at internal locations (Hylander 1984). Photoelasticity requires the use of a transparent model of the structure in exam, so it does not accurately reproduce true mechanical properties (Caputo and Standlee 1987). Analytical solutions are generally unviable because of the complexity of the geometry involved, the incomplete knowledge of the mechanical properties of the tissues and the complex time-dependent loading and boundary conditions.

The FEA-based stress analyses of a full mandible included gross simplifications for the model either mandible geometry or material descriptions and incorrect boundary conditions such as fixed supports (Ferre and Knoell 1977). In many cases two-dimensional representations were used (Haskell 1986).

Therefore accurate solutions for strain distribution in a whole mandible were hardly established using early modelling techniques.

For this reason appropriate anatomical design is required for entering a three-dimensional finite element modelling and analysis environment.

1.3 FEM models and differentiation criteria: materials, constraints, data acquisition

The modelling of accurate anatomy, appropriate loading, musculature, load distribution, functional movements, material properties and realistic supports for a mandibular model represents the evolution path of finite element models.

The assumptions which differentiate the past models from one another regard material and structural properties, load application topology, choice of restraints needed for the mathematical simulation to cover regional or full mandible analysis and computational capacity.

The focus to the assignment of material properties relates to the fact that the mandibular bone is principally made of two different types of bones: the cortical bone which forms

the shell of the jaw, and the trabecular (spongy, cancellous) bone, which is composed of plate-line bone partitions with bone marrow spaces of various sizes and shapes, containing the mandibular canal for inferior alveolar vessels, nerves and other cavities (Futterling et al., 1998).

It has been observed that in musculoskeletal structures like the human mandible the type of bone as well as the density changes strongly throughout the geometry. For this reason, averaging and assigning only one or two material properties through the all model can lead to inaccurate results (Futterling et al., 1998). However this has been the case in the past research work due to the lack of measuring methods and available data.

Bujtar (2010), for example, in a study on the rigidity of the mandible at three difference stages of life, observes how visco-elastic anisotropic features of the anatomy are rarely taken into account in predicting the behaviour of components of the facial skeleton when loading or trauma. Similar comments are made by Li (2009) in noting how the lack of local information on material properties results in a strong limitation of the realism of the model.

If a two-bone approximation is used, two encapsulated solids represent the trabecular and the cortical bone. The interaction between solids creates an issue on assigning boundary conditions. In fact, among fixed bond, slip contact and non-linear contact interface boundary conditions, numerous FEA have shown remarkable differences in resulting stress patterns.

In this work the author will use a linear isotropic approximation for the bone tissue although its stiffness will also be determined locally through a correlation with the apparent density. This choice is also due to the fact that the biomechanical configuration is believed to have a higher influence on the generated stresses and distortions during functional movements than the degree of anisotropy.

This is one of the features differentiating this work from other studies published in literature. The most common biomechanical scenarios used in mandibular simulations involve explicit bite forces and require the use of fixed supports around the bone for preventing rigid body movement. Others assign a vector load to a few muscles believed to

be active during clenching and constrain the movement of the condyles to achieve static equilibrium. Nevertheless, as noted by Bujtar (2010), the lack of articulation-like contact in the simulation which generates high stresses in the condyles has jeopardized the realism of the FEMs.

This study, on the contrary, assumes that the mandible is free to move during functional movements and requires that a complete set of the current active muscles is in equilibrium with the reaction exerted in the temporal-mandibular joint.

In order to represent the complexity of the inner structure of the bone, Ben-Nissan (1987) developed the first anatomically correct three dimensional model of the mandible for the analysis of functional distortions. Like a precursor to tomography which did not exist in early 1980s a young adult mandible was cast in polyester resin and cross-sectioned in 72 sections and digitised in order to get cortical bone outlines, cancellous bone layers and reference points for structural symmetry. By assigning two specific Young moduli for the cortical and the trabecular bone, Ben-Nissan defined a continuous range of possible values of elastic modulus of the homogeneous linear isotropic bone model. He further designed an interpolation between the behaviour of a fully cortical mandible and a fully trabecular one. This allowed to obtaining the results for distortion and stress/strain in a range of anatomically different mandibles under functional loading conditions, such as clench, opening and protrusion. In his model fixtures were only defined for three constraint points on three different directions at the symphysis where, in case of applied load, reaction forces would be null and the mandible in equiibrium. Using an anatomically correct structure, appropriate measured musculature, insertion and origins of muscles, three dimensional forces and most importantly appropriately constraining the model that is free to deform, Ben-Nissan's model was truly innovative at that time.

In a follow up study by Choi the mandible model and musculature were further refined. According to Choi (2004) the cortical and cancellous bone of the mandible can be considered to be transversely isotropic with a higher elastic modulus in the longitudinal direction and a lower elastic modulus in all transverse directions. In preventing any possible

rigid body motion, Choi fixes three nodes in space in a symmetry plane perpendicular to the intercondylar axis by using spring elements.

Ben-Nissan's use of dry mandibles for 3D modelling represents a trend followed by other workers in his field. Korioth et al. (1992) developed a three-dimensional model from the scan of a dry human mandible through computed tomography. More than his innovative non-destructive reproduction of the jaw morphology, Korioth's model considers the cancellous bone as trabecular bone without medullary spaces. As per the constraints used, Korioth fixed the solid model at the labial and occlusal thirds of the right first lower molar. Two of the models made in the early 1990s (Hart 1992 and Meijer 1996) modelled the border of the cortical plate and assigned different material properties for cortical and cancellous bone. Hart's model also used computer tomography to scan a dry jaw. Similarly to Ben-Nissan (1987), Hart focused on the behaviour of the mandible during functional ordinary movements like biting and loading due to mastication which provokes stresses in multiple regions. As Vollmer (2000) pointed out, Hart described the conformity between the calculated results and strain gauge investigations made by Hylander (1984) on a Macaca Facicularis mandible. Korioth et al. (1992) found that strains on a loaded in vitro mandible were in excellent agreement with the ones calculated by finite element analysis on the same specimen. Authors like Vollmer (2000) and Al-Sukhun et al. (2005) based the validity of their own models on the same conformity. They both used computed tomography to scan dry mandibles and assigned material properties according to the absorption values reported in the tomography results. According to this approach, Hounsfield units are measured by the computed tomography, transformed into bone density values and thereby correlated with Young's modulus (Vollmer, 2000). Both Vollmer and Al-Sukhun also measured mandibular surface strain using strain gauges, and medial convergence using a custom-fabricated linear variable differential transformer. Although using two different techniques for converting computed tomography scan data to density values and therefore stiffness, both groups found a good correlation between the experimental results and the FEM-based analysis outcomes. The experimental apparatus set up by Vollmer was limited in detecting the three-dimensional orientation of the reaction on the condyles. This model

lacked detailed knowledge of the material properties of the cancellous bone, the uncertainty of how to realistically distribute the muscle loading and the boundary conditions on the condyles. It must also be noted how, according to Vollmer (2000), the correlation between numerical and experimental data was found independently upon the location of the applied mastication forces.

1.4 Proposed FEA model: assumptions

1.4.1 Material mapping

As stated earlier the trabecular bone is composed of plate-like bone partitions with bone marrow spaces of various sizes and shapes and contains the mandibular canal for the inferior alveolar vessels and nerves and other cavities. The degree of anisotropy in the condyle increases from the superior to the inferior part and the trabeculae are more aligned towards the mandibular neck (Giesen 2000).

As stressed by Futterling (1998), in biomechanical structures like the human mandible the type of bone as well as the density is changing strongly throughout the geometry, thus averaging and assigning of only one or two material properties can lead to inaccurate results. However the bone mineral density and morphology is also subject-specific, since it varies with age and gender.

For this reason the model developed in this thesis takes into account the patient's original mandibular morphology and individual bone mineral density.

1.4.2 Biomechanics of the mandible

For a more comprehensive understanding of the specificity of our model, a brief overview on the main concepts involved in the finite element analysis and modelling of the human mandible is needed. The areas to be covered are: anatomy and biomechanics of the mandible, principles of finite element analysis, morphology and material properties of the mandible, load application under different loading conditions, boundary conditions,

computed tomography scan technique, FEA pre-processing software used and the relative outputs.

1.4.3 The anatomy of the mandible

The mandible is a bone suspended below the maxilla by muscles, ligaments and other soft tissues. It is composed of two vertical components, the ramii, joining at obtuse angles the horizontal body of the mandible which supports the teeth. The inferior margin of the body meets the posterior margin of the ramus in an area which is called angle of the mandible and which provides attachment to the masseter muscle in the external part and the medial pterygoid on the internal medial side. The coronoid and the condylar processes form the two areas of the superior border of the ramus. The temporalis muscle is attached to the coronoid process while the condylar process has a neck (where the lateral pterygoid muscle is attached) supporting an articular surface. This last one fits into the glenoid fossa of the temporal bone to form a movable synovial joint called "temporomandibular joint" (TMJ). The articular disk, composed of dense fibrous connective tissue, separates the fossa from the condyle neck and provides boundary lubrication when the condyle moves in the fossa during mandibular functional movements.

1.4.4 Musculature

Masseter, temporalis, medial pterygoid, lateral pterygoid and digastric (these last ones are attached in the inner counterpart of the symphysis) are generally addressed as the main muscles responsible for mastication. In particular, during a clenching movement, the masseter, the medial pterygoid and the temporalis muscles are mostly active, followed in intensity by the lateral pterygoid and the openers. The same muscles are involved in the wide opening movement with the exception of the temporalis. The medial pterygoid, combined with the action of the digastric and the openers, is instead responsible for depressing and protruding the mandible.

On the biomechanical of the mandible, this work aims to improve most of the previous models for its approach regarding the reaction forces acting on the condyles during

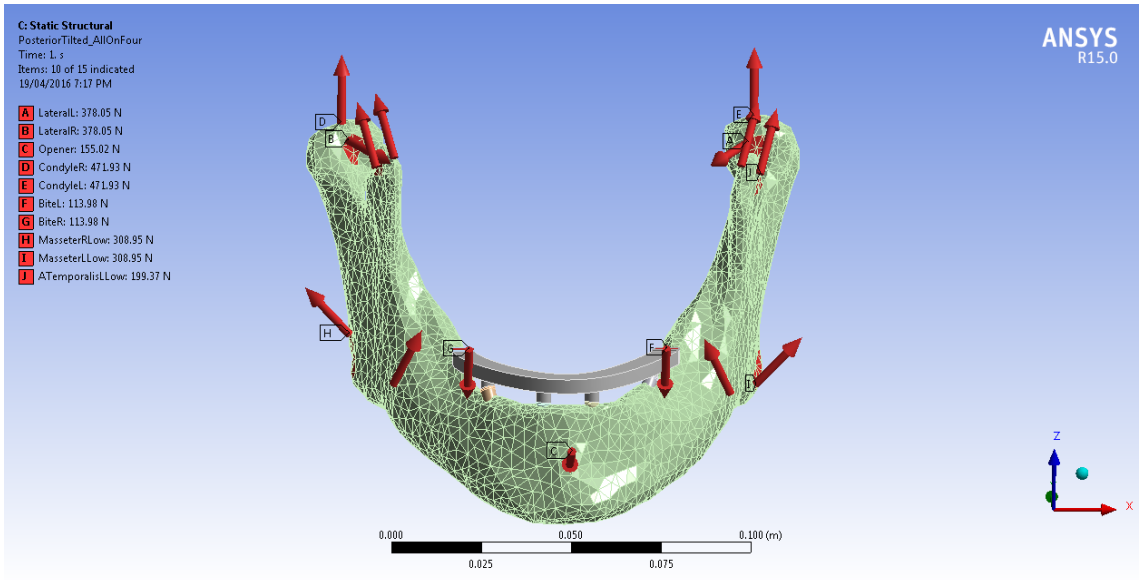

Fig. 1.1 Three-dimensional vector representation of the musculature and loads applied during a clenching movement, including joint reaction forces.

functional movements and the muscles insertion topology, which takes into account areas rather than single nodes. Considering that these two aspects will be combined with a subject-specific bone mineral density mapping at a local level and clinically relevant applications for image-guided surgery and implant-supported prostheses, it is envisaged that the proposed model has the potential to become significant among published simulations on the mandible.

1.4.5 Biomechanical equilibria and the reaction force

Early biomechanics workers suggested that there is no significant direct or indirect load acting on the TMJ. The most interesting interpretations in this direction are the ones by Frank (1950) and Gingerich (1971). Frank based his arguments on a radiographic analysis which showed that the condyle was never in direct contact with the articular eminence. Therefore he concluded that the condyle was not functioning as a fulcrum and therefore the mandible could not function as a lever. Gingerich stated that during biting action the jaw is functionally a link between the adductor muscle force and the bite force rather than a lever. Roberts and Tattersall (1974), in their simplified biomechanical model, state that there is no significant force at the temporomandibular joint during elevation of the mandible since

the masseter, temporalis and bite force vectors form a closed triangle showing equilibrium. It is now accepted that the mandibular biomechanical activity is comparable to a simplified class III level, in which the condyle acts as a fulcrum, the masticatory muscles as applied force and the bite load as resistance.

The approach used in the present work agrees with the assumption that there is a reaction force acting on the condyles during functional movements such as clenching and wide opening. The intensity and the direction of the three dimensional vector representing the reaction force in the simulation is calculated by balancing the equations for resulting force and momentum generated with respect to the intercondylar axis. Hence calculation of the total joint reaction force requires: the magnitude and direction of the bite force, the magnitude and direction of each acting muscle and the lengths of the moment arms of each muscle force.

Magnitude and direction of the bite force can be directly measured with force transducers (Hylander 1978) while the lengths of the moment arms can be generally estimated from lateral cephalograms. Therefore it is evident how the quality of these results could depend on the estimation of the intensity of all the muscle forces applied to our structure. Two methods have been successfully used to estimate these forces. One is the use of the integrated electroyogram (IEMG), chosen by Barbenel (1974) and Pruim (1978). Another method accepts the hypothesis that each muscle generates a force proportional to its cross sectional area. (Crowningshield 1978; Amis 1980). In the present work the author will use Ben-Nissan's (1987) measurements and calculations for the vectors representing the muscle forces since it combines both of the approaches above. Ben-Nissan's calculated values also refer to the muscle forces estimated by Barbanel (1975), Throckmorton (1985) and Pruim (1980). The muscle force exerted during isometric contraction is directly proportional to the IEMG in a quantitative relation which takes into account, for calibration purposes, the maximum value of a single muscle recorded during an experimental session.

1.4.6 Reaction force positioning issue

Another issue to consider in a critical review of the past biomechanical models is how the movement of the TMJ influences the location of the condyle reaction force. Since the articular disk is bound to the condyle by discal ligaments, the only physiological movement that can occur between these surfaces is a rotation of the disc on the articular surface of the condyle. Nevertheless, because the disk is not attached to the articular fossa, the former is able to slide on the condylar surface when the mandible is moved. In this work the dynamics of the condyle reaction are investigated in order to determine the influence of the positioning of the reaction force vector on the predictions on mandibular stress and strain.

Meijer (1996) investigated how applying the loads on a larger scale geometry influences a different biomechanical behaviour. Kavanagh (2008), whose model is also based on computed tomography scan data, uses areas instead of nodes for load application. Nevertheless he builds a model -exclusively for a resting position- which has condyles unrealistically fully constrained at the top surface.

In this current work the reaction force will be distributed over the condylar surface rather than a single node and its components will depend on the direction and magnitude of each muscle force component. Muscle forces are also distributed to an area realistically based on anatomy of the patient modelled. The necessity for reproducing a realistic model rests on a good level of detail of the scanned anatomical body, appropriate and realistic constraints and adequately placed musculature during common functional loadings of clenching and wide opening of the mandible.

For this reason the possibility to alter the area of application of condyle force reaction suits the actual complexity of the movements of the condyle during different functional movements. As Koolstra (2004) suggests, the deformations in the cartilaginous structures in joints are caused by the mutual displacements of the articulating body segments. Therefore the fact that the areas on the condyle where major stress occurs are shifted during the functional movements suggests that proper modelling and analysis requires attention on the reaction force position.

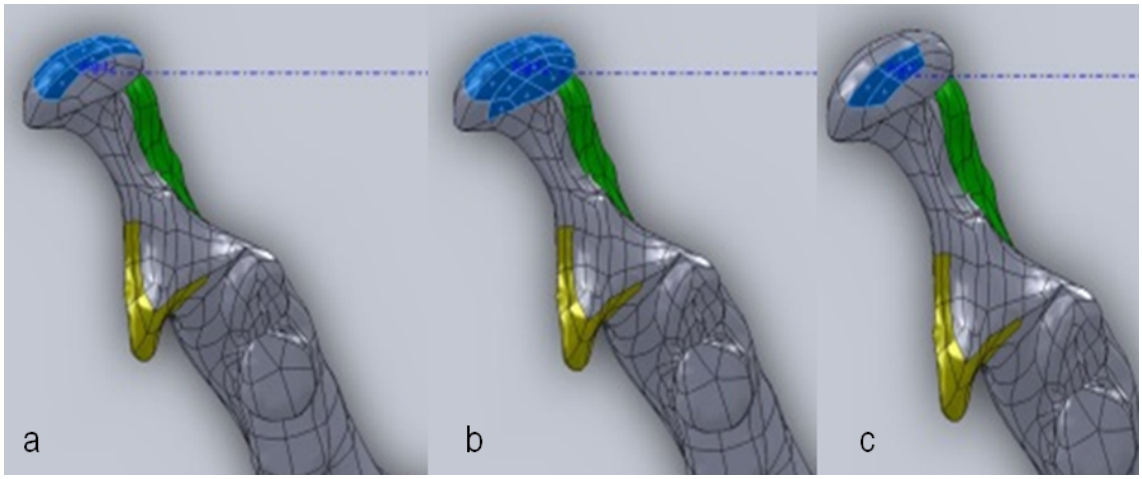

Fig. 1.2 a,b,c show how different areas can be chosen in the FEM pre-processor for the application of the reaction force on the right condyle (SolidWorks Educational Edition, Copyright c 1195-2008, Dessault Systemes).

1.4.7 Load application

One of the major improvements introduced by the proposed model which contributes to give more realistic results and accuracy in predicting stress and strain is the application of muscles forces on areas instead of single nodes. According to Vollmer (2000) there is uncertainty on how to realistically distribute the muscle loading and fix the boundary conditions at the condyle. Moreover, after recording experimental data with strain gauges, Vollmer proves that how changing the location of the biting forces significant changes in stress distribution and magnitude occurred near the condyles.

1.4.8 Finite element analysis application issues

Finite element analysis, in principle, solves a complex problem by redefining it as the summation of the solutions of a series of interrelated simpler problems. The complex geometry is decomposed into a set of “finite” dimensions which forms the “meshed” model of the analysed object. Each finite element is limited by nodes and, knowing its internal strain function, one can write equilibrium equations corresponding to each degree of freedom of each node. The analysis starts in dividing the complex body in exam into finite simpler elements through a user-controlled mesh generation. In case of a static structural analysis of a linear isotropic material, to each element density, modulus of elasticity and

Poisson ratio is assigned. Loads are applied at specific nodes or group of nodes and so it is for constraints by setting certain nodal displacements to known values. At this point the system composed by many linear algebraic equations for the many degrees of freedom is solved, so that for each node a vector of displacement is calculated (the solution of the system of equation depends on the boundary conditions imposed to the solid model in the way they contribute not to make the matrix of the linear coefficients singular). Finally it is possible to calculate the element strain and the stresses generated by the strain through an interpolation between nodes relative to the same element.

All three-dimension finite element models of the mandible require a meshed solid model in input. Earlier models used to interpolate digitalised sections of dry mandibles in order to reconstruct a solid body under the form of a CAD object readable by the finite element pre-processor. The use of laser (Tsukrov et al., 2009) or computed tomography scan on dry mandibles represented a significant improvement in determining a detailed morphology of the bone. Nevertheless the real innovation is the use of computed tomography to scan mandible from living subjects. As Taddei (2004) suggests, it is well known that Computed Tomography images can provide fairly accurate quantitative information on bone geometry since the attenuation coefficient of bone tissue is much higher than the one of the surrounding soft tissues, resulting in well contrasted edges. The units used for measuring the attenuation of the X-ray beams due to their interaction with the solid body are Hounsfield units (HU). Therefore the function imaged by the X-ray Computed Tomography is the distribution of the tissue linear attenuation coefficient.

1.5 Anticipation of research products and outline of the thesis

As it will be presented in the next Chapters, this research produced two significant outputs:

- The first one is a finite element model of a subject-specific mandible obtained using morphological and density data from a tomographic scan. This model uses a biomechanically correct complete set of muscle forces in equilibrium with the

condyle reaction, advanced material properties and an accurate mapping of both cancellous and cortical bone.

- The second output is the application of the FEM to validate an innovative system for image-guided surgery which is critically compared with existing computer-assisted surgery systems and finalised to safely perform complex surgical implant insertions like posterior angled or zygomatic implants.

In Chapter 3 calculation of stresses and distortions of the mandible during functional movements will be presented in order to validate the consistency of the predictions of the FEM prepared as per Chapter 2 with previously published models.

Once the consistency of this method is proven, the FEM will be applied to clinically significant scenarios. In Chapter 3 it will be initially used to investigate the biomechanical impact of a reference frame used by a new navigation system during surgery. A unique feature of this development also presented in Chapter 3 is the design of a methodology for determining the stiffness of the bone tissue from local density data derived from the CT scan and its integrated use in the FEM.

In Chapter 4 the biomechanical viability for the insertion of angled implants supporting full-arch prostheses will also be confirmed by the results obtained from the simulation for stresses and deformation of the bone tissue around the implant sites.

Chapter 6 will present the design, analysis and validation of a new navigation system for oral implantology including a software interface able to track in real time the position of cutting instruments against a virtually planned surgery. The potential of such system, anticipated by its suitability for the All-On-Four procedure described in Chapter 4 and 5, will be shown as applied to ultrasonic implant site preparation, as reported in Chapter 7. In this type of surgery the combined approach will result in improved accuracy and safety for complex implant insertions like zygomatic or angled implants. In describing the application of the FEA-validated navigation system to piezoelectric osteotomies, Chapter 7 will also present the results from preliminary clinical trials undertaken at University of Bologna (Italy), thus reinforcing the clinical significance of this research and development work.

1.6 Future developments

It is envisaged that the developed FEM could be applied to a number of medical orthodontic or maxillofacial diagnoses to determine a patient-specific treatment procedure and its associated ideal prosthetic restoration.

As per the image-guided surgery system, this approach could be used by dentists and maxillofacial surgeons for complex implant insertions and on a routine basis for better patient care.

Moreover, the combination of ultrasonic preparation and ad hoc guided surgery could improve the surgical viability of immediately loaded prosthetic restorations similar to the All-on-Four® approach.

Chapter 2

Preparation of a patient-matched biomechanically correct Finite Element Model of the human mandible for the evaluations of clinical scenarios

2.1 What is a Finite Element Model of the mandible

The Finite Element Method (FEM) is a numerical procedure for analysing structures and continua where the analysis would be too complicated to be solved satisfactorily by classical analytical methods.

Finite Element Analysis (FEA) solves a complex problem by redefining it as the summation of the solutions of a series of interrelated simpler problems. This requires to subdivide a complex geometry like the human mandible into a suitable set of smaller “elements” of “finite” dimensions, which, when combined, form the “mesh” model of the investigated structure (Choi 2005).

A FEM of the mandible which is morphologically and biomechanically correct is able to predict stresses and strain in the bone under certain loading conditions. It can be applied to quantify the stresses around the implant surfaces or simulate the invasiveness of a foreign

body used for reference during surgery.

In order for it to be accurate, the model must account the overall mandible structure as flexible and therefore calculate its stiffness across several iterations.

For this reason modelling the internal structure of the mandible with different bone structures and geometries becomes a necessary requirement for a correct biomechanical simulation of the mandible's behaviour.

In creating a model of a human mandible which can be used in a realistic simulation using FEM, the shape of the bone needs to be reverse-engineered from a living subject or a cadaver. Only in this way, in fact, the intricate and asymmetrical morphology of the mandibular bone can be truly modelled in three dimensions.

2.2 Three-dimensional model design procedure

2.2.1 Complexity of exterior shape and interior structure of the mandible

Modelling the human bone has been subject of extensive research in both maxillofacial and orthopaedic surgery.

The morphology of the human bone presents different complexity for different parts of the human body and at different observation scales.

Although the mandibular morphology can be classified into several configurations, like for example a U-configuration (undercut), a P-configuration (parallel), and C-configuration (convex), depending on the shape of the alveolar ridge, it becomes challenging to model the internal part of the mandible (Nickening 2015).

A tomographic scan is the only option for living subjects for inspecting the internal bone structure. The advantage of using a three-dimensional scan consists in the possibility of segmenting the raw images from the scanned volume to reverse-engineer the shape of the internal components of the bone.

At a microscopic level, the bone is composed by a matrix of cylinders forming a Haversian system (Nomura 2003). This consists of layers of cells laminated between the cylinders which are primarily made of calcium phosphate. When less densely packed, the macro-

scopic structure can be considered cancellous bone.

On a larger scale, bone occurs in two forms. The most obvious difference between these two types of bone is their relative densities or volume fractions of solids. Bone with a volume fraction of solids less than 70% is classified as cancellous or trabecular, that with a volume fraction of solids greater than 70% is classified as compact or cortical (Choi, 2013).

As per the cancellous or trabecular bone, mandibular trabecular pattern can present as either sparse, mixed dense plus sparse, or dense. Furthermore, the transitions from trabecula to intertrabecular spaces and the size and number of these spaces are highly subject-specific (Jonasson 2014).

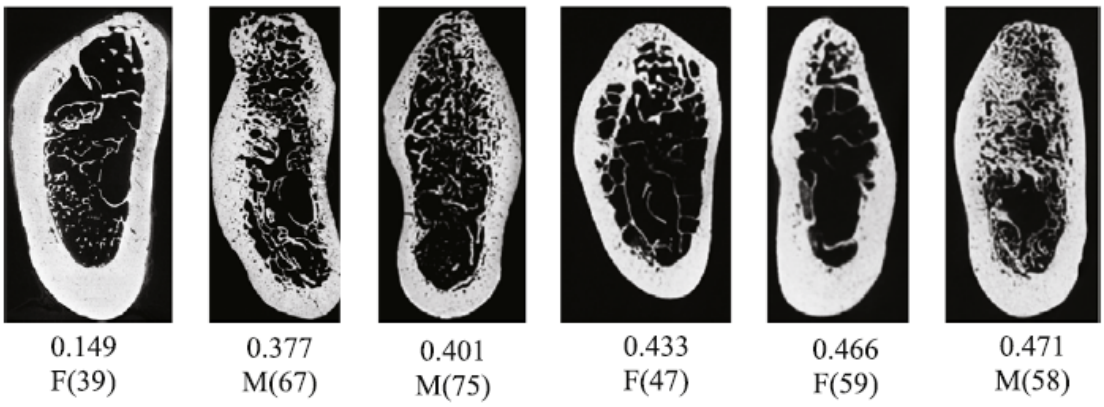

Fig. 2.1 Morphologically different bone samples acquired from a female and male mandible. For each bone sample the bone volume fracture is reported, together with the gender (F: female; M: male) and the age of the patients (From: Marcian 2014).

The distribution of the trabeculae, which has been found to affect the strength of the bone, is highly asymmetrical and is dependent on the subject's gender (Figure 2.1), age, eating and living habits. Models of the trabeculae have been particularly used to investigate the interface between implantable components and the bone tissue.

In a study which used micro-CT to model the architecture of the trabeculae around a series of dental implants, Marcian (2014) found that the strain distribution is first and foremost dependent on the shape of the bone and the morphology of the cancellous bone.

Due to the scale of these types of model and their high subject-specificity, they are not

suitable to predict accurately the overall biomechanical behaviour for which models generally use long bones.

2.2.2 Influence of the morphological complexity on the modelling

Whether the trabeculae are modelled as separate entities or not, the bone models are still topologically very complex and therefore they affect the performance and capacity of the simulation engine.

Differently from the one of structural studies in engineering simulations, the geometry of the bone is reversed engineered from organic shapes through a high number of local mathematical approximations of the physical surfaces. Smaller details in the bone geometry require a higher number of mathematical data approximating its morphology resulting in a simplified mesh of finite elements used for the FEM. As a consequence, during the last 30 years modelling biological structures using FEA has progressed with the increasing computing power of workstations.

To balance the complexity of the topological structures, FEA researchers were forced to use a number of approximations in the pre-processing stage.

In this current work the author had to choose which approximation to make in designing the required simulation which could be used to analyse clinical scenarios, like for example the invasiveness of a reference tool for surgical navigation mounted on a patient (see discussion in Chapter 3).

This study is aimed to build a functional model with subject-specific properties (patient-matched) and loading conditions while reflecting the internal morphology and composition of the mandible.

Where possible, the complexity of the model has been reduced to be less computationally expensive.

2.2.3 Bone surface reverse-engineering

A full CT scan of a patient's lower jaw was taken at Castlereagh Imaging (Parramatta, Australia) using a CT scanner (i-CAT, Xoran Technologies, Ann Arbor, MI). The raw DICOM (Digital Imaging and Communications in Medicine) data were imported into Amira (Visage Imaging, Inc., San Diego, USA) where combined threshold and region growing segmentation techniques were used to identify both cortical and cancellous bone.

The segmented layers or masks were smoothed with a maximum topological error of 0.5mm.

The product of the segmentation was a strongly bonded "watertight surface" (Hsu 2015) made of connected triangles and stored into an STL file (Ma 2001). In order to be used by the finite element pre-processor the surface must be interpreted as enclosing the solid model which will be used for the simulation.

Following that the file containing the triangulation of the surface is then converted into a collection of Non-uniform rational B-splines (NURBS) which approximate the curvature of groups of triangles. NURBS are mathematical objects commonly used in computer-aided design for their ability to represent complex shapes in a compact form. This method uses functions of two parameters mapping a surface in the three-dimensional space. The shape of the NURBS is determined by control points which are always either connected directly to the curve/surface or act as if they were linked by a rubber band. Depending on the type of user interface, editing can be carried out via element's control points, which are most common for Bézier curves (Gershenfeld 1999, Piegl 1989).

An ensemble of connected NURBS was exported in Rhino v4.0 (Rhinoceros3D, WA, United States) as an Initial Graphics Exchange Specification (IGES) or STEP file which can be read as a solid model when imported into a CAD software module (like for example Inventor (Autodesk, Inc., California, United States), Abaqus (Abaqus, Inc., Dessault Systemes, France) or Ansys (Ansys, Inc., Pennsylvania, United States)). Depending on the complexity and the connections between the NURBS some software package would not be able to interpret the model as solid.

2.2.4 The importance of Meshing

It is paramount to use a very regularly and homogeneously triangulated surface in generating a CAD model. The 3-Matic module from Mimics (Materialise NV, Leuven, Belgium) has been considered as the most suitable application for preparing a triangulated mesh to generate a solid model according to the following workflow:

- In the “Fix” tab the “Smooth” function was selected to remove unrealistic sharp edges from the mesh
- The number of triangles was reduced using a factor of “0.1” for maximum geometrical error
- Within the “Inspection scene” a “0.4” value for Height/Base triangle ratio was used
- The model was re-meshed with the following parameters:

  Threshold 0.3

  Geometrical error 0.1

  Max edge length 5.0

  Preserve surface contours ON
- The mesh was repeated for

  Threshold 0.4 (increased)

  Error 0.2
- Finally the function “triangles reduce preserving quality” was run to lower the count of the triangles used for the mesh in order to reduce its computational burden. Once the quality of the surface mesh was improved 3-Matic could generate a volumetric mesh if using the following parameters:
- Control edge length set to 5.0mm
- Threshold for shape measure “aspect ratio” set to 25

The mesh generated by the segmentation was also improved to ensure that it did not include any topological singularity i.e. holes, non-manifold edges, duplicate faces or spikes out of the tolerance limits.

In Rhino v4.0, the algorithm MeshToNurbs was utilised on each simplified model (<20000 triangles count reduction) to generate connected NURBS surfaces.

The NURBS were than exported to finite element analysis (FEA) pre-processor software

(Ansys) which imported them as solid models.
Additional CAD models were modelled according to the specific simulation. For example, as reported in Chapter 3, simulating the impact of reference tools for surgical navigation required modelling of a MINI dental implant and all the components of the reference frame. The extra CAD models were created in Autodesk Inventor (Australia) and fixed in their operational positions in the mandible model. Moreover, in the simulation described in Chapter 3, the models of both the cortical and trabecular bone were modified in order to match the surfaces of the implant model via a CAD-assisted Boolean operation.

2.3 Pre-processing the finite element model

The approximations used by researchers in biomechanical finite element simulations are generally related to the boundary conditions, loading cases and complexity of the solid models used. For modelling the mandible mainly a linear elastic isotropic model has been used to simulate the bone behaviour under loading conditions (Li 2009, Barao 2009, Kitagawa 2005, Qian 2009).
In case the finite element model investigates the behaviour of the human mandible during functional loading conditions, the use of a static structural analysis offers a suitable scenario for the simulation setup.
If we aim to investigate the mandibular behaviour in simulating a trauma, it might be necessary to perform a non-linear analysis due to the possibility of fracture of the modelled elements.

The author finds that the use of a linear static structural and non-linear explicit dynamics respectively for functional loading conditions and traumatology results in a good approximation of the human mandibular bone behaviour, as long as material properties and biomechanical conditions are realistically assigned.

In Chapters 3 and 4 the presented finite element model focuses on two main applications for respectively image-guided surgery and dental implantology.
In one case the model aims to evaluate the stresses generated on inserted implants during functional loading conditions like for example a clenching action.

In another the simulation is used to quantify the potential invasive effect of reference tools for image-guided surgery (in the case they are bone-supported).

For this reason this Chapter presents the development of a finite element model in which, in both linear and non-linear conditions, in deeper areas of the bones (which might host the interface with the implantable components), are characterised at a higher level.

2.3.1 The choice of material properties and analysis types

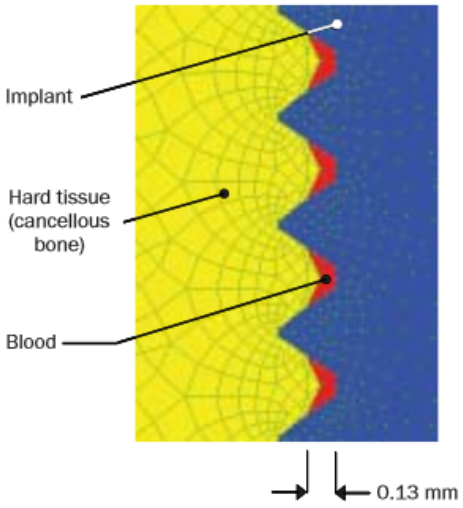

Fig. 2.2 Example of modelling the bone-implant interface: the model does not take into consideration the previous action of the drill tip used for socketing (From: Guan et al. 2009).

The model illustrated in Figure 2.2 utilizes a wide range of materials for the bone-implant interface region.

Guan et al. (2009) stated that increasing the number of materials used to model the region improves the accuracy of the simulation. However, the mentioned model does not take into account the effect of the stresses generated by the implant insertion around the flutes area, early osseo-integration or the presence of bone debris left from the socketing procedure by the longitudinal penetration of the drill tip.

The complex directionality displayed by the trabecular bone makes the choice of the analysis type and the accuracy in material properties more difficult. Although the majority of the models propose to use isotropic properties, most past experimental studies have

shown that the behaviour of the cortical bone is well approximated by a transversely isotropic symmetry (Lappi et al. 1979), while cancellous bone has probably orthotropic symmetry (Ashman et al. 1987, 1988; Conwin & Mehrabadi 1989; Nomura et al. 2003). A transverse system has 5 independent constants and for an orthotropic elastic material there are 9 independent properties: three elastic moduli, three Poisson's ratios and three shear moduli respectively for the three axes. In case the material is fully anisotropic, 21 independent components are required. Since 4 coefficients at most can be obtained from a test, there would be the need to test at least three identical specimens.

The difficulty for measuring the mechanical properties of the mandibular bone comes from the fact that bone is a highly heterogeneous and anisotropic material, although cortical bone is less heterogeneous than trabecular bone. Cancellous bone mechanical properties may vary from patient to patient or bone to bone by a factor of 2-5 (Rho et al. 1998) because of porosity, mineralization level and organization of the solid matrix (Bayraktar et al. 2004; Currey 2004). Moreover the need to test small specimens, aimed to reduce the inner heterogeneity, requires the use of specially designed extensometers attached to the specimen. Therefore platen displacements are often used resulting in end-effects obscuring the results (Brown et al. 2010).

This explains why, when elastic properties have been measured experimentally, independently from the type of modelling used, they can manifest a substantial difference depending on the position, the freshness, age of the subject and testing method used.

Although the present study focuses on a biomechanically and morphologically correct approximation of the bone made of two materials only, in an ultimate analysis, the author suggests to improve the quality of a linear isotropic finite element model of the human mandible (for implantology or image-guided surgery) through mapping the mechanical properties of micro-regions of the bone via local densities.
Such a model, in which each finite element is assigned accurate specific material properties, will refine the approximation used in other sections of this work and other previously published work where only two material properties have been assigned to cortical and cancellous bone.

2.3.2 Loading and boundary conditions

The elastic properties of a material are identified by: Elastic (or Young's) modulus, Shear modulus (or modulus of rigidity), Poisson's ratio and Bulk modulus. Using these properties it is possible to correlate the deformation which occurs in solid structures under a given load.

According to the Hooke's law the relation between stress (σ) and strain (ε) in a linear elastic isotropic material is:

$$\varepsilon_x = \frac{\sigma_x - \nu\sigma_y}{E}$$
$$\varepsilon_y = \frac{\sigma_y - \nu\sigma_x}{E}$$
$$\varepsilon_z = \frac{-\nu\,(\sigma_y+\sigma_x)}{E}$$

while for an isotropic material the elastic material properties are related by:

$$G = \frac{E}{2\,(1+\nu)}$$
$$K = \frac{E}{3\,(1-2\,\nu)}$$

with:

E: Elastic (or Young's) modulus;

G: shear modulus (or modulus of rigidity);

ν: Poisson's ratio;

K: Bulk modulus.

σ_x: stress component on the horizontal axis;

σ_y: stress component on the vertical axis.

Hence two independent parameters are sufficient to identify the stiffness of a solid: Young's Modulus and Poisson ratio.

Although Young's modulus and Poisson ratio are used as independent variables to calculate the stiffness matrices of the elements in the FEM, the author found opportune to include the Poisson ratio to correct the calculation of the Young Modulus from apparent density. The reason and the method, as given by Brown et al. (2010) and as it will be explained

Table 2.1 Elastic moduli found by different studies for human femoral cortical bone.

Author	Method	E (GPa)	Bone Status
Bayraktar et al. 2004	Tension	11-24	wet
Currey 2004	Tension	16.7	dry
Kaneko et al. 2003	Tension	19.3-26.3	wet
	Compression	20.4-26.4	wet
McCalden et al. 1993	Tension	9-21	wet
Reilly & Burnstein 1975	Tension	15.6-18.3	wet
Reilly et al. 1974	Tension	11.4-19.3	wet
	Compression	14.7-19.7	wet

further, relies on the uncertainty of the relation found by Carter and Hayes (1977) which uses the "classic strain" in the E formula and does not take into account the "plane stress".

Young's Modulus is the variable which quantifies the ability to withstand the stress generated by loading. Over many years there have been numerous attempts to experimentally determine the mechanical properties and specifically the **E** for both cortical and cancellous bone.

2.3.3 Cortical bone variations

Most of the experimental tests conducted to measure the elastic modulus in cortical bone have used relatively long sections of machined femoral bone.
In the decades before their work, Reilly & Burstein (1974) estimated that researchers measured Young's Modulus for cortical bone in the range 6-28 MPa. Values obtained from other researchers are summarized in Table 2.1.

Although no significant differences between tensile and compressive experimental setups have been reported for E (Reilly et al. 1974, Kaneko et al. 2003), it has been shown that cortical bone is stronger in compression then in tension, as outlined in Table 2.2.

Currey (2004) found that cortical bone with higher Young's modulus also has higher tensile yield stress, while its yield strain did not vary with Young's Modulus. These results suggest how bone yields at a particular strain rather than a particular stress.

Table 2.2 Mechanical properties measured for femoral cortical bone by different studies.

Author	**Method**	**Yield Stress (MPa)**	**UTS (MPa)**
Kaneko et al. 2003	Tension	84	96
	Compression	153	162
Reilly & Burnstein 1975	Tension		129
	Compression		193

Table 2.3 Relation between age of the subject and mechanical properties of the cortical bone.

Author	**Age**	**E (GPa)**	**UTS (MPa)**	**Ult. Strain (%)**
Burnstein et al. 1976	40-49	17.7	139	3.0
	80-89	15.6	120	2.4
McCalden et al. 1993	45		107	2.8
	85		82	1.5

Another cause of variation in the measured mechanical properties of the cortical bone is the age add gender of the subject, as described by Carter & Spengler (1978) and Keaveny & Hayes (1993) or by Burnstein et al. (1976) and McCalden et al. (1993). Results relative to these last studies are reported in Table 2.3.

2.3.4 Cancellous bone properties

The mechanical properties of cancellous bone are highly dependent on direction of loading, showing differences in case the applied force is aligned with the trabeculae or not.
This behaviour has been accurately observed by Cody et al. (1996) whose results for elastic modulus and ultimate tensile stress are summarized in Table 2.4.

It must be noted that the stiffness of the cancellous bone can be measured at a microscopic scale or “tissue level” using single trabeculae as specimens or at a larger scale where a portion of bone containing several trabeculae is tested (Brown et al. 2010).
In the first case nanoindentation and acoustic microscopy methods should be used to assess bone elasticity (Jirousek 2012).

Table 2.4 Range of femoral cancellous bone mechanical properties found by Cody (1996) (values are in MPa); AP: antero-posterior direction; ML: medial-lateral direction; IS: inferior-superior direction.

		Orientation	**Mean (MPa)**	**SD (MPa)**
NECK	E	AP	193	159
		ML	176	126
		IS	194	153
	UTS	AP	4.29	3.7
		ML	3.72	2.36
		IS	5.81	4.5
HEAD	E	AP	202	211
		ML	161	135
		IS	210	162
	UTS	AP	4.14	3.73
		ML	3.59	3.42
		IS	6.47	5.37

In a two-dimensional finite element model of the mandible focused on bone-implant interfaces, elaborated by Guang et al. (2009), it was shown how significant are the assumptions made on the thickness of the cortical bone, and therefore the ratio between cortical and cancellous bone type.

Using average standard values for the Young modulus of the two bone types (respectively $E_{cor} = 13GPa$ and $E_{can} = 7GPa$), Guang found that as the thickness used to model the cortical bone decreases, the ability of the cortical bone to support the load also decreases and therefore the magnitude of the stresses in the cancellous bone increases. From an engineering design point of you this is obvious and expected.

This behaviour is explained in the Figure 2.3 which summarises the findings of Guan's research work.

This finding supports the author's attention to the approximations made during the segmentation process to separate the cortical from the trabecular bone (shown in Figure 2.4, leading to the necessity of finding an alternative solution to the two-bone (cortical-cancellous) modelling approach, as visually explained in Figure 2.5 .

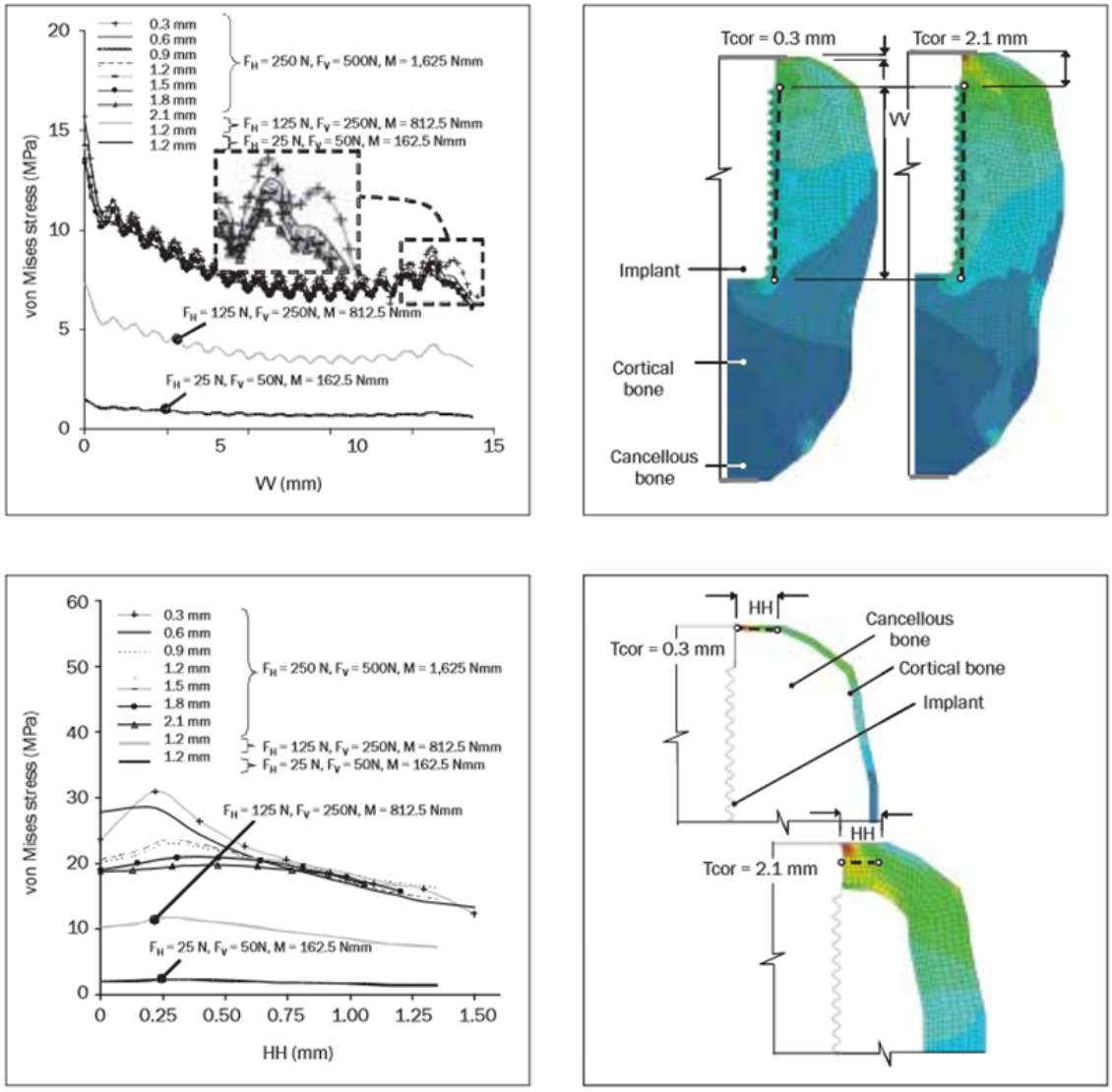

Fig. 2.3 Stress profiles along bone-implant interface with varying thickness assigned to the cortical bone (From: Guan et al. 2009). The plots report the equivalent stress variation (von Mises) on the bone interfacing respectively the implant proximal and longitudinal surface. Each curve is associated to a specific set of load application. Distances in longitudinal (VV) and radial direction (HH) from the implant head are reported in the horizontal axis.

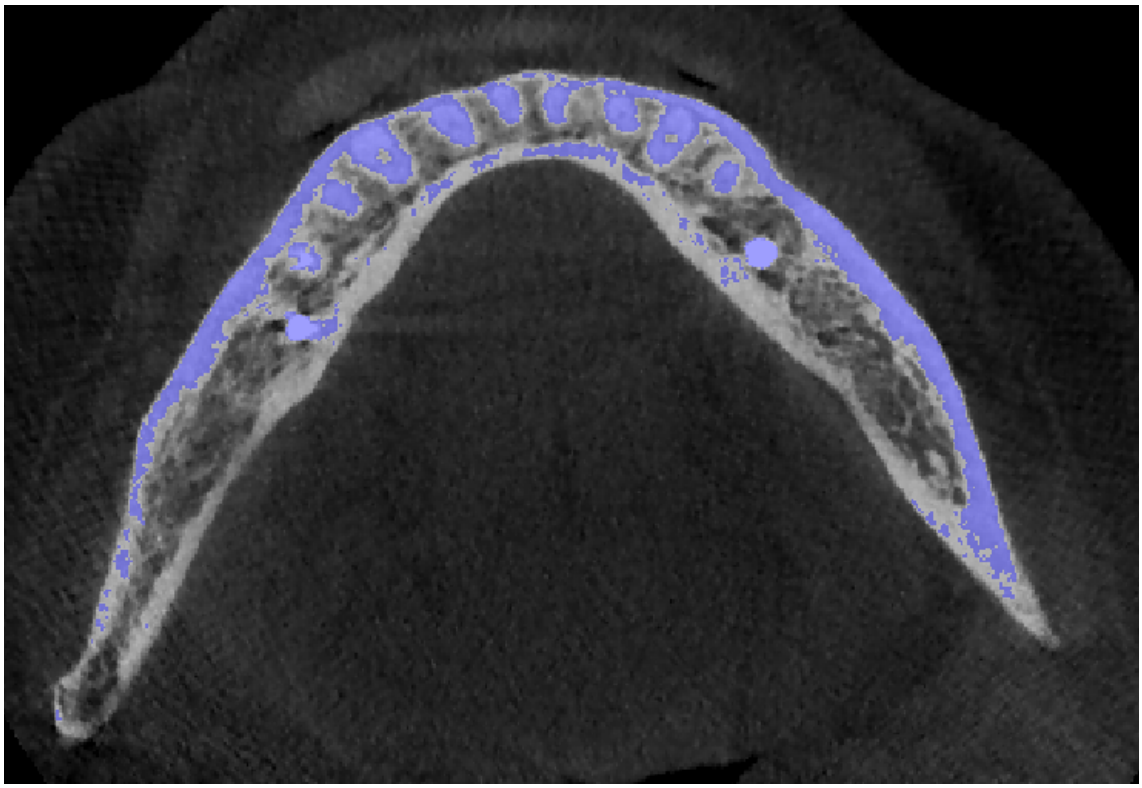

Fig. 2.4 Example of segmentation using a “threshold” function. This picture shows how the separation between cortical and cancellous bone is not easily detectable, neither via morphology nor via density (in this case CT numbers above a certain threshold value are coloured in violet).

2.3.5 Interface between bone types

Through an accurate segmentation of the mandibular bone from CT scan data denser areas can be identified against regions in which most likely trabecular bone, bone marrow, blood vessels, nerves or tendons are present.

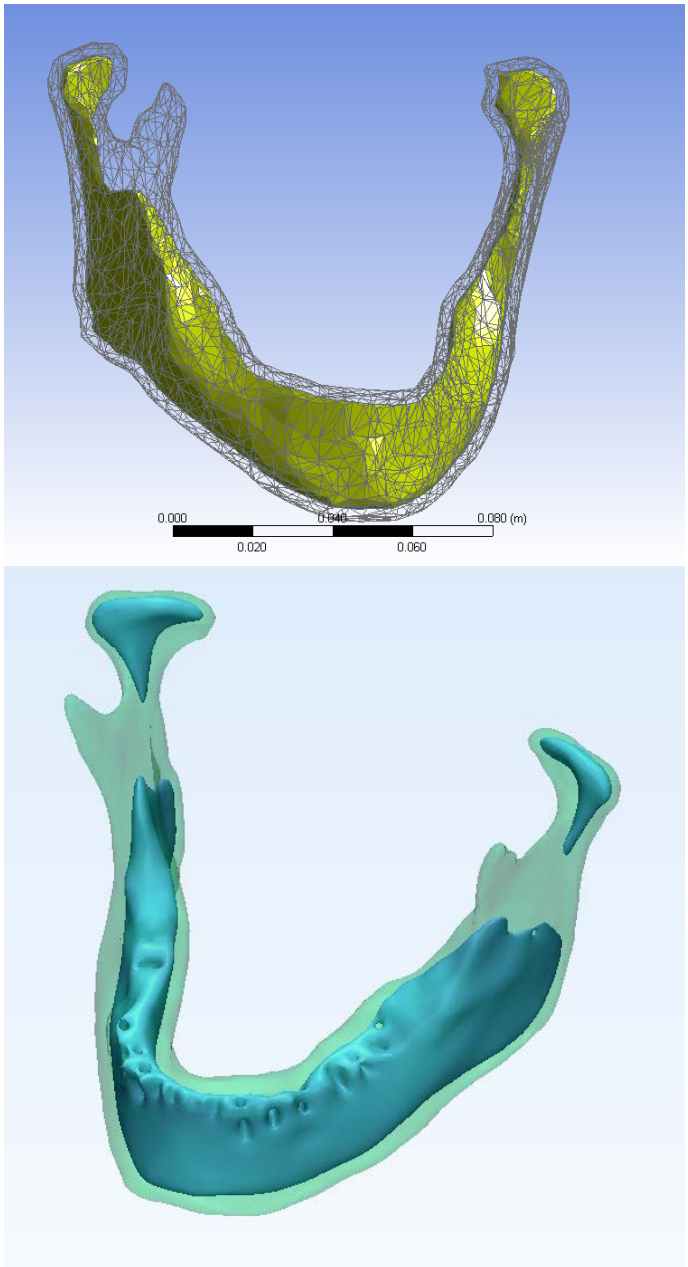

Fig. 2.5 Examples of cortical-cancellous bone model approximation prepared in Amira and visualised in Ansys softwares.

Because of the limited instruments available in segmentation editors, the variable resolutions of Computed Tomography scanners and the multiple slice reconstruction options, identifying the boundary region between cortical and dense cancellous bone, can

be subject to interpretation.

Moreover, additional inaccuracies can be encountered because of the eventual presence of existing dental implants, restorations or the preferential deflection of low energy tissues (Lewis et al. 2013). In addition it has been reported that artefacts could be present in the region to be segmented due to x-ray beam "hardening effects" (Schuller et al. 2015).

Under the circumstances and problems encountered, the majority of the mandibular models found in literature reverse engineer the human jaw using solid models: one for the cortical bone and another one for the trabecular bone based on femoral bone modelling proposed in 1980's. (Ben-Nissan 1987: Kitagawa 2005, Li 2009, Barao 2009, Bujitar 2010, Qian 2009, Ding 2009, Okumura 2010). Both models are prepared either in direct contact with the engineered model of the dental implants or through an interface region generally modelled as an offset of the surface of the implant.

2.3.6 Choice of material properties

Mechanical properties were obtained from previously published values and all materials were assumed to be uniform, linear and isotropic to facilitate a comparison with earlier models (Ben-Nissan 1987; Choi et al. 2005 and 2014). Additional information on the material properties used will be given in Chapter 3 where specific FEMs will be analysed and discussed.

2.3.7 Biomechanical considerations

Muscle forces have been assigned according to Ben-Nissan's study (1987) on a biomechanically correct loads set for clenching and wide opening functional movements.

Additional forces have been distributed according to the specific biomechanical scenario that the FEM of the mandible was applied to. For example, as analysed in Chapter 3, modelling the mandible during the tomographic scan or surgery while a surgical tool is in place requires the introduction of external forces acting on additional solid components connected to the anatomy.

Table 2.5 Reference system used for the FEM.

X axis	line joining geometrical centres of condyles
Y axis	perpendicular to x axis on the parallel to the occlusal plane
Z axis	perpendicular in the origin to X and Z axis

In general, for the whole duration of the simulations the mandible was considered in static equilibrium conditions, using the reference system described in Table 2.5.

Static equilibrium is given by solving the system formed by the vectorial equations for F_{BL} and M_{BL},

$$0 = F_{BL} + \sum_{n}(F_n) + F_{CL} \tag{2.1}$$

with F_n n-muscle force, F_{CL} condyles reaction and F_{BL} left bite force, and

$$0 = M_{BL} + \sum_{n}(M_n) + M_{CL} \tag{2.2}$$

with M_n n-momentum generated by the n-muscle force, M_{CL} momentum generated by the condyles reaction forces and M_{BL} momentum generated by the left bite force.
Differently from previously published models, uniquely in this work all forces and loads were applied and distributed to surfaces corresponding to the anatomically correct muscle attachment areas.

2.3.8 Algorithm for assigning nodal forces

The finite element model was pre-processed in Ansys (Ansys Inc., Cecil Township, USA) and exported into a neutral ASCII file. A dedicated algorithm was written in a C++ console application which processed the nodal loads. Through this module the forces acting on individual mesh nodes were calculated and equation 2.1 was solved for the variable F_{BL} applied in the centre of gravity of the left bite force application area.
Because of the additional degrees of freedom introduced by the use of areas instead of

nodes for load application, the model presents a non-zero resultant momentum whose influence on the simulation results is mitigated by adding soft springs uniformly distributed throughout the structure. This prevents any potential rigid body motion in the simulation setup.

2.4 Use of subject-specific material properties derived from CT scan data

One of the advancements that this research brings is the option to critically use local material properties derived from CT data to estimate the stiffness of the human mandible. This consists of a procedure which is able to convert HU values to densities and densities to local elastic moduli used to define the stiffness matrix of finite elements of the mesh.

2.4.1 Relation between HU and Density

One of the most prominent studies trying to find a law which correlates bone apparent density with CT numbers was undertaken by Rho in 1998. Rho specifies how a preliminary correction to the raw tomographic scalars has been made so that Hounsfield Units relative to a specific scan can be calculated as:

$$HU = 1000\,\frac{CT - CT_{water}}{CT_{water} - CT_{air}} \tag{2.3}$$

where CT_{water} and CT_{air} are the raw CT values of respectively a water sample contained in the field of view and air as averaged in a small volume of the scan (see Figure 2.6).

For this current study, a voluntary patient from University of Bologna was asked to keep a small water balloon in his mouth during the CT scan. Before the segmentation process, the values of the CT numbers in 10 locations within the balloon were averaged to calculate CT_{water}.

For the present study it was found that:

$$CT_{water} = 54$$

$$CT_{air} = 1024$$

which generates the following correction law:

$$HU = 0.93\,CT - 0.05 \tag{2.4}$$

Fig. 2.6 CT numbers correspondent to water are averaged over the scanned volume of a little water balloon (here circled in yellow) kept in the patient's mouth.

Since taking into account different bone types on a large number of samples, Rho's study is considered to have a high relevance in establishing a relation between HU and density. The relations for density $\rho(Kg/m^3)$ found by Rho are summarized in the Table 2.6 according to the specimens location.

Choosing cancellous bone for the investigation during the measurements resulted in a high experimental correlation for a wider range of densities. The superior correlation supports Rho's thesis for which CT numbers are a function of porosity rather than variations in mineralisation of the bone matrix.

Moreover, this thesis is in line with the author's assumption for which the cortical bone is a less porous and denser version of the cancellous bone.

Table 2.6 Relationship between CT numbers (expressed in HU) and density $\rho(Kg/m^3)$ for specimens from cancellous bone from different anatomical locations (modified from Rho 1998).

Proximal tibia cancellous bone	$\rho = 0.916\,CT + 114$
Proximal femur cancellous bone	$\rho = 1.067\,CT + 131$
Distal femur cancellous bone	$\rho = 1.205\,CT + 139$
Proximal humerus cancellous bone	$\rho = 0.624\,CT + 173$
Lumbar spine cancellous bone	$\rho = 1.122\,CT + 47$

In line with the relation found by Rho, Bujtar (2010 and 2014) uses the equation below to correlate bone density with Hounsfield Unit values from the CBCT image in case of mandibular bone:

$$\rho(Kg/m^3) = 1.14\,HU + 309 \tag{2.5}$$

After a dedicated review of the studies published so far on the correlation between elasticity and density for cancellous and cortical bone (summarized in Table 2.7) the author has decided to adopt Carter & Hayes's law (1977) for this study. This law is, in fact, the most referenced work in subject-specific Finite Element models (Schileo et al. 2007), which incorporated the ones by Bitsakos et al. (2005), Keyak et al. (1993), Ota et al. (1999), Perillo-Marcone et al. (2004), Taddei et al. (2004), Weinans et al. (2000) and Wong et al. (2005).

Assuming that the cancellous bone is a two-phase porous material, Carter and Hayes (1977) determined experimentally the constants A and B in the following power law:

$$Y = A\,(\rho)^B \tag{2.6}$$

where Y is a mechanical property (strength or Young Modulus) and ρ is the apparent dry density, calculated as the dry weight divided by the specimen volume (Keller et al. 1994, Keyak et al. 1994). In case of compressive Young's modulus they found the relationship:

$$E = E_c\,\varepsilon^{0.06}\,(\frac{\rho}{\rho_c})^3 \tag{2.7}$$

Table 2.7 Modulus-density relationships according to several studies published in literature (from Helgason et al. 2008).

Modulus–density relationships in the cited studies

Study	Site	Type of bone	Densitometric measure	ρ-range (g/cm^3)	E (GPa)	Test condition	Geometry $B \times W \times L$ or $D \times L$ (mm)	Strain rate (s^{-1})	n	R^2
Carter and Hayes (1977)	Pooled	Cortical and trabecular	ρ_{app}	0.07–2.0	$E = 3.79\dot{\varepsilon}^{0.06}\rho_{app}^{3}$	Confined compression	20.6 × 5	0.001–10.0	124	NR
Lotz et al. (1990)	Human femoral neck	Trabecular	ρ_{app}	0.18–0.95[RFG]	$E = 1.310\rho_{app}^{1.40}$	Platen	9 × 5	0.03	49	0.91
Lotz et al. (1991)	Human femoral metaphysis	Cortical	ρ_{app}	1.20–1.85[RFG]	$E = -13.43 + 14.261\rho_{app}$	3-Point bending	7 × 5 × 0.4	0.05	123	0.67
Snyder and Schneider (1991)	Human tibial diaphysis	Cortical	ρ_{app}	1.748–1.952	$E = 3.891\rho_{app}^{2.39}$	3-Point bending	2 × 2 × 40	0.001	45	$r = 0.75$[a]
Hodgskinson and Currey (1992)	Pooled	Trabecular	ρ_{dry}	0.094–1.111	$E = 3.98\rho_{dry}^{1.78}$	Platen	NR	0.0011–0.0033	57	0.91
Linde et al. (1992)[b]	Human proximal tibia	Trabecular	ρ_{app}	0.273[c]	$E = 4.778\rho_{app}^{1.99}$	Platen	7.5 × 7.5	0.01	31	$r = 0.89$[a]
Anderson et al. (1992)	Human proximal tibia	Trabecular	ρ_{dry}	0.14–0.48[RFG]	$E = 3.890\rho_{dry}^{2.0}$	Platen	10 × 10 × 20	0.01	31	NR
Dalstra et al. (1993)	Human pelvis	Trabecular	ρ_{app}	0.109–0.959	$E = 2.0173\rho_{app}^{2.46}$	Platen	6.5 × 6.5 × 6.5	0.001	57	0.58
Keller (1994)	Human spine	Trabecular	ρ_{ash}	0.028–0.182	$E = 1.89\rho_{ash}^{1.92}$	Platen	10 × 10 × 10	0.01	199	0.702
Keller (1994)	Human femur	Cortical and trabecular	ρ_{ash}	0.092–1.221	$E = 10.5\rho_{ash}^{2.29}$	Platen	8 × 8 × 8	0.01	297	0.849
Keller (1994)	Pooled	Cortical and trabecular	ρ_{ash}	0.028–1.221	$E = 10.5\rho_{ash}^{2.57}$	Platen	8 × 8 × 8 10 × 10 × 10	0.01	496	0.965
Keyak et al. (1994)	Human proximal tibia	Trabecular	ρ_{ash}	0.06–0.27	$E = 33.9\rho_{ash}^{2.20}$	Platen	15 × 15 × 15	0.01	36	$r = 0.916$[a]
Goulet et al. (1994)	Pooled	Trabecular	BV/TV	0.06–0.36	$E = 6.310(\mathrm{BV/TV})^{2.10}$	Platen	8 × 8 × 8	0.01	104	0.88
Keaveny et al. (1997)	Human lumbar spine	Trabecular	ρ_{app}	0.09–0.28	$E = 1.540\rho_{app} - 0.058$	End-caps[d]	8 × 16	0.005	9	0.64
Li and Aspden (1997)	Human femoral head	Trabecular	ρ_{app}	0.14–1.4	$E = 0.573\rho_{app} - 0.0094$	Platen	9 × 7.7	0.0033	49	0.59
Ouyang et al. (1997)	Human vertebra	Trabecular	ρ_{app}	0.46–0.71	$E = 2.3828\dot{\varepsilon}^{0.07}\rho_{app}^{1.88}$	Platen	10 × 10 × 24	0.00001–0.001	36	NR
Kopperdahl and Keaveny (1998)	Human vertebra	Trabecular	ρ_{app}	0.11–0.27	$E = 2.1\rho_{app} - 0.08$	End-caps[d]	8 × 16	0.005	44	0.61
Ciarelli et al. (2000)	Human proximal femur	Trabecular	BV/TV	0.15–0.40[RFG]	$E = 7.541(\mathrm{BV/TV}) - 0.637$	Platen	8 × 8 × 8	0.01	32	0.88
Morgan et al. (2003)	Human vertebrae	Trabecular	ρ_{app}	0.11–0. 35	$E = 4.730\rho_{app}^{1.56}$	End-caps[d]	8 × 16	0.005	61	0.73
Morgan et al. (2003)	Human proximal tibia	Trabecular	ρ_{app}	0.09–0. 41	$E = 15.520\rho_{app}^{1.93}$	End-caps[d]	8 × 16	0.005	31	0.84
Morgan et al. (2003)	Greater trochanter	Trabecular	ρ_{app}	0.14–0. 28	$E = 15.010\rho_{app}^{2.18}$	End-caps[d]	8 × 16	0.005	23	0.82
Morgan et al. (2003)	Human femoral neck	Trabecular	ρ_{app}	0.26–0. 75	$E = 6.850\rho_{app}^{1.49}$	End-caps and platens[d,e]	8 × 16	0.005	27	0.85
Morgan et al. (2003)	Pooled	Trabecular	ρ_{app}	0.09–0. 75	$E = 8.920\rho_{app}^{1.83}$	End-caps and platens[d,e]	8 × 16	0.005	142	0.88
Kaneko et al. (2004)	Human distal femur	Trabecular	ρ_{ash}	0.102–0.331	$E = 10.88\rho_{ash}^{1.61}$	Platens	15 × 15 × 15	0.01	49	0.775

Young's modulus (E) in GPa and density in g/cm^3. NR = not reported. RGF = read from graph. R^2 = determination coefficient.

[a] Pearson correlation coefficient, as reported in the original work.

[b] Reported results are for cylindrical specimens with diameter of 7.5 mm and a height of 7.5 mm. These specimens gave the highest correlation. In addition, mineral oil was used to eliminate frictional effects on the specimen–anvils interface.

[c] Average value. Range not reported.

[d] The free length of the bone specimen between the end-caps was reported.

[e] Fourteen specimens were tested in compression with platen end-conditions due to experimental difficulties.

Table 2.8 Experimental relationships between elastic modulus and strain rates.

ε	a
0.001	2.504
0.01	2.875
0.1	3.301
1	3.970

with E = compressive Young's Modulus in MPa, E_c = compressive Young modulus of compact bone with apparent density ρ_c tested at strain rate 1.0 Hz.
Using $E_c = 22.1GPa$ for compact bone with $\rho = 1.8\ g/cm^3$ the expression becomes:

$$E(GPa) = a\,\rho^3\,(\frac{\delta\varepsilon}{\delta t})^{0.6} \tag{2.8}$$

where: $a = 3.790$

$\rho : density$

$\varepsilon = \frac{\delta\varepsilon}{\delta t} : strainrate$

Since this relation will be used in a static structural finite element model, the influence of strain rate is considered negligible as the mandible will deform in quasi-static conditions. Table 2.8 shows the results for equation 2.8 at different strain rates.

Brown et al. (2010) applied an important correction to the apparent elastic modulus related to the Poisson ratio. The reason for this correction is that Carter & Hayes (1977) used the classic strain in the E formula and they did not taken into account the plane stress. Their original mechanical compression tests, in fact, were conducted under uniaxial strain conditions, not uniaxial stress.
Brown believes that Carter & Hayes's study did not correct for the plane strain condition when calculating Young's modulus from the experimental results. Therefore, for an apparent Young's modulus measured in the plane strain condition, E_{app}, the true Young's modulus E measured in the plane stress condition is given by:

$$E = E_{app}\frac{(1+\nu)(1-2\,\nu)}{(1-\nu)} \tag{2.9}$$

Given the difference range for Poisson ratio for denser cortical bone and cancellous bone, the author decided to use the following two laws for deriving Young's modulus from local density for cortical and cancellous bone:

$$E = E_{cor} = 0.74\,E_{app}\;(\nu = 0.3) \tag{2.10}$$

$$E = E_{can} = 0.47\,E_{app}\;(\nu = 0.4) \tag{2.11}$$

The possibility of applying an analytical correction for plane stress testing conditions is another reason why the author has chosen to use Carter and Hayes's law over relations found in other comprehensive studies.

Keller (1994), by way of example, found a similar law for femoral specimens:

$$E(GPa) = 10.5\,\rho^{2.57} \tag{2.12}$$

where ρ is the apparent dry density.

In that experimental setup, Keller (1994) used oil in the interface between the specimen and the compression testing jaws, which would make the correction for plain stress above not applicable. Moreover, Keller tested the specimens along their primary load axis only, which does not reflect the loading conditions the mandible is subject to during functional movements.

On this topic, Morgan et al. (2004) acknowledged how the anatomical site is significantly related to the bone tissue properties and their relation with density. Using a testing protocol

which minimises random error, it is found that:

$$E(GPa) = 6.950\,\rho^{1.49} \tag{2.13}$$

Although the robustness of Morgan's study, the author has decided not to adopt this law since it was obtained testing specimens with densities in the limited range $0.25 - 0.75\ g/cm^3$. On the contrary, mandibular cortical bone has been measured to reach densities of at least $\rho = 1.8\ g/cm^3$ (see Table 2.7).
The author believes that Carter & Hayes's work (1977) should also be used only considering which bone type it applies to. In this case, the association between density and elastic modulus (Lewis et al. 2013) needs to suit a whole mandibular bone.

Because of the natural curved shape of the human jaw it is not possible to obtain straight specimens for trabecular and hard bone which can then be tested via a traditional four points bend test. This is why pulse ultrasonic technique has been used to measure the elastic properties of cortical and cancellous bone (Rho 1998; Nomura 2001), allowing smaller samples to be tested. Because of the reduced size, average measurement of density would also be more relevant.

Using this method Rho (1998) confirmed that mechanical properties of both cortical and cancellous bone depend on porosity, architecture and bone mineral density. However, it is also found that although power fits approximate for the relationship between density and cancellous bone, linear relationships are the best predictors for axial moduli from the density of cortical bone.
Moreover, Rho finds that there is a difference in slope for the axial modulus versus the density for cortical bone for different parts of the body. Given that this behaviour is not present in the cancellous bone, it becomes evident how it is important to adopt different relationships for different bone types to derive elastic modulus from bone density.

According to the description of cancellous bone given at the beginning of this Chapter, the author proposes to keep Carter & Hayes's assumption for which cortical bone is simply denser cancellous bone. But it is also favourably concluded that CT scalars must be considered as a function of the porosity of the bone rather than a variation of the

mineralisation in the bone matrix. This would explain the higher correlation found by Rho between density and elastic modulus in case of porous cancellous bone with respect to cortical bone.

2.4.2 Mapping density and elasticity

In order to map the material properties of the mandibular model in this study a software application called Bonemat was utilised (Zannoni 1998; Taddei 2004 and 2007).
Bonemat has been developed for computational bone biomechanics by Istituto Ortopedico Rizzoli in Bologna, Italy, as a tool for mapping on a meshed bone model the elastic properties derived from Computed Tomography data.

The CT images and the finite element mesh were imported into the software and fused into a coherent representation. The product was exported as an updated FE mesh once the bone properties had been mapped.
A "VMEmesh" (Taddei 2004), which is a volumetric data structure able to store scalars for each voxel in the volume, was created directly from an Ansys ASCII archive (.cdb file) as prepared in Ansys software. The importer module correctly interprets data relative to nodes, linear and quadratic solid elements and material cards. For each element information regarding its static, mechanical, thermal or electrical properties is stored into a dedicated data structure.

Average material properties derived from the Hounsfield Unit (HU) of the tissue in that region were assigned to the finite elements of the bone mesh. This FE pre-processing operation resulted in a heterogeneous model based on the density information derived from the CT scan dataset. Density values were extracted from the CT numbers by using the relations discussed in the previous sections and applying a correction to compensate calibration errors due to the specific machine used for the tomographic acquisition.
From the HU-derived bone density the elastic modulus was calculated after a densitometric calibration. Up to three density-elasticity relationships corresponding to different density ranges and therefore potentially different bone types were specified.
The skeleton of the Bonemat algorithm is the numerical integration that maps the voxel-

wise properties of the CT grid to element-wise properties of an unstructured mesh grid. Input and output data within Bonemat are "VMEs". The VME is a node in a hierarchical tree which features a procedural core and generates an output data structure storing a pose matrix and a VTK (Visualisation Toolkit, www.vtk.org) visual dataset. The VME also generates an absolute pose matrix, which is an algebraic matrix representing the pose of the VME in the world reference system.
The input data were a VMEvolume derived from a stack of images of a mandibular CT scan in DICOM format and a VMEmesh.
The output of the operation was an updated VMEmesh in which each element had been assigned an elastic modulus value. Generated elements were grouped by their material card (which is the section of the neutral file containing the material properties) and could be classified by stiffness or density. An additional output was given, in terms of a frequency file, which listed how many elements shared the same elastic modulus.

The Bonemat application is non-dimensional, so the user is responsible for setting coherent measurement units to the variables. Using the discussed relations between density from CT numbers and elastic modulus from density, the following units for respectively input and output were used:

Density: g/m^3

Young/Elastic modulus: MPa

A minimum gap between two material cards was set. For example, given a typical elastic modulus range in the order of 50 to 20000 MPa, the user may want to avoid defining 19950 different materials but rather group them each e.g. 500 MPa, resulting in maximum 40 material cards.

By default, elastic moduli were assigned by Bonemat starting from the highest modulus among each element and then grouping to that value all elements within the specified "gap value". Then the algorithm searched again for the highest value among the remaining elements and looped until all elements were assigned an elastic modulus. This means that the distance from two consecutive elastic moduli bins was not necessarily the gap value.

Once the material properties had been assigned according to the CT values, as shown in Figure 2.7 the mesh was exported back to Ansys for the remaining finite element pre-processing operations: assigning boundary conditions, loads, solver type, inertia relief and non-linear deformation controls.

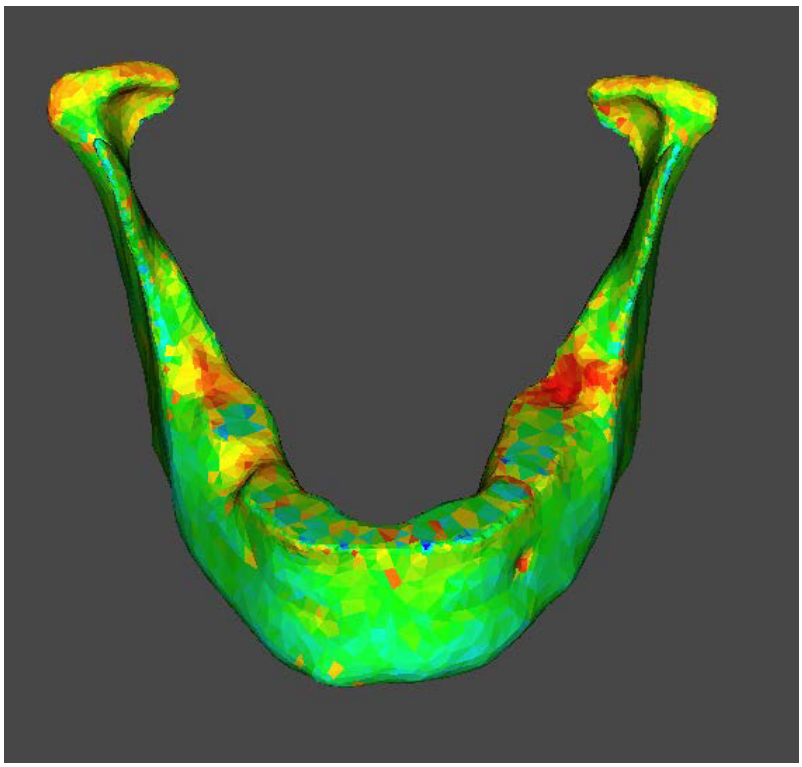

Fig. 2.7 Representation of the mesh in Bonemat after material properties have been assigned and mapped via Young's moduli. The different colours correspond to different material types.

2.5 Applications of the FEA

The FEM prepared is able to reproduce the mandibular morphology, structure and material properties at different levels of approximation. Moreover, the reverse-engineered models can be combined with CAD objects designed to model implantable components or tools used during surgery.

In force of its versatility and of its solid scientific background, the generic FEM could be applied to simulate realistic clinical scenarios.

Among these there is the simulation of the biomechanical impact on the human mandible of reference tools for surgical navigation and the modelling of different surgical techniques

deployed for full-arch restorations. Both simulations, together with the implications of their results on implant osseointegration, will be discussed in the following Chapters.

Chapter 3

FEM application to a new surgical navigation system reference frame

3.1 Introduction

The current navigation systems used in oral surgery which will be further reviewed in Chapter 5 utilise tools for aligning the virtual plan with the patient which are either quite invasive or reduce visibility and bone inspection capabilities.
At the same time, the accuracy of tracking oral anatomy in a patient is compromised by asynchronous movements of the mandible during surgery.
For these two reasons, the choice of the configuration and mechanics of the registration tools plays an important role in the overall success of the surgical procedure like an implant insertion in the mandibular or maxillofacial region.

As it will be further reported in Chapter 6, miniaturised components for patient's registration and instrument calibration have been developed for an innovative live tracking system. One of the aims of this development has been to limit the restrictions to the implant site imposed by a foreign device which might be introduced while trying to promote accuracy.

This Chapter explains the methodology and results of the analysis of the biomechanics of the mandible during the tomographic scan and a surgical procedure while a miniaturised

reference tool for patient alignment is in place. It also shows how the FEM used to generate a realistic simulation is based on a subject-specific anatomy and a biomechanically correct set of muscular forces.

In the following Chapter it is demonstrated that the stresses and distortions found for the bone (hosting the implants) are comparable with the previously published clinical data. The high accuracy given from the navigation procedure in implant placement (as illustrated in Chapter 6) also proves the effectiveness of the reference assembly system.

It will be shown that the proposed computerized navigation system (using mounted miniaturised reference frame with fiducial markers) enables more accurate and safe implant placement in both the lower and upper human jaw that increases the long term success rate.

3.2 Background

Due to the complexity of the underlying anatomy and biomechanics, oral and maxillofacial surgery often requires a highly skilled experienced surgeon for the operations to be accurately performed.

Currently a series of surgical planning techniques based on three-dimensional imaging are utilized to assist the surgeons to improve the surgical outcomes. The surgical difficulties arise in the assessment of the intraoperative position, misidentification of skeletal contours around the mandibular anatomy and the skull base (Bell 2010) and isolation of the alveolar nerve and the blood vessels distributed in the maxillary sinus. In addition, inserting an implant requires taking into account the quality of the bone in the surgical site.

Recent developments in 3D analysis using Computed Tomography (CT) and surgical simulation methods have managed to provide additional accuracy in the diagnosis and planning (Somogyi-ganss 2013). The 3D virtualization of an implant insertion, for example, is used to generate the design of surgical drill guides which are then manufactured via 3D printing techniques and deployed during surgery. As a result, the templates assist by identifying and guiding the location, angle and depth of the osteotomy or implant insertion (Eggers et al. 2009).

Although offering additional guidance, the use of a surgical drill guide in oral and maxillo-

facial surgery might result in poor bone visibility and limited intra-oral access due to the reduced inter-occlusal gap. The deployment of such system also requires the temporary fixation of anchor screws into the patient's anatomy (Arisan et al. 2010).
However, as for the cases involving severe atrophic edentulous maxilla, the stability of the drill guide compromises the accuracy of the translation of the preoperative imaging to the operating theatre. In any case this type of computed assisted surgery introduces a delay between the surgical planning and the operation due to the time needed to design and manufacture the template.
In addition to this, the surgical template utilised might interfere with the cutting blades or flutes and there is no substantial procedure to verify its correct placement at the beginning and throughout the duration of the surgical procedure.

A clinical application of intraoperative image-guided navigation seems to overcome the limitations introduced by the use of surgical drill guides.
In addition to the real-time instrument tracking and adequate bone quality inspection, it has been reported that this technology is exceptionally helpful in oral and maxillofacial surgery (Mohagheghi et al. 2014).
The method and the procedure is based on the spatial registration of the intraoperative position of the surgical cutting/socketing instrument with the patient's anatomy previously reconstructed from CT or magnetic resonance images (MRI). Different systems might utilize different technology for tracking: infrared, optical or electromagnetic. All systems require the characterisation of the surgical instrument in use and the image-to-world alignment (Dang et al. 2012) between the patient and the virtual model.

Some current navigation systems for oral implantology perform this registration using physical radiopaque markers which are screwed into the patient's maxilla or lower jaw (Kim et al. 2015; Kang et al. 2014; Chen et al. 2011). Some others use anatomical landmarks as "fiducial" points for the alignment operation while a few of them have designed a planar markers holder supported by the patient's denture (Casap et al. 2004 and 2008). All of the navigation systems for oral implantology reviewed seem to deploy

registration tools which are either quite invasive or/and, as stated earlier, reduce visibility and bone inspection capability.

This current study represents development, analysis and modelling of an innovative system for oral and maxillofacial intra surgical navigation and its use of miniaturised components for patient's registration and instrument calibration, which does not restrict the surgical view or access. While it is shown how the reference tool has been designed to promote stability, its impact on the mechanics of the mandible during the scanning and surgical procedure is evaluated and analysed via a patient-specific finite element simulation.

Problems related to accidental interference during surgery and the effect of the weight of the device on internal mandibular stresses and distortions are also modelled and investigated.

3.3 Materials and Methods

3.3.1 Image-guided Surgery System

The image-guided surgery system presented and analysed in this study has been developed in conjunction with University of Technology, Sydney, BresMedical Pty Ltd (Sydney, Australia) and the University of Bologna (Italy). Differently from other navigation systems found in literature (Lakatos et al. 2014; Pellegrino et al. 2014; Somogyi-ganss et al. 2013), its design and development is specialised for oral and maxillofacial surgery and provides an intuitive set of small registration tools to be routinely and easily used by the practitioners.

A software application was specifically developed within this thesis work specifically for this system and has been designed to run on a processing unit connected to the stereoscopic camera Polaris Vicra (Northen Digital, Toronto, Canada) and a digital display.

Through this software, a scalar volumetric data set is reconstructed from the patient's Cone Beam Computed Tomography (CBCT), MRI or CT scan. In case of oral or maxillofacial implant insertion, the software interface is composed of a 3D rendering view and multiple volumetric slices.

Dynamically interacting with the volumetric cuts the user virtually places and transforms

to accurate positions the desired implants from an embedded library. Virtual denture components associated to the implant are also given for reference to guide the implant positioning and preview the prosthetic result. Once the practitioner has fixed the implants, axis and position of the implants on the panoramic profile become parameters for updating the navigational views.

Implants are automatically selected according to their vicinity to the tracked surgical tip and the orientation of the volume slices is determined by the spatial parameters of the nearest implant.

In order for the navigation system to accurately track and display the drill tips and cutting instruments in their correct position and orientation, the tracking camera must identify the physical position of reflective markers rigidly mounted both on the patient's anatomy and on the instrument itself. Each tool is uniquely identified through the geometrical pattern in which the optical markers are organised. While the reference tool is fixed onto the surgical instrument via an ergonomic saddle, the tool is mounted on the patient via a reference plate connected by a three dimensional joint to the optical markers frame. In case of edentulous patients the reference plate is mounted onto a 3.25mm implant (IBT8.5 manufactured by Southern Implants, Irene, South Africa). For partially edentulous patients the connector can be fixed to a tooth-supported resin template.

When preparing an edentulous patient for surgery and before the CT scan, the surgeon is required to mount a radiopaque reference tool, called fiducial markers plate (FMP), on the connector.

Due to the high contrast offered by of the radiopaque material embedded in the FMP, its geometry is detected by the software during the navigation operation setup to finalise the image-to-world registration. To maximize the accuracy of the registration process the position of the FMP with respect to the patient's anatomy must be preserved between the scan and the surgery.

On its distal end the FMP has a spherical connection to the optical patient reference tool (OPRF) which keeps the reflective balls in their unique configuration. While the FMP can

be used just once for the registration procedure, the OPRF must be maintained in optical direct contact with the tracking camera during navigation.

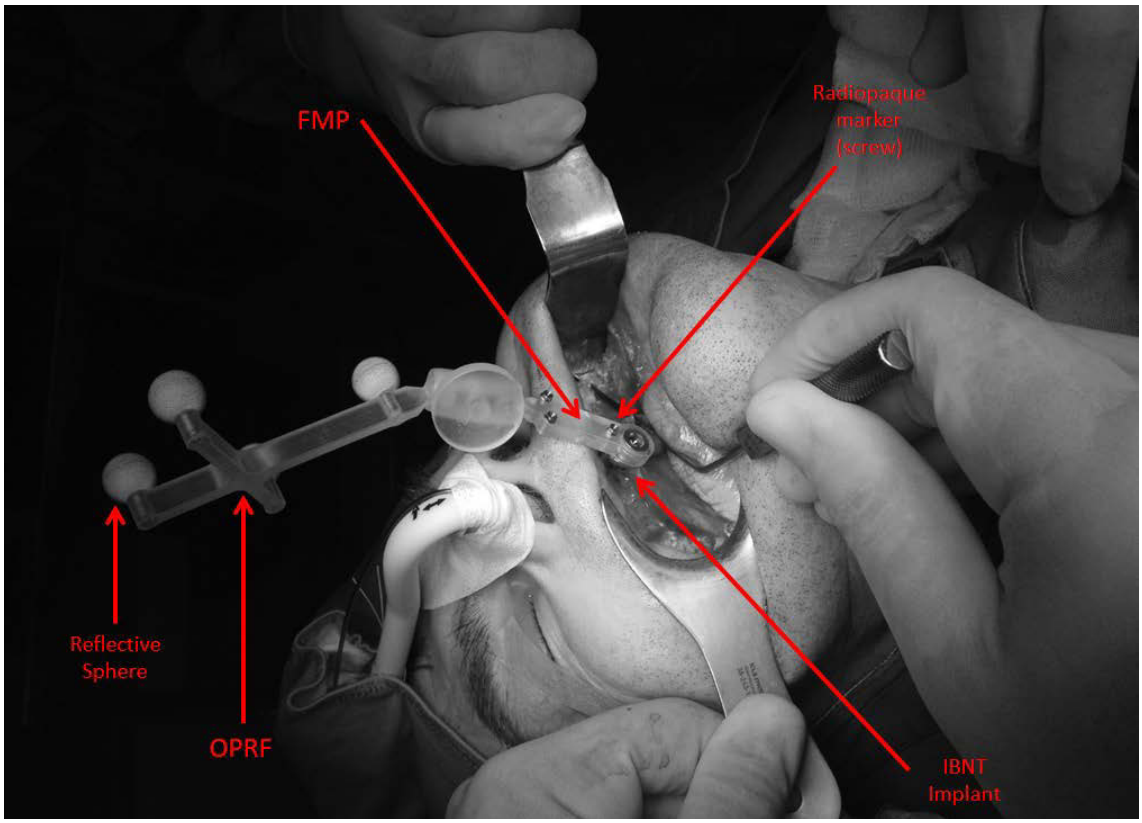

Fig. 3.1 Reference frame assembly for navigation during surgery in case of an edentulous patient showing the components mentioned in section 3.3.1.

A more detailed description of the navigation system is carried on in Chapter 6. Instead in the following sections the author will evaluate the risk impact generated by the presence of the reference tool during the surgery and the forces and stresses which it causes on the patient's anatomy. This analysis will be carried out by applying **the Finite Element Model of the human mandible prepared for clinical applications and described in details in Chapter 2** to the realistic biomechanical scenarios as discussed in the following section.

3.3.2 FEMs and scenarios

Different solid models, boundary and loading conditions have been used in building the following FEMs. First and second molars were chosen to compare with the previously published distortion works under functional loading.

(i) M1a: simulation of stress and distortions in the 1^{st} and 2^{nd} molar region of the mandible during clenching and wide opening using a two-bone approximation

(ii) M1b: simulation of the stresses generated on the implant and the surrounding bone by the attached navigation reference frame during the tomographic scan and the surgical procedure

(iii) M2: simulation of stresses generated on the implant and the surrounding bone by accidentally putting pressure on the reference frame while the patient is in a rest position

(iv) M3: simulation of stress and distortions in the 1^{st} and 2^{nd} molar region of the mandible during clenching and wide opening using local elastic properties derived from CT scan data

3.3.2.1 M1a modelling

The first model uses a "two-bone" approximation, from two materials mapping cortical and cancellous bone. Density and elastic properties were assigned as described in Table 3.1.

Mechanical properties were obtained from previously published values and all materials were assumed to be uniform, linear and isotropic to facilitate a comparison with earlier models (Ben-Nissan 1987; Choi et al. 2005 and 2014). A summary of the material properties used for models M1a, M1b and M2 is reported in Table 3.1.

The biomechanical configurations examined in this study are the ones associated with the mandibular position during the tomographic scan and the actual surgery.

In both these situations, the reference tool for the navigation system is required to be mounted on the patient. In the first case the patient is recommended to keep the jaw in a clench position by mimicking a symmetric biting action. In the second case, during surgery, the patient's mouth must be wide open to grant access to the implant site.

For this reason the functional movements of respectively clenching (symmetric bit-

Table 3.1 Material properties used in the mandibular FEA model for the bone tissues, the implant, the Fiducial Markers Plate (FMP), the Optical Patient Reference Tray (OPRT) and its subcomponents.

	Young's Modulus (GPa)	**Poisson Ratio**
Cortical bone	17.2	0.30
Cancellous bone	1.29	0.30
Implant	107	0.33
FMT	2	0.35
OPRT frame	113	0.34
Reflective spheres	2	0.35
Spheres support	200	0.26

ing) and wide opening have been associated with the two configurations.

As stated earlier the main idea using these two-bones model is to compare the results of the FEM with the ones obtained by previously published models.

For this reason, model M1a uses the same loading conditions from Ben-Nissan's study (1987) since they are considered to be the most realistic biomechanical configuration used in a FEM pre-processing stage available in literature.

Two significant improvements were introduced in M1a:

- the solid model used for the FEM is derived from a segmentation of the CT scan of a living patient, and not reconstructed from a digitization of a cadaver dry mandible
- the loads representing the action of the muscles acting on the mandible have been applied to areas as opposed to nodes since surfaces seem more suitable to simulate muscle attachment regions. From an anatomical point of view this is a more correct approach.

A detailed summary of the three-dimensional force components of applied loads is reported in Table 3.2 and Table 3.3 while a visual representation of the muscle vector forces is shown in Figure 3.2.

The cortical and cancellous bone interfaces were assumed to be perfectly bonded as its natural state.

Table 3.2 Force vectors magnitudes expressed in Newtons for X, Y and Z directions used in this model; abbreviations: **MeL**, Medial Pterygoid Left; **MeR**, Medial Pterygoid Right; **MaL**, Masseter Left; **MaR**, Masseter Right; **TeL**, Posterior Temporalis Left; **TeR**, Posterior Temporalis Right; **ATeL**, Anterior Temporalis Left; **ATeR**, Anterior Temporalis Right; **LaL**, Lateral Pterygoid Left; **LaR**, Lateral Pterygoid Right; **Op**, Opener; **BL**, Bite Left; **BR**, Bite Right; **CL**, Condyle Reaction Left; **CR**, Condyle Reaction Right.

	Clenching		
	Fx	Fy	Fz
MeL	-41.9	-29.7	170
MeR	41.9	-29.7	170
MaL	200	-53.6	304.3
MaR	-200	-53.6	304.3
TeL	50.6	102.9	238.1
TeR	-50.6	102.9	238.1
ATeL	50.6	102.9	238.1
ATeR	-50.6	102.9	238.1
LaL	-215.5	-307.6	-43.2
LaR	215.5	-307.6	-43.2
Op	0	133.2	-79.3
BL	0	54.7	-100
BR	0	54.7	-100
CL	0	63.8	-167.6
CR	0	63.8	-167.6

Table 3.3 Muscle Force components expressed in Newtons used in **wide opening** functional movement model.

	Wide Opening		
	Fx	Fy	Fz
MeL	-24.5	0	60.6
MeR	24.5	0	60.6
MaL	44.7	0	121.2
MaR	-44.7	0	121.2
LaL	-197.2	-281.6	156.1
LaR	197.2	-281.6	156.1
Op	0	135.6	-75.1
CL	0	213	-300.3
CR	0	213	-300.3

Because of the irregular anatomical profile, it was important to allow a certain tolerance for the contact between the cortical and trabecular bone as segmented from the volumetric images. This was performed by adjusting the "Pinball region radius parameter" in the Ansys Workbench pre-processor.

3.3.2.2 M1b modelling

The second model also uses a "two-bone" approximation and includes the implant and the reference tool required by the navigation system. The implant was positioned in the symmetry plane of the mandible. As per the feedback obtained by a number of surgeons in Bologna, it is reasonable to assume that the implant would be inserted in this position for three main ways:

- an implant is used to support the reference frame in case the patient is fully endentulous
- the central position facilitates access for the bone osteotomy to both the left and right side of the mandible, as requested for a full arch restorative surgery
- the central position corresponds to a site in-between teeth # 11 and # 21

The following associations between biomechanical scenarios was also made for the simulation setup:

- reference frame in place during surgery with wide opening functional movement
- reference frame in place during scan with clenching functional movement

Because of this association the same load set as in M1a was used.
For the two scenarios stresses generated by the reference frame during surgery and the CT scan on the central implant and the surrounding cortical and cancellous bone were evaluated, with the following specifications:

- bite forces were considerably reduced to simulate the modest clenching action on the plastic splint fitted to the CT/CBCT scan.This was based on the conditions reported by Sun (2013)
- condyle reaction forces were adjusted to balance the bite forces
- weight for the reference tool was taken into account during the simulation

A detailed summary of components of the applied loads is reported in Table 3.4 and 3.5 while a visual representation of the muscle vector forces is shown in Figure 3.2.

Tolerances used for the contact between the cortical and trabecular bone as segmented from the volumetric images were applied by adjusting the “Pinball region radius parameter” in the Ansys Workbench Mechanical FEA pre-processor.

Cortical bone and implant interfaces were assumed to be in no separation and the tools assemblies were modelled as bonded (Table 3.6).

3.3.2.3 M2 modelling: accidental interference

Accidentally interference with the reference frame can be considered a risk associated with the use of the registration tool during CT scan or surgery. Because of the cantilever action offered by the span of the rigid frame over the supporting implant, it is important to investigate the consequences that an accidental longitudinal or radial hit could have on the bone tissues and the implant itself.

Table 3.4 Force vectors used in simulating soft clenching action during scan. Magnitudes are expressed in Newtons for X, Y and Z directions used in this model; abbreviations: **MeL**, Medial Pterygoid Left; **MeR**, Medial Pterygoid Right; **MaL**, Masseter Left; **MaR**, Masseter Right; **TeL**, Posterior Temporalis Left; **TeR**, Posterior Temporalis Right; **ATeL**, Anterior Temporalis Left; **ATeR**, Anterior Temporalis Right; **LaL**, Lateral Pterygoid Left; **LaR**, Lateral Pterygoid Right; **Op**, Opener; **BL**, Bite Left; **BR**, Bite Right; **CL**, Condyle Reaction Left; **CR**, Condyle Reaction Right.

Clenching Load Set (Scan scenario simulation) (N)			
	Fx	Fy	Fz
MeL	-41.9	-29.7	170
MeR	41.9	-29.7	170
MaL	141.9	-53.6	304.3
MaR	-141.9	-53.6	304.3
TeL	50.6	102.9	238.1
TeR	-50.6	102.9	238.1
ATeL	50.6	102.9	238.1
ATeR	-50.6	102.9	238.1
LaL	-115.5	-307.6	-43.2
LaR	115.5	-307.6	-43.2
Op	0	133.2	-79.3
BL	0	54.7	-400
BR	0	54.7	-400
CL	0	63.8	-467.6
CR	0	63.8	-467.6

Table 3.5 Muscle Force components used in simulating wide opening action during surgery.

Wide Opening Load Set (Surgery scenario simulation) (N)			
	Fx	Fy	Fz
MeL	-24.5	0	60.6
MeR	24.5	0	60.6
MaL	44.7	0	121.2
MaR	-44.7	0	121.2
LaL	-107.2	-281.6	156.1
LaR	107.2	-281.6	156.1
Op	0	135.6	-75.1
CL	0	213	-300.3
CR	0	213	-300.3

Table 3.6 Boundary conditions for the FEA modelling.

Cortical bone - Cancellous bone	Bonded
Cortical bone - implant	No separation
Cancellous bone - implant	No separation

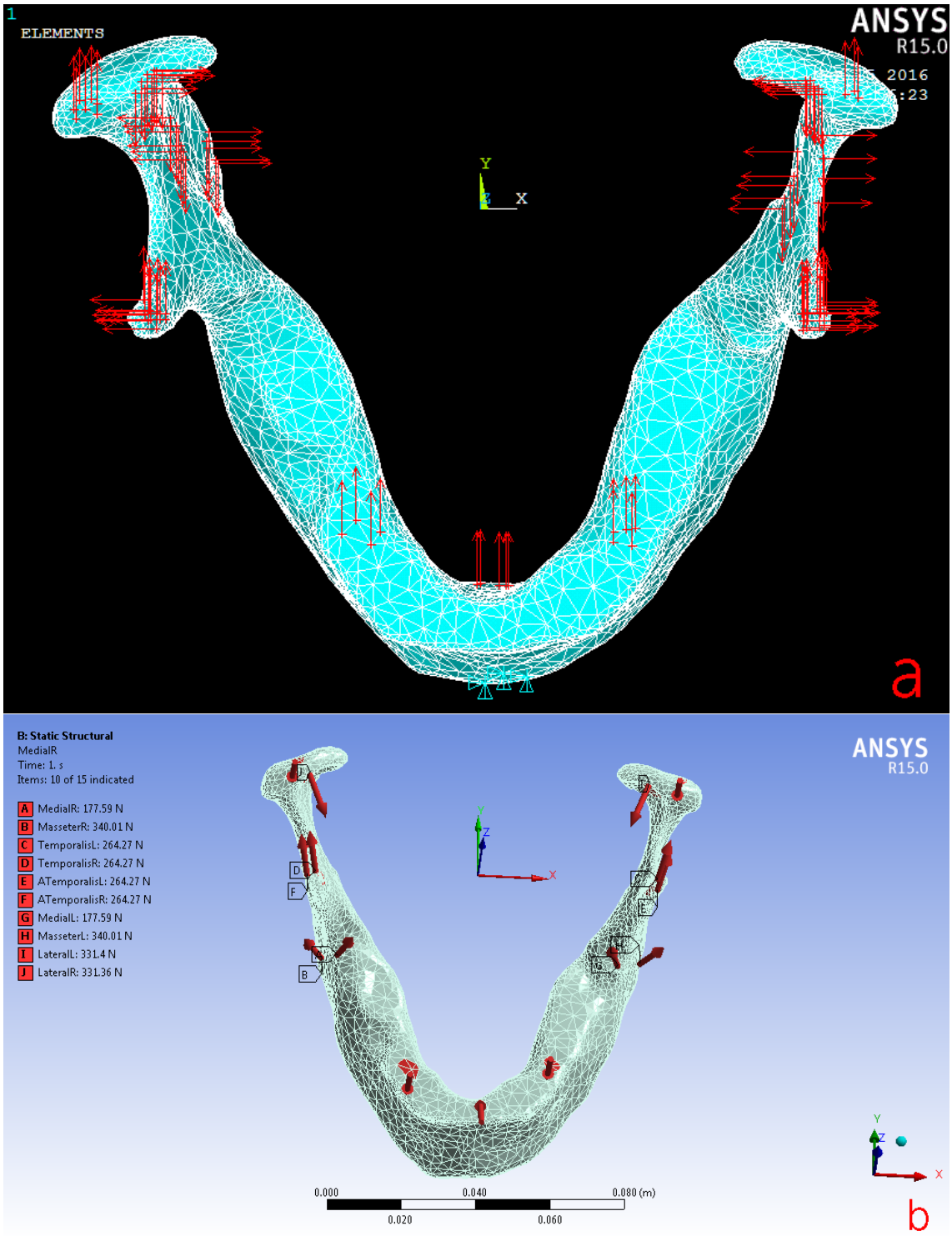

Fig. 3.2 Visual representation of muscle force vectors and application areas using Ansys Workbench Mechanical (b) and Ansys Mechanical APDL via neutral file input (a).

A lateral view of the meshed mandible model with implant supported reference tool and accidental hit application point is shown in Figure 3.3.

The sub-components of the reference frame were considered bonded to one another and also bonded to the implant. This accidental hit was simulated by applying a load at the most distal point of the reference tool with respect to the implant.

In case of a longitudinal hit the load was applied on the vertical axis perpendicular to the occlusal plane.

In case of a radial hit the load was applied on the same surface but tangential to the anteroposterior plane.

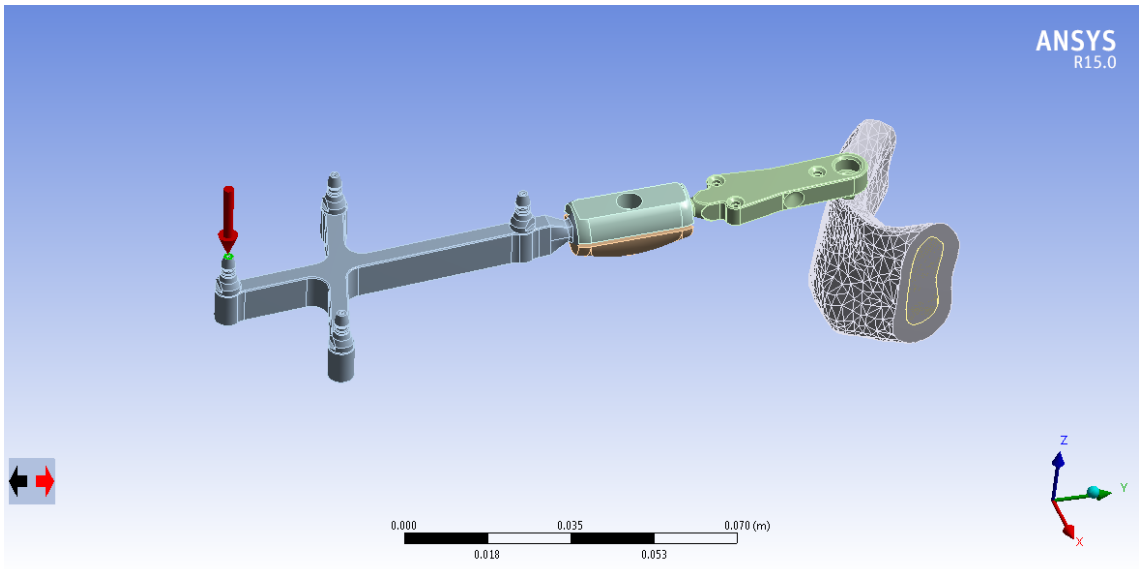

Fig. 3.3 Section of a mandible model with an example of implant supported reference tool (reflective balls, tightening screw and radiopaque markers have been excluded from the model to facilitate convergence of the mesh.

Introducing one or more external forces to the biomechanical configuration created by the mastication muscles required to formulate assumptions on how to balance the new system of equilibrium equations for the FEM.

Reaction to the external hit is believed to be exerted by more than one set of muscles and dependent on the morphology of the jaw and the biomechanics of the temporomandibular joint where the condyle reaction takes place. For this reason the author decided to simplify the simulation by using of fixed supports on the lateral surfaces of a section of the mandible, in order to prevent rigid body motion and divergence in the solution of the static structural

problem.
The following assumptions were also used:

- Cancellous-cortical bone approximation
- Contact pairs as in M1

The solid models used for M2 were derived from the segmentation of a different mandible with respect to cases M1 and M3. The main difference is on the level of "atrophy" recorded on the mandible and the cortical/cancellous bone ratio in a mesio-distal section of the jaw.

The author believes that in this simplified simulation, since masticatory muscles forces are not taken into account, it is important to use a poor bone quality to justify the "atrophy" recorded and to amplify the consequences of an external interference with the reference frame.

In M2 three different implant models have been used to compare the resultant stresses. The aim is to find the "smallest implant" which can be inserted without losing its capability of supporting the reference tool safely in regards of its internal structure and the integrity of the surrounding cancellous and cortical bones.

Three implants were used in the modelling. Of the three implants, two have been selected within Southern Implants Hex catalogue, measuring 3.35 mm in diameter and respectively 8.5 mm and 10 mm long. These implants have external hexagonal connection, for which the reference frame support is designed, and are the most common used sizes for non-angled mandibular implants within the Southern Implants set (Figure 3.4).

Together with the first two implants, another implant was specifically designed for this simulation and then manufactured by Russel Symes & Co (NSW, Australia).
The main features of this novel implant, which for convenience is called "mini-implant" within this work, are:

- 10.00 mm length
- 2.00 mm hexagonal head

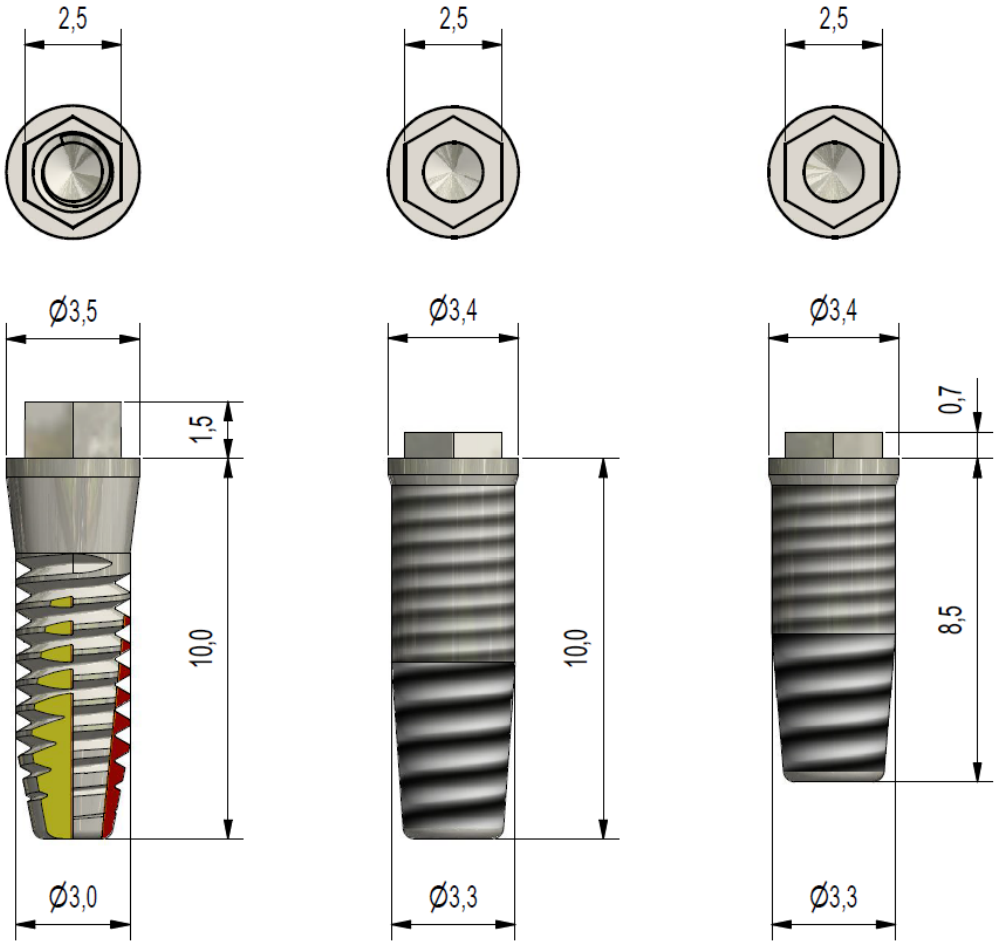

Fig. 3.4 Different implants used in M2. The picture shows how the **MINI-implant** (left) presents a smaller diameter and taller implant head to promote anchorage to the reference tool. Implant IBNT8.5 is overall shorter than IBNT10 (centre) and the MINI-implant (left).

- 3.00 mm diameter

The small diameter used is meant to minimise the invasiveness on the patient, mostly considering that this is a temporary fixture inserted only in edentulous subjects from the day of the scan to the day of the surgery.

The hexagonal head, taller with respect to the first two implants used during the simulation, is meant to enhance the stability of the frame via a 2mm screw. For convenience, the same Titanium screw used as fiducial marker, illustrated in detail in Chapter 6, is utilised to anchor the reference frame to the implant head.

The finite element simulation was run for three models with three different implants. The different implant sockets were designed through Boolean operations to fit a current implant.

3.3.2.4 M3 modelling

In the previous models, the use of CT scan for imaging the mandible saw a representation of a solid bone being reversed engineered through a contour extraction procedure.
The scan data can also be interpreted by the scalar values associated to each voxel.
If on one side these numbers can be associated to grey values for imaging the tomographic slices, on the other side, there are a number of studies trying to validate a relation, for Computed Tomography, between voxel scalars, Hounsfield Units (HU) values and averaged local density (Rho, 1995; Taddei, 2004 and 2007; Schileo 2008).

In this modelling method the mechanical properties of the mandible were determined in two stages:

- In the first step the apparent specific density of each element of the model mesh was calculated by linear association with the HU of the voxels enclosed in that element, following the procedure created within this research work and reported in Chapter 2.

- In the second step the elastic modulus was correlated to the apparent bone density according to the experimental results found in literature.

As a result, after aligning the mesh with the tomographic scan, a finite element model was prepared in which local material properties were assigned to every single element of the mesh.

Such a model represents an alternative to the two-bone model approximation and it offers the benefit of combining an accurate mesh of the external surface of the bone, easily segmented via the high contrast between cortical and surrounding soft tissue, with a density-based mapping of local stiffness.

3.4 Results and Discussion

A static structural finite element simulation was run in Ansys applying an external force on the reference tool, simulating gravity and a possible accidental mechanical interference during surgery.

Meshing M1 resulted in 138650 nodes and 78389 tetrahedral elements.

In M1b the implant was modelled with 8745 nodes and 4420 elements while meshing the cancellous bone itself resulted in 28306 nodes and 15622 elements.

In literature there are not explicit guidelines for interpreting the results of stress analysis on the human bone, whether to use principal stresses (tensile or compressive) or equivalent stresses. (Choi 2005 and 2013). One of the reasons is that the ultimate stress depends on the direction of loading, other than age, sex and healthiness of the subject. According to Reilly and Burnstein (1975), the ultimate tensile stress of human cortical bone can range from 121 to 135 MPa and the ultimate compressive stress ranges from 167 to 205 MPa.

Other investigations into the stresses for the mandibular bone under loading recorded values for the cortical bone between 21 and 150 MPa (Korioth et al. 1992; Lin et al. 2000; Menicucci et al. 2001; Hirabayashi et al. 2002; Eskitascioglu et al. 2004).

Ultimate stress values for cancellous bone vary instead between 1 and 20MPa.

Knowing the factors involved that influence the properties such as gender, age, morphology of the mandible, the medical condition of the patient sample size used and method utilised with the quality of the bone , its wetness or dryness, it is not surprising that different publications report different values.

Table 3.7 Maximum Von Mises stresses recorded during functional movements in Choi (2005).

	Von Mises stress (MPa)	
	Cortical	Cancellous
Clenching	38.91	4.27
Opening	35.47	2.56
Protrusion	35.44	2.56

Because the main purpose of M1a and M1b models was to verify the reliability of the FEM by comparing its results to literature of mandibular models, this study choose to calculate von Mises (or equivalent) stresses according to the equation 3.1. The justification is that, although brittle, the mandible is formed by more or less dense porous material. For that the behaviour of an eventual fracture is likely to resemble the beginning of the deformation of a ductile material. A quite large number of works on FEA on orthopaedic and dental applications use Von Mises equivalent stresses and hence this work reports von Mises stresses.

Von Mises stress is calculated from the six stress components normally present in homogeneous structures which can be defined safe under load when the generated stress is less than the absolute value of the yield stress in tension or compression (tested during uniaxial loading).

$$\sigma_{vonMises} = \frac{[(\sigma_{xx} - \sigma_{yy})^2 + (\sigma_{xx} - \sigma_{zz})^2 + (\sigma_{yy} - \sigma_{zz})^2 + 6\,(\sigma_{xy}{}^2 + \sigma_{xz}{}^2 + \sigma_{yz}{}^2)]^{\frac{1}{2}}}{\sqrt{2}} \quad (3.1)$$

For evaluating the reliability of the simulation, this work was compared with models presenting the same biomechanical configurations. In 2005 Choi published the highest von Mises stresses observed in the mandible during clenching and wide opening (Table 3.7) using the same load set of this work, which was firstly calculated from cross section of cadaver muscles by Ben-Nissan in 1987.

3.4.1 M1a model

In M1amodelling, the mandibular distortion in respect to the 1^{st} and 2^{nd} molar region were obtained by probing the deformed model on a surface comparable to the size and the dimension of a molar tooth. Additional verification came from plotting the resulting stresses in bands clearly visible through the molar regions and normalised to the ranges of stresses observed in the areas of interest, as illustrated in Figure 3.5. The maximum

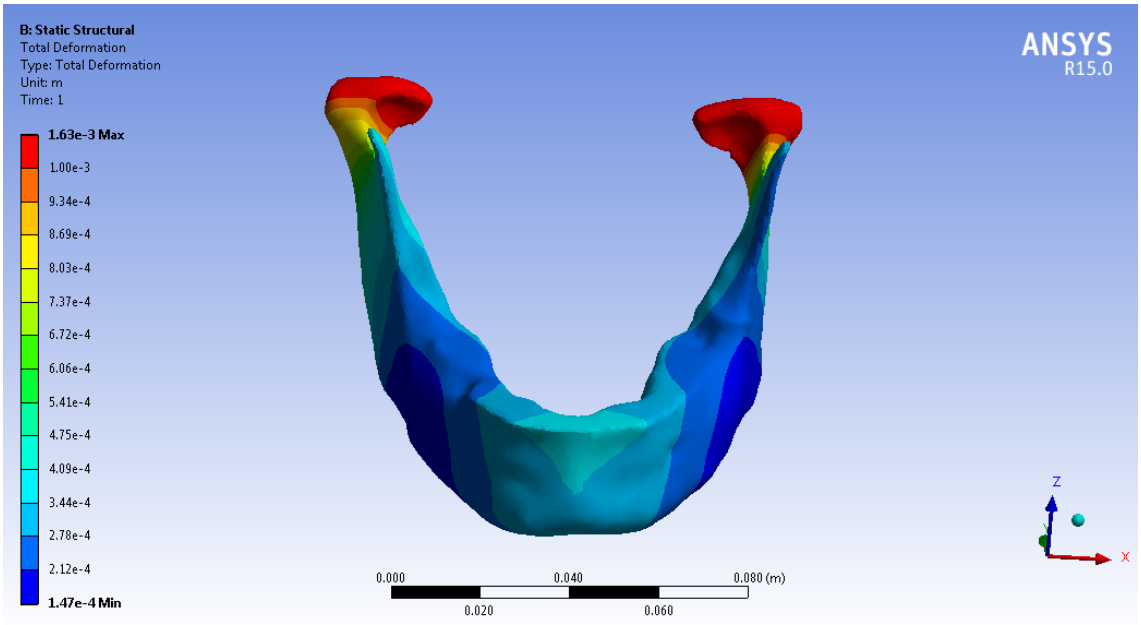

Fig. 3.5 Example of deformation colour bands for visualising the simulation results. The deformation scale (visible on the left) has been normalised to promote discretisation of colours, and therefore distinct stress ranges, in the molar regions.

deformation of 0.96 mm during clenching was located on the left condyle. This result was expected as Ben-Nissan's model presents a distortion larger than 1.00 mm in the condyle region. The mentioned work, in fact, applies the same biomechanical load set to a wet mandibular bone modelled as two bodies made respectively of cortical and trabecular tissue with Young's modulus of respectively 17.2GPa and 1.3GPa. This current work utilises more anatomically correct muscle loading and appropriate mechanical properties modelled from the patient matched CT scans.

A maximum distortion in the range 0.32-0.35 mm was found for the molar regions for clenching and between 0.30 mm and 0.32 mm for wide opening. As it can be seen in Table

Table 3.8 Results for maximum distortion in the first and second molar region measured by FEA or with a number of different methods during clenching and wide opening movement compared with previous investigations.

		1st molar (mm)	2nd molar (mm)
This work	Clenching	0.35	0.32
	Wide Opening	0.32	0.30
Kollner (1978)	Wide Opening	0.2	
Ben-Nissan (1987)	Clenching	0.3 – 0.4	0.32
	Wide Opening	0.43	0.51
Gates & Nicholls (1981)	Wide Opening		0.31
Chen (2000)	Wide Opening	0.44	

3.8, distortions obtained for 1^{st} and 2^{nd} molar region are also aligned with other results recorded in literature for similar mandibular models.

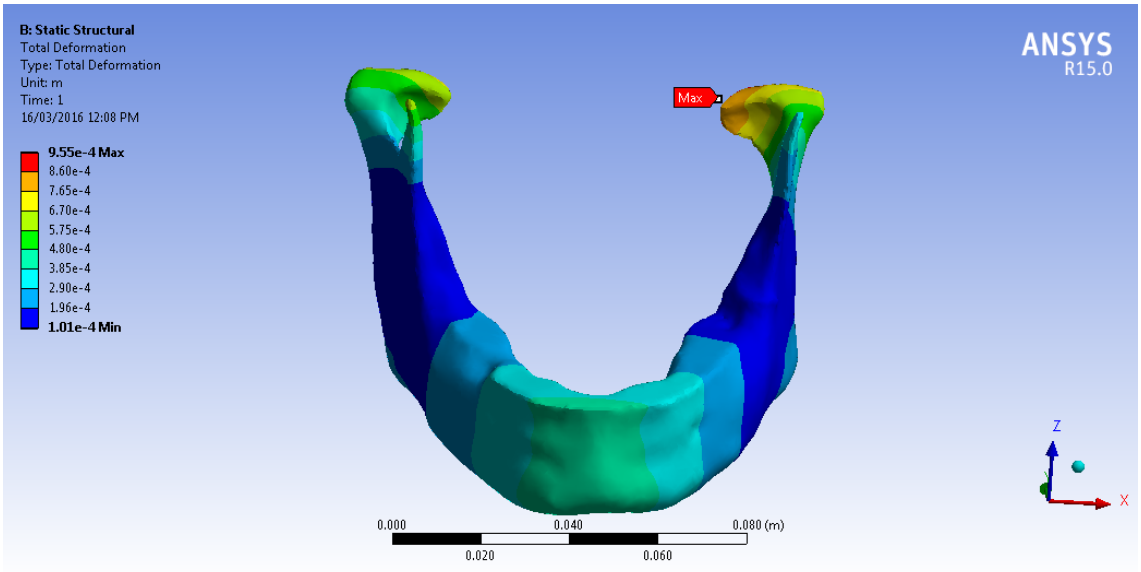

Fig. 3.6 Deformation during clenching. Maximum deformation is observed in the left condyle. The asymmetric deformation between the two condyles is due to the lack of symmetric morphology in the subject-specific mandible.

Maximum von Mises stress concentration for the presented model was registered in the right coronoid process. This behaviour is most likely due to the very thin section of the bone model which generates sharp features during meshing.

Differently from models previously published in literature, models M1a and M1b are made of a separate solid representing the cancellous bone inside an external shell representing

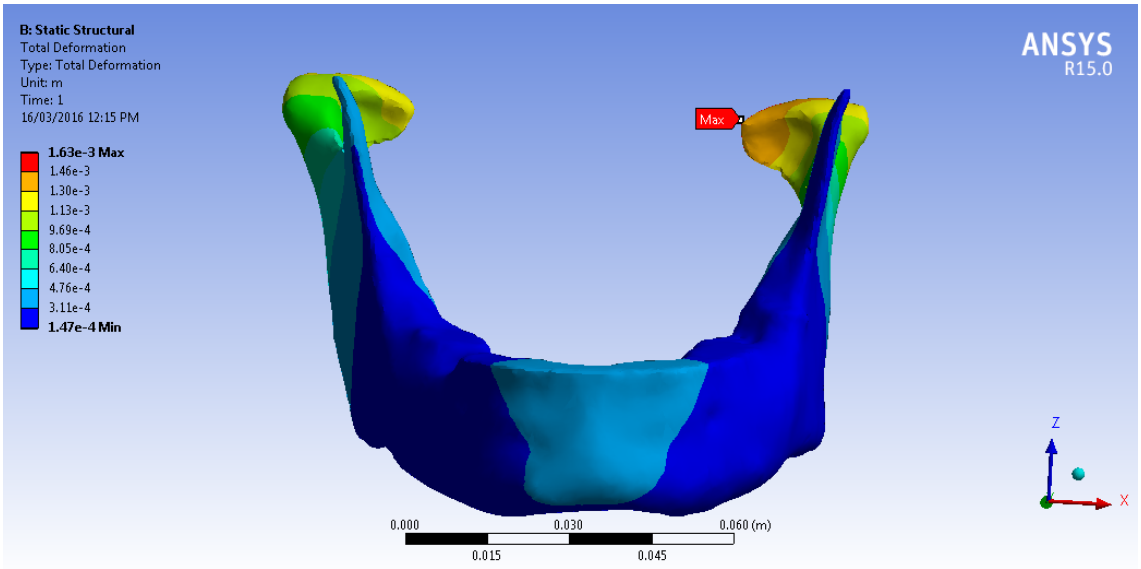

Fig. 3.7 Deformation during wide opening. Maximum deformation is observed in the left condyle. The asymmetric deformation between the two condyles is due to the lack of symmetric morphology in the subject-specific mandible. The deformation of the condyle is also subject to the structural static problem FEM setup: hypotheses on how constraining to the maximum deformation of the condyle could better reflect the dynamics of the temporomandibular joint will be discussed at the end of this Chapter.

the surface of the cortical bone. Following that, regions like the coronoid processes result in very thin walls which are often difficult to mesh through an automatic mesh generator (feature required for organic subject-specific shapes). On the contrary, models made using only one solid with averaged material properties are not exposed to these modelling singularities.

The combination of thin walls and poor local mesh features creates unrealistic maximum equivalent stresses which must be interpreted and, if necessary, discarded (see Figures 3.8 and 3.9).

As a result, the simulations recorded maximum principal stresses of 75 MPa during wide opening located on the left mandibular notch (thin wall) and 79 MPa during clenching on the bony ridge of the right coronoid process. These results, as stated earlier, are unrealistically high.

Results for 1^{st} and 2^{nd} molar regions show von Mises stresses between 23 MPa and 25 MPa for clenching and between 9 MPa and 11 MPa for wide opening, as reported in Table

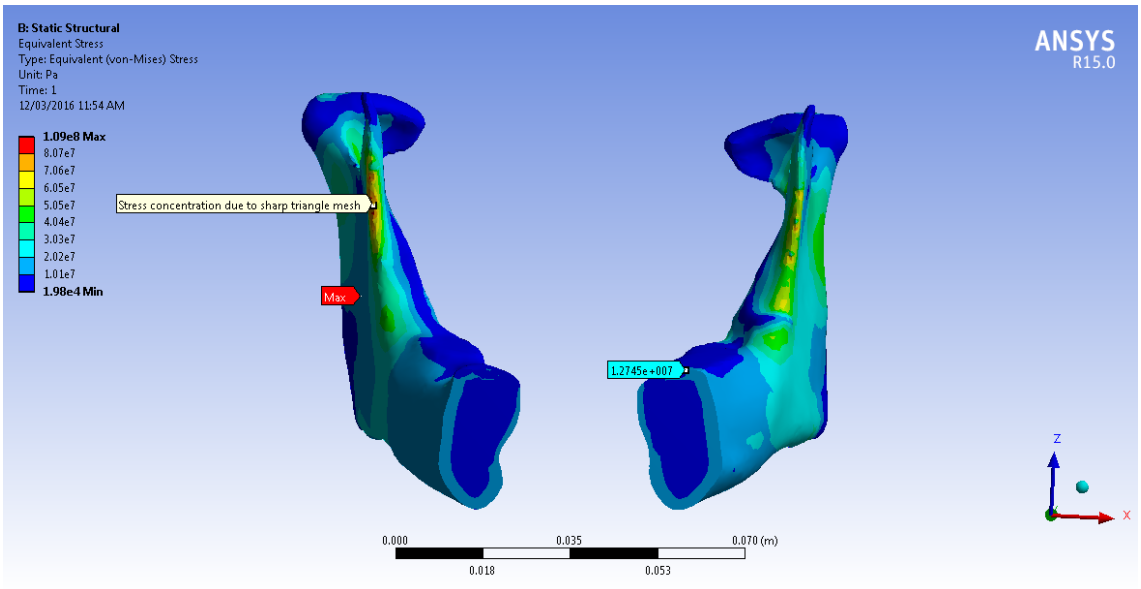

Fig. 3.8 Stress distribution during clenching. The section on the first molar region shows the different stress distribution for cancellous and cortical bone due to their different material properties.

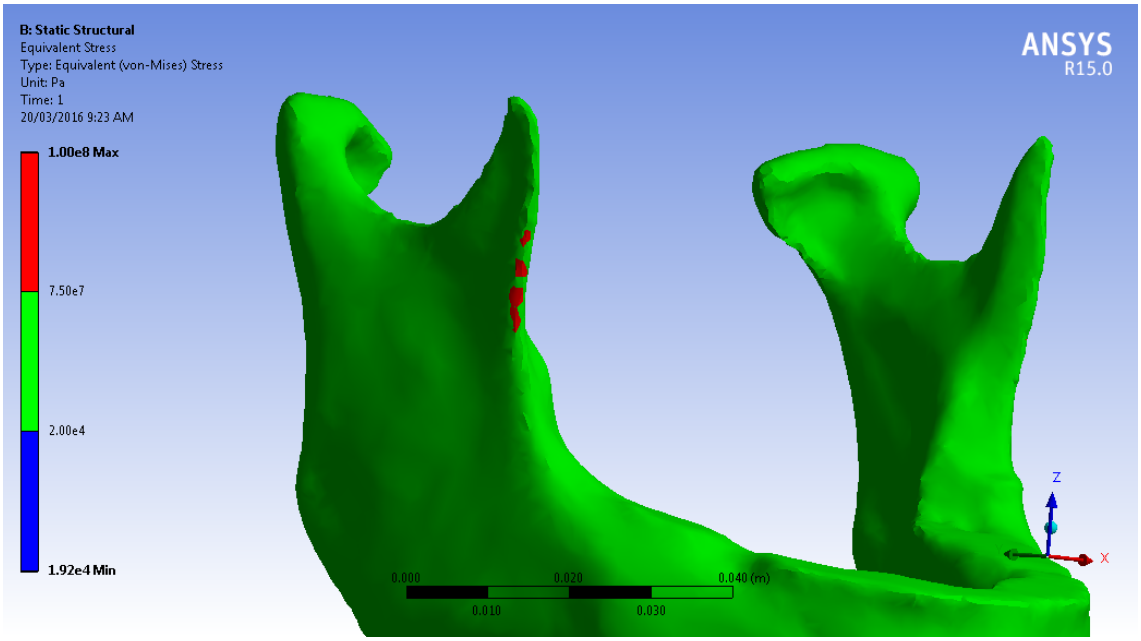

Fig. 3.9 This figure shows the only regions in the FEM where equivalent stress is higher than 75 MPa during clenching. This plot shows how there is stress concentration in the coronoid process which is believed to be a consequence of the quality of the triangles in meshing thin areas.

3.9. These results are comparable with the ones obtained by Ben-Nissan (1987) and Choi et al. (2005) with an FEM based on a similar biomechanical configuration and realistic.

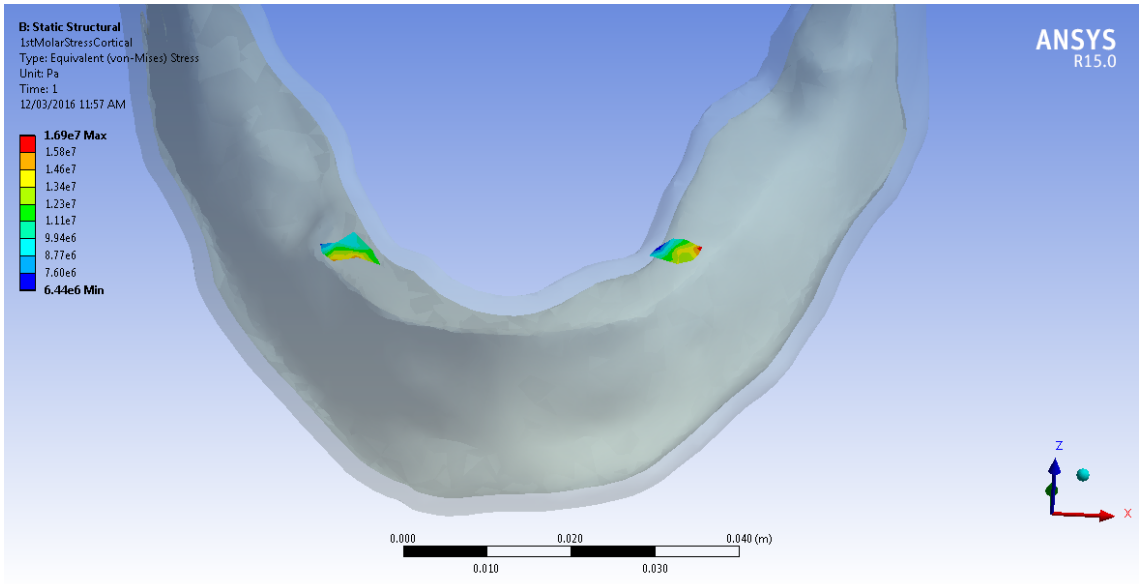

Fig. 3.10 Probing of the equivalent stress in the molar region.

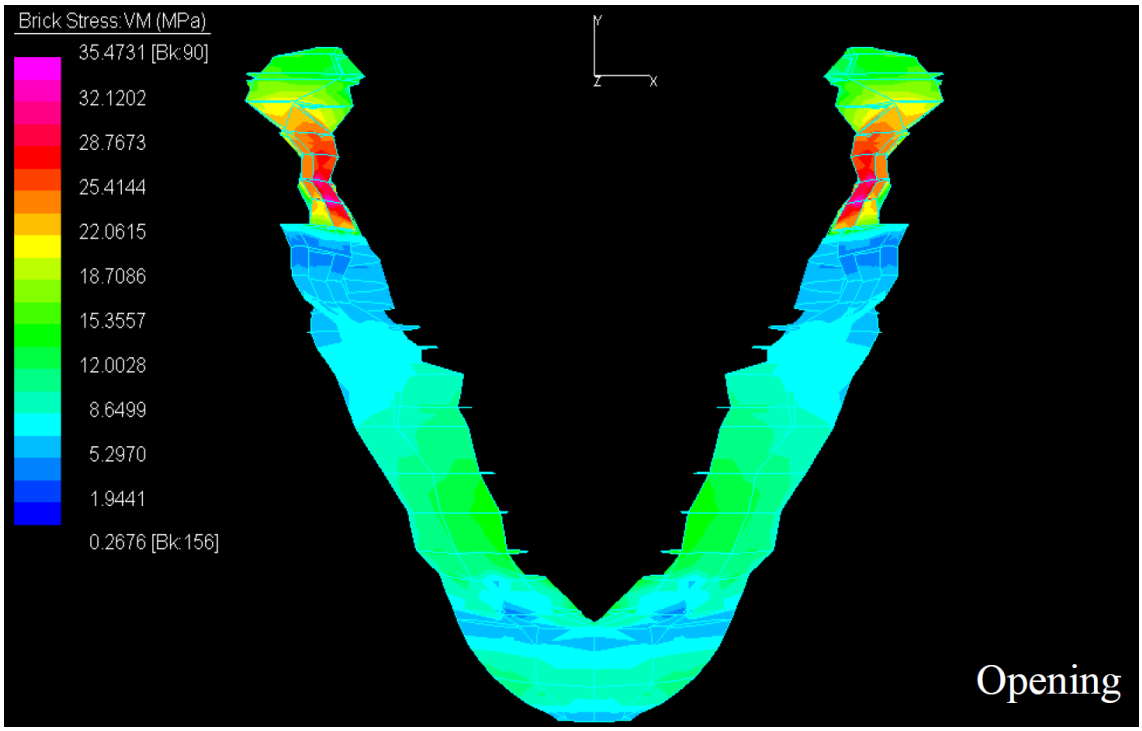

Fig. 3.11 Graphic results obtained by Choi (2005) for von Mises stresses in the mandible, from which a range of values for the 1^{st} and 2^{nd} molar region are derived for comparison with the stresses obtained in M1.

Based on the fact that these results were aligned with stress and distortions found for a wet human mandible during a bilateral clenching and wide opening functional movements

Table 3.9 Results for maximum von Mises stress in the first and second molar region during clenching and wide opening movement.

		1st molar region von Mises stress (MPa)	2nd molar region von Mises stress (MPa)
This study	Wide Opening	9.1	11.2
	Clenching	25.4	23.8
Choi (2013)	Wide Opening	10-12	9-11
	Clenching	16-18	13-15

Table 3.10 Results for maximum von Mises stress on the implant surface during clenching and wide opening movement.

	von Mises Stress (MPa)	Principal Stress (MPa)
Wide Opening	26	20
Clenching	33	28

as reported in studies like Ben-Nissan's (1987), Gates and Nicholls' (1981), Choi's (2005), the author proposes to deploy the present model to analyse the biomechanical impact of a reference system for navigated surgery.

In particularly, it is envisaged that such simulation has grounds to realistically predict stresses and distortions in the implant site supporting the reference frame.

3.4.2 M1b model

Results were obtained for model M1b where stresses are generated by the introduction a MINI-implant supporting a reference frame during CT scan (illustration in Figure 3.3) and relevant surgery. They are shown in Table 3.10 and in Figures 3.13 and 3.14.

The stress generated on the implant was also recorded by means of a longitudinal probe calculating the stress profile along the inertia axis of the implant.

Figure 3.12 clearly shows that during clenching the von Mises stresses are much higher than in the opening movement. Overall it can be shown that clenching produces larger stresses.

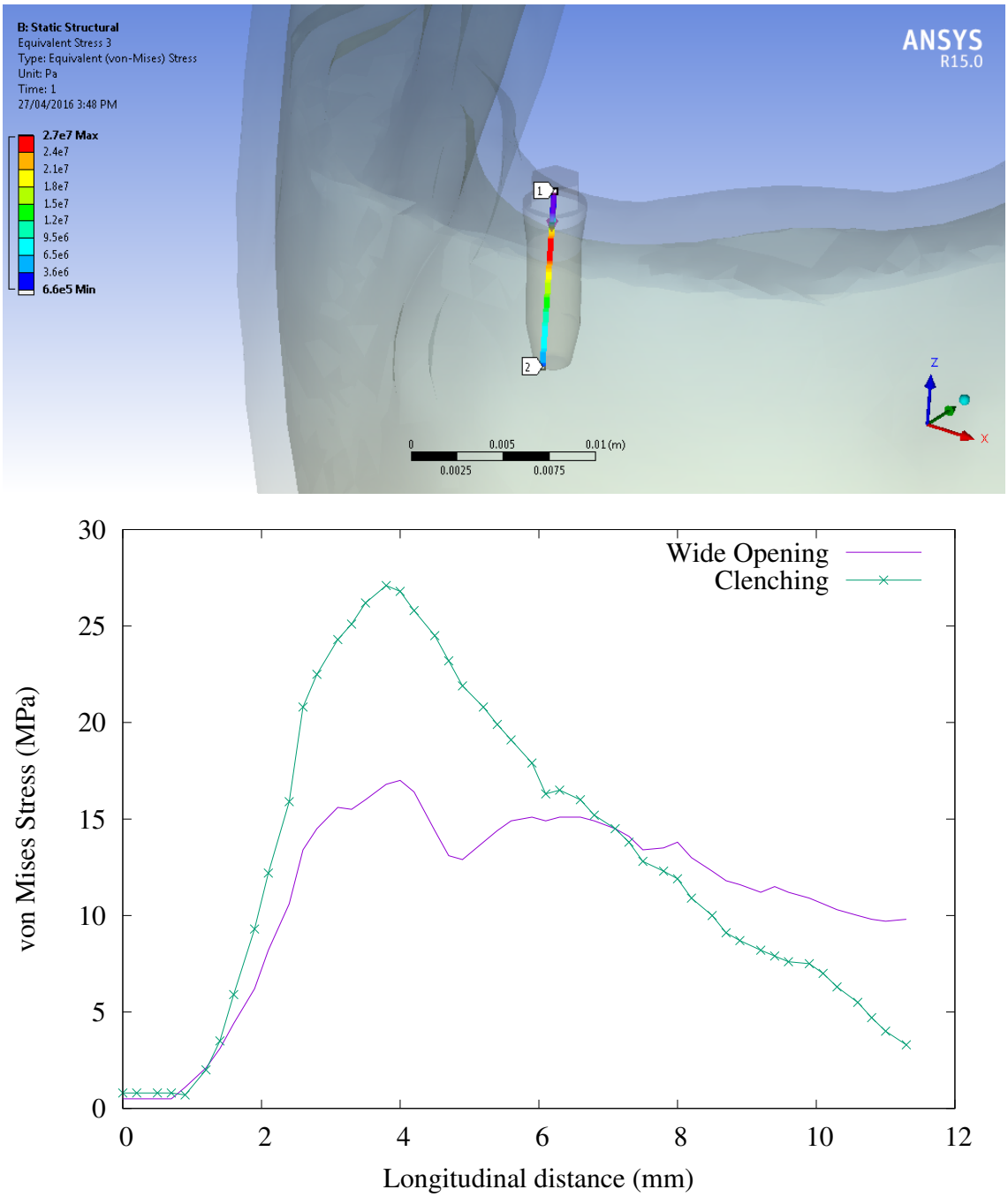

Fig. 3.12 Equivalent stress along longitudinal path on implant surface registered during clenching and wide opening movement. The stress values on the x-axis (MPa) are plotted versus the longitudinal distance (in mm) from the implant hexagonal head. The curve with higher stresses is relative to the clenching movement.

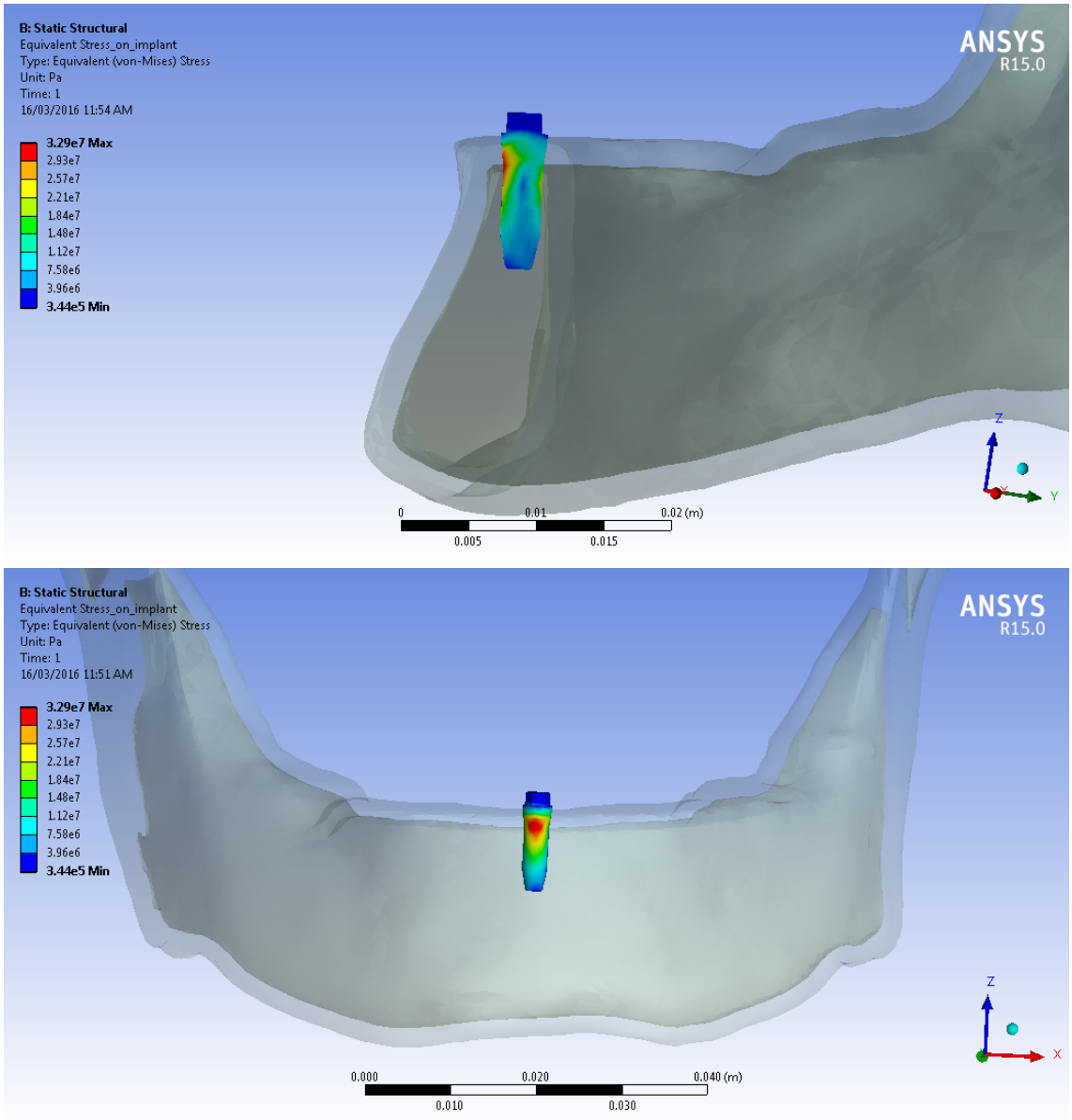

Fig. 3.13 Stress distribution on the implant body during scan (clenching position): section view (top) and anteroposterior view (bottom).

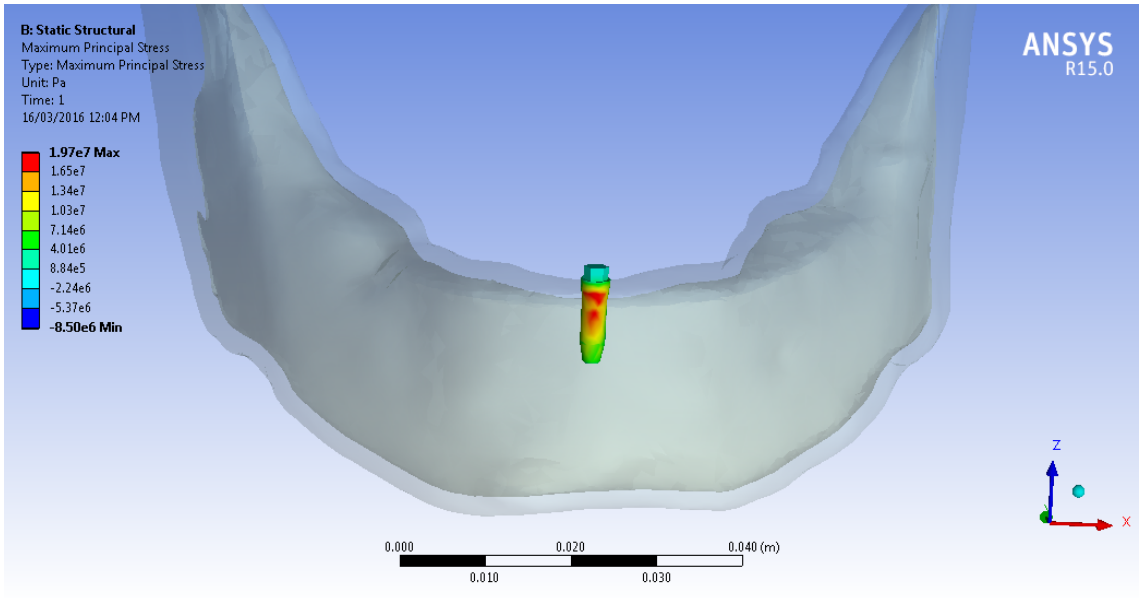

Fig. 3.14 Anteroposterior view of the mandible which shows the stress distribution on the implant during surgery (wide opening movement).

Table 3.11 Results for maximum equivalent stresses (von Mises) in respectively cortical, cancellous bone and implant structure in case of a 10 *N* vertical hit when different implants are used.

	Max stress on implant surface (MPa)	Max stress on cortical (MPa)	Max stress on cancellous (MPa)
IBNT 8.5	317	138	97.1
IBNT 10	260	47	2.9
MINI-implant	278	60	2.4

3.4.3 M2 model

In M2 an accidental vertical hit was simulated during the scanning procedure by modelling an external force of 10 *N* magnitude acting on the distal end the reference tool perpendicularly to the occlusal plane. The choice of this force module was based on clinical observations made by several surgeons from the Clinical Odontoiatrica at University of Bologna.

Results, which are summarized in Table 3.11, were obtained for the three sub-models corresponding to the use of two standard implants and the “mini-implant” specifically designed for the navigation system.

The simulation indicates that the stresses generated by the use of a small IBNT8.5 implant

(Southern Implants, Pretoria, South Africa) are considerably higher than the ones resulting from the use of a 10 mm long implant (IBNT10). Although IBNT 10 stresses are within the limit of the survival, the IBNT8.5 will induce very large stresses within the adjacent bone and will be detrimental under these accidental impact conditions.
If it is a MINI-implant used to support the reference frame during an accidental hit, the generated stress are comparable with the ones associated to the insertion of IBNT10.

In all cases the generated equivalent stresses reported in Table 3.14 for IBNT 10 seem to be lower than the ultimate stress for both the Titanium alloy implant and for the cortical and cancellous bone (Li et al. 2013, Keller et al. 1994).

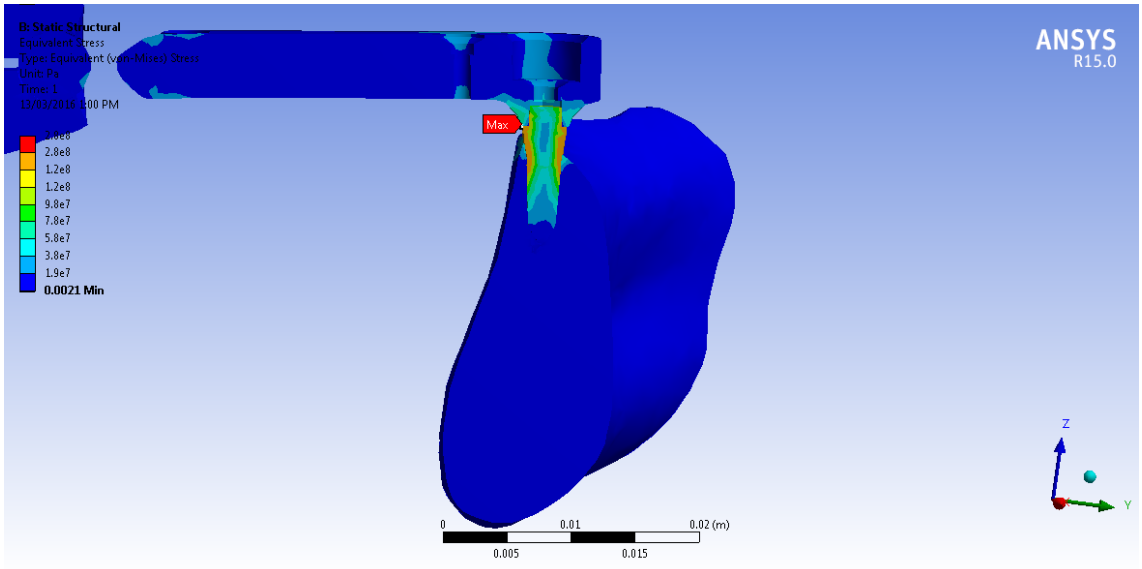

Fig. 3.15 Stress distribution due to accidental vertical hit down during scan in cortical bone, cancellous bone and MINI-implant.

3.4.4 M3 model

The choice of the material properties in the FEM relative to M3 relies entirely on the relations used to convert CT numbers into density and then Young's Moduli.

The distribution of CT numbers, as averaged inside each finite element and calculated for the entire mandible mesh, indicated two peaks of maximum concentration. Given the anatomy of the mandible, it is reasonable to assume that these two peaks correspond respectively to CT numbers relative to cancellous and cortical bone type. Also, in line with the definition of cortical bone given in this work, for which it is considered a denser form

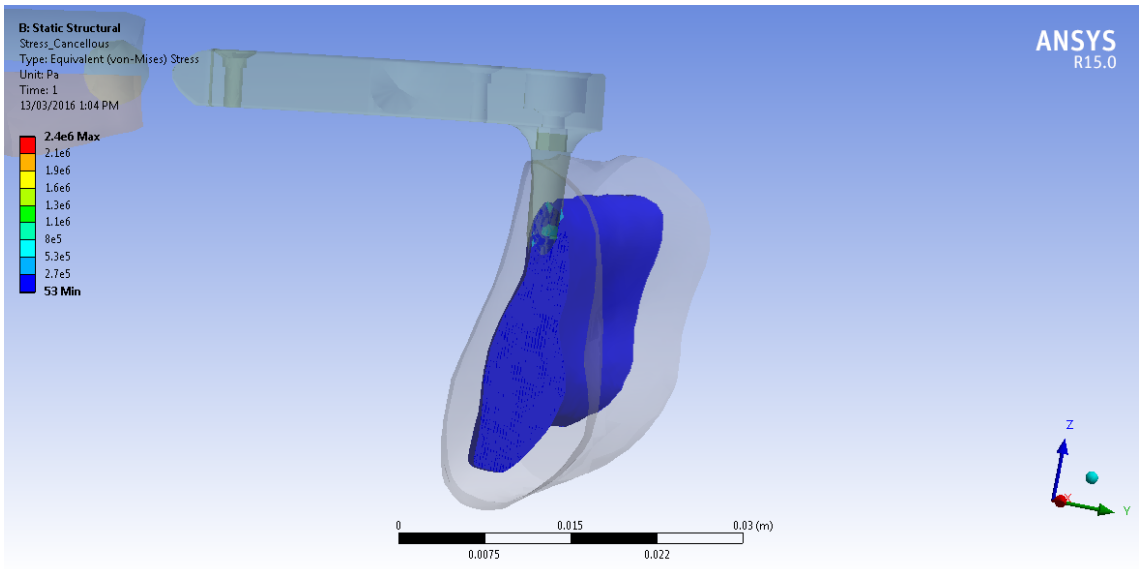

Fig. 3.16 Stress distribution due to accidental vertical hit down during scan in cancellous bone.

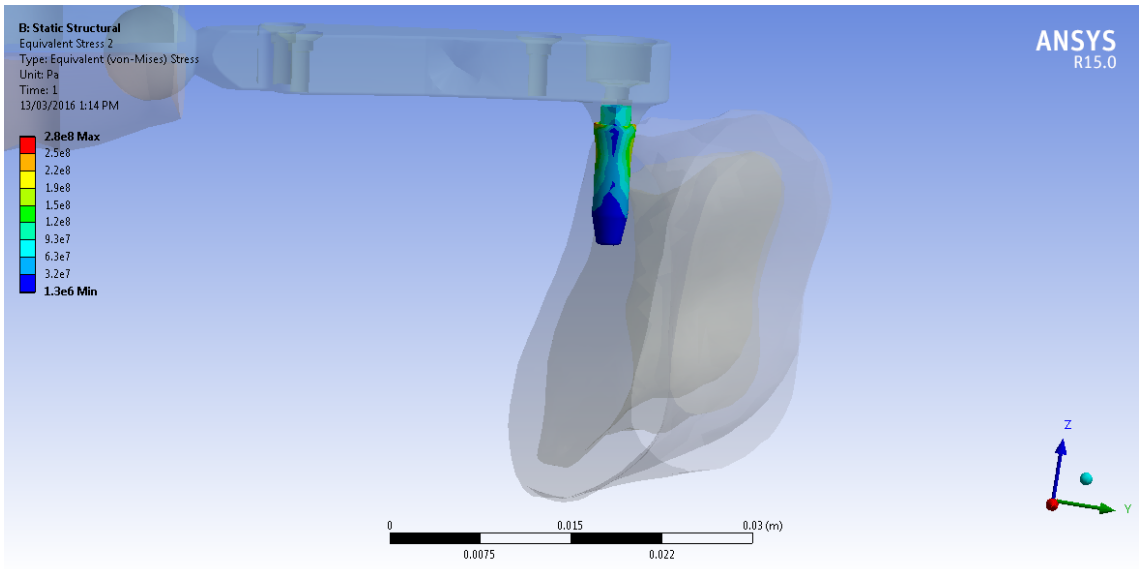

Fig. 3.17 Stress distribution on the MINI-implant during an accidental vertical hit.

of the same porous structure which the cancellous bone is made of, we expected to see a continuous trend representing the progressive concentration of trabeculae reaching the most compact bone configuration.

This behaviour is illustrated in the Figure 3.18 which reports the frequency of CT numbers for the present study. CT numbers are given in output from the Tomographic Scan machine and are scalars associated to the spatial coordinates within the scanned anatomy. They reflect the level of absorption of X-Ray radiation from the imaged sample (here a human body) and are computed following a combination of the radiation absorbed by either a single or fan of emitted beams. The location of the left peak corresponding to

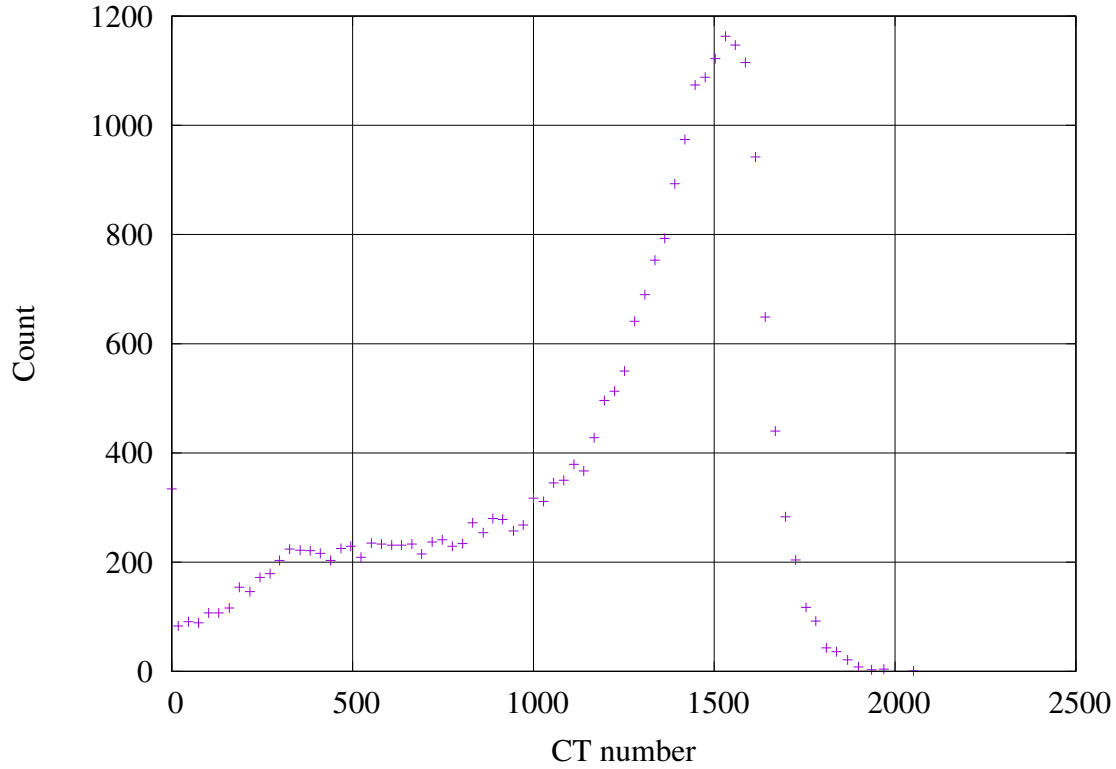

Fig. 3.18 Distribution of CT numbers in the mandibular mesh. Values of CT numbers are reported on the X-Axis while their relative count within the scan of a human mandible is on the Y-Axis.

the soft bone is also found through the ratio Cortical/Cancellous bone for this particular bone mesh. During the segmentation process the ratio of the volumes of the solid models corresponding respectively to hard and soft bone was estimated to be:

$$V_{can}/V_{cor} = \frac{23140\ mm^3}{67331\ mm^3} = 0.34$$

For this reason it is reasonable to suppose that the highest concentration of cancellous bone should have a count of:

$$N_{can} = 0.34\, N_{cor} = 560$$

Applying Carter & Hayes's relation (1977) for converting density to Young's modulus, inclusive of Brown's (2010) correction (as explained in Chapter 2),

$$E(GPa) = 2.80\, \rho^3 \tag{3.2}$$

Using Bujtar's empirical law (2010) for deriving densities from Hounsfield Units (obtained normalising CT numbers for air and water)

$$\rho(Kg/m^3) = 1.14\, HU + 309 \tag{3.3}$$

The resulting frequency of Young's Moduli (in gaps of 30Mpa) in the mesh (Figure 3.19) shows that the peak corresponding to denser bone is between 20GPa and 30GPa. Because this value is not aligned with the most significant works published in literature (as reviewed by Helgason 2008) the author has decided to reject this finding and, therefore, its associated workflow.

Alternatively, this study used an inverse approach to determine the stiffness of the mandible from the distribution of the CT scan numbers. The method uses the following hypotheses:

(a) The right peak for high CT numbers corresponds to Cortical bone in the volume mesh, with the CT number

$$CT_{cor} = 1616$$

(b) The relationship which correlates CT numbers to density is linear

(c) Average Young's moduli for Cortical and Cancellous bone (as used by Ben-Nissan (1987) whose load set is being used in this study) are

$$E_{cor} = 17.2GPa \tag{3.4}$$

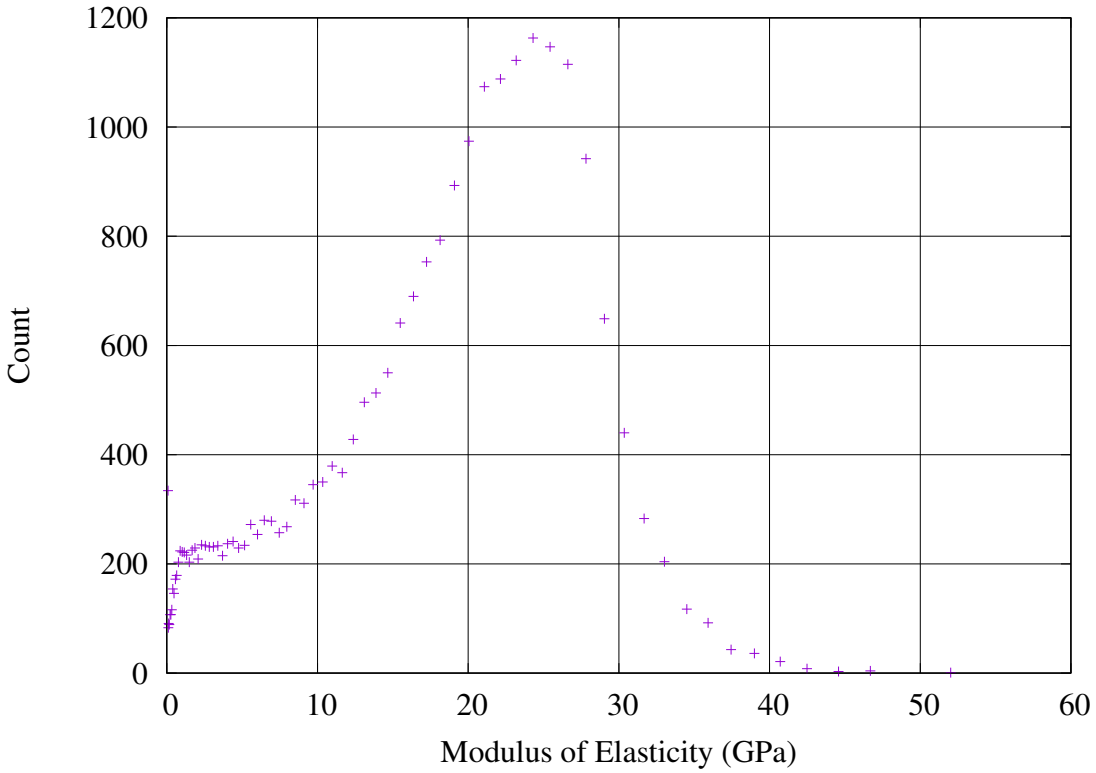

Fig. 3.19 Frequency of Young's Moduli in the mandible mesh. On the x-axis Young's Moduli E (GPa), on the y-axis count of E for incremental intervals of 30MPa.

$$E_{can} = 1.3GPa \tag{3.5}$$

(d) As reported in Chapter 2, the law for converting density to Young's modulus is Carter & Hayes (1977) (corrected by Brown(2010)):

$$E(GPa) = 2.80\,\rho^3 \tag{3.6}$$

Using 3.4 and 3.5 into 3.6 we obtained:

$$\rho_{cor} = 1.83\ g/cm^3$$
$$\rho_{can} = 0.76\ g/cm^3$$

Considering that:

$$\rho_{air} = 1225\ g/m^3$$

the plot shown in Figure 3.20 is obtained for the relationship between CT numbers and density, where the CT numbers corresponding to cortical and cancellous bone have been assumed to be the ones corresponding to the frequency peaks associated to the two bone types. The data have been interpolated with a linear law using Gnuplot (www.gnuplot.info)

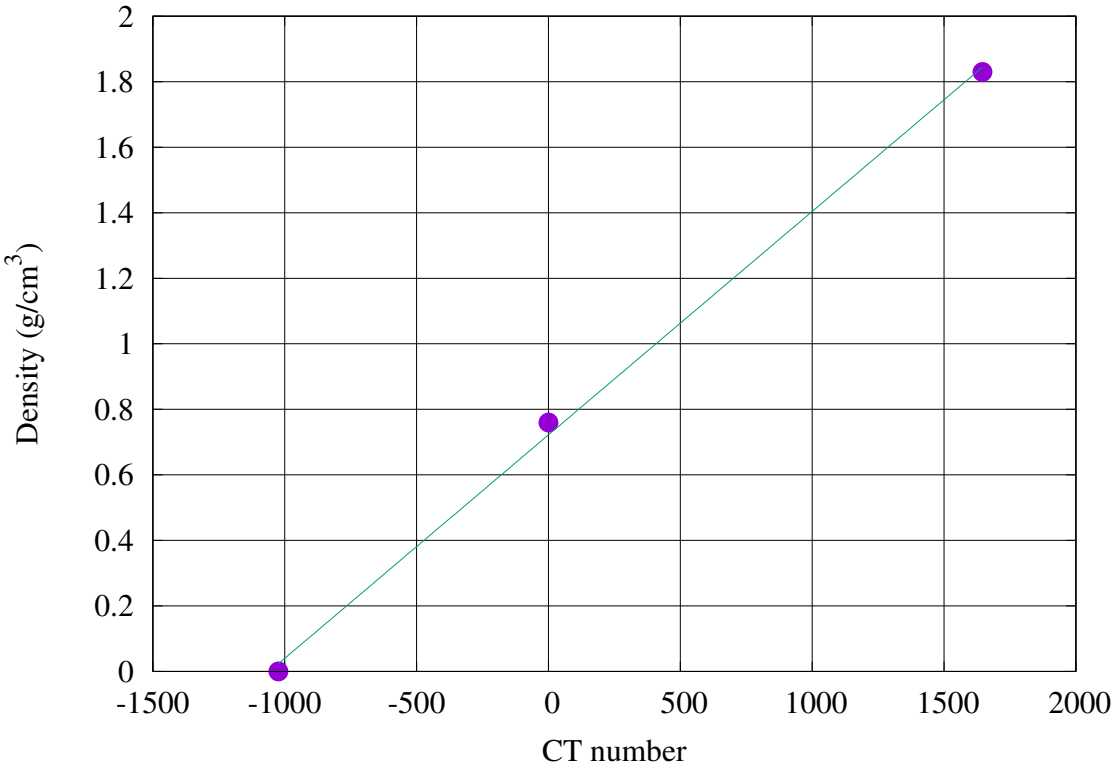

Fig. 3.20 Relation between CT numbers (X-Axis) and density (in g/cm^3 on the vertical axis) obtained following the hypotheses discussed in the section above.

for calculating a and b in the equation

$$\rho(g/cm^3) = a\,CT + b$$

resulting in the inverse approach linear relation

$$\rho(g/cm^3) = 6.82 \cdot 10^{-4}\,CT + 0.722 \tag{3.7}$$

Using 3.6 and 3.7 in the Bonemat GUI this study determined the frequency plot for respectively Young's moduli and density of the mandible (Figures 3.30 and 3.31) and the values obtained were used as material properties in the FEM pre-processor. For M3, results were obtained for the mandibular distortion and stresses in respectively the 1^{st} and 2^{nd}

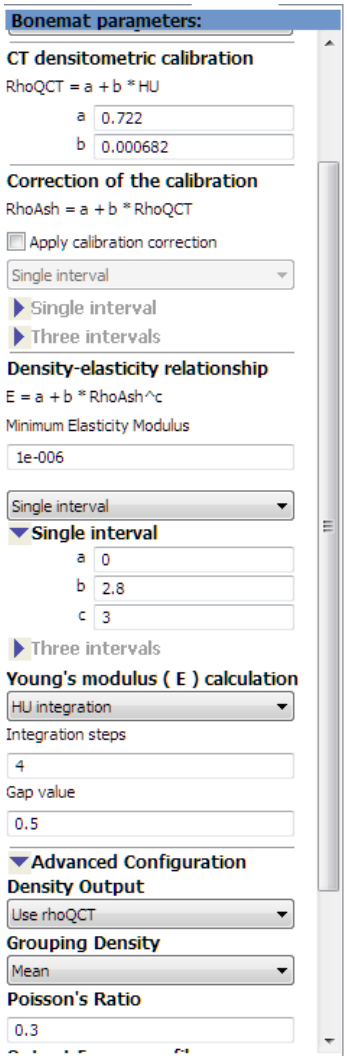

Fig. 3.21 Bonemat GUI showing all the parameters used to generate the conversion from CT numbers to Young's Moduli for a specific finite element mesh.

Table 3.12 Results for mandibular deformation in M3 during wide opening compared with the values obtained in M1.

Wide Opening – Deformation (mm)			
	2nd molar region	1st molar region	Max
M3	0.15-0.18	0.12-0.15	1.29
M1	0.30	0.32	1.63

Table 3.13 Results for mandibular deformation for M3 during clenching compared with the valued obtained by M1.

Clenching – Deformation (mm)			
	2nd molar region	1st molar region	Max
M3	0.12-0.15	0.09-0.12	1.00
M1	0.32	0.35	0.96

molar region by probing the deformed model on areas comparable to the dimension of a tooth. The results are shown in Table 3.12 where also a comparison with M1 is given.

This study observed how probing stresses in the molar region produces more heterogeneous results with respect to the same operation in a two-bone model. This is mainly due to the fact that each finite element is characterised by a different elastic modulus. As a result a wider range of stresses can be observed within small probed regions. In this scenario, in order to visualise stresses from the simulation in a meaningful range, this study has sampled the results for equivalent stress between 0 and 20 MPa. This facilitated the observation of colour bands corresponding to stress levels for the 1^{st} and 2^{nd} molar region (see Figures 3.22 and 3.23).

The calculation of local material properties for the finite element mesh generates the distributions for E and ρ shown in Figure 3.30.

Maximum principal stresses in cancellous and cortical bone were compared to the published values for ultimate tensile strength. Results suggest how neither the position during the surgical procedure nor mechanical interference with the reference tool would harm the patient not damage the structure of the implant even in case of an accidental hit directed along the implant axis (described as “axial” or “vertical” hit).

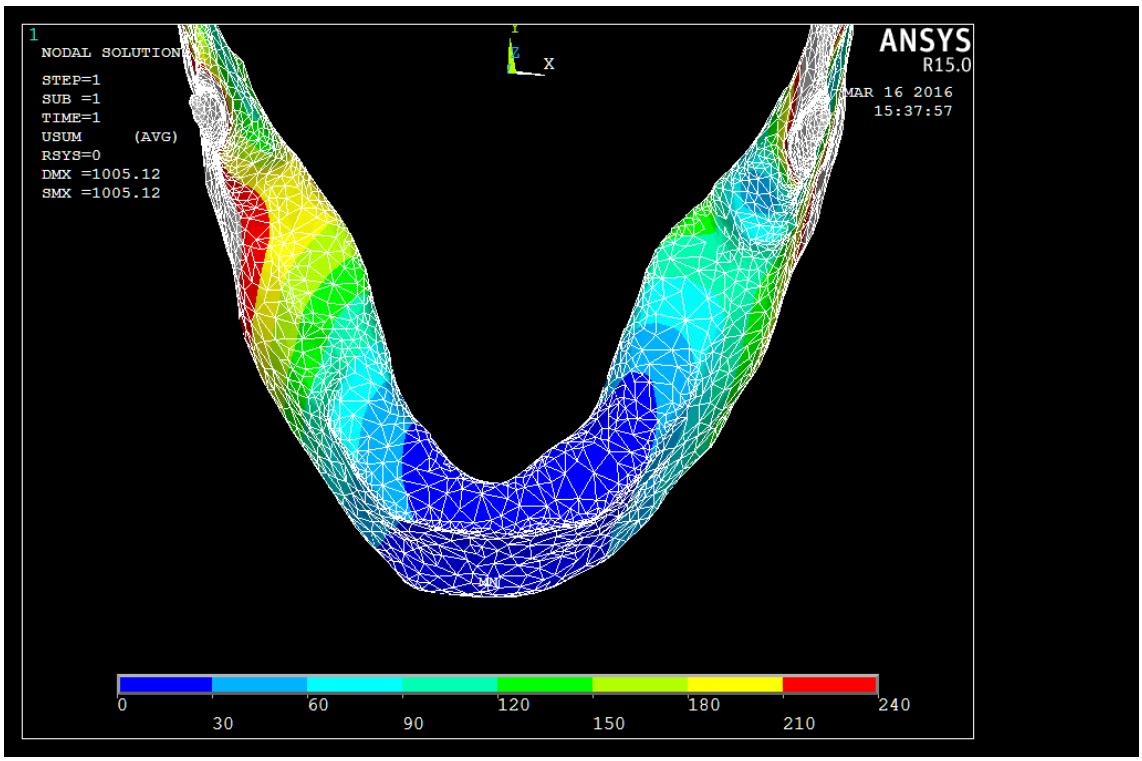

Fig. 3.22 Colour bands corresponding to deformation during clenching. The colour scale has been normalised to highlight deformation ranges in the molar regions (values are in μm). These results have been post-processed within Ansys APDL.

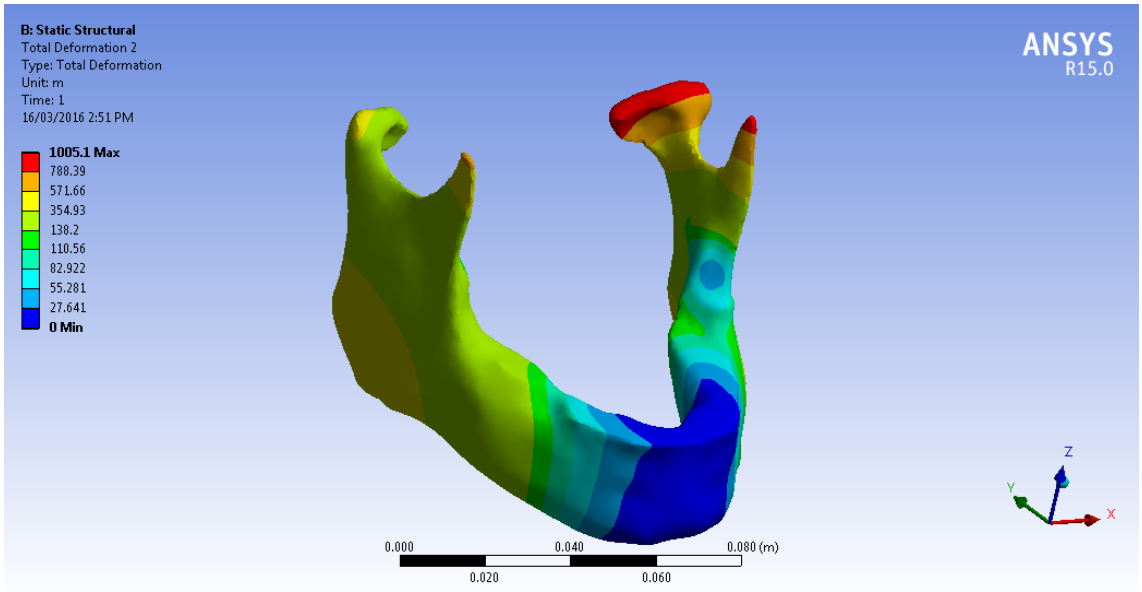

Fig. 3.23 Results for deformation during clenching visualised in Ansys Workbench Mechanical.

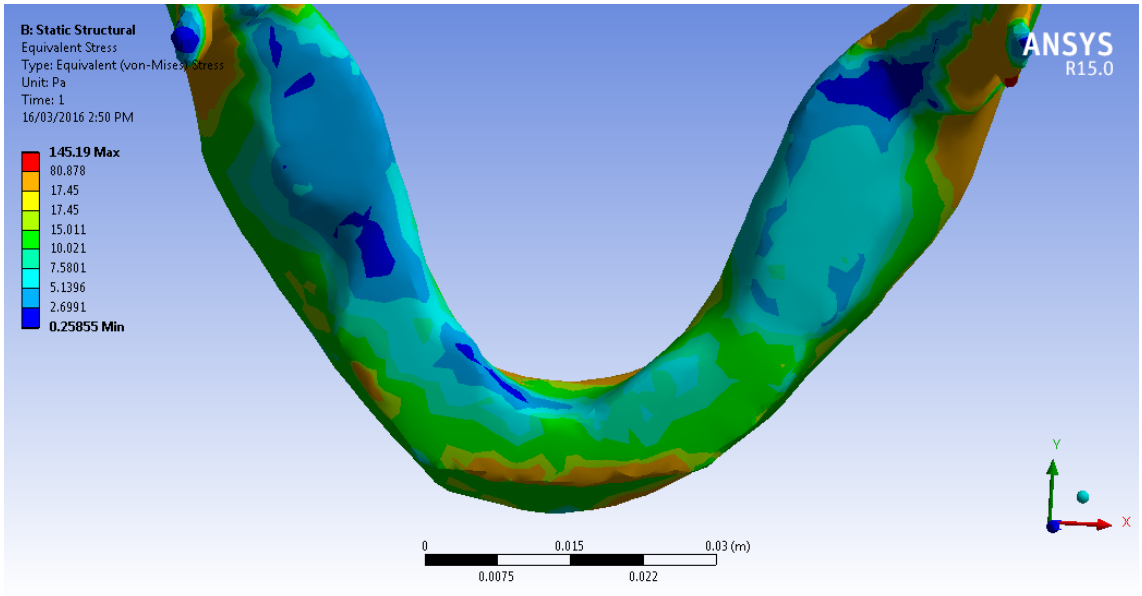

Fig. 3.24 Equivalent stresses in the molar regions during clenching. Units are MPa.

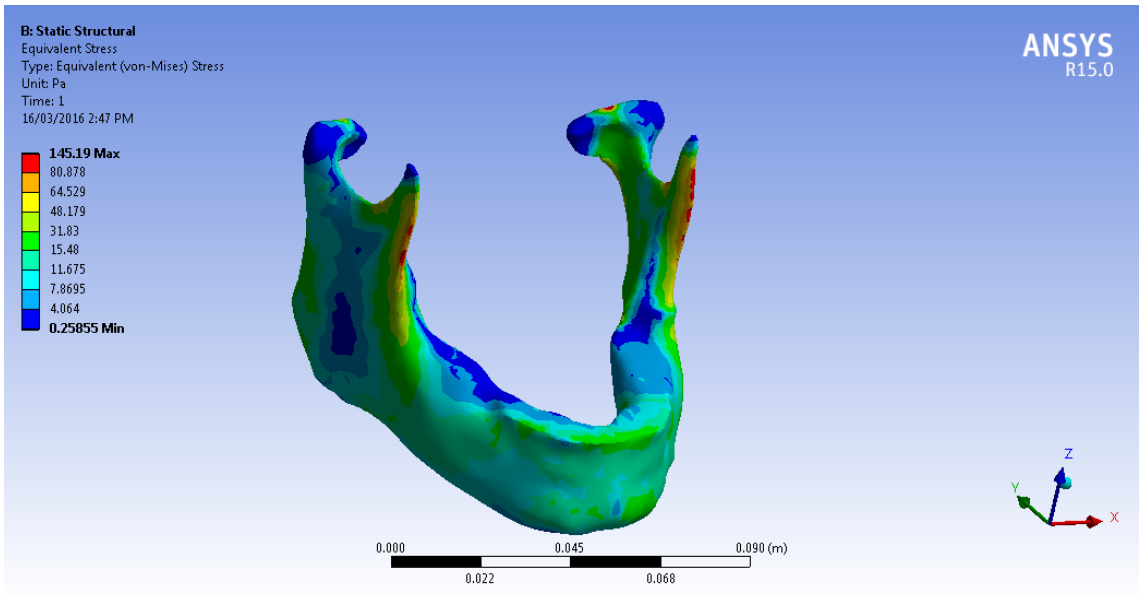

Fig. 3.25 Equivalent stresses during clenching showing high stresses on the coronoid processes. This is another result which confirms the compatibility of M3 with M1. Units in the colour legend are MPa.

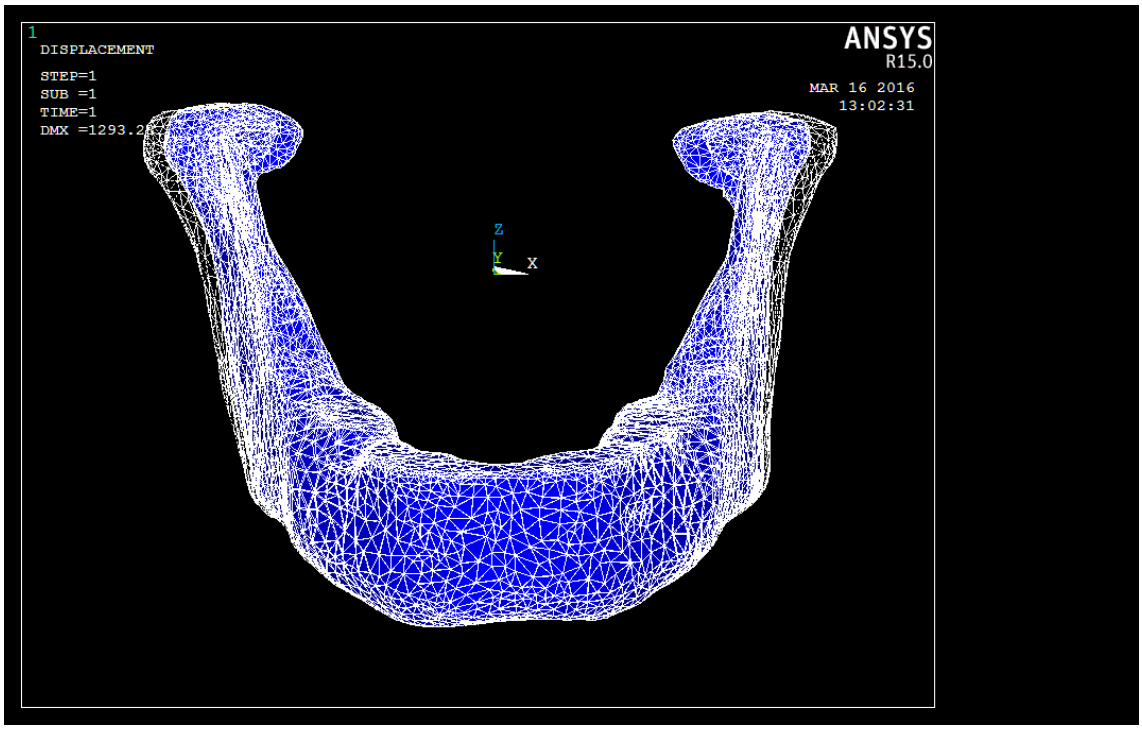

Fig. 3.26 Deformed shape (coloured) versus undeformed shape during wide opening movement.

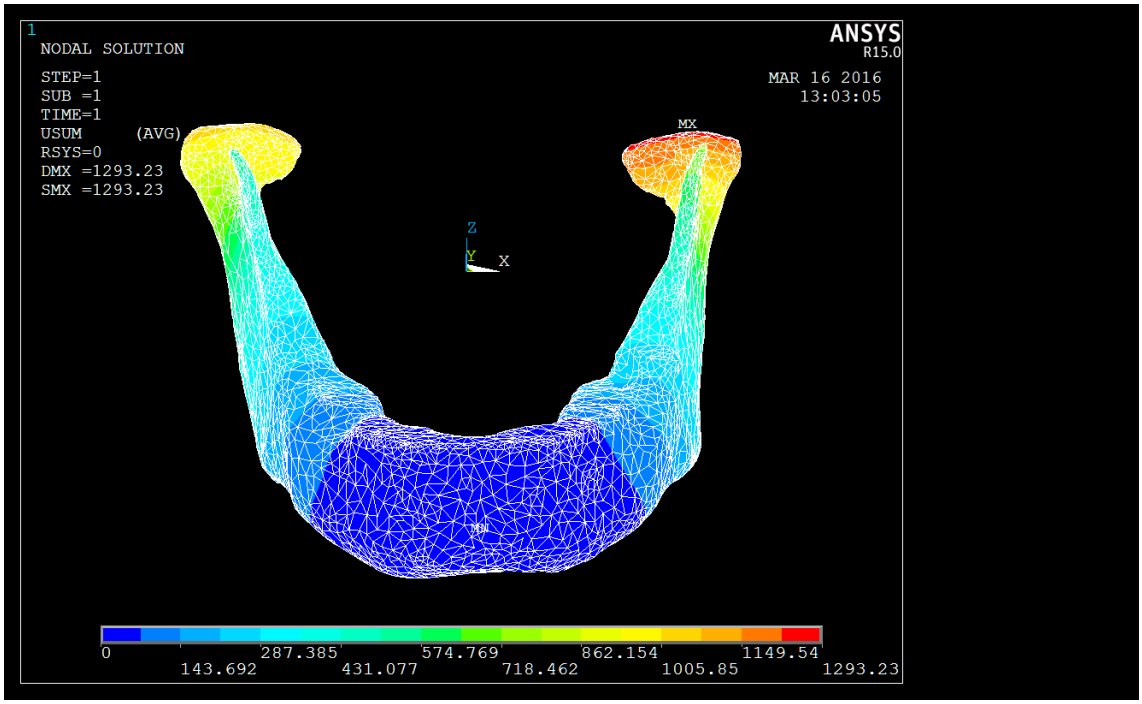

Fig. 3.27 Mandibular distortion during wide opening movement. The maximum value is observed on the left condyle, in line with the results obtained for M1, due to the inwards deformation of the condyles (units are Pa).

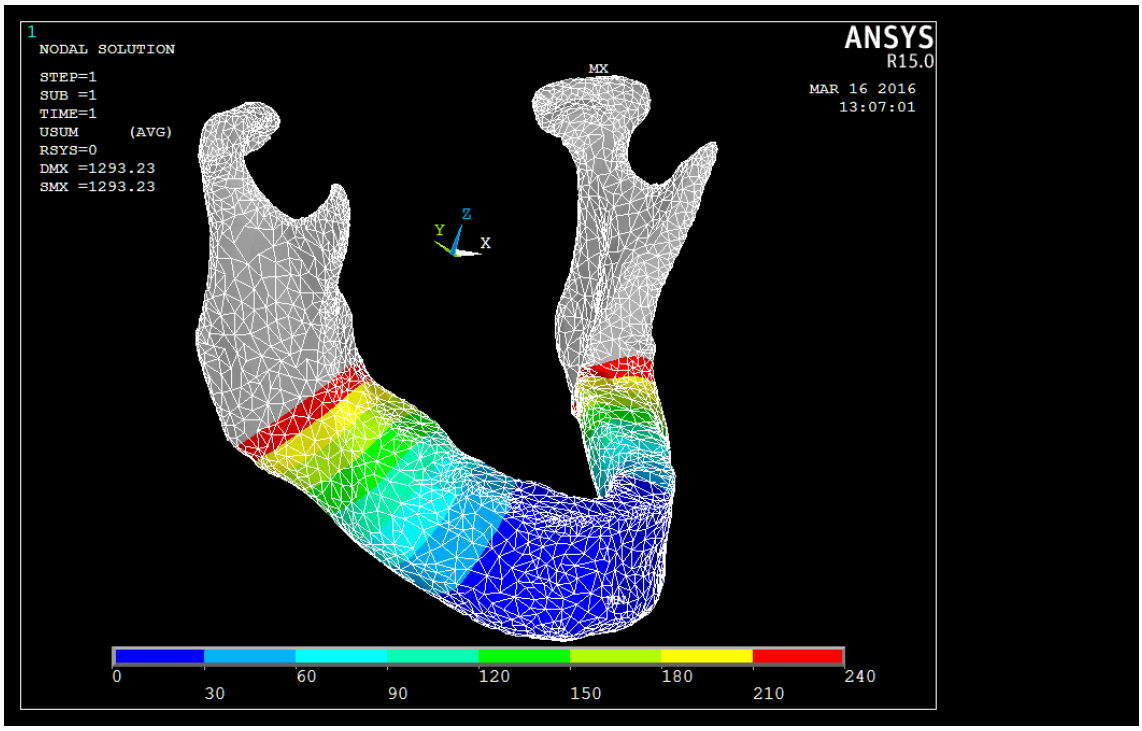

Fig. 3.28 Colour bands corresponding to deformation during wide opening. The colour scale has been normalised to highlight deformation ranges in the molar regions (values are in μm).

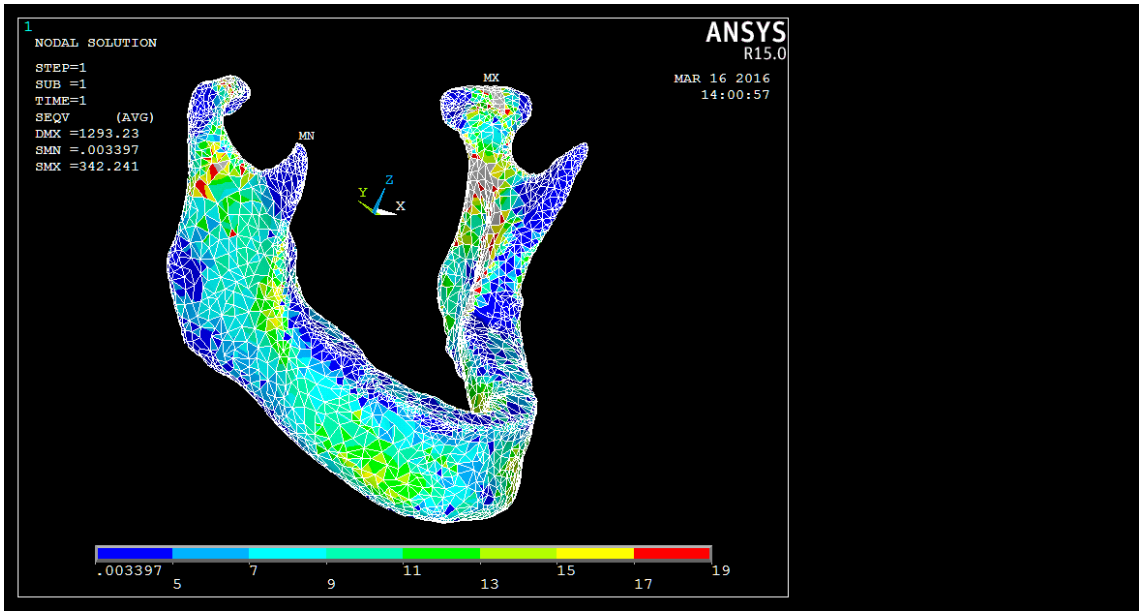

Fig. 3.29 Equivalent stresses during wide opening showing higher stresses on the coronoid processes. These results have been post-processed in Ansys APDL and the units are Pa.

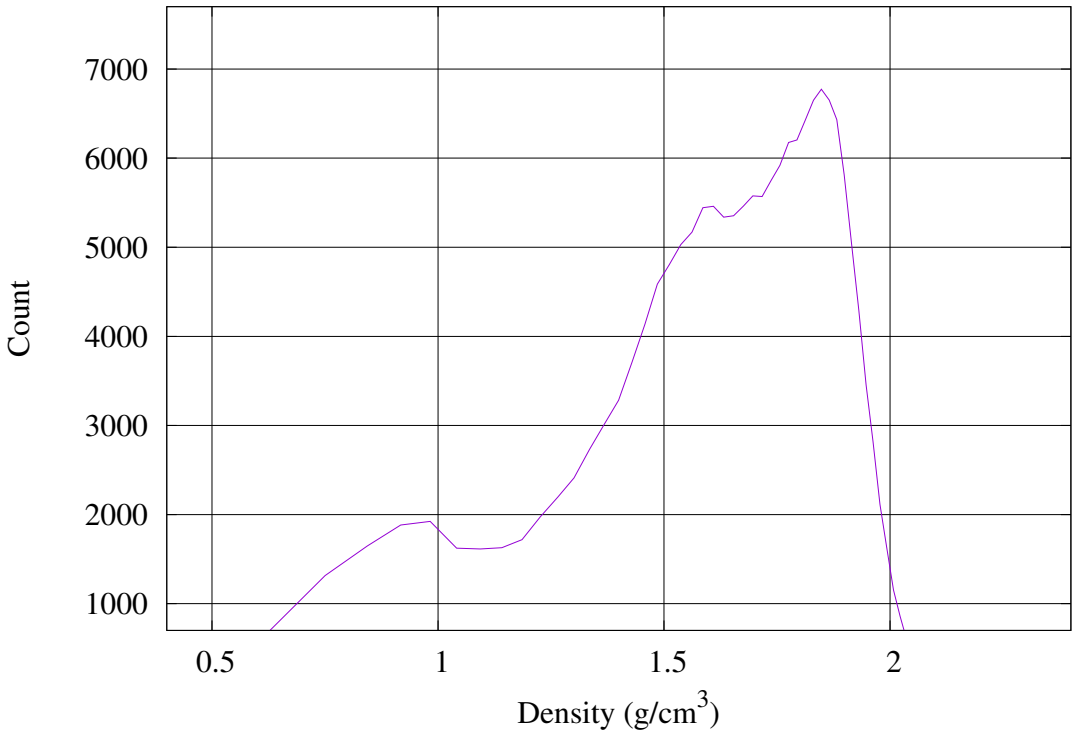

Fig. 3.30 Frequency of calculated densities in the mandible mesh. On the x-axis density (g/cm^3), on the y-axis count of ρ for incremental intervals.

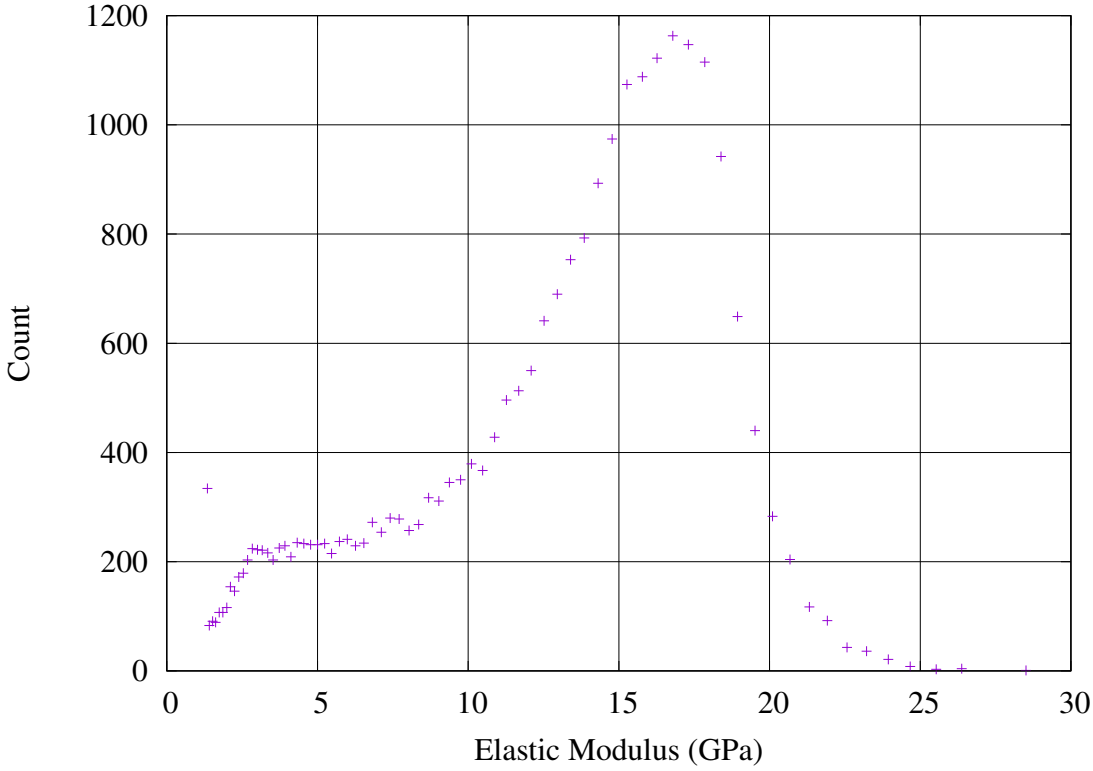

Fig. 3.31 Distribution of Young's moduli in the finite element mesh calculated using an inverse approach. On the x-axis Young's modulus E (GPa), on the y-axis count of E for incremental intervals.

Table 3.14 Comparison of the stress values obtained for cortical and cancellous bone respectively using Keller's empirical law and the finite element simulation object of this study. Density values are in g/cm^3 while stress is calculated as Principal stress. Values are in MPa.

	ρ	S (Keller et al. 1994)	M1a	M2	M3
Cortical bone	1.00	117	79	58	149
	1.25	180			
	1.50	255			

From Keller et al. (1994) the ultimate stress S is estimated by the following law:

$$S(MPa) = 117\,\rho^{1.93} \tag{3.8}$$

Assuming that the densities for the cortical bone are within the range specified in Table 3.14, calculations show how the generated stresses are below the values predicted using Keller's empirical law.

3.5 Clinical considerations and Conclusions

A separate clinical study is being undertaken to evaluate the precision of the developed navigation system in conjunction with BresMedical Pty Ltd (Sydney, Australia) and the University of Bologna (Italy) after obtaining the approval of the Italian Ministry of Health and the Independent Ethical Committee of the University of Bologna.
The results illustrated in this work seem to verify that the Optical Patient Reference Frame assembly for patient-scan registration is stable and can be safely applied for the image-to-world registration procedure.

In this Chapter the risk associated with the presence of the navigation reference tool into the patient's mandible during surgery has been evaluated. The study in Chapter 7 proves how the use of this device facilitates the registration of the anatomy with the virtual planning and produces a high level of accuracy in guiding the implant insertion.

The dimensions of the Fiducial Markers Plate are visibly smaller than the radiopaque reference frames used in other navigation systems for oral and maxillofacial surgery and

there is no need to distribute the markers around a wider area surrounding the implant site in order to increase accuracy. The number of fiducial points is reduced to three and their co-planarity does not affect the quality of the registration.
On the contrary, the geometrical plane formed by the markers is used in an algorithm which finds its intersection with the centreline of the fiducial points in order to calculate the actual coordinates of the most superficial point (Figure 6.8). As a consequence the transformation matrix is more precisely calculated since the procedure uses the 3D coordinates of the real homologous point of the one touched during the three-touch registration procedure other than the centroid of the fiducial marker (Fitzpatrick et al. 1998).

Although the reference assembly composed of the FMP and the OPRF is flexible and can be rotated in three degrees of freedom thanks to a double spherical joint, its location is mostly extra-oral and may generate discomfort due to its weight and by way of an accidental interference with the surgeon's operations.

The author investigated a finite element model of the human mandible to validate the risk of bone damage associated with the use of the navigation system reference tool. In this model external and internal morphology of the mandible was derived through segmentation of the CT scan images of the patients. In addition, the author designed a method for creating a more subject-specific model of a living patient (in comparison to dry cadaver bone) in which the local bone density is evaluated for each finite element in the meshed model by an integration of CT scan values.

A more refined approximation of the bone elasticity was obtained through a correlation with the local density instead of averaging the mechanical properties of cancellous and cortical bone. In particular, this model allowed improving the following approximations:

- separation between cortical/cancellous regions during the image-processing stage, potentially leading to an arbitrary thickness assigned to the cortical bone which has been proven to have a high influence on the overall distribution of stresses in the mandible

- averaged material properties assignments, quantified by numerous authors within a quite wide range and depending on multiple independent variables like bone position,

orientation, wettability, age, gender, healthiness and the mechanical testing method used.

The FEM results show how the stresses generated around the implant socket by accidentally hitting the reference tool are comparable with the stresses calculated for the jawbone during functional movements as reported in some reviewed studies. The stresses within cortical and cancellous bone are lower than the ultimate stress limits for the bone as investigated by Keller in 1994. The stresses generated on the implant surface, during surgery, scan or an accidental interference with the reference frame, are also within the intrinsic structural limits of the implant as per its material properties.

The reliability of the FEM has been proven against studies published in literature for stresses and distortions during functional movements. For this reason, the designed FEM simulation has been used to predict stresses and distortions around implants of different size/length and to estimate the most effective implant solution for supporting the navigation system reference assembly.

This designed model has found that a miniaturised component can be used to support the frame. This is made by an implant supporting the assembly necessary to provide optical and radiopaque reference to respectively the tracking camera and the registration procedure designed for the intra-surgical navigation system. The developed implant aims to promote stability of the reference frame without exposing the surrounding bone to additional risk of fracture or tear.

Based on these results, it can be assumed that neither during the scanning procedure (stage during which the tool must be mounted) nor during the surgery, a modest accidental force exerted on the OPRF would generate a risk of bone damage or fracture for the patient.

Image-guided implant insertion through live tracking of surgical instruments is more interactive, flexible and reliable than the use of dental drill guides which do not offer any feedback regarding the accuracy of the template or the position relative to the anatomic structures (Bell 2010; Chen et al. 2011; Casap et al. 2004).

The system used in this study could reduce the dimensions of the tools required for transferring the surgical plan into the patient's anatomy. This promotes visibility withstanding

accuracy and safety. It could facilitate surgical guidance in cases such as implant placement in sites of bone regeneration or limited inter-occlusal distance and its tools are specifically designed to be clinically easy to use.
This is one of the reasons why the navigation system could become of routine use in intra-oral surgery just as surgical drill guides.

Finally, a novel procedure for deriving local material properties from CT scan data has been developed. The reliability of the resultant finite element model has been verified against the equivalent simulations undertaken using a two-bone approximation with averaged material properties.
This scenario improves the potential of the developed biomechanically correct FEM.
It can be efficiently applied for cases in which the CT scan reveals severe atrophy, poor bone quality, oncological cases in which modelling the anomalies as separate meshes can be too arbitrary and assigning material properties should be subject to an evaluation of the local densities.

The presented finite element model could be improved by restraining the maximum inward deformation of the condylar processes during clenching. From the oral morphology it is evident how this movement is restrained by either the temporomandibular fossa (mechanical action) or by the subject himself who receives a pain feedback once the high deformation begins to generate high stresses. According to these considerations, two options to improve the developed FEM are:

- to run a quasi-static structural simulation for which the action of the lateral pterygoid muscle ceases once the deformation has reached a threshold level
- to introduce the model of the temporomandibular fossa into the simulation which is initially not in contact with the condylar process. This approach would take the simulation to the next level of complexity of Explicit Dynamics.

Chapter 4

Effects of deep cortical and angulated implants-supported prostheses on the osseointegration process by a Finite Element Study

4.1 Introduction

This Chapter describes the application of the finite element model of the human mandible, developed in the Chapter 2, to clinically relevant conditions and situations with the aim to improve currently used implant insertion and surgical techniques. These include insertion and immediate loading of prostheses supported by angled (or angulated) implants and deep cortical anchorage of axial (perpendicular to the occlusal plane) implants of reduced diameter.

FEA has been used by several authors to predict dental implant loading (O'Mahony 2001; Huang 2006) and for microstructural analysis (Korioth 1992; Niebur 2000; De Santis 2005).

By way of applying FEA to a model which is biomechanically correct, morphologically subject-specific and validated against previous studies, the author aims to analyse the

benefits towards primary and secondary stability of implants inserted using innovative surgical approaches.

The study was directed to utilise a novel technique for implant socket preparation like ultrasonic drilling and image-guided surgery. It is envisaged that by using this method the surgeon can safely insert angled implants in posterior areas or with deep cortical anchorage which could offer a superior osseointegration and biomechanical advantage in supporting dental prosthesis.

4.2 Background

4.2.1 Use of dental implants

Osseointegration has been defined as the formation of bony interface connecting the bone to the surface of an implant (Bragger 2005).

Since the introduction and redefinition of osseointegration were made by Swedish (Branemark 1983, Branemark et al. 1997) and Japanese group (Kawahara et al. 2003) groups over several decades ago, dental implants have become a successful restorative modality in clinical dentistry, with a report of over 90% success rate (Adell 1990).

In case of dental implants for oral and maxillofacial surgery, they are generally used to support partial or full-arch prosthetic dentures. In partially edentulous patients, an implant can be inserted to support an artificial resin tooth via a metallic abutment.

Fully edentulous patients are generally given the option to use removable dentures or implant supported/retained ones. The use of dental implants to support dentures generates long-term benefits for the patients (van Staden 2006): improved appearance, comfort, speech clarity and self-esteem and most importantly allows them to function normally. With the implant, the patient can eat more conveniently and limit the future bone loss while restoring his facial skeletal structure.

All these advantages are maximised when the implant is inserted according to an immediate loading protocol (Barone 2003). This procedure eliminates the discomfort associated to the delayed prosthetic treatment and it has been validated by numerous

studies (Tarnow 1997; Schnitman 1997; Taylor 2002) converging on the conclusion that completely undisturbed healing of the implant-bone interface is not necessary for successful osseointegration to occur. On the contrary, premature loading might lead to fibrous encapsulation, as described by Albrektsson in 1981.

Dental implants are also used in presence of different degrees of atrophy, when the surgeon is forced to prepare adjacent anatomical regions like the pterygoid or the zygomatic bone seeking for a stable implant anchorage.

Although the multiple benefits associated to their usage, only a small percentage of patients receive single or multiple dental implants in Australia (McClarance 2004). The reason is likely to be linked both to the initial costs and to the average 5% implant failure rate reported over a 5 year period generally due to a combination of poor manufacturing, lack of skills in the implantation procedure (Porter 2005) and inadequate surgical plan.

4.2.2 Insertion procedure

As explained in Chapter 4, a surgical plan for positioning the implants virtually is generally carried out in a three-dimensional environment using commercial software like NobelClinician™(NobelBiocare, Kloten, Switzerland), Simplant® (Dentsply Sirona, York, Pennsylvania, United States), 3Diagnosys® (3DIEMME, Como, Italy), CoDiagnostix™(3DDX, Boston, United States), ImplaNav™(BresMedical, Sydney, NSW Australia) on the base of tomographic data of the patients, obtained via a Computed Tomography or Cone Beam Computed Tomography scan.
The surgeon can plan the optimal final position of the implant or implants according to its vicinity with delicate anatomical structures like the nerves, the cortical walls, the maxillary sinuses, the nasal cavity or the orbits.

According to traditional techniques, the osteotomy begins with an incision into the gingival tissue at the implant site followed by a pilot hole performed using a round cutting bur. Rotary cutting tips of progressive diameters are then used to extend the diameter of the implant socket in the cortical and cancellous bone until the required diameter is reached for insertion via implant cutting or forming (van Staden 2016).

Constant irrigation via saline solution helps in reducing the heat generated by the cutting action of the blurs and in removing bone debris from the socket.

Implant site preparation can also be performed using an ultrasonic differential socketing approach, as introduced by Vercellotti in 2004. The differential preparation allows widening of a socket wall by the 3-dimensional cutting action including lateral movements of blurs and tips (Vercellotti, 2004). Different studies have examined how ultrasonic osteotomy can produce a better shaped socket when compared with conventional rotary instruments (Stacchi et al. 2013, Scarano et al. 2014).
The implant is then inserted by way of a manual ratchet or using a motor at a speed not superior to 40RPM at a torque superior to 40Ncm.

4.2.3 Influence of peri-implant stresses on osseointegration

During the implant insertion the difference in width between the prepared socket and the implant affects the amount of compressive stress generated in the bone-implant interface. For cortical dense bone a high stress could obstruct the bone supply to regions of the implant site and provoke microscopic cracks in the bone matrix. At the same time stress shielding might take place and, as a consequence, dissolution of the bone tissue in minerals via osteoclasts, also known as bone resorption, is likely to occur in the 3-6 months following the implant insertion compromising the mechanical stability of the implant in the coronal region.

On the other hand, if the implant socket is too large for the implant, the generated stress is not high enough to promote bone remodelling and the formation of lamina dura (Natali 2006) around the implant. This is the scenario in which remodelling can turn on to reduce whole-bone strength by removing some cancellous and endocortical bone (Okumura 2010) resulting in poor osseointegration and hence coronal micro-movements.

Both of these scenarios are caused by an unfavourable level (high and low) of stress in the bone-implant interface which jeopardizes the implant stability resulting in movements of the coronal part of the implant up to a complete loosening of the structure and implant failure.

Although there is no conclusive study determining the optimal stress level which stimulates osseointegration (not surprising due to the number of factors involved), the design of load-bearing dental implants should aim to keep the peak stress in the supporting bone below its micro-damage threshold while exceeding at the same time its remodelling threshold (Frost 2001).

This is why it is necessary, regardless from the implant insertion and positioning technique adopted by the surgeon, to simulate the stresses generated in the implant site before and after surgery.

Because the highest risk scenario for osseointegration is represented by immediate prosthesis loading, it is crucial to evaluate stresses and distortions introduced by the presence of an implant supported prosthesis attached straight after the implant insertion during functional movements like mandibular clenching.

4.2.4 Influence of implant diameter and loading direction on osseointegration

The influence of implant diameter and length on the resulting stresses generated by immediate prosthesis loading has been studied in different published studies through a number of finite element simulations.

In 2009 Guan published a two-dimensional FEM which took into account the presence of blood around the flutes. This affected the percentage of osseointegrated interface for immediate loading which was assumed to be at around 50% as reflected in the coefficient of friction used in the simulation. The stresses used by Guan for cortical and cancellous bone were derived for different biting force directions in the ranges theorized by Choi (2005), with horizontal force between 25N and 250N and vertical force between 50N and 500N. Masticatory forces associated with the activity of mandibular muscles during a clenching action and the stresses and distortion they generate were not taken into account in the simulation. With this setup, Guan found that the stresses within both cancellous and cortical bone decrease when the length of the implant increases. A reduction in the stress

in the cortical bone is also observed for a bigger diameter implant (5.5mm) although the main influent factor producing high stresses is the applied load and moment.

Other results were found by Choi (2005), whose analysis concluded that the implant length, root taper configurations and the implant's mechanical properties have no effect on the distortion observed in and around the implant as well as on the mandible during all three functional movements (clenching, wide opening and protrusion).

According to Choi, the magnitude of the tensile, compressive, and Von Mises stresses recorded in and around the implant are influenced more by the implant length than the root taper angles. Also his study found that although high magnitudes of stresses were recorded on the implants, only a small portion was transferred to the surrounding osseous structure.

By modelling only a thin section of the mandible near the implant site, Li (2009) finds that in posterior areas, where the mandible can be assessed as type II-III bone, the implant length is more crucial in reducing bone stress and enhancing the stability of the implant-abutment complex under either axial (100N) or buccolingual load (30N at 45 degrees). It has to be noted that this was a partial modelling rather than an anatomically correct full 3D model. Biomechanically, it was reported by Li et al. in 2009 that the best configuration can be achieved for implants with diameter bigger than 4.0mm and length over 9.0mm. Similarly to Guan (2009), this study also does not take into account mastication forces other than a bite force acting on a prosthetic tooth. In addition, results are limited by strong assumptions made on material properties and morphology in the finite-element analysis.

Similar conclusions are presented by Ding (2008) in a three-dimensional model of the mandible in which implants of increasing diameters are immediately loaded. According to this study loading the peri-implant bone during healing seems to be beneficial towards osseointegration provided that there is no concentration of high stresses on the mesial and

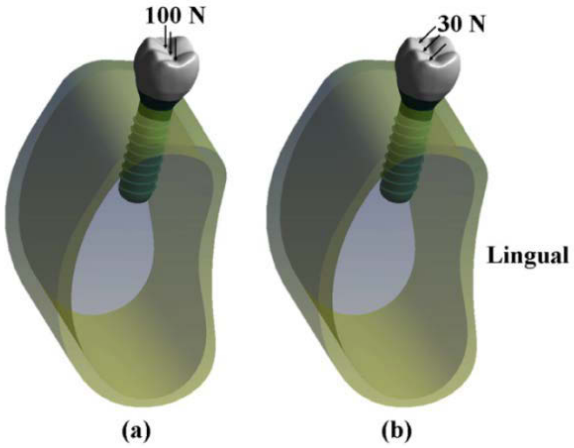

Fig. 4.1 Graphic representation of vertical and buccolingual load components in a three-dimensional FEM pre-processor (from Li 2013).

distal surfaces of the cortical bone around the implant neck (in case with vertical loading) and on the buccal surface (with buccolingual loading).

Using FEA many authors have proved how the tissue in contact with the neck region of the implant is where bone resorption generally occurs (Lozada 1994; Rieger 1990; Meijer 1992; Tada 2003; Petrie 2005; van Zyl 1995; Tepper 2002). Ding's findings support the thesis that non-axial loading has often been related to marginal bone loss and consequent failure of the implant or prosthetic component (Himmlova 2004; Brunski 1988; Barbier 1998). Another relevant conclusion of this study is the trend of the generated stress for increasing implant diameter: using a 4.1mm diameter implant results in a significantly lower stress than a 3.3mm one but not statistically different from the stresses found using a 4.8mm diameter implant.

Also Qian (2009), in a study which simulates the behaviour of the implant neck for buccolingual loading with an inclination ranging from 0 to 85 degrees, finds that the use of a larger diameter implant decreases the stress/strain sensitivity to the loading angle. In addition, the published FEM finds that the best biomechanical environment is created by a configuration in which the threads of the implant neck are below the upper edge of the cortical bone.

Larger implants promote greater stability also according to Okumura (2009) who finds that high stresses around the implant are mainly due to the thin layer of cortical bone generally found in posterior areas of the mandible (bone type II-III).

4.2.5 Bone-implant interface

Many studies found stress patterns where the maximum stresses are located around the implant neck. As outlined by Kitagawa (2005), failures are due to the load transfer caused by the difference in rigidity between the dental implant and the surrounding bone and hence stress shielding. For this reason modelling the interface should improve the realism of the finite element simulation.

Among fixed bond, slip contact and non-linear contact interface boundary conditions, numerous FEA models have shown significant differences in values and distribution of the peri-implant stresses (Meyer 2004).

Overall it is accepted that the implants are bonded to the bone strongly and in case of failure their removal generates problems. As reported by Gotfredsen in 2000, the removal of implants with rough surfaces often results in fractures within the bone far from the implant surface (Gotfredsen in 2000). Based on these observations Li (2009) suggests that the implant should be bonded to the bone in the FE simulation setup. Li (2009) study focuses on the micro-movements of the implants in case of immediate loading by single tooth or full-arch prostheses, being this connected immediately after the implant insertion.

A number of other authors characterise the interface behaviour according to the degree of osseointegration of the implant which is supposed to take place in the first 6-9 months following the surgery.

Many authors, including Ding (2009), Geng (2001) and Lin (2009), assume that contact in the implant-bone interface for immediate loading is frictional with coefficient equal to 0.3.

Based on past FEA work in orthopaedics, a number of workers prefer to use a strongly bonded-type of contact because it simplifies the finite element problem by reducing the

solving time and minimizing the exhaustion of the hardware resources (Takahashi 2010; Hussein (2015), Mariano 2012; Naini 2011; Fazi 2011).

According to the author, the fact that under frictional sliding the contact zone transfers pressure and tangential forces but no tension is too restricting when the simulation is aiming to predict the stresses generated on (a ceramic-like material as) the cortical bone.

4.2.6 The problem with larger implants

As stated earlier larger implants shows less or lower stresses within the structure and adjacent bone then smaller implants. On the other hand other studies have shown that 5.0mm diameter implants have a higher failure rate than 3.75mm or 4.0mm diameter implants (English 2000). According to Ding (2009) this is most likely to the result of the heat generated during the preparation for a larger implant and the subsequent bone damage.

As it will be further discussed in Chapter 7 of this work, according to many investigators, using traditional twist drills, where the cutting action is performed by mechanical rotation of the cutting edges of the cutting tool tips, generates considerable heat which is then dissipated or dispersed into the surrounding bone (Cordioli & Majzoub 1997; Mishra & Chowdhary 2014).

An alternative method is the use of piezoelectric osteotomy. If implant socketing was to be performed using piezoelectric osteotomy instead of rotary instruments, there would be an abundant irrigation on the implant site. As a direct consequence, the generated heat would be reduced while the surgeon would have more access to deeper bone during the socket preparation. Therefore both primary and secondary stability could be improved while decreasing the risk of postoperative necrosis (Jo et al. 2011; Tehemar 1999).

4.2.7 Posterior mandible preparation

In the present work the author aims to validate an improved clinical procedure combining implant size, length and insertion angle with accurate and less invasive preparation of the posterior area of the mandible and immediate prosthesis loading.

Positioning implants in the posterior mandible is a necessity introduced by the use of implant supported O-rings (Winkler 2002) and dentures for full-arch restoration in edentulous patients.

One of the most popular surgical techniques based on Branemark's early 1980s work for restoring dentition in the lower mandible is the "All-on-four®" surgical protocol introduced by NobelBiocare (Kloten, Switzerland). It consists of 4 implants supporting an immediately loaded fixed prosthesis on an edentulous mandible.

The condition for the implants to osseointegrate is to limit their movement during the healing period. This implies achieving good primary implant stability during implant insertion. Pilliar (1986) and Szmuckler-Moncler (2000) quantifies the maximum allowed movement to less than 100 μm. This is very reasonable knowing that the natural tooth moves around 80 to 90 μm during the functional movements.

Among the factors which contribute to the success of the All-on-Four® procedure, there is the skill of the surgeon who is expected to achieve a bottom cortical anchorage where possible, an insertion torque between 30 and 50 Ncm and Resonance Frequency Analysis values superior to 70. These represent clinically accepted values as per oral surgeons at Clinical Odontoiatrica from University of Bologna, Italy. According to the mentioned surgeons, over torqueing, for example, might increase the level of dying osteocytes in the area which would lead to bone resorption and therefore discourage the remodelling of the bone. Moreover, the consulted surgeons believe that operating in the posterior mandible the choice of the implant site is also crucial, since the presence of dense cortical bone in the interface with the implant neck is preferred. Implants with sharply pitched threads also constitute an advantage as much as longer implants do.

Based on these observations the author's thesis is that with a differential ultrasonic preparation of posterior tilted implants, performed under live tracking of surgical instruments and the possible contribution of a double cortical anchorage, both primary and secondary stability of the implants can be maximized.

The introduction of the concept of tilted implants comes from the difficulty in achieving a good anteroposterior (A-P) distance between the couple of anterior implants and the couple of posterior implants used for a full arch restoration by using only axial inclinations (Figure 4.2).

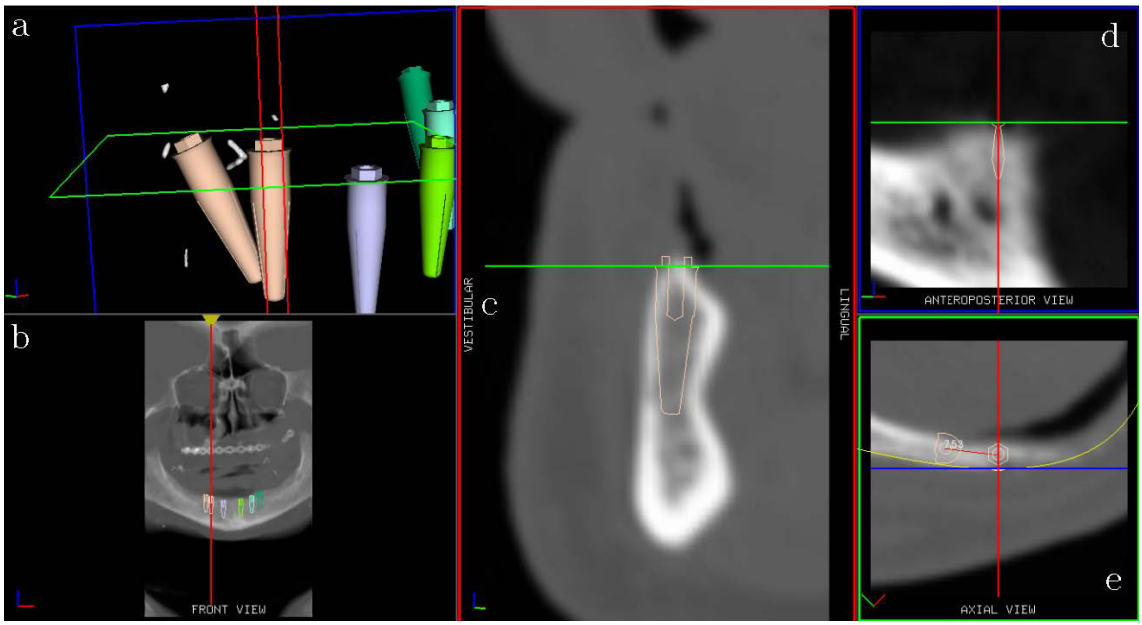

Fig. 4.2 Evidence in the virtual planning of the increased antero-posterior spread achieved by the use of tilted implants. In particular the three-dimensional view (a) shows how the implant head can result in a more posterior location with respect to the use of an axial implant in the same location. The improved AP spread is quantified in this case to 7.53mm by a 2D measurement on the coronal plane (e).

As reported by Rutkowski (2015) the minimal A-P spread to place a fixed prosthesis for the edentulous mandible is half the length of the cantilever generated by the posterior end of the prosthesis on the posterior implants (Figure 4.3).

An insufficient A-P spread can generate a mechanical failure due to implant overload. From the excessive over loads a vicious cycle of recurring problems such as micro-damages, resorption, bone remodelling, increased porosity and therefore more micro-damage which leads to loss of the bone and subsequent implant failure.

From a clinical point of view, the placement of angled implants requires operating in the vicinity of the mental nerve (posterior branch of the inferior alveolar neve). This complication, combined with the risk of losing the prosthetic axis during the socketing procedure due to horizontal sliding, makes the use of computer guided treatment planning

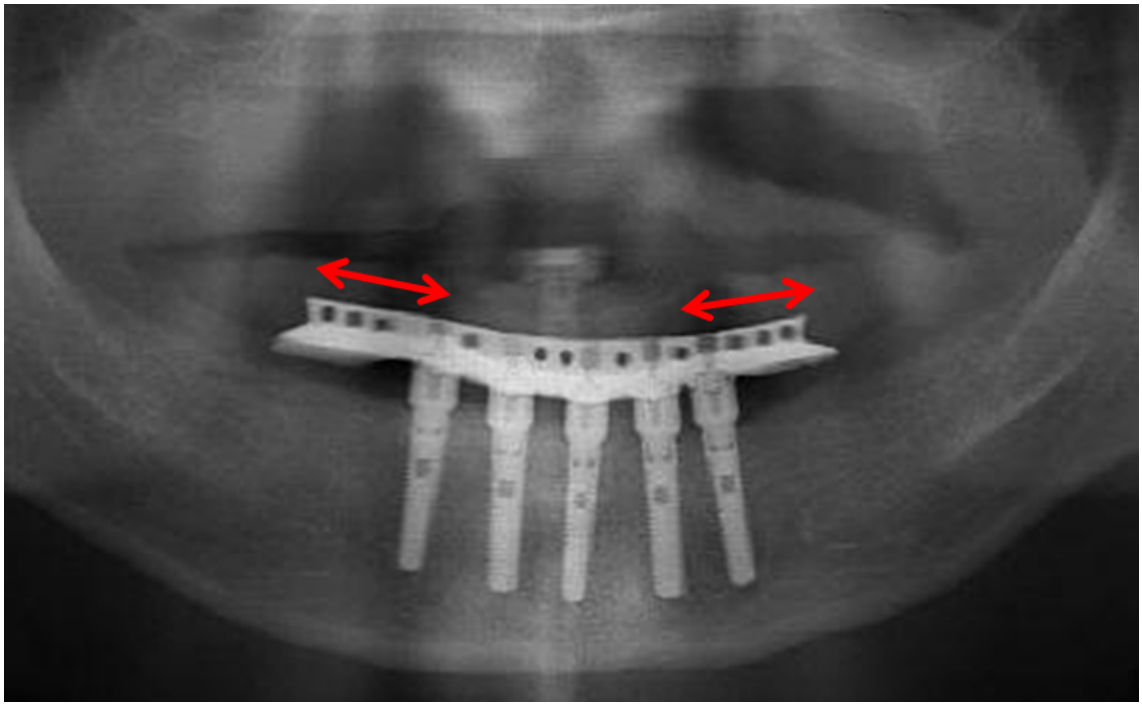

Fig. 4.3 Posterior unsupported extension of an overdenture. The anterior position of the axial implants avoids an interference with the alveolar nerve. The bilateral posterior spread of the overdenture is responsible for the cantilever effect on the left and right posterior implants.

and placement preferred.

To solve this problem currently a range of templates are used. The author believes that in the case of angled implants the use of surgical templates, (which is currently the most popular computer-aided surgery technique), is not functional and it can be recognised that it is clinically unpractical for the following reasons:

- In posterior locations, where the space for osteotomy is already reduced by the presence of the maxilla, the surgical templates adds a vertical offset which requires the use of a drill tip extender
- Angled implants must be inserted from a posterior inclination through the drill extender

Alternatively the use of image-guided surgery, by way of the developed navigation system presented in Chapter 6, represents a viable option for the guided insertion of the posterior tilted implants according to the All-on-Four® bone preparation protocol. Being

able to control in real time the socket axis and without any additional offset on the mandible the surgeon would be able to perform the socketing procedure with accuracy.

In addition, using ultrasonic preparation method via piezoelectric inserts for implantology, the safety of the procedure would be maximised. This technology, introduced by Mectron S.R.L.(Genova, Italy, allows to performing osteotomies using micro-vibrations with high intraoperatory surgical control, precision and safety because of its selective bone cutting (different ultrasonic frequencies act only in hard mineralised tissues) (Vercellotti 2004, Stubinger et al. 2008, Pereira et al. 2014) without affecting the near alveolar nerve.

4.2.8 Double-cortical ultrasonic preparation

With the introduction of ultrasonic inserts for implantology, Piezosurgery® (developed by Mectron S.R.L) offers the hardware to achieve a deeper implant site preparation.

As it will be explained in detail in Chapter 7, which will analyse and report the advantages of applying a navigation system to piezoelectric socketing, the first preparation on the implant site is performed via surgical bits with a very sharp termination (radius < 0.5mm).

The process of the drilling is based on the vibrating action of the piezoelectic tip at ultrasonic frequencies (as opposed to a rotary one). This insert allows preparing deep cortical bone without the risk of sliding along the cortical wall. Sliding along the inner wall would, in fact, generate a deviation from the planned socket axis as shown in Figure 4.4.

While approaching the final socket depth, by way of radial extensions as much as vertical penetration, the surgeon can follow the live progress of the osteotomy on an image-guided surgery system.

By using Piezosurgery® with navigation, the surgeon would be able to verify in real time that the actual implant socket is aligned with the prosthetic axis as virtually planned. Additionally, the procedure can aim to achieve a deep cortical anchorage for the implant

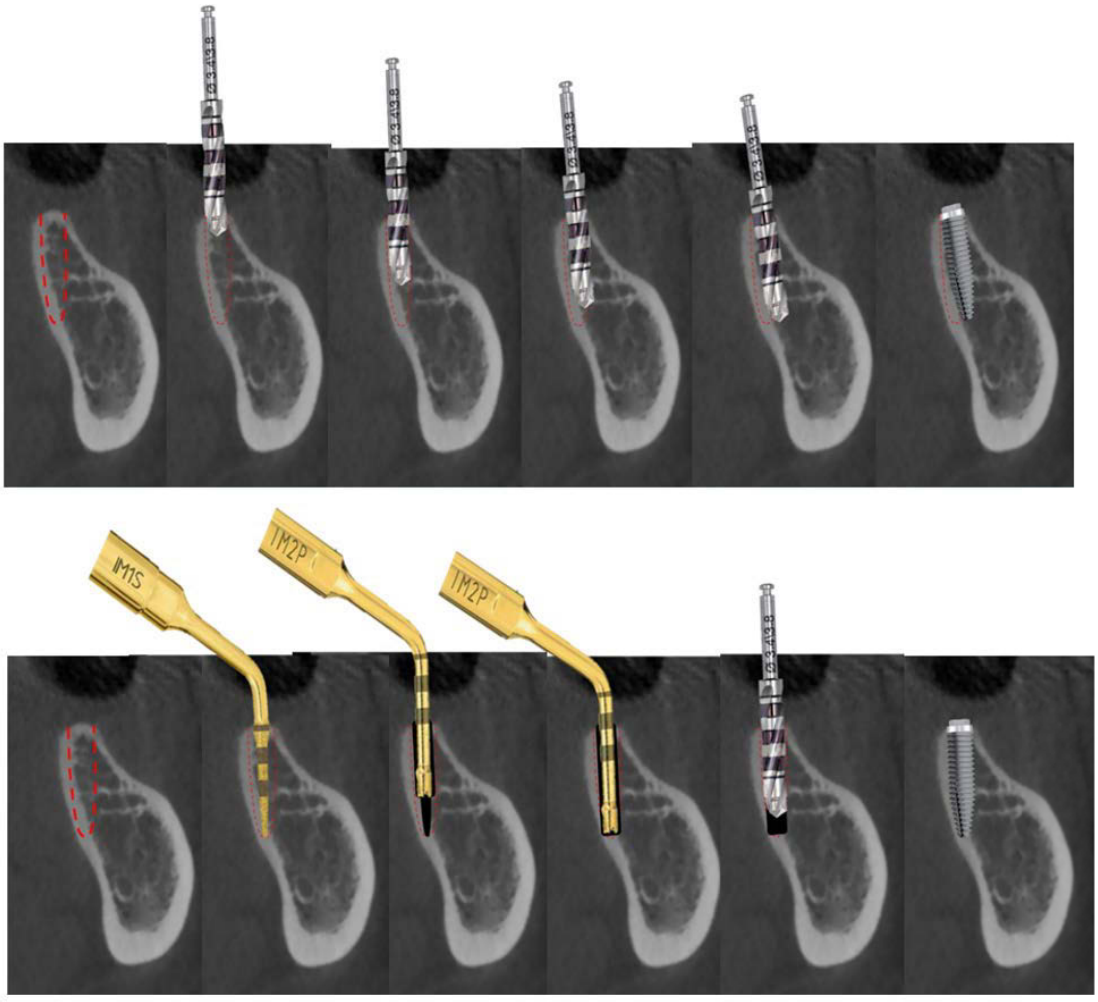

Fig. 4.4 (Top) Rotary drill tip's misalignment with the prosthetic axis due to an implant shift caused by the contact between the tip and the lingual cortical wall; (bottom) deep bone preparation using a combined piezoelectric and traditional osteotomy.

even in cases for which there is a high risk of perforating the lingual cortical wall.

Deep cortical anchorage and tilted implant insertion are therefore two surgical techniques promoted by the combined used of ultrasonic preparation and image-guided surgery. The following sections will explain how the author prepared a finite element simulation to analyse the potential biomechanical advantages of inserting implants in the posterior mandible by following this approach.

4.2.9 Biomechanics of the mandible

Most of the reviewed finite element studies on implant-supported prostheses in edentulous mandibles do not include complete biomechanical models.

In order to evaluate the stresses in the cortical and cancellous bone around the implant neck, an external load is generally applied either axially or with a buccolingual inclination on the prosthesis immediately supported by the implant. In other cases the load is applied to the distal end of an overdenture or a milled bar supporting an overdenture to quantify the cantilever action on the posterior implants.

There are only a few complete 3D models of the mandible since most models only consider a section of the mandible in posterior regions (Li 2009; Guan 2009; Okumura 2009; Motoyoshi 2009; Kitagawa 2005). Others - although musculature not properly assigned or not properly constrained - are built using the whole mandible and a three-dimensional set of forces (Bujtar 2010; Hussein 2015; Ding 2009; Ammar 2011; Rubo 2009; Barao 2009 and 2013). In most of the studies reviewed, the solid model is over-constrained to prevent rigid body movement due to either unbalanced mastication forces or the introduction of an external force on the prosthesis.

The author finds that over-simplifying the muscle load set or over-constraining the solid model decreases the reliability of the finite element model in predicting the total stresses

generated around the immediately loaded implants. For this reason, a fully balanced and correct muscular load set during clenching will be used as a necessary complementary boundary condition to the simulation.

4.2.10 Factors influencing the insertion of an implant and summary of hypotheses

In the reviewed studies the variables affecting the osseointegration of immediately loaded posterior implants and the realism of the relative FEA simulations are:

- Implant length
- Implant diameter
- Abutment height
- Taper of the implant
- Bone quality, in particular:
  - material properties of the bone
  - bone isotropy approximation
  - thickness of the cortical bone
- Angle of insertion
- Bone-implant interface modelling

The benefits introduced by a navigated differential ultrasonic preparation for implant insertion are:

- Reducing the risk of slipping on the cortical wall which alters the planned prosthetic axis
- Higher penetration capacity using pointy tips

- Penetration safety in regards to the vicinity with lingual floor, canine and alveolar nerve
- Live feedback regarding prosthetic axis and vicinity to nerve
- Avoiding the overheating generally caused by the preparation of larger sockets

The deployment of an All-on-Four® surgical protocol might imply that:

- The A-P spread between anterior and posterior implants must be not less than two times the distance between implants
- Axial implants cannot be positioned too posteriorly due to a minimum length (7mm) required
- Mechanical failures and bone resorption are likely to be caused by to the use of a long cantilever action and axial implants
- There is a vicious cycle of loading, micro-damage, more porosity until failure
- The insertion of posterior angled implants requires the assistance of a computer via image-guided surgery or dental drill guides which are unpractical in posterior areas.

In addition, the author supports the following hypotheses:

i Osseo-integrated implants are subject to lower stresses during biting

ii The use of frictional sliding contact for the bone-implant interface results in lower stresses since tensile components of the stress are not taken into account

iii Using a navigation system the surgeon can verify the axis of the implant socket even during a deep preparation

iv Using a biomechanically correct set of mastication forces, in the scenario of a functional loading movement, improves the realism of the finite element simulation when external loads are applied to an implant-supported prosthetic component

v In order to improve the clinical relevance of the model, the virtual insertion of posterior implants must be carried out in a surgical planning environment which shows the internal structures of the mandible including cortical/cancellous bone boundary and the alveolar nerve

4.2.11 Biomechanical and clinically relevant output of the present model

Using the factors explained above, the author has applied the biomechanically and anatomically correct model already adopted for investigating distortions of the mandible during functional movements (Chapter 2 and 3) to the case of immediately loaded posterior implants. In particular, the following assumptions considered and conditions are investigated:

- Using bonded-type contact, and not frictional contact, longer (15mm) implants of standard diameter (4mm) to support immediately loaded prosthesis generate lower stresses in the surrounding bone
- Bottom cortical anchorage can contribute to reduce the stresses around the implant site without the need for using a bigger diameter
- The use of angled implants (diameter less than 5mm) for posterior sites in All-on-Four® configuration generates smaller coronal micro-movements with respect to axial implants due to the improved A-P spread and the reduced cantilever action.

4.3 Method

4.3.1 Implant Planning

A tomographic scan of a fully edentulous patient was taken using a Computed Tomography (CT) scan (i-CAT, Xoran Technologies, Minnesota, USA) with a 0.3mm voxel resolution and DICOM export functionality.

The patient had been referred to Sant'Orsola Hospital (Bologna, Italy) by a dental practitioner and did not receive extra radiation for the purpose of this investigation. The

subject was considered not taking any medications, had normal diet and did not have a history of bone diseases such as osteoporosis.

The choice of CT was preferred to Cone Beam CT (CBCT) because it can image the alveolar nerve at higher contrast. In addition, the superior capability of the CBCT in rendering the periodontal ligament and the tooth root does not improve the diagnosis in case the patient is edentulous.

As stated in Chapter 2, the DICOM images were loaded in the software developed for image-guided surgery whose design, clinical application and hardware integration will be further discussed in detail in Chapter 6. In this chapter the primary aim is to show its application to this specific biomedical modelling and the clinical problem.

A preliminary function within the software application is dedicated to the creation of a panoramic profile on the occlusal plane. This operation is performed by picking several points on the bite line joined in a spline. Once the spline is created and rotated in the

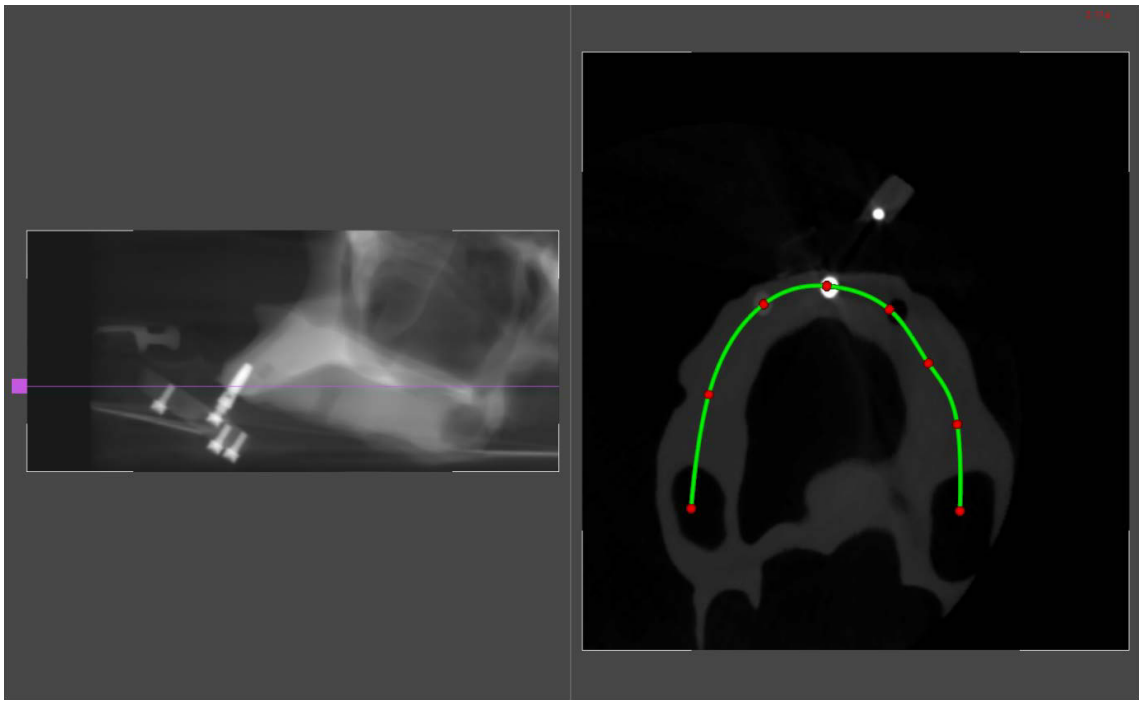

Fig. 4.5 Software view which allows the creation of a panoramic profile within the software application developed for image-guided surgery: by picking landmarks in the axial volumetric slice (on the right) a spline is automatically computed and used to direct the main transformation of the volumetric cuts used in the following implant virtual planning operation.

anteroposterior and sagittal planes, it is used to direct the orientation of three orthogonal slices which probe the volume. By inspecting the radiographic images contained in the slices and fine-tuning the position of a master slice in the vestibulo-lingual direction, it is possible to rotate the virtual implants to the desired inclination, at a safe distance from the alveolar nerve and without penetrating the lingual cortical wall (Figure 4.6).

Fig. 4.6 Compound view of the scanned anatomy during the implant virtual planning operation. The proposed position of the implants can be checked for interference with the alveolar nerve within a vestibulo-lingual slice (c) and via an antero-posterior cut (d). This software GUI snapshot is relative to the implant planning for an All-on-Four procedure with posterior tilted implants. By using the planning module in the developed software the user can accurately plan the insertion angle of the implants, measure the distance from the apex to the nerve and aim to a set a bicortical anchorage without penetrating the lingual wall.The user can also check the position of the implant in a radiographic image corresponding to an axial volumetric slice (e) and an orthopantomography of the patient (b).

4.3.2 Biomechanical models

Due to their clinical relevance, surgical plans were completed for five different biomechanical scenarios:

I **I1**: Two axial implants of 4mm diameter inserted in the left and right posterior region with deep cortical anchorage

II **I1c**: Two axial implants of 5 mm diameter in the left and right posterior region with crestal cortical anchorage only (control group for I1)

III **I4**: Two anterior axial implants and two posterior tilted implants for the support of an All-on-Four® prosthesis with maximum A-P spread allowed clinically

IV **I4c1**: Two anterior axial implants and two posterior axial implants for the support of an All-on-Four® prosthesis with posterior axial implants insertion points corresponding to the position of posterior angled implants insertion points (first control group for I4).

V **I4c2**: Two anterior axial implants and two posterior axial implants (more protruding with respect to I4c1) for the support of an All-on-Four® prosthesis with maximum A-P spread allowed by the use of axial implants without interference with the alveolar nerve (second control group for I4).

4.3.3 FEM pre-processing

Once the virtual surgical planning was complete the implants were exported in STL file format to a CAD software (Autodesk, Inc., California, United States), to be aligned with their respective engineer model.

The use of non-reverse engineered models for the implants, as opposed to solid models derived from the STL file, improves the regularity of the mesh generated by the FEA pre-processor and the following Boolean operations.

The mandible mesh was created from DICOM images according to the **procedure described in Chapter 2**.

Modelling the internal boundary of the dense cortical layer is a crucial operation since the biomechanical simulation is aiming to check the effect of a double cortical anchorage of the implant.

This is why the mandible was digitally reconstructed using a two-bone approach and two volumetric meshes corresponding to the inner cancellous and outer cortical bone.

4.3.4 Control groups

The choice of the control groups reflected the need to reproduce realistic biomechanical configurations which, according to the author, were directed to improve the primary stability of immediately loaded implants such as deep cortical anchorage and posterior tilted implants. For I4 and I4c1-2 the prosthesis was modelled as a curved beam with

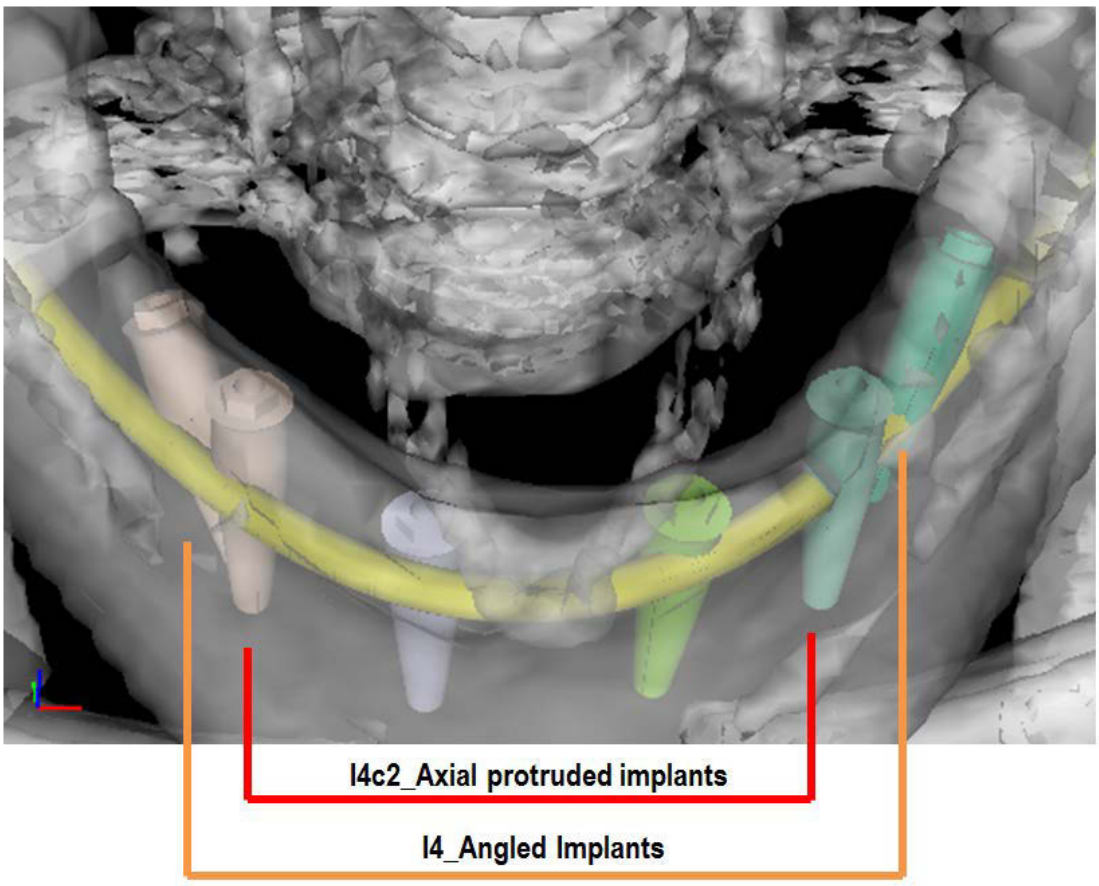

Fig. 4.7 Superposition of the I4 and I4c2 scenarios in a three-dimensional view of the virtual planning environment. Although the two central anterior implants are common to the two configurations, the surgeon can either choose to use tilted or axial implants in posterior positions. The choice of axial implants of the same length of tilted implants forces a more anterior ("protruded") insertion in order to avoid the loop of the mental nerve.

rectangular cross section fused with the supporting implants (Figures 4.10 and 4.11). It was chosen not to use the engineering model of an abutment screwed onto the implant head in order to eliminate additional variables from the stress analysis. In fact, as it has been observed by Rangert (1989), and Skalak (1983) and reported by Rubo in 2009, a perfect fit between the implant, the abutment and the prosthetic component combined to

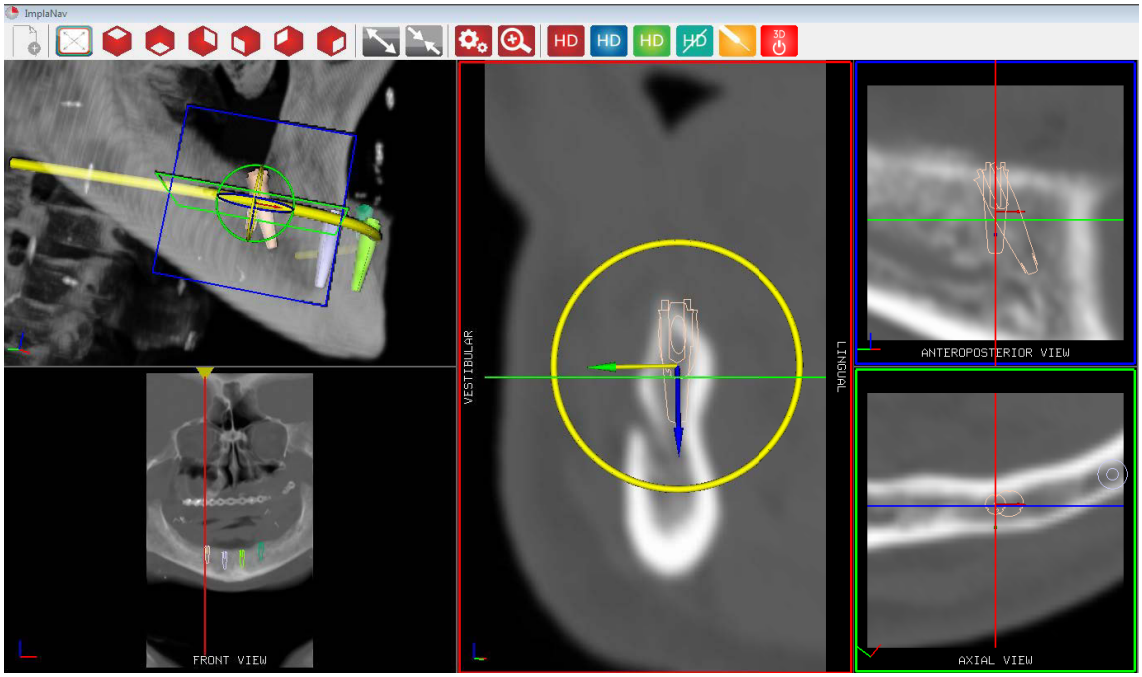

Fig. 4.8 Virtual planning for the control group I4c1. In order for an axial implant to be inserted as posteriorly as a tilted one (the two implants heads are overlapping in the figure), the overall implant length must be shorter in order to avoid an interference with the alveolar nerve.

the framework rigidity is essential to the longevity of the implantation. Instead, the implant

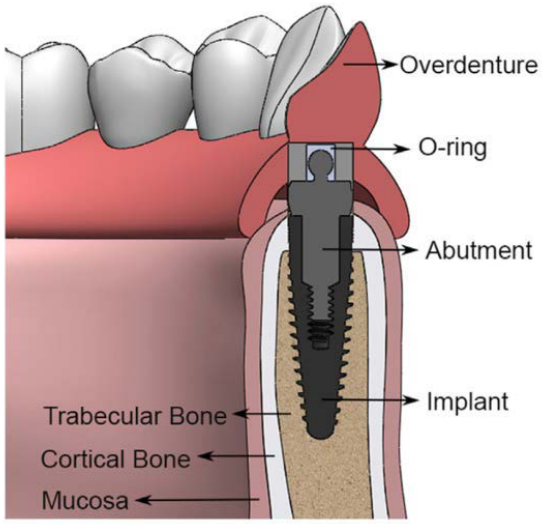

Fig. 4.9 Typical assembly for single tooth prostheses, consisting of an abutment which is connected to an overdenture via a specific connection (from Topkaya 2015).

heads were attached to the curved beam by way of a vertical extrusion simulating the angled abutment, the head-abutment interface and the abutment-beam anchorage as one solid connection (Figure 4.9).

In model I4, the posterior length of the prosthesis was designed to suit a full arch restoration procedure. The model was also checked for compatibility with the maximum cantilever action allowed on the posterior implants correspondent to two times the A-P spread.

For the control groups I4c1-2, the same curved beam used in I4 was fused to the anterior and posterior axial implants by way of similar abutments-like connections. The position of the two anterior implants was deliberately left unchanged in order to better identify the biomechanical impact of replacing the angled implants in posterior areas with axial ones.

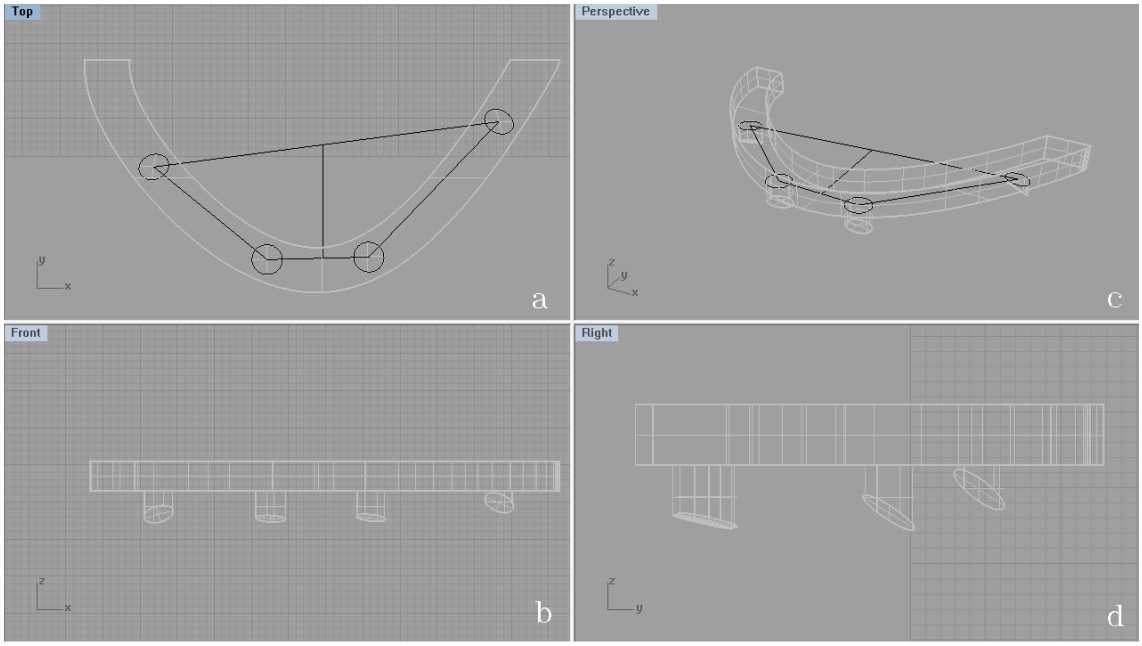

Fig. 4.10 CAD modelling of the overdenture used in the finite element simulations in a compound view environment: (a) top view, (b) front view, (c) perspective view and (d) right view. The abutments are modelled as vertical extrusions from the head of the implants fusing with a curved beam.

4.3.5 Significance of control group I4c1

In order to assist with validating the author's thesis, in the control group I4c1 angulated implants are **replaced with more anterior and shorter axial implants**. From a clinical

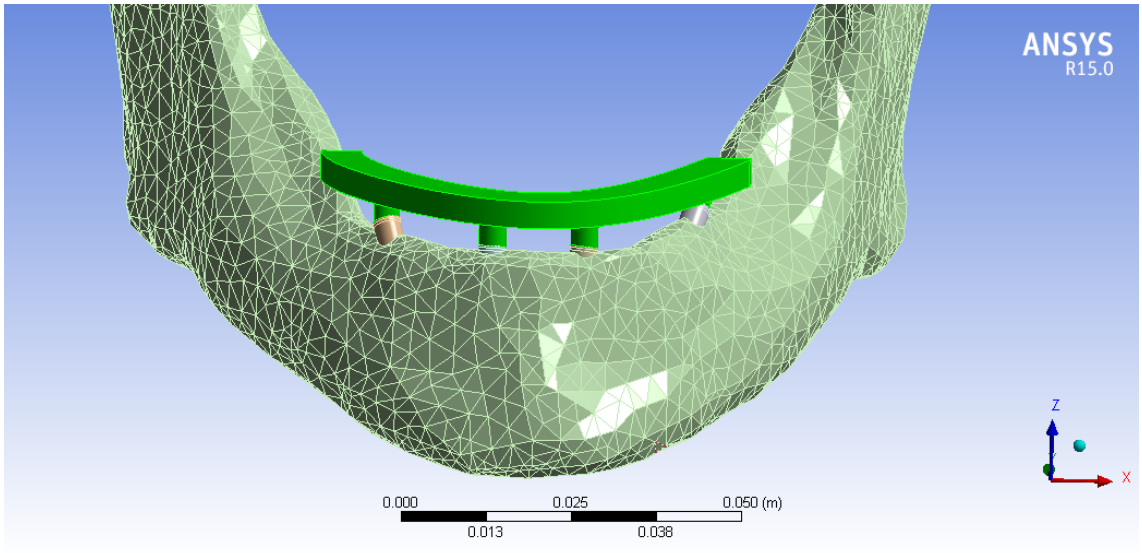

Fig. 4.11 Three-dimensional model of the human mandible used in the presented FEMs, including cortical and cancellous bone, 4 dental implants supporting a curved beam simplifying an All-on-Four fixed prosthesis.

point of view, the choice of axial implants to support the posterior region of the denture has three major implications:

- The implants must be shorter than the tilted ones in order to avoid an interference with the alveolar nerve (as shown in Figure 4.8)
- Also to avoid damage to the nerve, the axial implants are generally placed just above the mental foramen which implies that the implant heads are in a more anterior position with respect to the angled implants
- As a consequence of the "protruded" position, the A-P spread between anterior and posterior implants is reduced and the cantilever effect of the distal end of an implant-supported denture is amplified, potentially resulting in micro-movements of the posterior implants, high stresses and risk of bone resorption.

It must be noted that, although the risk of damaging the nerve is high, shorter (max 8.5-10mm long) implants can be inserted as posteriorly as the tilted implants. Being the final position of the distal end of the implant very close to the nerve, this procedure should be performed with the assistance of surgical dental drill guides or image-guided surgery for better patient care and safety.

Because of the original A-P spread, the author has chosen I4c1 as main control group. This presents posterior axial implants which are 10mm long and whose insertion point corresponds to the insertion point of a tilted implant in the same location, as shown in Figure 4.8.

From a clinical point of view, restorations of a full arch are mostly performed when a patient has a severe atrophy due to previous bone resorption or surgical osteotomies. In these cases the probability that there is enough bone above the alveolar nerve for anchoring an axial implant is low.

Furthermore, the use of computer-assisted surgery or image-guided surgery for implant insertion is not always available. This is why the model designed for I4c1, although preserving the biomechanical advantage, is not always clinically applicable.

On this principle the second control group I4c2 was designed to validate the efficacy of the tilted implants surgical procedure. A more clinically viable approach is represented by the insertion of the two posterior axial implants more anteriorly with respect to the mental foramen, as shown in Figure 4.12. This is the configuration which is expected to offer less mechanical support to the denture due to the augmented cantilever action on the posterior implants. For this reason, the second control group was considered weaker than I4c1 in validating the thesis that the tilted implants configuration in I4 is the most advantageous one.

The clinical feasibility of the final implant position was diagnosed in the surgical virtual planning environment in which implant insertion and end point have been planned and pre-visualised against the tomographic images. A practical example relative to this is shown in Figure 4.13, where the vicinity of the planned implant with the adjacent nerve is quantified by 2D measurements).

This approach is as an improvement of past mandibular models, since the implants in those studies were inserted in posterior areas with approximation, without being able to visually inspect their interference with the nerves, tooth roots and the lingual wall.

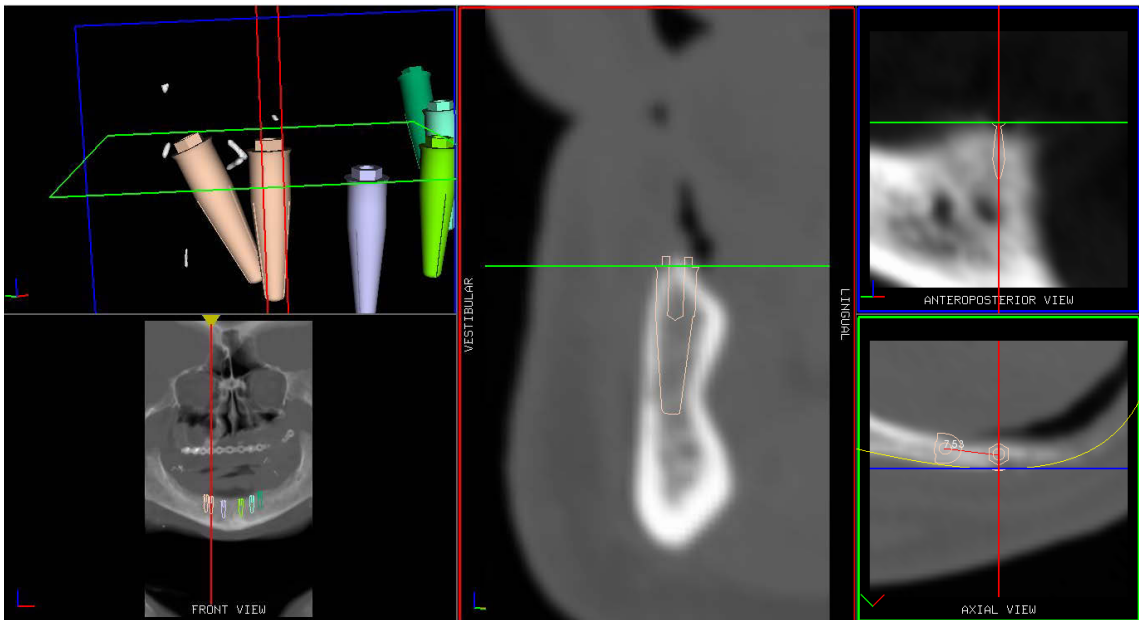

Fig. 4.12 Virtual planning relative to the scenario I4c2 superimposed with the titled implants used in I4. The choice of axial implants as long as the tilted ones requires a "protruded" position in order to avoid the alveolar nerve and have a deep penetration in the cancellous bone as shown in the central slice.

In a different effort to enhance the realism of the model for determining stresses and distortion in the mandible with the use of an All-on-Four® prosthesis, the bite forces have been applied to the posterior ends of the curved beam. This configuration is meant to maximise the cantilever effect on the posterior axial or tilted implants. Two stepped surfaces have been created and identified in the FEA pre-processor for load application, as shown in Figure 4.14.

4.3.6 Implant position planning for I1 and I1c

To estimate the biomechanical impact of deep cortical anchorage, the position of the implant in the FEM was carefully planned in the surgical navigation software (as shown in Figure 4.15).

The anchorage of the implant was considered as "double-cortical" of "bi-cortical" when the interfaces between the implant and the cortical bone were located both in the crestal region and at the bottom of the insert.

For the position of the implants to be clinically relevant, as discussed with dental surgeons from the University of Bologna, the sockets were planned more anteriorly with

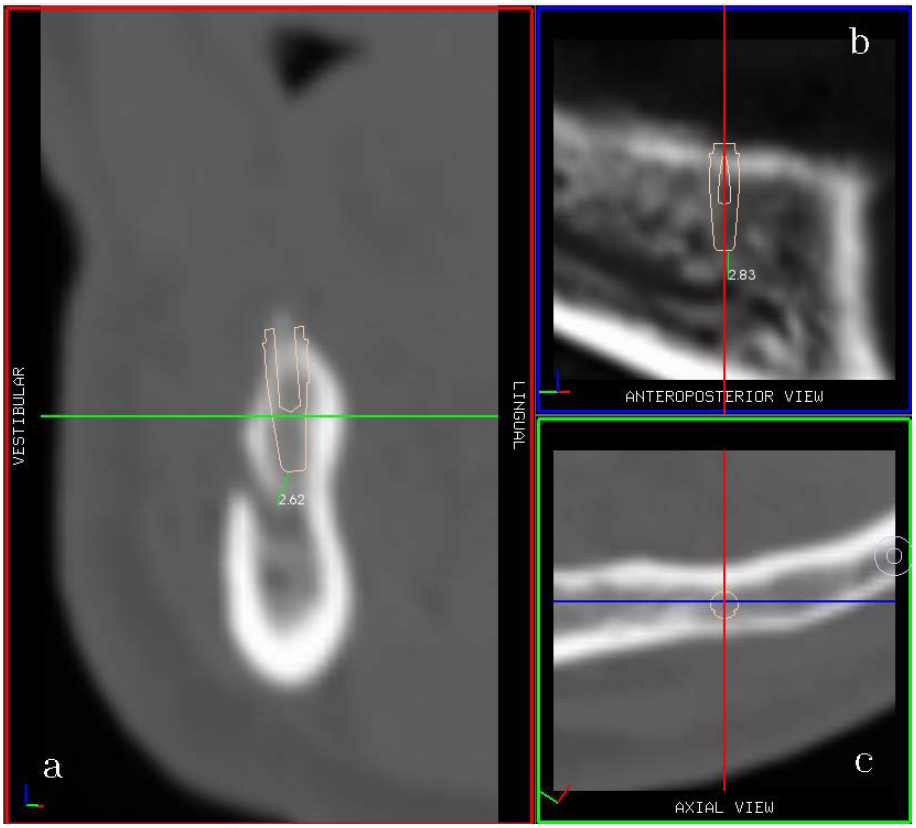

Fig. 4.13 Measurement of the distance between a posterior axial implant and the near dental nerve (mm). Due to the developed software the models used for FEA are clinically relevant and the biomechanical scenarios are more realistic. Distances can be quantified in 2D by a dedicated "meter" function and through volumetric slices along various axes: (a) vestibulo-lingual, (b) antero-posterior and (c) axial direction.

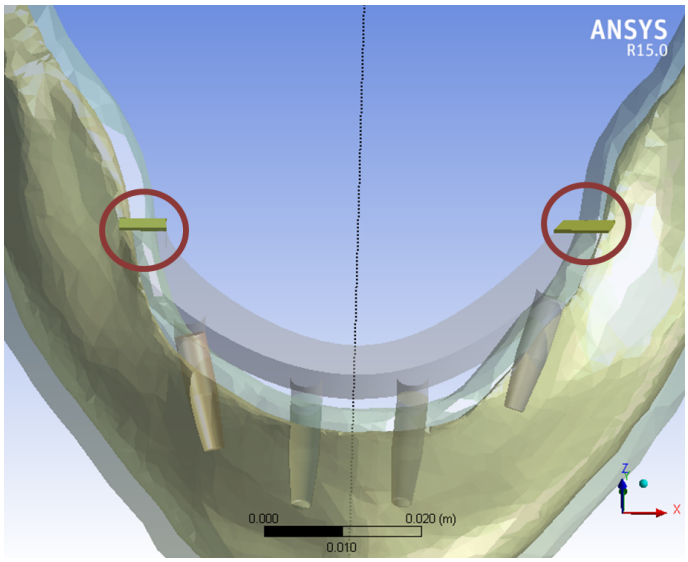

Fig. 4.14 "Steps" used for bite force application on the posterior ends of the curved beam modelling an implant-supported prosthesis.

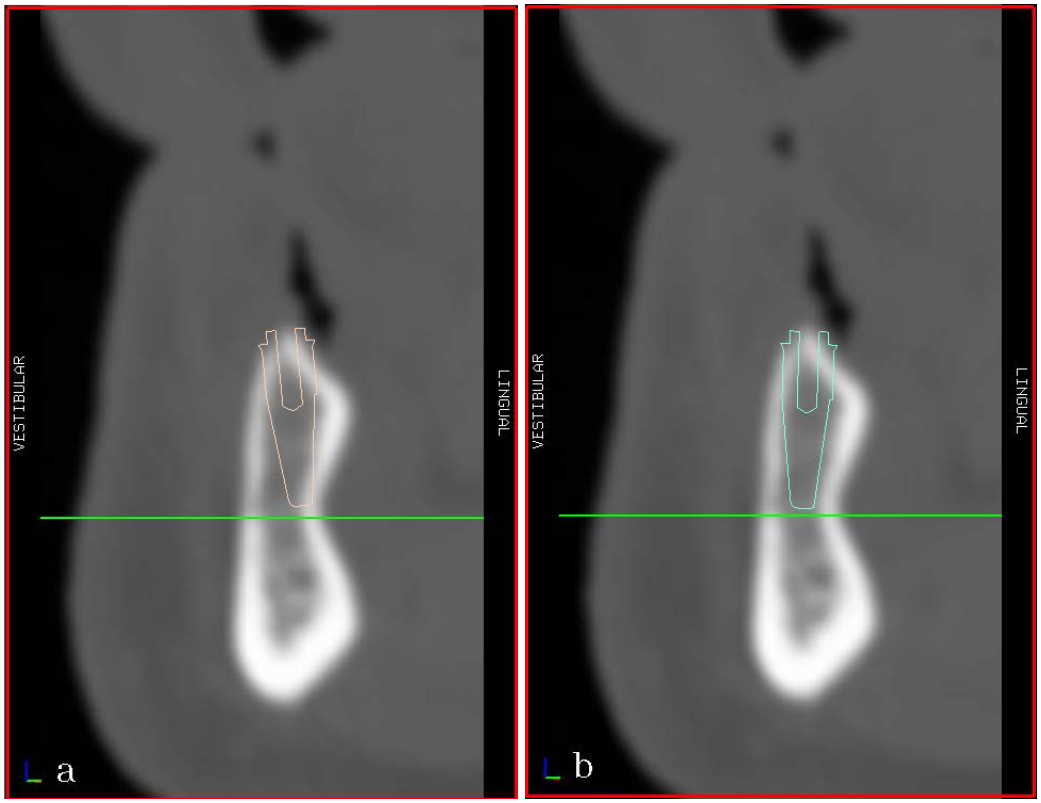

Fig. 4.15 Deep cortical anchorage (a) versus crestal-only cortical preparation (b). The planning software module is used to verify that the implant does not penetrate the lingual wall (a) and has enough cortical support at the implant neck by inspecting the surrounding bone quality via radiographic images.

respect to the mental foramen. In fact, trying to achieve double cortical anchorage in regions where the alveolar nerve is present represents a clinical hazard for the patient and therefore an unpractical procedure. If required, the possibility for the distal end of a mandibular implant to be anchored or at least landed on the cortical bone, as shown in Figure 4.15(a), requires a self-tapping implant or a deep preparation of the cortical bone.

Inserting a self-tapping implant might result in high compression sites due to the larger amount of bone debris being pushed through the threads, and consequent risk of further bone resorption.

On the other hand, "under-preparing" the cortical bone requires a firm grip of the surgical drill tip to the cortical wall with the risk of penetrating through the mandible in the lingual side.

For the reasons above it is suggested that such a delicate procedure should be performed using a navigation or image-guided surgery system to verify the preservation of the prosthetic axis.

In addition, the use of an ultrasonic socket preparation by allowing deep preparation (under-preparing) with pointy tips as shown in Figure 4.16, introduces no risk for the near soft tissues which is an excellent clinical advantage (Figure 4.16).

Fig. 4.16 Piezosurgery® inserts for ultrasonic differential preparation of the implant socket. The sharp and pointy insert IM1S supplied by Mectron S.R.L. (Carasco, Italy) allows a deep preparation without the risk of sliding along the cortical wall. As a result, both primary stability of the implant and the precision of the prosthetic axis are enhanced.

4.3.7 Load set and boundary conditions

For all the models the biting force was modelled as an external load complementary to the full muscle loads set during clenching.

In I1 and I1c the biting force was modelled as a 100N force acting on the implant head with a 35 degrees bucco-lingual inclination (Figure 4.17). This value based on previously published work is reasonable (Hylander 1975).

In I4 and I4c1-2 100N bilateral bite loads (perpendicular to the occlusal plane) were applied to the posterior ends of the curved beam ("steps" in Figure 4.14) in order to simulate a maximum cantilever action of the prosthesis over the posterior implants.

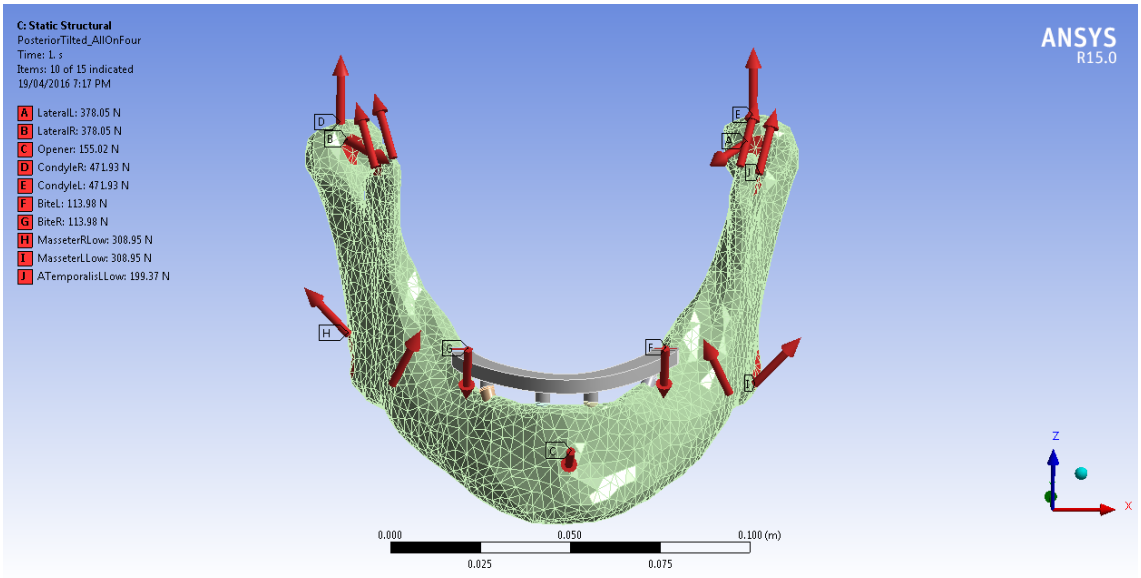

Fig. 4.17 Graphical representation of the loads used in the FEM to represent the activation of the muscles involved in the biting action with 4 implants (clenching).

Differently from most of the published models, this work recalculated the mechanical equilibrium for the system following the introduction of an external force without adding constraints.

For I1 and I4 the resultant scenarios were a bilateral bite system in equilibrium with both ipsilateral and contralateral condyle reaction.

Equilibrium equations were calculated using the complete set of muscles involved during clenching, condyle reaction forces in the articular fossa and the external bite force

acting on the prosthesis.

$$M_x = P_y\, a_z + P_z\, a_y = 0 \tag{4.1}$$

$$P_{iy} = 0 \tag{4.2}$$

$$P_{iz} = 0 \tag{4.3}$$

where:

P_{iy} = sum of projections of all forces on the antero-posterior axis

P_{iz} = sum of projection of all forces on the craniocaudal axis

a_y = projection on the y-axis of the vector identifying the force application point

a_z = projection on the z-axis of the vector identifying the force application point

M_x = momentum was calculated with respect to the intercondylar axis.

Using the assumptions for which:

- loads and muscle forces are symmetrical with respect to the A-P plane cutting the centre of the mandible ($P_{ix} = 0$)
- balancing reaction to the additional bite force is carried out by the condyles (reactive forces) only
- based on the equilibrium there is no condyle reaction force in the sagittal direction (X-axis)
- the reaction forces calculated in the anteroposterior direction under equilibrium conditions are equal amounts in magnitude for the two condyles

the system of equations 4.1-4.3 can be solved for the vertical and buccolingual components of the reaction forces acting on the condyles. The complete load set used for the four models is summarised in Table 4.1.

Table 4.1 Force vectors magnitudes expressed in Newtons for X, Y and Z directions used in the clenching model; abbreviations: **MeL**, Medial Pterygoid Left; **MeR**, Medial Pterygoid Right; **MaL**, Masseter Left; **MaR**, Masseter Right; **TeL**, Posterior Temporalis Left; **TeR**, Posterior Temporalis Right; **ATeL**, Anterior Temporalis Left; **ATeR**, Anterior Temporalis Right; **LaL**, Lateral Pterygoid Left; **LaR**, Lateral Pterygoid Right; **Op**, Opener; **BL**, Bite Left; **BR**, Bite Right; **CL**, Condyle Reaction forces Left; **CR**, Condyle Reaction forces Right.

	F_x	F_y	F_z
MeL	-41.9	-29.7	95
MeR	41.9	-29.7	95
MaL	200	-53.6	229.3
MaR	-200	-53.6	229.3
TeL	50.6	102.9	163.05
TeR	-50.6	102.9	163.05
ATeL	50.6	102.9	163.1
ATeR	-50.6	102.9	163.1
LaL	-215.5	-307.6	-43.2
LaR	215.5	-307.6	-43.2
Op	0	133.2	-79.3
BL	0	54.7	-100
BR	0	54.7	-100
CL	0	63.8	-467.6
CR	0	63.8	-467.6

Table 4.2 Material properties used for the mandibular FEA model

	Young Modulus (GPa)	Poisson Ratio
Cortical Bone	17.2	0.3
Cancellous Bone	1.29	0.3
Implant	107	0.3

4.3.8 Comparison with fully constrained model

As reviewed in the previous sections, most of the mandibular FEA models found in literature do not include the forces exerted by the muscles during mastication and jaw movement is generally constrained at the condylar region or in other anatomical locations such as the base of the mandible.

It is anticipated that in addition to patient-based CT data for modelling and a correct biomechanical set of loads representing the muscle forces (distributed to area rather than to an insertion point) during clenching, the use of reaction forces in the temporomanidbular joint adds a significant realism to the FEMs presented in this work.

Aiming to estimate the influence of this improved biomechanical scenario, the author run five additional models correspondent to I1, I1c, I4, I4c1-2 with the biomechanical simplification which sees all muscle forces suppressed and replaced with fixed supports at the muscle attachment areas.

4.3.9 Material properties and pre-processing

The criteria for choosing material properties in pre-processing the FEM were the same used and explained in Chapter 2. Both the mandible and the implants were meshed with higher order 3-D 20-node solid elements which exhibit quadratic displacement behaviour. The elements were defined by 20 nodes having three degrees of freedom per node: translations in the nodal x, y, and z directions. Soft springs were added to prevent any remaining rigid body motion.

4.3.10 Post-processing

The stresses generated in the different biomechanical configurations were evaluated for both the implants and bone interfaces. Because of the approximations used for defining the contact type between the implant and the surrounding bone, stresses recorded on the implant-cortical bone interface (where the largest micro-motions occur) might be diverging due local singularities of the mesh.

For this reason the stress values were probed along linear paths near the implant socket (see Figure 4.18). **Since for the scope of this work was aimed to identify regions of maximum stresses, radial and longitudinal probing paths were chosen only after observing the directions of maximum deformation of the implants** (where maximum stresses are most likely to occur, as shown in Figure 4.19).

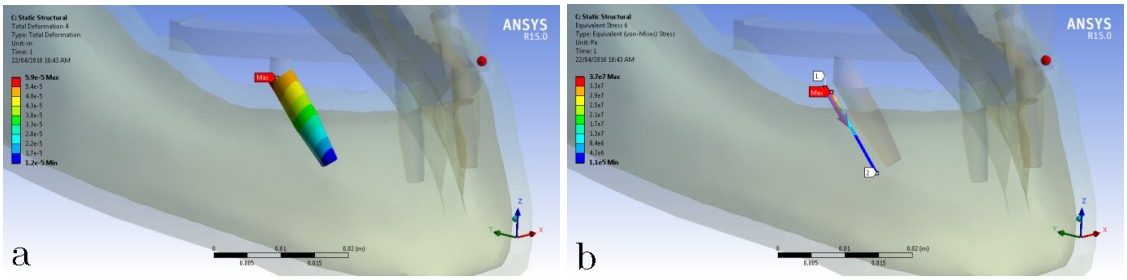

Fig. 4.18 Probing of stresses along the implant socket (b) using a probing line parallel to the implant axis at a distance of 1mm from the implant surface. The choice of the starting point of the line of nodes, where the maximum equivalent stress generated is sampled, is made according to distribution of the maximum deformation of the specific implant (a). In this case, the probing path is designed posteriorly with respect to the implant because the deformation pattern (a) shows how that the highest values are recorded on the lingual side of the posterior implant neck.

Stress distribution on the implant surface and the bone cortical and cancellous interfaces is reported in detail in Appendix A.

As a result, this study evaluated the stress distribution around the implant site along a vertical line of nodes parallel to the axis of the socket (at 1mm distance from the implant surface, as shown in Figure 4.18) and at 4-5mm radial distance from the implant head along the crestal bone, as shown in Figure 4.19). This stress reporting technique is consistent with other significant studies reported in literature (Van Staden 2006; Guan 2009).

Moreover the proposed probing method is clinically relevant since the maximum stress in the implant socket could be registered along the longitudinal axis of the inserted implant and fall out of the range of stresses stimulating osseointegration.

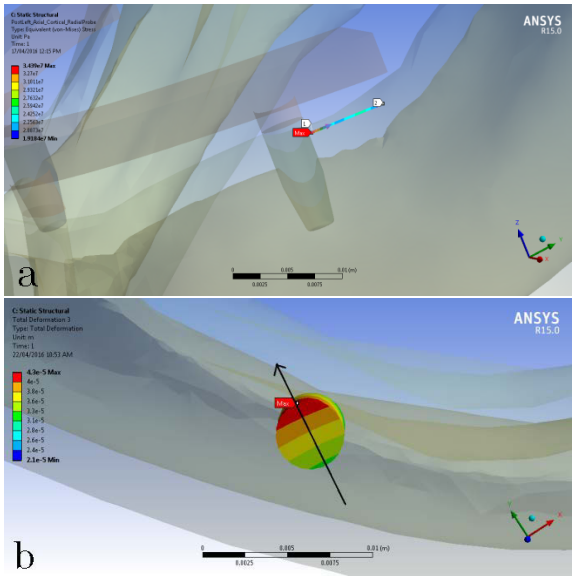

Fig. 4.19 The radial line of nodes (a) is oriented according to the deformation pattern of the specific implant observed in (b), as similarly shown in Figure 4.18

Additional results were obtained by probing maximum equivalent stresses on the implant interface with the cancellous bone (where the reduced deformation of the implant is unlikely to generate singularities in the FEM) and by measuring the total micro-motion of the coronal termination of posterior and anterior implants. Results were also compared with the maximum allowed distortions favourable for osseointegration.

4.4 Results

4.4.1 Angled insertion versus axial implants

Using the surgical planning module in the software application developed for the navigation system which will be discussed in detail in Chapter 6, angled implants were virtually placed in the posterior mandible at a minimum distance of 2.5mm from the alveolar nerve. In I4c1 the axial implants were positioned at a minimum distance of 2mm from the canine nerve (see Figure 4.13).

The clenching movement generates a deformation of the mandible with the condylar processes bending inwards and generating stresses along the mandibular ramus and upper body as shown in Figure 4.20.

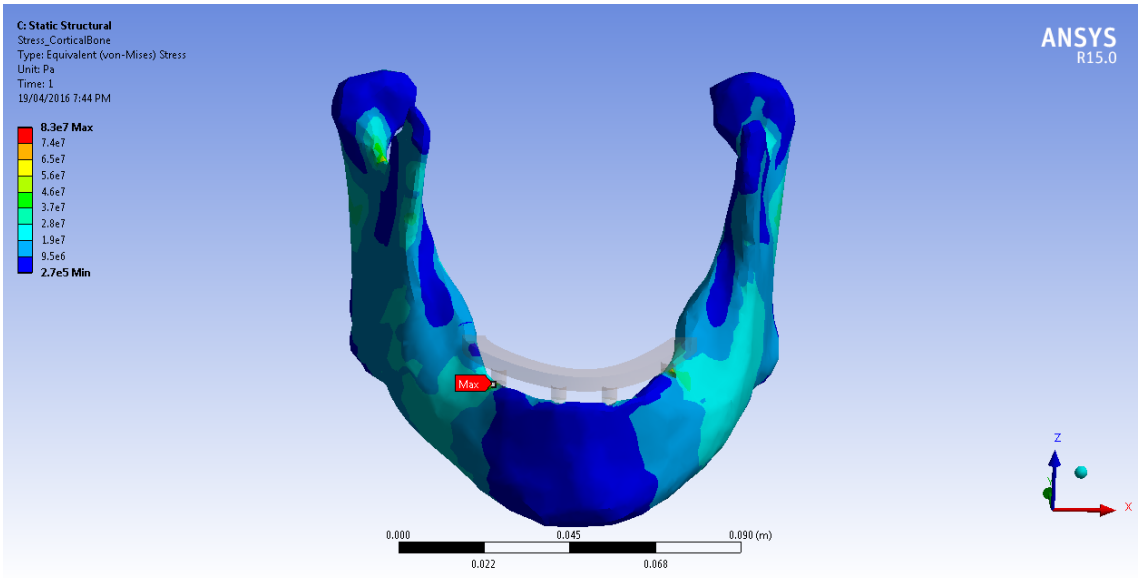

Fig. 4.20 Von Mises (equivalent) stress distribution on the mandible relative to model I4.

The maximum equivalent stresses recorded on the implant surface in I4 were 122MPa and 111MPa respectively for the posterior left and right tilted implant.

Higher maximum stress values for the posterior implants were observed for axial implants inserted above the alveolar nerve, with 151Mpa for both the left implant and the right implant. **These values are high for the trabecular and cortical bones if transferred at the interface but they are reasonable for the titanium implants.** Stress distribution on

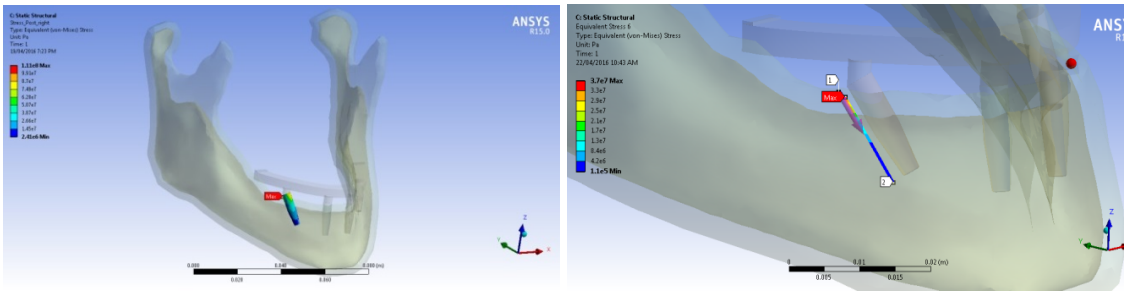

Fig. 4.21 Equivalent stress distribution relative to I4 respectively on the posterior right implant surface (left) and along the surrounding bone tissue (right).

the implant surface and the bone cortical and cancellous interfaces is reported in detail in

Table 4.3 Results for deformation and stresses on implant surface and socket region obtained for the scenario I4 using a complete clenching loads set.

	Full biomechanical scenario (clenching loads set)				
		Max Implant Stress (MPa)	Max Implant Deformation (μm)	Max Cancellous Stress (MPa)	Max Probe Stress (MPa)
I4	Post Left	122	55.8	4.4	45
	Post Right	111	58.8	3.4	37
	Ant Left	49	51.7		
	Ant Right	59	46.0		

Table 4.4 Results for deformation and stresses on implant surface and socket region obtained for the control group I4c1 using a complete clenching loads set.

	Full biomechanical scenario (clenching loads set)				
		Max Implant Stress (MPa)	Max Implant Deformation (μm)	Max Cancellous Stress (MPa)	Max Probe Stress (MPa)
I4c1	Post Left	151	45.4	9.0	26
	Post Right	151	42.7	10.4	14
	Ant Left	57	41.5		
	Ant Right	57	36.8		

Appendix A.

Results for stresses and distortion relative to the implant and bone interfaces in the scenarios I4 is reported in Table 4.3, while the results for the control group I4c1 are reported in Table 4.4.

The highest recorded stresses generated along implant socket by using tilted implants was in the range 37-45MPa compared to 14MPa and 26MPa **recorded for the interface** around axial implants in I4c1. These values are within the comfortable range of stresses for the cortical and cancellous bones.

The difference between axial and tilted implants in terms of implant deformation, which implies micro-movement of the implant with respect to the surrounding bone tissue, was recorded to be around 10 μm. In the simulation the posterior left axial implant deformed a maximum of 45 μm against the 56 μm of the tilted implant. As stated earlier the normal

tooth moves around 80 to 90 μm during the functional movements and these are very reasonable values recorded under simulation conditions.

Deformation patterns were similar for I4 and the relative control groups and maximum deformations were recorded in the coronal part of the implant generally correspondent to the posterior end of the implant head, as shown in Figure 4.22.

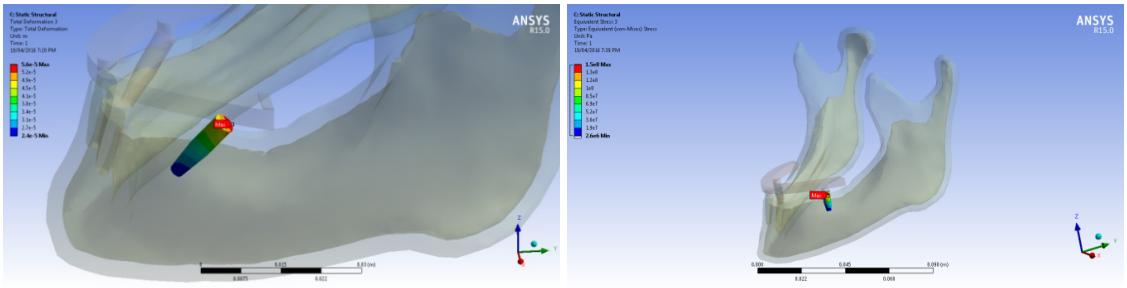

Fig. 4.22 Equivalent stress distribution on the posterior right implant surface relative to I4 (left) and I4c1 (right). Stress distribution on the implant surface and the bone cortical and cancellous interfaces is reported in detail in the Appendix A.

Results reported in Table 4.3 and 4.4 show a significant difference between axial and angled implants (100% or more) registered for the maximum stress generated on the cancellous bone at the implant interface (also see Figure 4.23).

While 4.4MPa and 3.4MPa were recorded for respectively the posterior left and right angled implants, the axial correspondent implants (model I4c1) generated maximum stresses of 9MPa and 10.4MPa on the trabecular bone interface. The same behaviour for

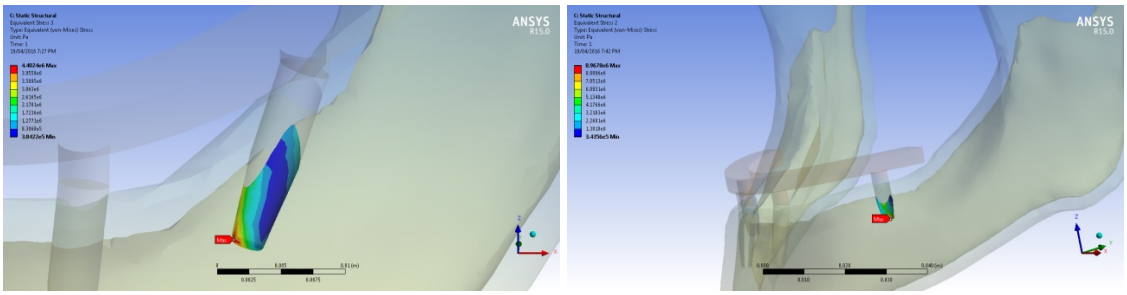

Fig. 4.23 Comparison between equivalent stress distributions and maximum values obtained for a left posterior angled implant, relative to model I4 (left) and axial implant (right) relative to the first control group I4c1.

the implant-soft bone interface was obtained with the constrained version of models I4 and

Table 4.5 Results for deformation and stresses on implant surface and socket region obtained for the scenario I4 using a simplified biomechanical configuration.

	Simplified biomechanical scenario (constraints on muscles)				
		Max Implant Stress (MPa)	Max Implant Deformation (μm)	Max Cancellous Stress (MPa)	Max Probe Stress (MPa)
I4	Post Left	84	16.4	1.1	19
	Post Right	131	19.3	1.6	11
	Ant Left	23	10		
	Ant Right	54	11.9		

Table 4.6 Results for deformation and stresses on implant surface and socket region obtained for the control group I4c1 using a simplified biomechanical configuration.

	Simplified biomechanical scenario (constraints on muscles)				
		Max Implant Stress (MPa)	Max Implant Deformation (μm)	Max Cancellous Stress (MPa)	Max Probe Stress (MPa)
I4c1	Post Left	84	14.1	2.6	10
	Post Right	122	14.8	5.5	29
	Ant Left	17	8.8		
	Ant Right	41	10.2		

its control groups. Results of the FEA run on those simplified biomechanical models are reported in Table 4.5 and Table 4.6. The maximum generated stresses were 1.1MPa and 1.6MPa for angled implants against 2.6MPa and 5.5MPa for axial implants, showing an increase of the stress levels up to 344%.

Maximum stresses in the constrained model were similar between tilted and axial implants. A maximum value of 84MPa resulted for both the axial and tilted posterior left implants while the maximum stress on the posterior right axial implant was 9MPa lower than the 131MPa value recorded for the posterior right angled implant.

Overall, the constrained models reported lower implant deformations and stresses in the implant-bone interfaces than the models with active muscles, as reported in Table 4.4. These results could also be compared with maximum values of strength for cortical and cancellous bone found in literature and reported in Table 4.7.

Table 4.7 Fracture toughness, compression strength and elastic modulus maximum values found in literature for trabecular and cortical bone.

	Trabecular bone	**Cortical bone**
Fracture toughness (MPa/$m^{0.5}$)		2.5-6 $^{(GibsonandAshby1997)}$
Compression strength (MPa)	0.03-46.5 $^{(Goldstein1987)}$	133-193 $^{(GibsonandAshby1997)}$
Elastic Modulus (GPa)	10.4 ± 3.5 $^{(Rhoetal.1993)}$	18.6 ± 3.5 $^{(Rhoetal.1993)}$
	<1 $^{(Goldstein1987)}$	

Table 4.8 Results for deformation and stresses on implant surface and socket region obtained for the second control group I4c2 using a complete clenching loads set.

Full biomechanical scenario (clenching loads set)					
		Max Implant Stress (MPa)	Max Implant Deformation (μm)	Max Cancellous Stress (MPa)	Max Probe Stress (MPa)
I4c2	Post Left	184	43.7	5.8	21
	Post Right	229	44.6	5.2	34

Deformations on the angled implants for the constrained model were higher than on the axial implants although the differences were only in the range 2.3-4.5 μm. Without mastication forces, the maximum stress registered in the cortical bone-implant interface was in the range 11-19MPa for the tilted implants and 10-29MPa for the axial implants.

As expected, for all of the All-on-Four® models, maximum equivalent stresses and micro-movements relative to the anterior implants were lower than the ones registered for the posterior implants (Table 4.4).

The use of longer axial implants (15mm) in the second control group I4c2 positioned more anteriorly with respect to the alveolar nerve generated the highest stresses on the implants (184MPa and 229MPa) and micro-movements in the same range of the more posterior axial implants (43.7 microns and 44.6 microns). As per the maximum stresses at the bone-implant interface, they were in the range 21-34MPa for the cortical tissue and around 5.5MPa for the cancellous bone. These results are summarised in Table 4.8. By constraining the model with long axial implants at the muscle attachment areas both

Table 4.9 Results for deformation and stresses on implant surface and socket region obtained for the second control group I4c2 using a simplified biomechanical scenario.

Simplified biomechanical scenario (constraints on muscles)					
		Max Implant Stress (MPa)	Max Implant Deformation (μm)	Max Cancellous Stress (MPa)	Max Probe Stress (MPa)
I4c2	Post Left	147	16.0	3.3	14
	Post Right	130	16.4	2.6	18

Table 4.10 Results for deformation and stresses on implant surface and socket region obtained for the model I1 using a complete clenching loads set.

Full biomechanical scenario (clenching loads set)					
		Max Implant Stress (MPa)	Max Implant Deformation (μm)	Max Cancellous Stress (MPa)	Max Probe Stress (MPa)
I1	Left	67	46	4.0	18
	Right	43	40	2.9	16

stresses and micro-movements, as reported in Table 4.9, were reduced with respect to the clenching model although they showed the same patterns observed for I4 and I4c1.

4.4.2 Deep cortical anchorage versus larger implants

In model I1 the use of 4mm diameter implants anchored to both the crestal bone and deep to the cortical wall (see Figure 4.26) reported maximum equivalent stresses on the **implant surface** between 43MPa and 67MPa and maximum crestal movements of 40 and 46 μm, as summarised in Table 4.10. Both resultant micro-movements and implant stresses were comparable with the ones recorded for the control group I1c with the use of larger (5mm diameter) implants with only crestal cortical anchorage, respectively 48-67 MPa and 41-44 μm (see Table 4.11).

As shown in Table 4.12 and Table 4.13, excluding the masticatory forces in the simulation resulted in lower stresses on the implant interface (15MPa for the larger implants and 19-27MPa for the deep cortical ones), smaller micro-movement of the implant heads (around 5 μm) and lower stresses in the implant socket (between 2.6MPa and 4.4MPa).

Further figures and plots relative to the FEMs results are reported in Appendix A.

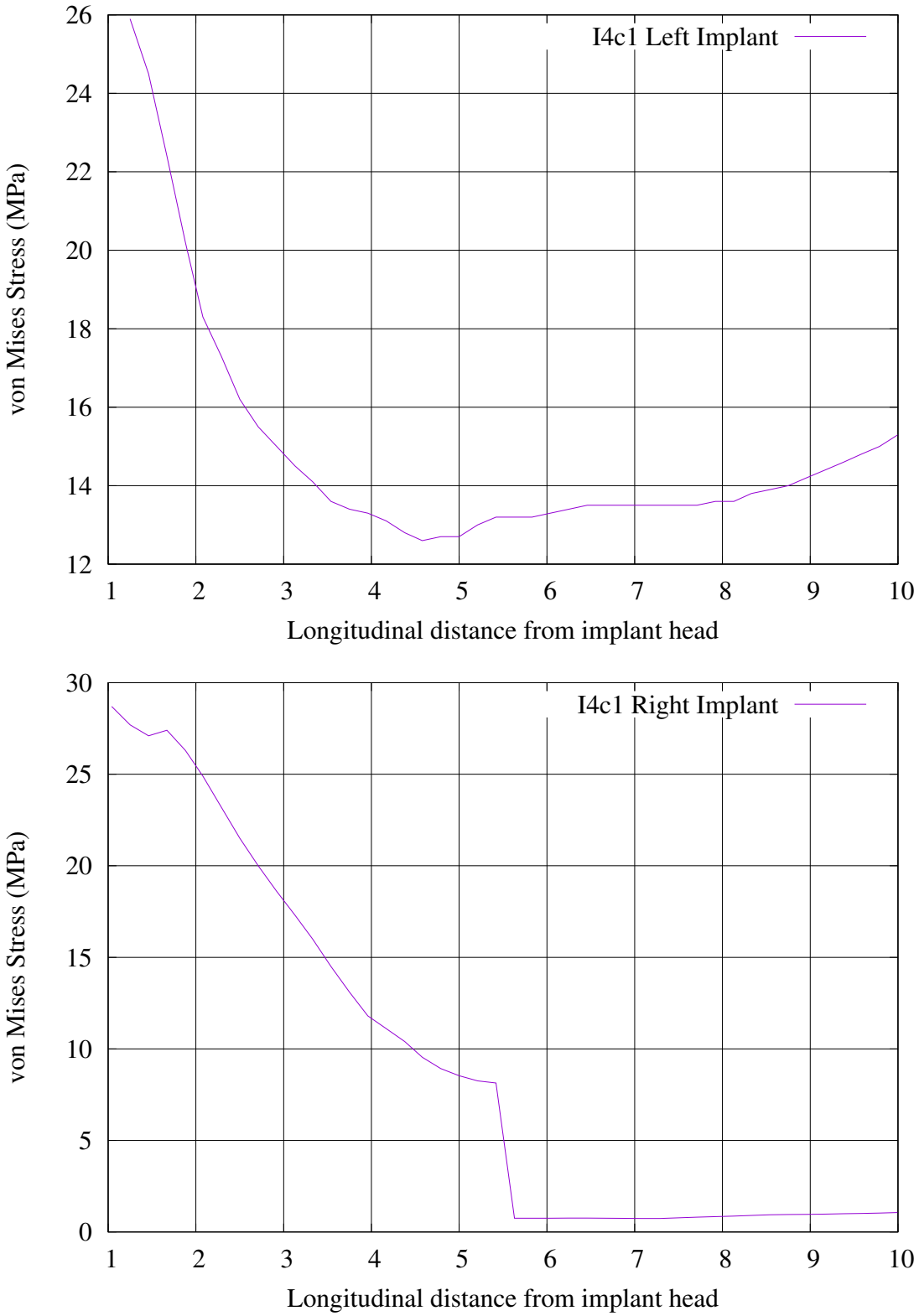

Fig. 4.24 Equivalent stress curves obtained for the left and right posterior implants by probing longitudinally the results for model I4c1 at 1mm distance from the implant socket. Units are MPa for the vertical axis and millimetres for the horizontal axis. The discontinuity in the stress curve is due to transition between cortical and cancellous bone which are modelled using different elastic moduli.

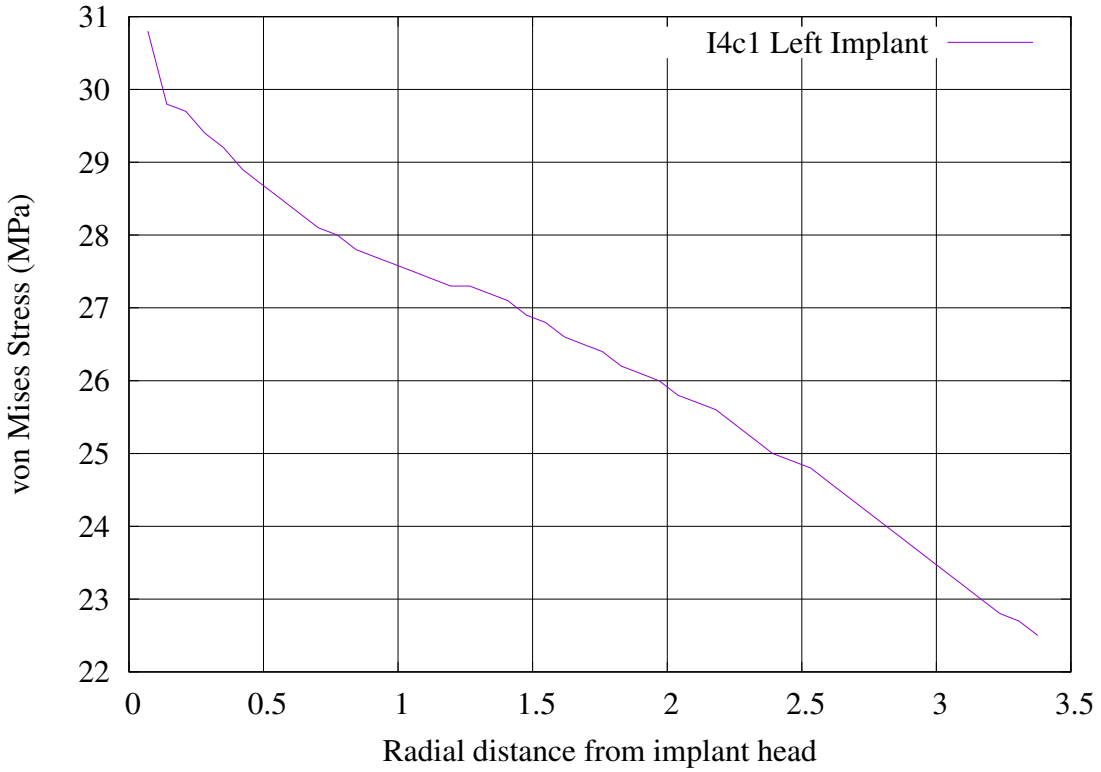

Fig. 4.25 Equivalent stress curves obtained for the left posterior implant by probing radially the results for model I4c1 relative to the cortical bone surface.

Table 4.11 Results for deformation and stresses on implant surface and socket region obtained for the control group I1c using a complete clenching loads set.

Full biomechanical scenario (clenching loads set)					
		Max Implant Stress (MPa)	Max Implant Deformation (μm)	Max Cancellous Stress (MPa)	Max Probe Stress (MPa)
I1c	Left	51	41	6.1	13
	Right	48	44	5.3	9

Table 4.12 Results for deformation and stresses on implant surface and socket region obtained for the model I1 using a simplified biomechanical configuration.

Simplified biomechanical scenario (constraints on muscles)					
		Max Implant Stress (MPa)	Max Implant Deformation (μm)	Max Cancellous Stress (MPa)	Max Probe Stress (MPa)
I1	Left	19	4.9	0.3	2.6
	Right	27	6.1	0.5	4.4

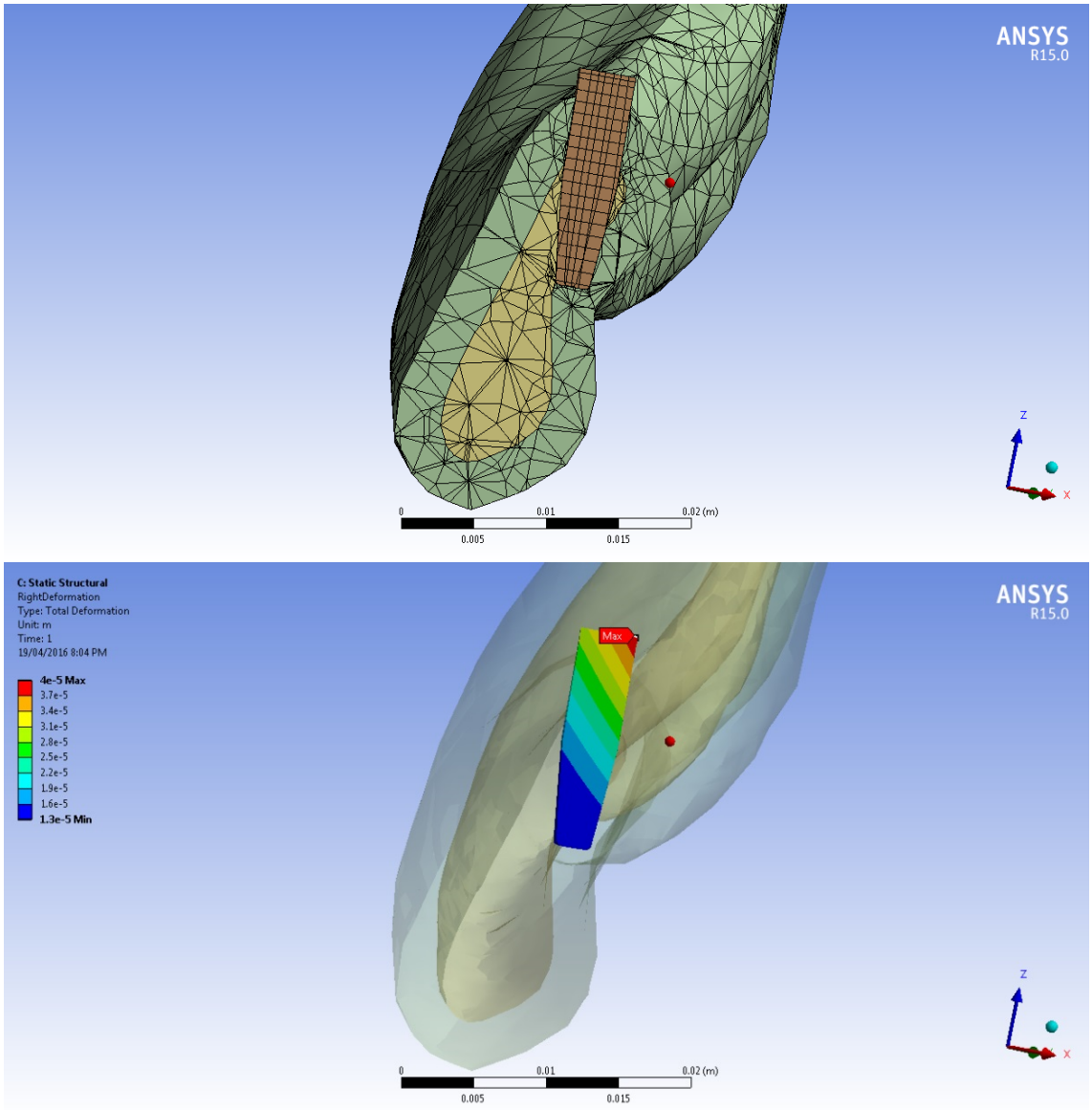

Fig. 4.26 Section showing the deep cortical anchorage used in model I1 (top) and equivalent stress distribution during clenching (bottom). Additional Figures providing information on the stresses at the bone interface are reported in Appendix A.

Table 4.13 Results for deformation and stresses on implant surface and socket region obtained for the control group I1c using a simplified biomechanical configuration.

Simplified biomechanical scenario (constraints on muscles)					
		Max Implant Stress (MPa)	Max Implant Deformation (μm)	Max Cancellous Stress (MPa)	Max Probe Stress (MPa)
I1c	Left	15	5.2	1.1	3.0
	Right	15	5.9	1.0	3.7

They show the results for stresses at the implant surface (Figures 3, 4, 6, 8, 10, 22, 25, 26) , cortical and trabecular bone interfaces (Figures 5, 9, 24, 27, 27), probing paths near the implants (Figures 1, 2, 11-21) and implant distortions (Figures 7, 23) in all the studied configurations.

4.5 Discussion

4.5.1 All-on-Four® and osseointegration

According to the results obtained for the All-on-Four® models during clenching, the cantilever action generated by the biting forces produces higher stresses on posterior axial implants then on angled implants (angles in patient-specific cases were >30°) as well as on their respective interfaces with the surrounding cancellous bone.

This behaviour is already present in the I4 model against the control group I4c1 in which the cantilever action is minimized by pushing the implant insertion points as posteriorly as the tilted implants' head. The use of tilted implants (according to the resulting patient-specific angles) results in lower generated stresses than axial implants during biting when all the other mastication forces are taken into account, which is in the most realistic scenario.

However conflicting results have been published in the literature, like Hussein and Rabie (2015) and Bonnet (2009) who found antagonistic results. Their thesis is that the use of posterior angled implants generates higher stresses on the implant and the surrounding bone tissues. These results are not surprising knowing that specified angles will generate biaxial forces that will introduce different stress levels at different insertion angles. The work in this thesis specifically found that if an angle or tilting is utilised lower stresses are observed **within the implant**.

As per the stresses generated on the implant socket, the higher values in the case with tilted implants are most likely due to the craniocaudal load transfer from the bite force. The implant-cortical tissue interface has a larger area in the case of a tilted implant because of its orientation, therefore more load is transferred to it.

For all the FEMs, the stresses registered along the implant socket were lower than the thresholds for cortical bone yielding found by Burstein (1976) and referred in various simulations by von Staden (2006). The max recorded values were also compatible with the range 21-50MPa reported by Bujtar (2010) and Choi (2005) for different values of thickness of the cortical bone.

In case of axial implants, the load is transferred vertically (distally) to deeper regions. This explains the higher maximum stress values found for the implant-cancellous bone interfaces as opposed to the tilted implants case.

The theory of the load discharge to the trabecular bone is reinforced by the findings relative to the use of long axial implants in I4c2. Longer implants have a larger portion of their surface in contact with the cancellous bone, which results in a lower pressure if the load remains constant. Since the stress on the implant-cancellous bone interface is lower for long implants, it is reasonable to conclude that the vertical component of the load is similar for both posterior axial and more anterior longer implants (respectively the two control groups). Instead, the horizontal component of the load is larger in the case with less posterior implants due to the more significant cantilever action resulting from the reduced AP spread.

In fact, stresses for both implant (184-229MPa) and implant socket (21-34MPa) in I4c2 are higher than the ones generated by the use of more posterior axial implants.
The micro-motions resulting from the FEMs show how they should not prevent a successful outcome of the All-on-Four® insertion procedure, which according to Pilliar et al. (1986) should not exceed 100 μm during the healing phase. As per the two anterior implants, the smaller micro-movements and stresses recorded show how, in an investigation of the potential osseointegration of an All-on-Four® prosthesis, the analysis of the deformation of the posterior implants should be sufficient to justify osseointegration.

4.5.2 Deep cortical implant planning

In a clinically valid biomechanical scenario the results obtained using the finite element method showed how the use of smaller diameter implants with, where possible, deep anchorage to the cortical bone, generates lower stresses on the implant itself and the trabecular bone with respect to larger diameter implants inserted axially (perpendicularly to the occlusal plane).

The under-preparation associated to the insertion of a deep cortical implant should be performed using image-guided surgery, given the importance of the angle of insertion and the control over the depth of penetration in the lingual wall.

The use of ultrasonic preparation can reduce the risk of damaging the patient's soft tissues promoting double cortical anchorage even when close to the nerve.
These results are in contrast with studies found in literature which state that it is necessary to use larger implants to achieve a better primary stability and therefore osseointegration (Guan 2009, Qian 2009, Okumura 2009).

On the contrary to this, by applying fixed constraints at muscle attachment locations, I1 and I1c do not produce significantly different results for stresses on the implants and at the cortical interfaces along the socket.
For this reason, the author believes that it is the whole clenching movement, rather than the biting force alone acting on the inserts, to have the highest impact on osseointegration of dental implants.

Smaller implants, which have been strategically positioned in a virtual planning environment based on a three-dimensional tomographic scan, have better chance to bond to the bone tissue due to the reduced micro-movements during the healing period. In addition, the preparation of smaller sockets reduces the heat generated by the cutting instruments, and hence resulting in a more favourable bone healing and superior secondary stability.

4.6 Conclusions

The finite element models prepared in this study are clinically relevant.

The findings in this chapter have been directed to studies on the All-on-Four® surgical technique and osseointegration factors.
In addition a number of variables were taken into account in evaluating stresses and distortions for clinical feasibility in terms of final implant position under specific biomechanical configurations.

As a result, the models are not perfectly symmetrical since they are based on a tomographic scan of the patient-specific mandible. Both the implant insertion and the angle of tilt might be different for left and right mandible, since the insertions have been planned according to the adjacent anatomy, in particular the alveolar nerve, the mental foramen and the lingual wall.

The combination of ultrasonic (piezoelectric) implant site preparation, intra-surgical navigation and simulation via finite element analysis has validated a combination of surgical procedures consisting in:

- Using angled implants even in posterior areas
- Using small diameter implants even where the superficial layer of cortical bone is thin (posterior mandibular bone)
- Under-preparing the cortical bone without using self-tapping implants trying to promote double cortical anchorage.

With the aid of image-guided surgery, angled and smaller diameter implants can be safely inserted into posterior areas of the mandibles and they have more chances to fully osseointegrate due to:

- the limited micro-movement of the implant on the bone crest

- lower stresses in the trabecular bone whose irregular inner structure is in itself subject to random localised failure (associated to the reduced cantilever action validated through FEM)
- the reduced diameter needed for primary stability
- the minimally invasive insertion technique with less generated heat (because of the reduced diameter first and also by the optional use of ultrasonic preparation)

Through the anatomically correct patient matched modelling and biomechanical completeness of the proposed model, together with the critical choice of the approximations used in the FEM, the realistic features and the clinical viability of the scenarios used, this thesis give a workable clinically applicable process for simulating the behaviour of implantable prostheses on the human mandible.

Further improvements to the presented FEMs might be achieved by refining the engineering design of the implants. The use of finer FE mesh to model the bone-implant interfaces more accurately will allow better understanding of the osseointegration and hence further design modifications.

Adaptive meshing techniques, like "ALE" (Arbitrary Lagrangian-Eulerian) by Abaqus software (Abaqus, Inc., Dessault Systemes, France), could be used to take into account the deformation of the cortical bone during the implant insertion and the preservation of a more complex bone-implant interface.

Moreover, the implant insertion itself could be dynamically simulated using Explicit Dynamics with focus on the improvement that piezoelectric surgery introduces by removing more bone debris from the osteotomy site.

Finally, the procedure explained in Chapter 2, for which subject-specific bone mineral densities obtained from the CT scan data are used to map material properties, could be applied to the dynamic insertion model.

Chapter 5

A critical review of currently used Image Guided and Computer-Assisted Surgery systems: current research, state-of-the-art models, techniques used for image-to-world registration and analysis of invasiveness

5.1 Introduction

Due to the complexity of the underlying anatomy and biomechanics, oral and maxillo-facial surgery often requires a highly skilled surgeon for the operations to be accurately performed.

Designed to assist the practitioner with achieving the most successful result, a series of surgical planning techniques based on three-dimensional imaging can now improve the surgical outcomes. The surgical difficulties arise in the assessment of the intraoperative position, misidentification of skeletal contours around the mandibular anatomy and the

skull base (Bell 2010) or isolation of the alveolar nerve and the blood vessels distributed in the maxillary sinus. In addition, implant surgery needs to take into account the quality of the bone in the surgical site.

Recent developments in 3D analysis via Computed Tomography (CT) which can be used in patient specific modelling and surgical simulation methods have managed to provide additional accuracy in diagnosis and planning.

Several studies report how such computer-assisted surgery systems (CAS) enhance the precision of implant positioning when compared with traditional approaches (Hoffmann et al. 2005, Kramer et al. 2005).

This Chapter covers image guided and computer-assisted surgery systems in oral implantology, current research, state-of-the-art models, techniques used for image-to-world registration and analysis of invasiveness.

5.2 Computer-assisted surgery and the use of drill guides

In a commonly used procedure, after obtaining a CT scan of the patient which allows patient specific modelling by three-dimensional rendering and virtual surgery planning, the surgeon can pre-visualise one or more implants in their final desired position, check their distance from the cortical walls or surrounding nerves and plan a prosthetic restoration.

The 3D virtualization of an implant insertion can also be used to generate, via software, the design of physical guides (templates) for the drilling procedure. Such templates are either bone or teeth supported and require matching the patient's oral anatomy. Because of the shape complexity they are generally manufactured via 3D printing technology.

The template is deployed during the surgery when the practitioner anchors it to the patient's bone. The stabilized template is featured with cylindrical sockets whose axes are aligned with the ones of the implants in their planned positions.

As a result, the template guides the location, angle and depth of the osteotomy or implant insertion (Eggers 2009).

For a better understanding of drill guide system, the author will discuss the steps involved using three of the most popular solutions used worldwide: NobelGuide® (Nobel-

Biocare, Kloten, Switzerland), SurgiGuide® (Materialise, Leuven, Belgium) and Sirona Connect (Sirona, Long Island City, NY, USA).

In the NobelGuide® system, the initial step involves taking a dental impression of the patient and digitising it utilising proprietary laser scanning hardware (NobelProcera 2G).

A tomographic scan is taken of the diagnostic tooth setup, also including the soft tissue surrounding the teeth. After importing the tomographic data, the surgery is planned in the proprietary software *NobelClinician*™ and from this dental drill guides are created depending on the intended patient treatment (the guides can either be guided pilot drilling or fully guided implant insertion) (Figures 5.1, 5.2 and 5.3).

Fig. 5.1 Digitisation of a prosthetic component using NobelProcera laser scanner (*source*: https://www.nobelbiocare.com).

For fully edentulous cases, the clinician takes an impression of the patient and creates a master cast sent to a dental laboratory to shape prostheses. The tooth setup is then utilised to create a radiographic guide which is scanned in the ideal position on the patient following a double-scan protocol. The correct alignment of the scanned guide in two different scans is aided by radiopaque markers highly visible in the tomographic images (Figures 5.4 and 5.5).

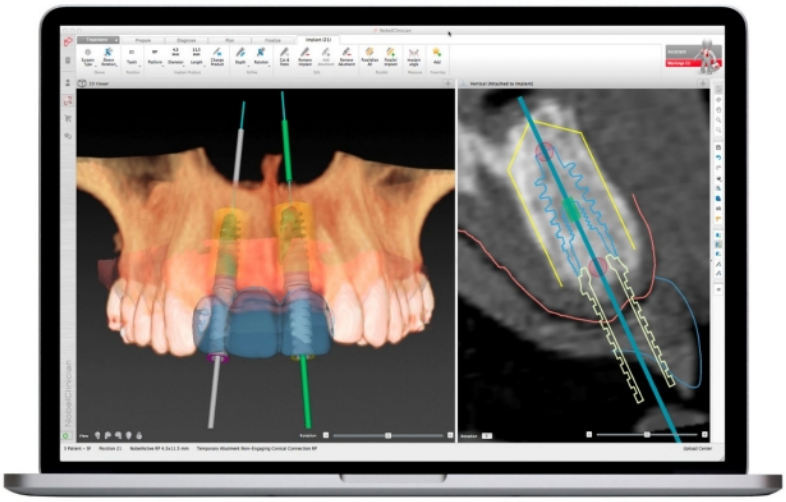

Fig. 5.2 CBCT data viewing and surgery planning using NobelClinician™(*source*: https://www.nobelbiocare.com).

Fig. 5.3 Examples of dental drill guides for partially edentulous patients (*source*: https://www.nobelbiocare.com).

Having the provisional prosthesis superimposed to the actual patient's anatomy, the template serves as a reference for the virtual implant insertion. This planning is then utilised to design and manufacture a template which embeds metallic sleeves for guiding the surgical drill. Once manufactured the surgical template is fixed on the patient matching the bone tissues' profile and stabilized using anchor screws or pins.

As shown in the Figures 5.6-5.9 drill guide systems produced by Materialise can be

Fig. 5.4 Radiopaque markers in the radiographic template used for identifying the prosthetic outcome

Fig. 5.5 Surgical guide for edentulous cases (*source*: https://www.nobelbiocare.com/au/en/home/products-and-solutions/treatment-concepts/guided-surgery.html).

designed and manufactured to be bone-supported, mucosa-supported or teeth-supported according to the specific patient case. In most cases the template is manufactured via additive 3D manufacturing technology, but there are cases in which it is produced through traditional manufacturing mills, like for example in the Sirona Connect system procedure.

The Sirona Connect workflow uses CEREC AC with Bluecam or Omnicam optical

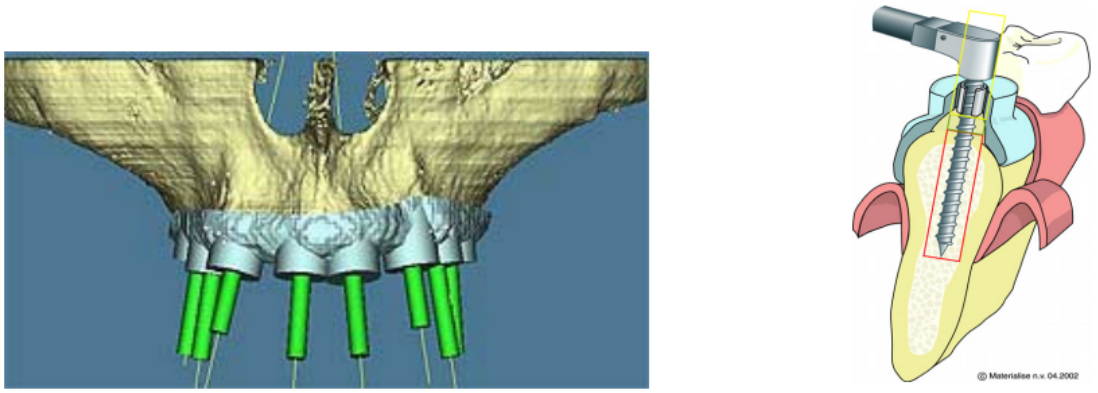

Fig. 5.6 Materialise edentulous surgical guide design in bone-supported case (*source*: http://oo.simplant.com/Dental).

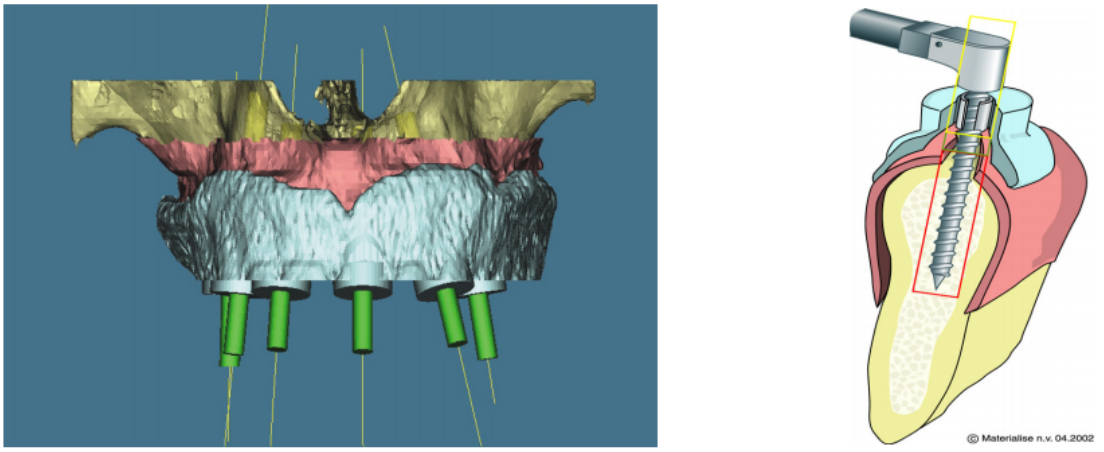

Fig. 5.7 Materialise edentulous surgical guide design in mucosa-supported case (*source*: http://oo.simplant.com/Dental).

scanners to create a 3D impression of the patient's case. A 3D image is taken via X-Rays through the Sirona DVT device (Figures 5.10-5.12). The implant is then planned within GALILEOS Implant Software which is coupled with Sirona DVT. This data is utilised to create a template on the Sirona inLab milling device generating the final dental drill guide for almost any case, including edentulous and teeth supported cases.

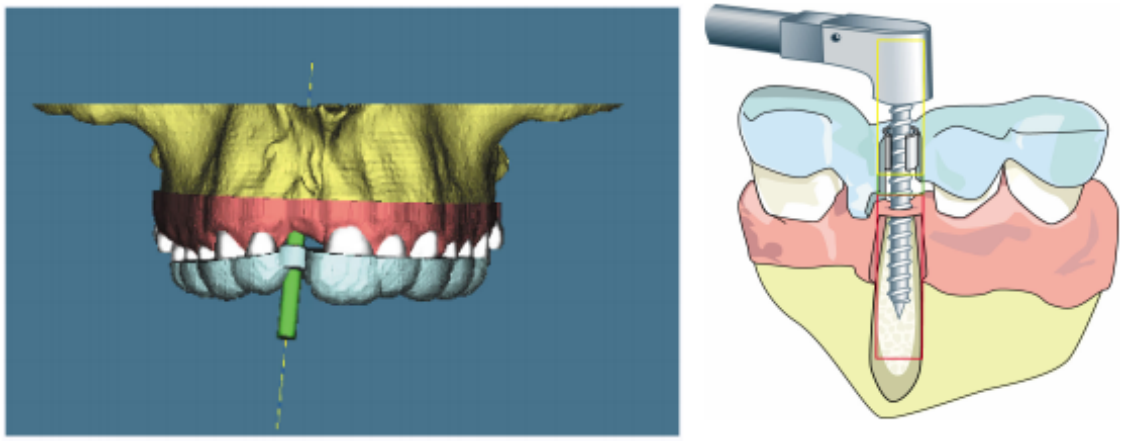

Fig. 5.8 Materialise teeth-supported surgical guide design (*source*: http://dental-depot.com/materialise/pdf/Cookbook.pdf)

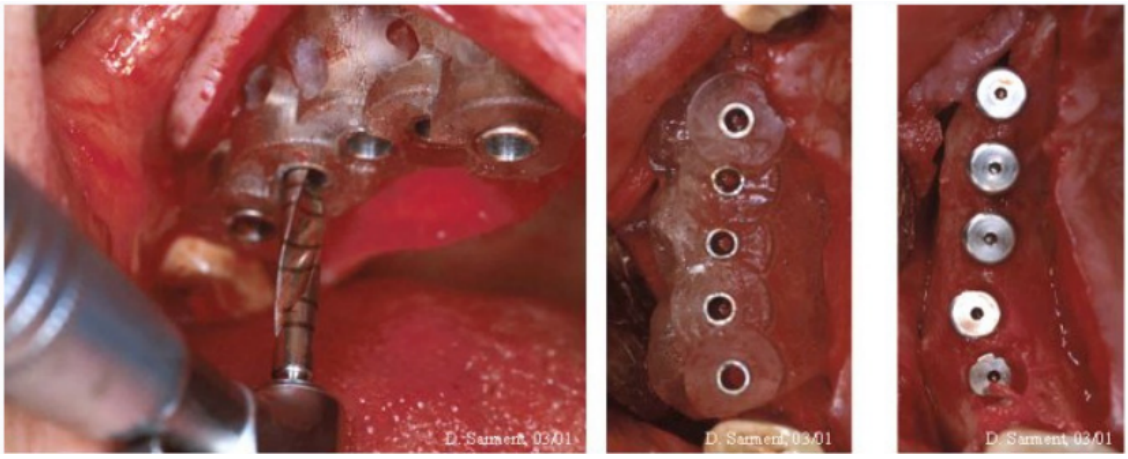

Fig. 5.9 Materialise surgical drill guide application (*source*: http://osseotech.com/materialises-safe-surigical-guide-system/).

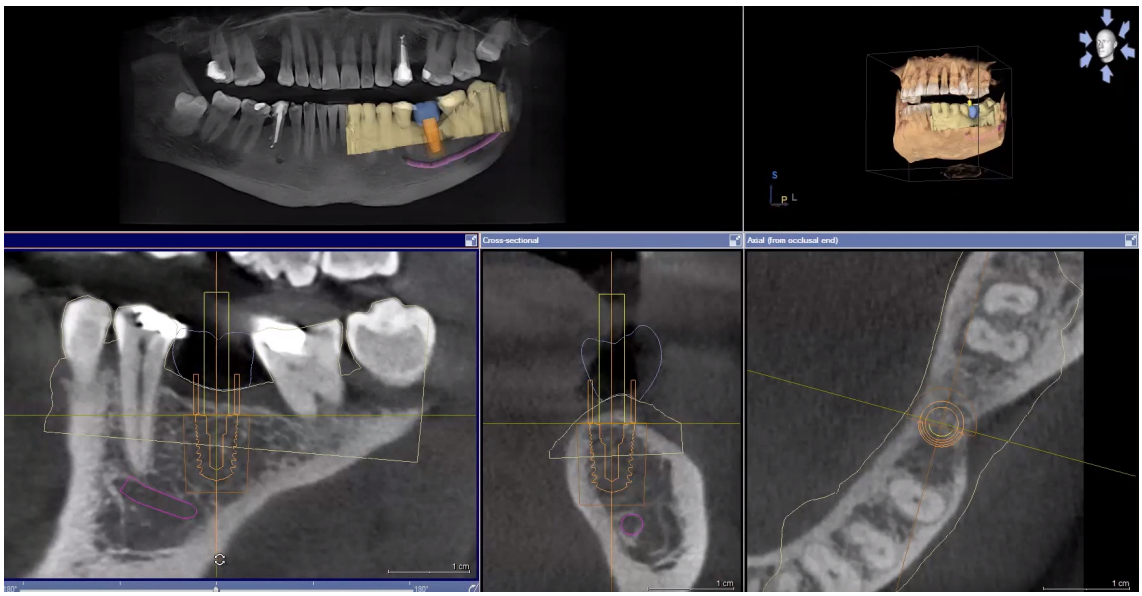

Fig. 5.10 Sirona virtual surgery planning (*source*: www.sirona.com).

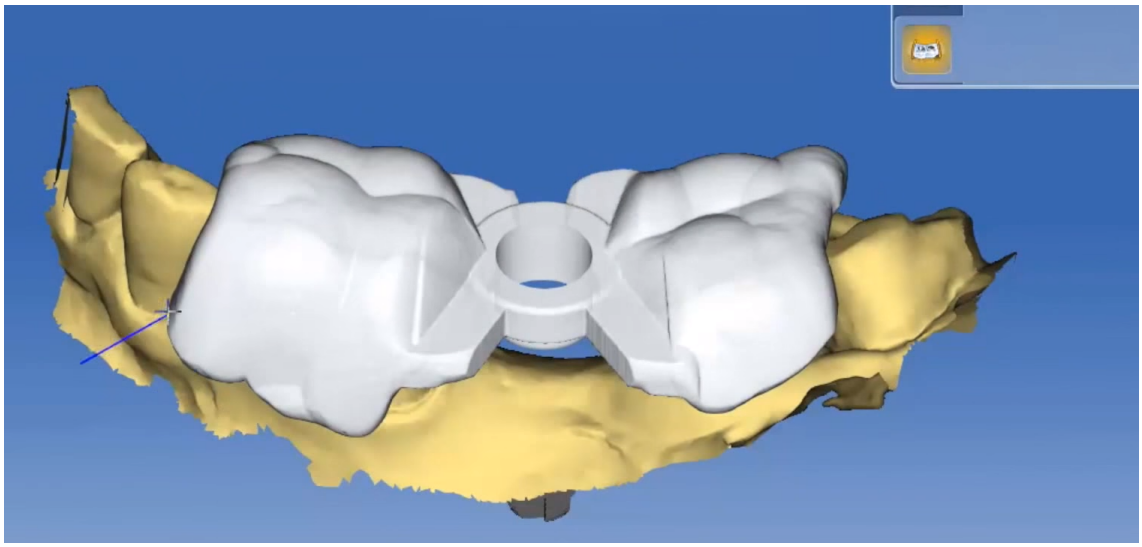

Fig. 5.11 Sirona surgical guide design (*source*: www.sirona.com).

Fig. 5.12 Sirona surgical guide placement during surgery (*source*: http://www.sirona.com/ecomaXL/files/5 Sirona PR CEREC Guide 2.pdf).

5.3 Problems associated with the use of drill guides

5.3.1 Limited access and visibility

Although offering additional guidance, the use of a surgical drill guide in oral and maxillo-facial surgery might result in **poor bone visibility and limited intra-oral access due to the reduced inter-occlusal gap**.

For example the insertion of angulated implants in the All-On-Four® treatment concept by NobelBiocare requires access to posterior areas in angled positions (Figure 5.13). In addition the presence of the surgical template offsets the drill insertion point vertically generating the need for a drill extender. In such a contest the surgeon's ability to assess the quality of the bone by determining the resistance offered by the tissues might be significantly impaired.

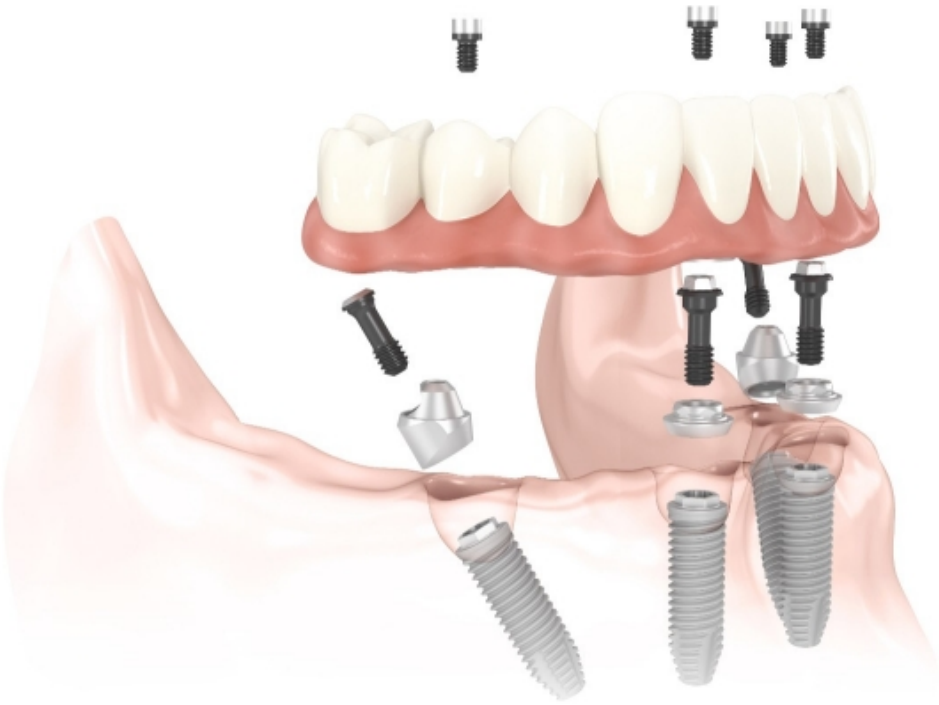

Fig. 5.13 All-on-4® treatment concept for full mandibular arch restoration (*source*: https://www.nobelbiocare.com/us/en/home/products-and-solutions/treatment-concepts/all-on-4.html).

Drill-guides are mostly used for complex cases where it is hard to find spatial reference from surrounding anatomical points i.e. full arch reconstructions in edentulous patients. In

these patients the template limits the possibility to visually inspect the quality of the bone during the drilling procedure and adds an offset in the posterior regions of the mandible already difficult to access for socketing using contra-angle handpieces (see Figure 5.13).

In a study by Schneider (2015) it was stated that the use of drill guide can lead to inaccuracy due to the manufacturing process of the cylindrical sockets. He reports how there is the possibility of a consistent lateral shift of about 0.75 mm of the drilling action when a sleave is inserted into the 3D-printed the template.

5.3.2 Invasiveness

The deployment of drill guides in an edentulous scenario might result too invasive since it requires anchorage to the patient's bone through (three) temporary fixation screws (Arisan 2010).

Temporary fixations can become even more invasive in cases of severe atrophic edentulous maxilla, where the lack of stability of the drill guide compromises the accuracy of the image-to-world registration. On the other hand, if the guide is misplaced because not fixed properly, and since the surgical template utilised interferes with the cutting blades or flutes during socketing, there is no substantial procedure to verify its correct position at the beginning and throughout the duration of the surgical procedure.

5.3.3 Delay

In any case this type of computed aided surgery introduces a delay between the surgical planning and the operation due to the time needed to design and manufacture the template.

Once the surgeon has completed the virtual planning, the patient's file is sent to the software provider who manufactures a surgical guide according to the plan and the desired prosthetic restoration. The manufacturing and shipping progress can generally last between one and four weeks.

Table 5.1 Comparison of the accuracies in mm for different systems for IGS and CAS found by Somogyi-Ganss (2015) in terms of **lateral** entry and apical point errors.

	Straumann	**Simplant®**	**NobelGuide®**	**Navident**
Mean entry point	0.9+/-0.48	0.7+/-0.54	0.81+/-0.55	1.14+/-0.55
Max entry point	4.66	2.92	4.31	3.64
Mean apical point	1.71+/-0.86	1.46+/-0.76	1.91+/-0.94	1.71+/-0.61
Max apical point	5.05	4.99	6.23	3.92
Axis error	3.31+/-1.86	3.09+/-1.9	4.24+/-2.66	2.99+/-1.68
Max axis	12.52	14.58	17.05	11.94

5.3.4 Accuracy

In a significant study made by Somogyi-Ganss (2015), the accuracy of three widely used drill guides systems has been evaluated in vitro against a navigation system designed by Claron Tecnology (Toronto, Canada, re-branded in 2015 as ClaroNav) on a set of 400 matched measurements for implant insertions performed by a total of five clinicians. The tested drill guide systems are Simplant® by Materialise Dental (Leuven, Belgium), Straumann® Guided Surgery (Institut Straumann AG, Basel, Switzerland) and NobelClinician™. The results of this study, which are summarised in Table 5.1, show how the maximum deviation from the planned fixtures is between 1.49 mm and 1.91 mm and it is recorded at the apical point as opposed to the entry point.

It is obvious that these results confirm how a source of error is the correct fit of the guide onto the patient's anatomy. A template fit is generally dependent on the morphology of the bone surface and the quality of the CT data set used for the reconstruction of the bone surface in the planning software (Ruppin, 2008). If the template is not properly fit onto the patient's anatomy a minor error at the entry point can be amplified during the osteotomy at the apex level (Somogyi 2015). For this reason it has been reported that a possible misplacement (or movement of the splint) during the surgical treatment can compromise the overall accuracy (Di Giacomo et al. 2005).

Like Somogyi-Ganss's (2015), a different study undertaken in 2008 by Ruppin found that the accuracy achieved by Materialise Simplant® system (Materialise Dental, Leuven,

Table 5.2 Comparison of the accuracies in mm for different systems for IGS and CAS found by Ruppin (2008).

	Simplant Surgiguide®	**RoboDent® LapDoc Accedo®**	**Alma Virtual Patient®**
Lateral deviation	1.5+/-0.8	1+/-0.5	1.2+/-0.6
Depth deviation	0.6+/-0.4	0.6+/-0.3	0.8+/-0.7
Axis Angular deviation	7.9+/-5.0	8.1+/-4.6	8.1+/-4.9

Belgium) is comparable with two live tracking systems: Artma Virtual Patient (Baumgartner & Rath, Munich, Germany) and RoboDent® LapDoc Accedo (RoboDent GmbH, Berlin, Germany).

In 2008 Ruppin reported the results obtained using the two tracking system against the dental drill guide system in terms of the lateral deviation on the entry point and the deviation on the insertion depth of the implant and the angular discrepancy on the implant axis (Ruppin, 2008). The study carried out by Somogyi-Ganss can be considered less accurate because the procedure adopted for the segmentation of the post-operative implant surfaces was standardised, and a correction for the external hexagon on the implant introduced inaccuracies. In addition, in their work the CT data sets of the preoperative and postoperative anatomy were matched using fiducial markers, however in comparison Ruppin used 20 cadaver mandibles.

The results of this comparison are reported in Table 5.2.

5.4 Image-guided surgery as alternative to CAS drill guides

A clinical application of intraoperative navigation seems to overcome the limitations introduced by the use of surgical drill guides.

Image-Guided Surgery (IGS) is used in a variety of medical procedures, for example by orthopaedic, oral-maxillofacial, brain, sinus and spinal surgeons to help clarify complex anatomy encountered during surgical interventions or procedures. In sinus surgery, for example, IGS is used to identify complex anatomy in procedures such as revision sinus

surgery, distorted sinus surgery, extensive sino-nasal polyposis, surgery relating to disease that abuts the skull base, optic nerve or carotid artery, and more.

By generating three-dimensional volumetric representations or images of the maxillo-facial area, IGS allows surgeons to evaluate a patient's anatomy before surgery and can assist with planning the placement of implants in their ideal preferred positions. However, although the use of IGS is a state-of-the-art approach, this technique is presently used at the discretion of the operating surgeon and is not investigational. This is mainly because the accuracy resulting from transferring images to surgical reality has been, and continues to be, one of the most challenging problems of both IGS and Computer Assisted Surgery (Pellegrino 2014).

IGS could have a crucial application in oral implantology where poor implant positioning increases the risk of failure due to mechanical overload of the surrounding bone tissues.

Despite some advanced IGS and CAS approaches being used, still there is a continuing need for the improvement of computer-implemented methods, systems and/or devices for image based (or assisted) surgical planning and/or navigation.

The technology is based on the spatial registration of the intraoperative position of the surgical cutting/socketing instrument with the patient's anatomy previously reconstructed from CT or Magnetic Resonance Imaging (MRI). Different systems might utilize different technology for tracking: infrared, optical or electromagnetic methods. However all systems require the characterisation of the surgical instrument in use and an image-to-world alignment between the physical patient and the virtual model (Dang 2012).

Some current navigation systems for oral implantology perform this registration using physical radiopaque markers which are screwed into the patient's maxilla or lower jaw (Chen 2001; Kang 2014; Kim 2015).

Some others use anatomical landmarks as fiducial points for alignment, while a few of them deploy a planar fiducial markers holder supported by the patient's denture (Casap 2004 and 2008, Taraschi 2010). All of the navigation systems for oral implantology

reviewed seem to use registration tools which are either quite invasive or/and reduce visibility and bone inspection capability.

To show how different IGS systems use more or less invasive reference markers and registration techniques, as well as various surgical applications, a few of the most popular systems for surgical navigation are critically reviewed in the next sections.

5.4.1 Stryker: II-Cart (3D C-ARM Registration vs Pair Point)

Stryker Germany (Freiburg, Germany) uses an image guided surgery system called II-Cart. The images obtained through the CT scan and reconstructed as a volume via dedicated software are spatially registered with the patient with the aid of Titanium screws used as radiopaque reference.

The screws are inserted into the patient's skull (in paranasal or mandible location) for cranial surgery, and then displayed through a fluoroscopic C-arm intensifier (Figure 5.14). The C-Arm method utilises an automatic inbuilt registration procedure which actuates markers on a flat panel detector. However, if a C-Arm intensifier is not utilised, the implanted Titanium screws are actuated to perform the registration procedure (Nagasue 2009). In both cases, a reference frame must be attached to the cranium via three screws resulting in a very invasive procedure.

The accuracy of the Navigation System II-Cart has been estimated to be 1.26 +/- 0.12 mm, using the C-arm based registration, and 1.53 +/- 0.51 mm using the Titanium screws as fiducial markers. In both cases the accuracy has been measured in vitro, through the use of a pointy probe and comparing the difference between virtual coordinates from the 3D geometry data set and real-world coordinates (Nagasue 2009).

5.4.2 Medtronic: O-ARM and Stealth TREON

The last surgical navigation system released by Medtronic (Minneapolis, MN, USA) is StealthStation S7 which uses an electromagnetic head-mounted frame. This communicates with the trackers embedded in the surgical instrument in order to determine the location of its tip in three dimensions. However, the majority of the studies published give details

Fig. 5.14 (Left) Stryker II-Cart navigation system assembly; (right) C-Arm-based registration procedure during ENT Surgery Otolaryngology (*source*: http://www.stryker.com).

regarding the StealthStation TREON unit. When the O-ARM is used, the TREON system identifies the markers in the CT data and requests the user to locate them on the real patient. Temporary mini-screws placed in the anterior and posterior mandibular alveolar crest might be used as fiducial markers.

When compared with other commercially available systems, the TREON system offers a greater access to the body as well as less radiation exposure.

In 2007 Wittwer published a study to evaluate the discrepancy in the final implant position via a comparison between the post-operative CT scans and the virtual plan. The study evaluated the precision of the StealthStation image-guided surgery system reporting an average deviation of 1.0 mm (Wittwer, 2007).

Different evaluations were carried on four fresh cadaveric heads in a study by Strong in 2008. In this study 15 fiducial markers were used (1.5mmX18mm Titanium screws) positioned across the skull at anatomically relevant locations. The setup is shown in Figure 5.15. By measuring the average deviation between the three-dimensional coordinates of the

reference points, the accuracy of the system was estimated to be around 0.9 mm (Strong, 2008).

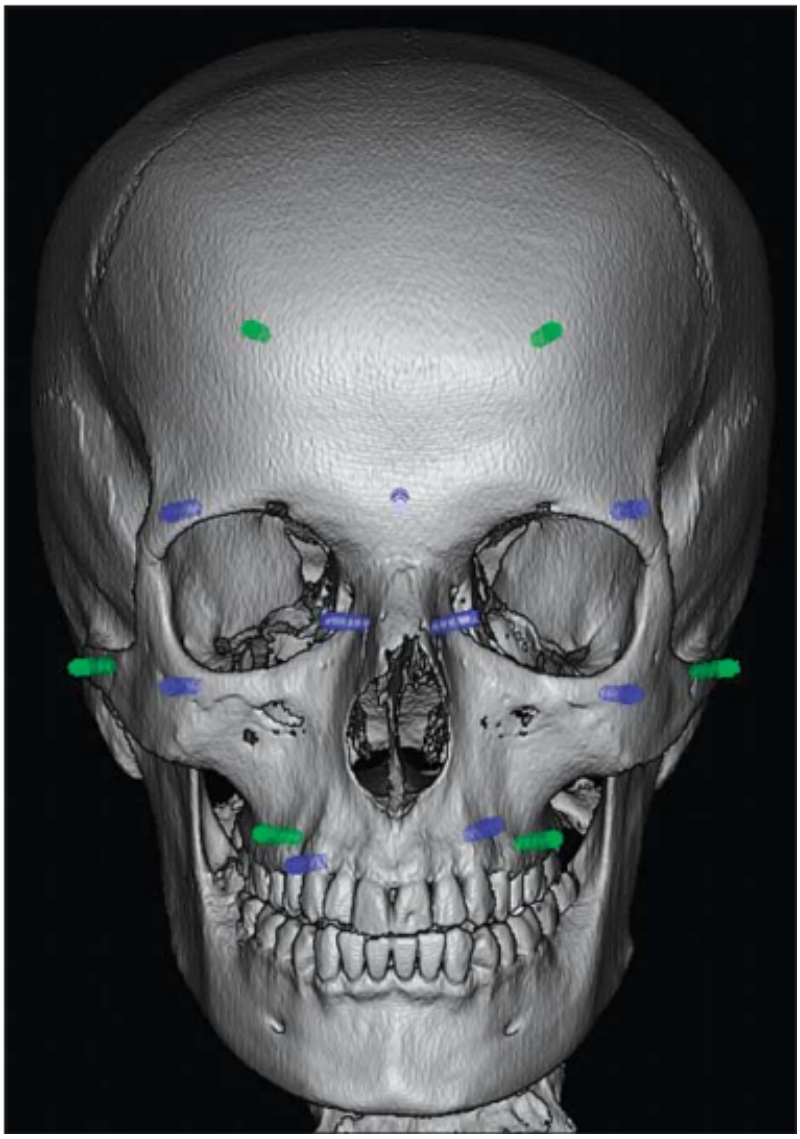

Fig. 5.15 Strong's experimental setup: the green screws are used as registration markers, whereas the blue markers are meant to establish the average point deviation of the probe (from Strong 2008).

5.4.3 Claron: Navident®

ClaroNav developed a system for image guided surgery, Navident®, including a proprietary stereoscopic camera called MicronTracker.

The Navident system uses an automatic registration method prompt by a pin extruded from a thermoplastic teeth-supported jig called JawTag while no evidence of solutions for edentulous cases has been published yet.

The Navident system is reported to have an angular axis accuracy of 2.99° +/- 1.68° compared to 3.09° +/- 1.9° of a dental drill guide as reported by Navident's sponsored study by Somogyi-Ganss in 2015. A spatial deviation of 1.71 +/- 0.61 mm against 1.46 +/- 0.76 mm when using a dental drill guide is also reported in the results.

5.4.4 BBraun: OrthoPilot

BBraun (Melsungen, Germany) has two different versions of its navigation system called OrthoPilot. One version is utilised for superficial skin-based landmarks registration, the other for registration via bone landmarks. It is deployed for total knee arthroplasty and high tibial osteotomy for either bone or soft tissue navigation.

The OrthoPilot system fixes optical navigation markers into the tibia and femur tracked through the use of the stereoscopic camera NDI Polaris Spectra (Northern Digital, Waterloo, Canada). Active markers are used to increase localisation accuracy. In one version, the user is required to touch landmarks that are fixed to the skin at the hip, knee and ankle. This is aimed to digitise each joint and identify its centre of rotation.

Alternatively, a series of landmarks can be touched in order to digitize the joint of interest. Being the registration carried out through acquiring the position of physical markers by touch, for this navigation system no tomographic scans are required resulting in less radiation exposure for the patient (Schmidt 2007, Seo 2012).

5.4.5 Blue Belt Technologies: Navio PFS

Blue Belt's (Plymouth, MN, USA) Navio PFS navigation system does not use CT or MRI scans to reconstruct a three-dimensional model of the patient but anatomical landmarks and surface mapping. Studies show that it takes approximately 5 minutes to create a model of the knee via touching anatomical points which will be exposed as part of the surgical procedure via a dedicated probe.

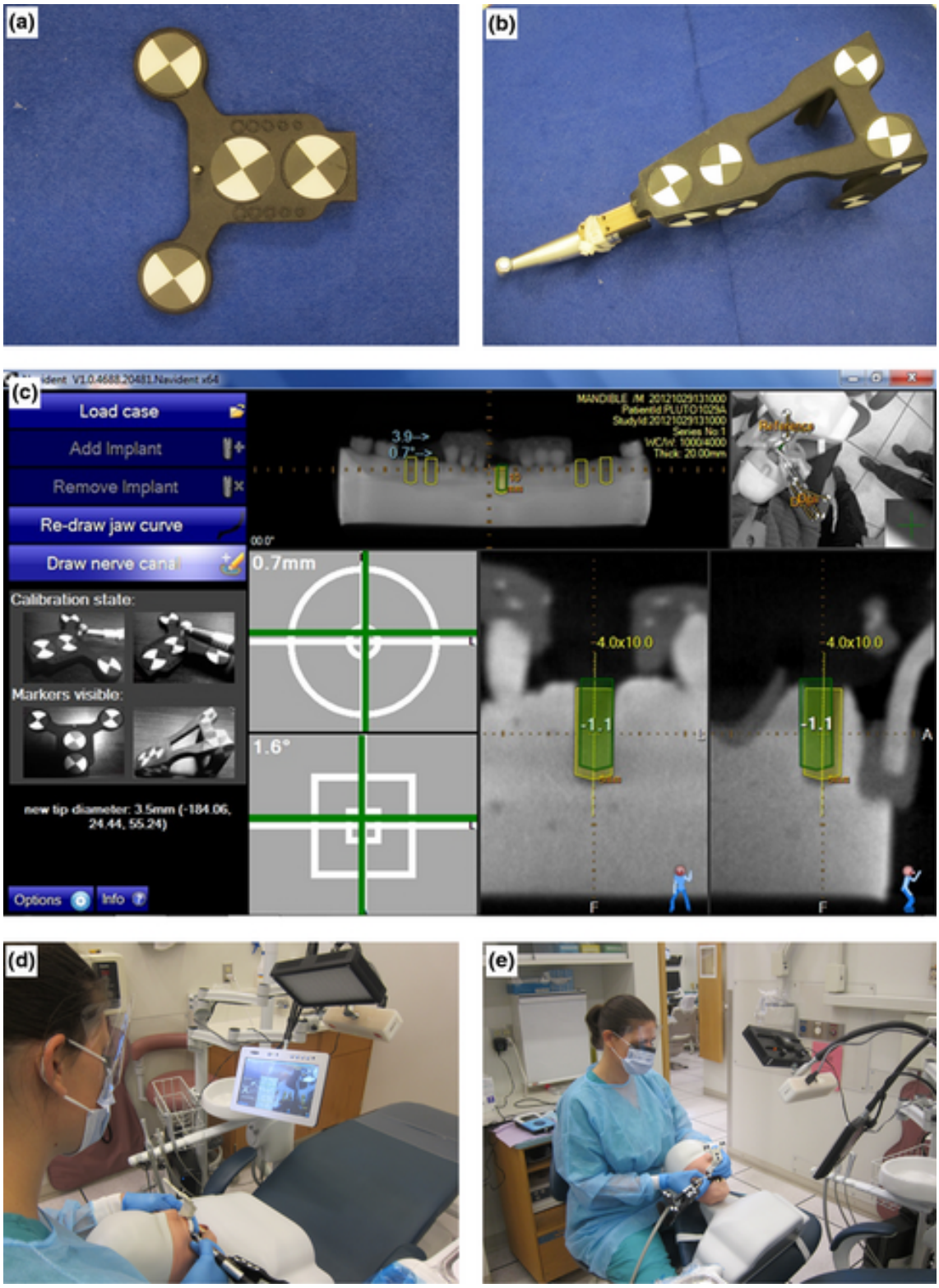

Fig. 5.16 ClaroNav's reference tools (a,b); (c) Navident's software interface during surgical navigation; (d,e) Navident system while being used on mannequin (*source*: www.claronav.com).

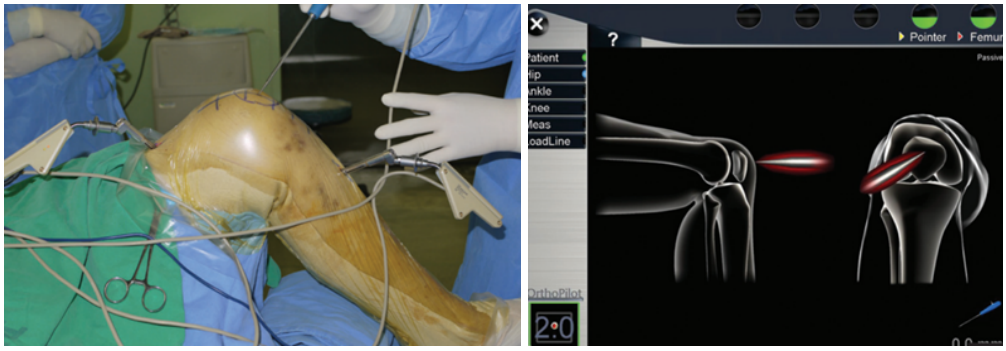

Fig. 5.17 Digitization of patient's knee (left) and relative OrthoPilot's software interface (right) (*source*: http://www.orthopilot.com/).

According to Lonner (2015) the system has errors ranging from 0.88 mm to 2.27 mm and between 1.04° and 1.88° implant insertion angular error measured for femur resection. Accuracy registered for tibia resection is instead between 0.95 mm and 2.43 mm.

Fig. 5.18 Blue Belt's Navio PFS probe (http://bluebelttech.com/).

5.4.6 BrainLab: Vector Vision

In 2001 Siessegger published a study about the insertion of dental implants guided by BrainLAB (Feldkirchen, Germany) technology Vector Vision II. This infrared optical tracking system is integrated with planning software which uses three orthogonal volumetric slices aligned with the CT scan volume.

The alignment between the patient and the virtual surgery environment is performed using a head-mounted gig which needs to remain in the same position during the timeframe between the CT scan and the surgery (Siessegger, 2001). The use of this locating frame itself leads to potential inaccuracies due to potential shifting of the registration headgear. This system is optimised only for maxillary implantology.

In a dedicated study, Sun (2013) attempted to evaluate three different methods for registering the patient's anatomy with the Vector Vision system: software registration by BrainLAB's Z-Touch laser scanner, an anatomical point based registration using the Soft Touch pointer, and one based on an attached gig. The third method uses a tooth supported fiducial marker template registration plate where fiducial markers are pointed by the Soft Touch device.

Sun reports that by using the Z-Touch laser scanner the success rate of the registration procedure is 39% against the 95% of the anatomical landmarks-based registration and the 100% of the fiducial tray-based one (Sun, 2013).

The Z-Touch Laser scanner was also utilised in another clinical pilot study by Li (2015), who estimates the accuracy of the BrainLAB system to be 0.8 mm. In this investigational setup, Li used a splint fabricated from acrylic resin to fix the position of the mandible with respect to the maxilla. Also Lubbers et al. (2010) tested the accuracy of different registration methods utilising the BrainLAB VectorVision system. This time the use of Titanium screws mounted on the provisional maxillary prosthesis produced submillimeter accuracy, performing significantly better than the 2 mm error obtained by using the laser scan Z-Touch. In the last years BrainLAB refined its navigation technology with modules specialised in total joint replacement, orthognathic surgery and maxillofacial reconstruction (Vector Vision II system).

In a 2014 study, Novelli showed the combination of pre-surgical planning performed with iPlan 3.0 CMF software with Vector Vision II (BrainLab, Feldkirchen, Germany) for surgical navigation and surgical stereolithographic models (Novell 2014).

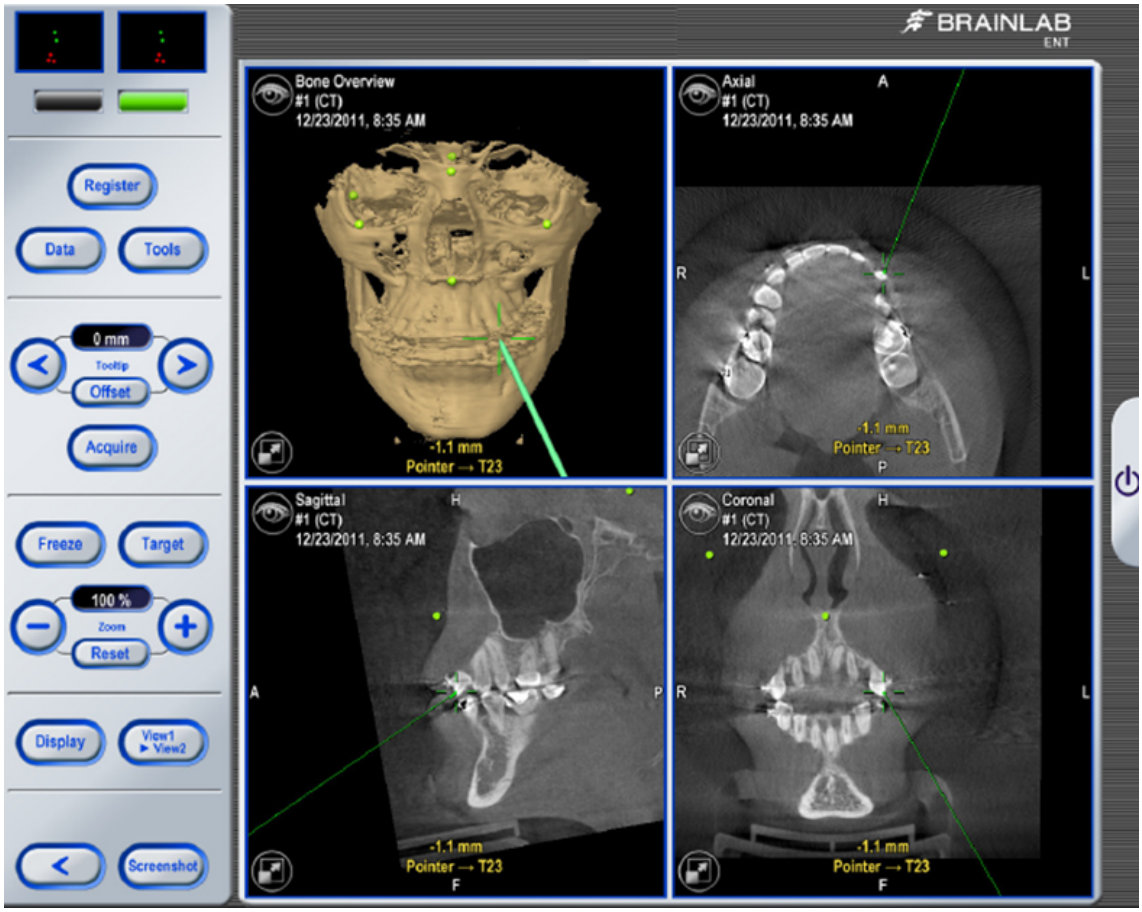

Fig. 5.19 Snapshot of Brainlab's software application showing the virtualisation of a probe in a three-dimesional view (top left), axial view (top right), sagittal view (bottom left) and coronal view (bottom right). The device is used to touch the tip of teeth in the anatomic landmark-based registration (*source*: https://www.brainlab.com/en/surgery-products/overview-spinal-trauma-products/image-registration/).

Fig. 5.20 Model showing splint used for registration (from Li 2015).

Fig. 5.21 Titanium screws used as fiducial markers mounted on the patient's maxillary prosthesis (https://www.brainlab.com).

In order to register the patient with the virtual setup the surgeon must refer to at least four radiopaque markers which are mounted on a mouth splint and via self-drilling screws fixed in the superior orbital frame.

Fig. 5.22 Occlusal splint with five hexagonal-headed screws (Vector Vision II system) (*source*: https://www.brainlab.com).

5.4.7 x-Nav

The X-Guide system designed by X-Nav Technologies (Lansdale, PA, USA) allows the placement of virtual teeth for better aesthetic planning. It can be used with an intraoral scanner to further plan an ideal restorative outcome with opposing teeth in occlusion.

Differently from Striker and Medtronic's navigation system, x-Guide uses three-dimensional bar-code patterns as passive reference in the patient's and instrument's markers frame. As a result, the system can continuously track in the three dimensions running an algorithm which does not need to interpolate between multiple two-dimensional reference patterns.

As claimed by the developers of this system (http://www.x-navtech.com/), the user can achieve an outstanding precision in implant placement by live tracking its position, angle and depth.

The three-dimensional bar-code fitted reference tool is mounted on a dedicated hand-piece and must remain attached in the same position at all times during surgery.

Fig. 5.23 Self-drilling screws fixed on the superior orbital frame (Vector Vision II system) (https://www.brainlab.com).

Table 5.3 *Source* of inaccuracies from CAS and IGS systems

Surgical drill guides	**Navigation systems**
Quality of the tomographic scan	
Volume reconstruction	
Manufacturing accuracy	Image-to-world registration
Socket diameter	Round-off errors on mathematical transformations
Splint anchorage on bone crests	Human error due to misalignment with virtual planning

No clinical studies have been published on this system to date.

5.5 Discussion

Independently from which system is used for IGS or CAS, there are some common limitations which are summarised in Table 5.3.

According to the systems reviewed in the previous sections, not every solution for image-guided surgery available today brings improvements against manual insertion methods (Brief 2005). It can be added that the use of drill guides does not translate into an optimal method in terms of accuracy, invasiveness, diagnosis, versatility and easiness of its use.

5.5.1 Invasiveness

Differently from drill guides, navigation can be used with a combination of flapless and raised flap surgery, minimizing pain and discomfort for the patient in the immediate postoperative period (Hultin 2012; Hammerle 2009; Brodala 2009). This aspect can become relevant in case of patients with cardiovascular disease who are often undertaking an anticoagulation therapy. For these patients a trans-gingival approach using navigation would minimise the resection of highly vascularised tissues.

In addition, navigated placement of an implant allows the use of a mucosal blur tip, reducing the surgical trauma in delicate cases such as immediate prosthetic loading (Meyer 2003, Szmukler-Moncler 2000).

In case of edentulous patients BrainLAB's radiopaque screws and ClaroNav's metal pins introduce a level of invasiveness which is comparable with the deployment of anchor screws used to fix surgical guides. In case of severe atrophy in the maxilla, where surgery would certainly benefit from computer guidance, such temporary screws could result too invasive and therefore no drill guide or navigation procedure could be engaged.

5.5.2 Visibility

Through the use of intraoperative navigation intraosseous structures are easily observed and their individual characteristics can be identified. In particular, the surgeon can inspect the density of the bone and the anatomy adjacent to the implant site which some studies see as regulating the degree of deformity of the tissue in the microenvironment of loaded implants (Meyer 2001).

Also in terms of visibility, some navigation systems do not offer advantages with respect to drill guides. ClaroNav's thermoplastic template, for example, may restrict the possibility to visually inspect the area surrounding the implant site, as shown in Figure 5.24. Access to the surgical site could potentially be obstructed by the reference tools used to locate the surgical drill. The Navident system requires a three-dimensional plastic frame to be attached to the handpiece which could interfere, because of its size, with the patient's jaw or other surgical instruments in use during surgery.

5.5.3 Dynamic approach in surgery

All navigation systems generally allow for the surgery plan to be changed from when the tomographic scan is taken until the day of the surgery. This makes image-guided surgery more dynamic with respect to surgical guides which are designed and manufactured according to one surgical plan only.

Since navigation systems do not require a patient-specific template to be manufactured, they don't introduce an extended lead time before the intended surgery. This makes them more agile and applicable to trauma surgery.

Fig. 5.24 ClaroNav's navigation setup showing dimensions of respectively handpiece reference frame (left) and patient's gig (right) (www.claronav.com).

Although being dynamically planned, some navigation system do not allow for a change in the reference setup from the scan to the surgery. ClaroNav's JawGIG (as shown in Figure 5.24), by way of example, is meant to serve automatic image-to-world registration via a software function which identifies contour and orientation of a radiopaque component embedded in the thermoplastic splint. The day of the surgery the optical reference tool can be attached to the splint in one 3D position only in order for the registration to be automatically processed. If the optical reference frame limits the surgeon's visibility, it cannot be deployed and the guided surgery cannot proceed.

5.5.4 Clinical relevance

Accuracy of implant placement is the main purpose for using a guided system. It has been well recognised that inadequate insertions and mechanical stresses caused by parax-ial forces on the surface of the implant often result in peri-implant osseous atrophy or premature loss (Hobkirk 1998).

One of the strongest advantages of tracking the live position of a surgical cutting tip is the contextual visualisation of information from the CT/Cone Beam Computed Tomography (CBCT) scan. For this reason the surgeon can inspect the quality of the bone by its surface analysis around the implant site through a local cross section of the scanned volume.

By evaluating the bone density through radiographic images during the surgery the practitioner can plan the position of the implant to promote primary stability (Hoffmann 2005). There are number of studies reporting how being able to assess the bone quality on-the-fly and therefore how optimising implant positioning might reduce the need for bone augmentation procedure and grafting (Casap 2004; Hultin 2012).

On the contrary, as observed for X-Nav Technologies, ClaroNav, BrainLAB or Striker, the user is forced to use a special handpiece for navigated surgery. The reference frame is generally fixed on the drill in a specific position which cannot be altered during the surgery. If the handpiece needs to be rotated around its inertia axis to be used on the opposite oral arch, the fixed reference frame could not be optically tracked.

In order for two-dimensional sections of the tomographic volume to be used as a live diagnostic tool, their orientation needs to be accurately selected. Some of the navigation systems reviewed above utilise, in their software interface, a collection of volumetric slices which are orthogonal to one another and oriented according to the main axes of the scanned volume (for example in BrainLAB Vector Vision). As it will be pointed out in the following Chapter 6, for the surgeon to assess the quality of the bone in the implant site, the radiographic slices must follow the orientation of the specific implant planned for that particular socket. In this way the displayed anatomy corresponds to the one which will be directly involved in the drilling procedure since it corresponds to the tissues aligned with the drilling direction of the drill tip.

In order for a live tracking system to be clinically relevant, it must also be applicable to the surgical instruments used during osteotomy, socketing or bone harvesting. Optimally the surgeon should be able to apply the reference tools needed for the image-to-world

registration both on the drills and on the patients almost seamlessly and without altering the ordinary technical performances of the cutting instruments.

In terms of clinical application of computer-aided surgery systems, it must be noted how the use of live tracking technology does not require the insertion of a splint with pre-drilled sockets to mechanically guide the resection procedure. This is particularly useful for the insertion of posterior, zygomatic or pterygoid implants with implant sites generally atrophic. There are several studies which quantify the difficulty of placing drilling templates for zygomatic implants against their use in mandibular or maxillary cases. An in vivo study published by Vrielinck (2003), for example, finds that using the Simplant/Surgiguide® system the apical deviation between surgical planning and post-operatively evaluated position of pterygoid implants is around 7.8 mm while the implant axis angular deviation is >10°.

5.6 Concluding Remarks on CAS systems

This critically review of CAS systems has shown how there is a need to develop an alternative navigation system for oral implantology which should be clinically-ready and suitable for use in multiple implant surgery procedures. Provided that accuracy is preserved, the hardware tools of such a system should encourage bone inspection. At the same time the user should be able to dynamically orient the reference frame to enhance access to the surgical site and use the same set of tools for superior and inferior jaw or, most importantly, for posterior areas.

The alternative navigation system should be clinically applicable for those cases in which the deployment of drill guides is more difficult, like zygomatic or pterygoid implants, which require a dedicated surgical instrument which the reference tools must be attached to.

If during a diagnostic scan the surgeon needed to use a temporary bone-supported fixation, whether this is a pin, a screw or a more complex supporting frame, the impact of this insert should be validated towards patient's safety.

For this reason in Chapter 6 this thesis presents the development, analysis and modelling

of a new innovative system for oral and maxillofacial intra-surgical navigation and its use of miniaturised components for patient's registration and instrument calibration.

The author will prove how this system does not restrict the surgical view or access since the reference tools have been designed to promote stability and minimise invasiveness. The impact on the mechanics of the mandible during the scan and surgical procedure is analysed throughout this research via a finite element model based on the patient's anatomy and a biomechanically correct set of muscular forces and appropriate mechanical properties. Patient's safety considerations have been drawn according to the results of the FEM simulation as reported in Chapter 3.

Chapter 6

Design, development and analysis of a new and unique Navigation System for oral image-guided implantology, focus on an innovative miniaturized reference tool, dedicated software application, registration procedure, hardware-software integration

6.1 Introduction

The ability to generate three-dimensional volumetric representations or images of the maxillofacial area has allowed surgeons to evaluate the patient's anatomy before surgery and assist with planning the placement of implants in their ideal or preferred positions. However, the ability to transfer image information to surgical reality has been, and continues to be, one of the most challenging issues of image-guided surgery (IGS) or computer-assisted

surgery (CAS), (Brief 2005, Casap 2004, Lubbers 2011, Luebbers 2008, Pellegrino 2014, Sun 2013, Wittmann 2011).

Despite of multiple IGS or CAS solutions being already available on the market place (as explained in the previous Chapter) there is a continuing need to improve computer-implemented methods, systems and/or devices for image-based or image-assisted surgical planning and/or navigation.

It has been reported that the CAS systems reviewed in Chapter 5 do not assist with intrusiveness and a number of previously explained problems. For example they do not offer the possibility to check the correct position on the bone of a drilling template (Arisan 2010, Mischkolowski 2006).

As per the systems specialised in live tracking the position of cutting instruments, strong limitations come from the invasiveness of the hardware components physically attached to the surgical tools, as well from the complexity of the software interfaces and their accuracy. Thus, although the potential of such systems in assisting the accurate placement of implants in delicate regions of the oral cavity, none of the reviewed CAS or IGS solutions seem to be clinically efficient, versatile and accurate at the same time.

The aim of the research work described in this Chapter was the development of a surgical navigation system able to assist with patient cases which other computer-assisted surgery or image-guided surgery techniques cannot be applied or utilised for.

The main methodology followed in this development was to reduce the human error during dental implantology via a continuous feedback with the pre-operation surgical plan. Such procedure is expected to improve the outcome of the surgical operation as much as to provide an additional verification and monitoring instrument complementary to the equipment already used by the practitioners.

As the following sections in this Chapter will show, the result of our development is an integrated software-hardware system able to track in real time the position of a dental drill tip during osteotomy and to create its dynamic representation over a surgical plan based on a patient specific tomographic scan.

6.2 Method of development and procedure

The basic requirements around which an image-guided surgery system should be developed are:

- The tracking technology used
- The user interface and controls offered to the user
- The workflow which harmonises the integrated hardware/software system

6.2.1 General hardware requirements

A preliminary assessment of the clinical needs which an IGS system should address determined that:

- The tracking method should not interfere with the existing instrumentation used by the surgeon during the procedure
- The dimensions of the tracking device should be minimised in order to be easily fitted into an existing surgical environment
- The hardware components needed for the tracking operation should be compatible with standard disposal and sterilisation protocols

Although our research identified a few existing infrared tracking technologies, specifically one from Northern Digital (Waterloo, Canada) was suitable to fulfil these requirements, however additional specific hardware components had to be prototyped to assist with the following aims:

- Achieve minimal interference with the implant insertion procedure
- Guarantee maximum implant site visibility
- To be compatible with existing multiple bone preparation technologies
- To be easily applied and used

Hence the research was directed at developing innovative hardware components which could bridge a reliable tracking technology with its effective clinical application to either ordinary or more complex patient clinical cases.

6.2.2 General software requirements

The fundamental functions of a software application for image-guided surgery are:

- To communicate with the tracking hardware and translate the received information into spatial coordinates defined in the same reference system of the patient's
- To offer the possibility to plan the surgery before the physical operation, which implies to virtually plan the insertion of one or more implants in a compound-view interface
- To give an accurate virtual representation of the surgical drill during the physical procedure and display/quantify its deviation with respect to the planned surgery

In order to improve its clinical performance, the software application should be able to use the information from the live tracking technology with complementary computer-assisted technology, like for example dental drill guides. For this reason it should also include a function to generate the design of a drill guide according to the proposed surgical plan.

Because of the modularity and complexity of the software application and the specificity of the hardware tools designed to fulfil its clinical requirements, this research focused on a specific workflow for IGS able to combine with efficacy software operations with ad hoc engineering solutions.

6.3 Design

6.3.1 System components

Figure 6.1 shows the main components proposed for a navigation system based on a pre-operative implant planning. The assembly includes an input device, a display device

(such as a monitor), and a computer system which runs the software application. An infrared stereoscopic device sends positional data from reference tools mounted on surgical instruments to a computer system. When a dedicated operation in the software application

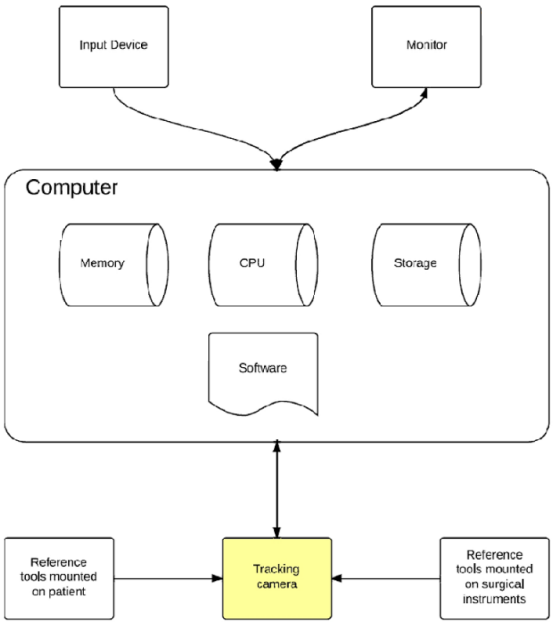

Fig. 6.1 Schematic representation of the main components of a surgical navigation system.

interrogates the tracking hardware, the stereoscopic camera detects the real-world physical position and axial orientation of reflective passive markers (shown in Figures 6.17 and 6.23). The real world physical position and axial orientation of one or more surgical instruments are then transformed into spatial coordinates relative to the same virtual environment where one or more images of the patient's anatomical structures are represented.

In this way the precise position and axial orientation of the surgical instruments during the surgical operation can be visualised. In the same display window of the software application that presents information on a display device to the user, the position of the tracked instrument is presented together with one or more pre-planned implant locations.

6.3.2 Operational workflow

A computer-implemented method was developed to be effected by a software application written in C++ in for WindowsOS environment, compiled using CMAKE (Kitware, New

York, United States) and VisualStudio2010, finally deployed into an executable using Nullsoft Scriptable Install System (http://nsis.sourceforge.net).

A detailed description of the steps designed for this method is reported in Appendix B at the end of this thesis.

Since the surgical plan is based on a tomographic scan, the guided procedure requires the user to import a patient's CT scan from a stack of DICOM files. This format represents a standard in medical imaging and could be managed via the software library DICOMOffis (OFFIS e.V, Oldenburg, Germany) once linked in the software application.

At the beginning of the operational workflow a volume is reconstructed according to the patient's tomographic data, as input for two guided surgery workflows: drill guide generation or live tracking.

6.3.3 Surgical drill guide template workflow

Two procedures for creating a drill guide template were implemented in the software application: a two-scan procedure and a one-scan procedure.

The main difference between the two methods is the technique used to digitize the radiographic template on which the surgical template is designed.

In the one-scan procedure, a dedicated software module was designed to identify the radiographic template in the scan through its distinct radio-opacity.

In the two-scan procedure, the radiographic template is identified in two consecutive scans via a different software operation which aligns the series of radiopaque "fiducial" markers picked in both radiographic volumes at different thresholds of grey values (Figure 6.2).

Once a drill guide template has been separated from the surrounding anatomical structures, its digital surface can be edited using the software application. Compound views were designed to allow the user to plan and navigate the implants insertion. Such views are oriented according to the patient's panoramic profile which is created in a separate module of the software application.

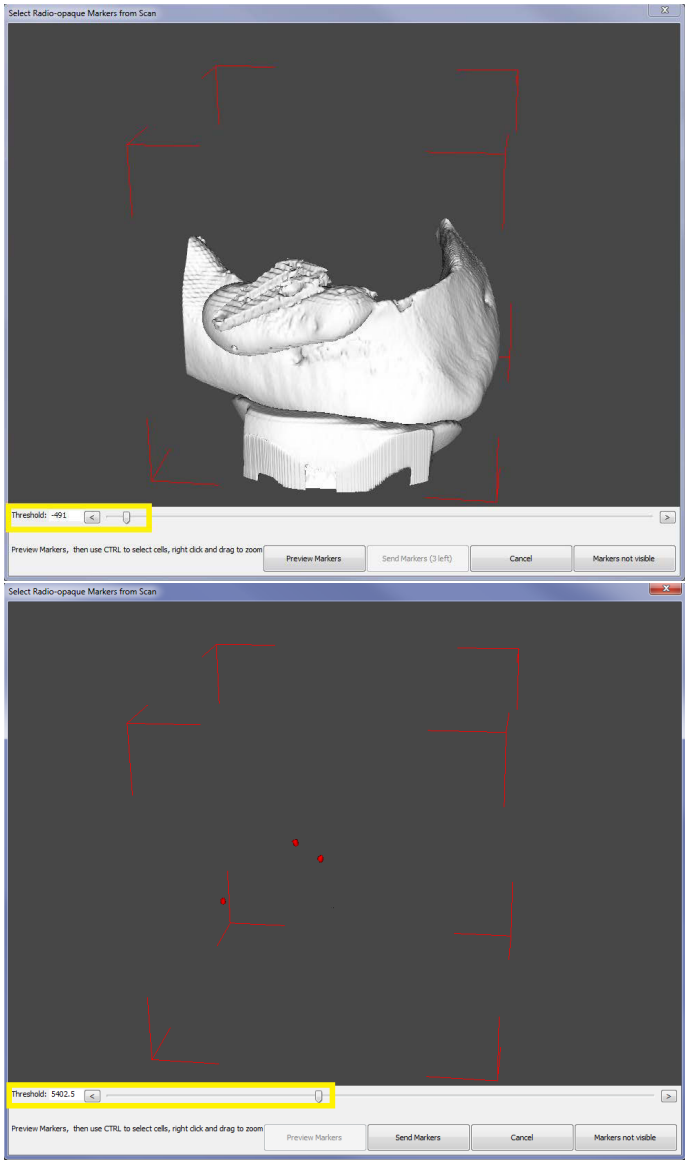

Fig. 6.2 Digital extraction of fiducial markers (top) from segmenting the isosurface of the radiographic template (bottom) at different threshold values.

In order to simulate the surgery, another module was designed to allow the user to select implants from a library provided in an embedded database. Alternatively, an external application also created in C++ and developed in a Qt environment (www.qt.io) allows to create customized inserts. Desired insertion and apical points of the implant are placed as landmarks in a main slice view and used by the algorithm to move a virtual implant. When all the implants are fixed in their final position the user can proceed to the generation of a surgical guide. This function requires a Boolean operation and creates in output a cylindrical socket in the guide.

From a clinical point of view, the use of a drill guide implies that:

- There will be an offset due to its thickness and this will require the use of drill bits extenders
- The socket is formed by progressive circumferential extensions by using drills of increasing diameters

For the reasons above a dedicated drilling procedure for drill guide deployment had to be designed and is described respectively in Figures 6.3 and 6.4.
The shape of a surgical guide is complex since it must fit onto the patient's mucosa or bone tissue so prototypes were manufactured via Selective Laser Sintering by Advanced Manufacturing Services (Ingleburn, Australia) after being exported in the most popular file format for subject-specific instrumentation: STL (Gur 2014, Ventola 2014, Naftulin 2015). If IGS is used as complementary to a drill guide, such combined software/hardware system would provide a feedback in real time on the correct positioning of the template. Mainly the software application was designed to perform image-guided surgery independently from the use of a surgical guide, as explained in the next section.

6.3.4 Image guided surgery navigation workflow

The most significant CAS option implemented in the software for guiding the implant insertion is the use of a navigation system which tracks the surgical instrument(s) on the pre-operative virtual plan.

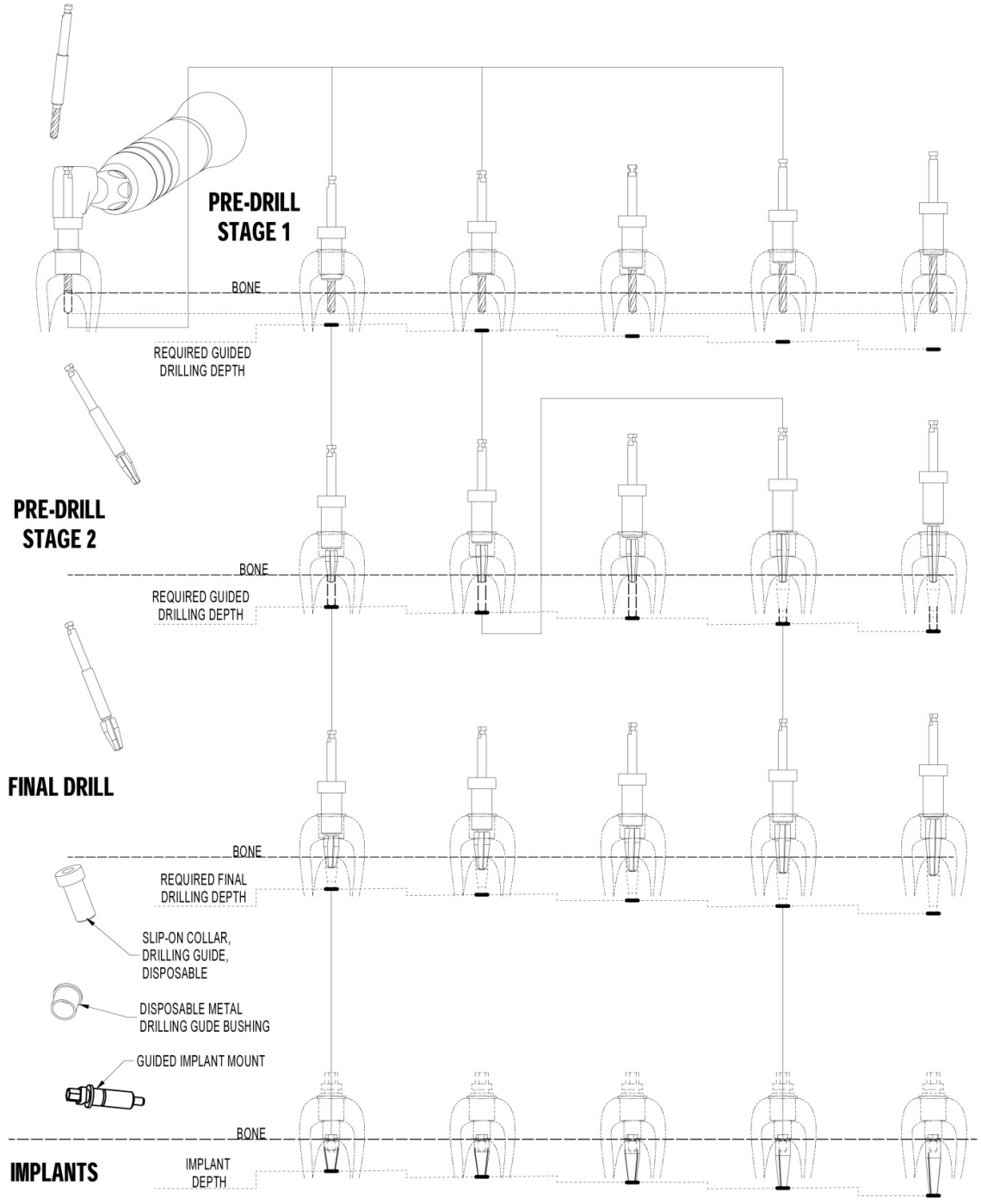

Fig. 6.3 Drilling sequence with preparation via surgical guide without the insertion of a drill extender (developed in conjunction with BresMedical Pty Ltd – Australia).

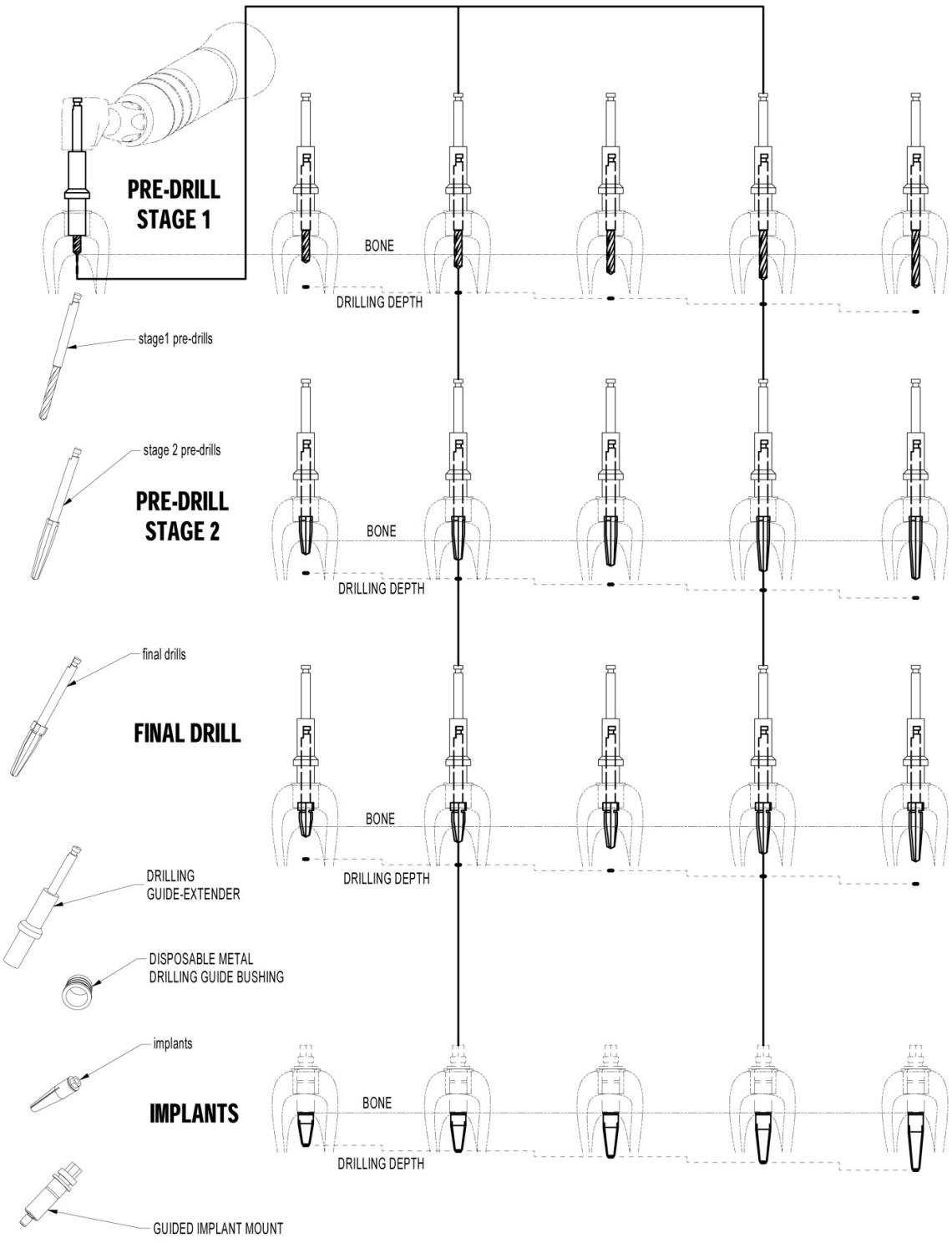

Fig. 6.4 Drilling sequence with preparation via surgical guide using drill extenders (developed in conjunction with BresMedical Pty Ltd – Australia).

This procedure requires the identification of radiopaque markers serving the alignment of the virtual images with the physical patient. A module for creating a panoramic profile able to simplify both surgical plan and navigation was included in the software application. The position of the panoramic profile gets adjusted along two axes until it is aligned with the mandibular or maxillary arch.
Based on the orientation of the panoramic profile the software simulates the insertion of implants using customised libraries present in the software application or created via a dedicated module.

A detailed description of the navigation procedure as implemented in the software application is also reported in Appendix B.
According to the navigation workflow, once the surgical plan is complete, a reference marker tool, described in detail later in this Chapter, is mounted on a surgical instrument like a contra-angle handpiece for implantology (Figure 6.17). In order to promote stability in the image-to-world registration, this research determined that in the case of a completely edentulous patient the reference tool should be mounted on an implant whose biomechanical impact has been validated through finite element analysis (in Chapter 3). Otherwise, if the patient is not completely edentulous, the reference tool can be mounted on a teeth-supported template.

First of all during the process a plastic plate hosting the fiducial markers and supporting the reference tool via a three-dimensional joint is mounted on the implant. Afterwards, the patient's anatomy is imaged via a CT/CBCT scan with the fiducial markers in place, either bone or teeth-supported. On the day of the surgery the reference tool is attached to the patient's reference frame. In the surgical navigation workflow, the tracking camera assembled detects the position of a first reference tool mounted on a surgical instrument and a second reference tool mounted on the patient which is also connected to the fiducial markers. The patient reference tool is only mounted on the day of the surgery and is removed at the end of the procedure.

Once the navigation operation is launched both reference tools should be detected by the navigation system in order to proceed to the "image-to-world" spatial alignment. After

this registration the fiducial markers plate can be removed and the implant site can be navigated through the software interface, meaning that a precise virtual representation of the real-world position and axial orientation of the surgical instrument in the same reference system of the patient's anatomy is provided.

The workflow proceeds to the calibration of the cutting tips. To calibrate a surgical instrument a customised tool was designed for identifying the axis of the cutting tips. In the specific case of non-cylindrical tips, like for example inserts for ultrasonic osteotomy, additional tools had to be designed (Figure 6.5) and manufactured via subtractive or additive technology in conjunction with BresMedical and Advanced Manufacturing Services (Ingleburn, Australia). The calibration procedure is carried out in two steps: the calibration of long probe followed by one of a shorter tip. The aim of using a long probe for calibration is to physically extend the axis of the surgical tip. In case this tip is straight, its equivalent with a longer shaft is used. In case of inserts used for piezoelectric surgery, the axis to be identified corresponds to its apical cutting end.

Once the Graphical User Interface (GUI) indicates that the calibration is accurate, the fiducial markers are touched with the sharp termination of the short calibration probe (Figure 6.6). If the calibration feedback is positive, the user is called to select the drill type and/or the implant type mounted on the surgical instrument.

A specific software module was created in order to let the user switch between the currently tracked drills or implants. This particular operation responds to the need of having an agile navigation workflow where no ad hoc calibration is required for each tip.

The "image-to-world" registration allows an accurate mapping of the scanned physical images to virtual environment. If successful, the surgical instrument can be properly tracked in the physical environment and precise images of the position and axial orientation of the surgical instrument will be visually presented to the clinician or user.

6.3.5 Registration procedure: software design

The main component of the tracking hardware is a stereoscopic camera manufactured in Canada by Northern Digital. This choice was mainly due to the fact that its Application

Fig. 6.5 Piezoelectric handpiece long probe calibration, CAD model (top) and physical prototype (bottom): the top clamp holds the terminal cutting part of the piezoelectric tip in axis with the rest of the calibration device, ensuring stability during the pivoting action.

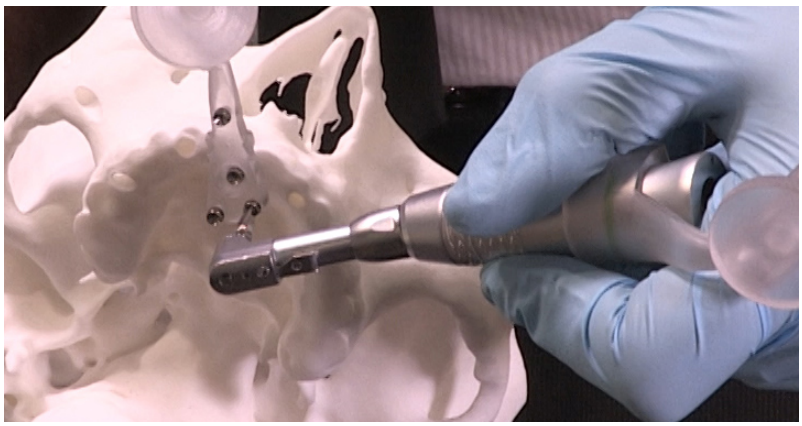

Fig. 6.6 Picking of radiopaque markers with a piezoelectric handpiece calibration probe.

Programming Interface (API or API's) are publicly accessible. Using the API's, the tracking algorithm designed for the software application is able to provide in output the 3D positions of each reference tool. Calibration, registration and live tracking can then be performed by dedicated algorithms written in C++ on the base of the OpenMAF platform (Rizzoli Orthopaedic Institute, Bologna, Italy) in order to interpret and represent the 3D positional data.

The algorithm transforms the 3D positions into spatial coordinates in the same virtual environment of the radiographic volume. The transformation is based on the calculation of a matrix built according to the general Iterative Closest Point registration algorithm (Lange 2003, Lee 2010, Cleary 2005, Zhang 2006).

The calibration algorithm calculates the average physical point of the drill tip and of its axis from two different frame collections. Live tracking requires that the information from the calibration and the registration matrix are combined with the current coordinates read by the camera's firmware.

This live calculation is carried on a dedicated thread within the operating system using the MafThread function within the Open Multimodal Application Framework (Viceconti 2007 and 2011).

6.3.6 Registration procedure: hardware components

Initially, a rigid component holding the radiopaque reference needed for the image-to-world registration which was designed as a plastic/aluminium plate with cavities arranged in a specific configuration and filled up with soft highly radiopaque material (Figure 6.7). For its established radio-opacity properties, Guttapercha (Katz, 1990) was initially used. Because of the radio-intensity of the tomographic scanner, the density of the phantom and the orientation of the volume itself, preliminary tests revealed how the radiopaque fillings can be imaged as irregular shapes at different thresholds of grey values. Being the selection of the threshold a user-defined operation, this variable condition could have brought ambiguity in identifying the fiducial markers. This behaviour is illustrated in Figure 6.8.

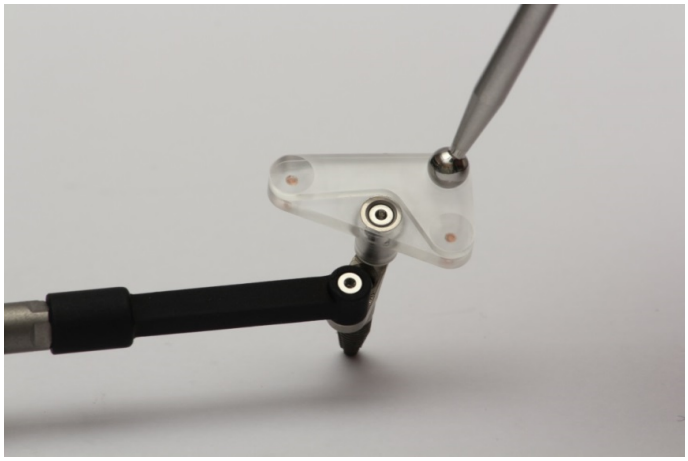

Fig. 6.7 Fiducial radiopaque markers realised by pressing Guttapercha into a plastic plate with cylindrical sockets.

The registration of the patient is based on algebraic transformations which in input use three-dimensional coordinates of the surfaces derived from the segmentation of the radiopaque markers. The reference point in each surface is associated with the one physically picked by the user during the procedure. This is why it is crucial that for a correct calibration the user should physically touch a surface point which has a unique virtual representation in the software.

On this concept Titanium screws with a sunken conical head were designed and adopted as fiducial markers. This solution offers a dual benefit: helping locating the surface top point by centring the physical probe and being a rigid radiopaque structure which can be rigidly fixed into the implant or teeth-supported reference plate.

6.3.7 Centroids experiment

In order to quantify these deviations due to the different shapes of the markers at different thresholds, a dedicated experiment was set up. The experiment required the creation of a dedicated algorithm for calculating the centroids of the isosurfaces segmented from the tomographic volume.

A CBCT scan of a phantom containing position of the three Titanium screws was taken and uploaded into a software application. The centroids of the screws were calculated for different thresholds as reported in Table 6.1. From the engineering model of the screw

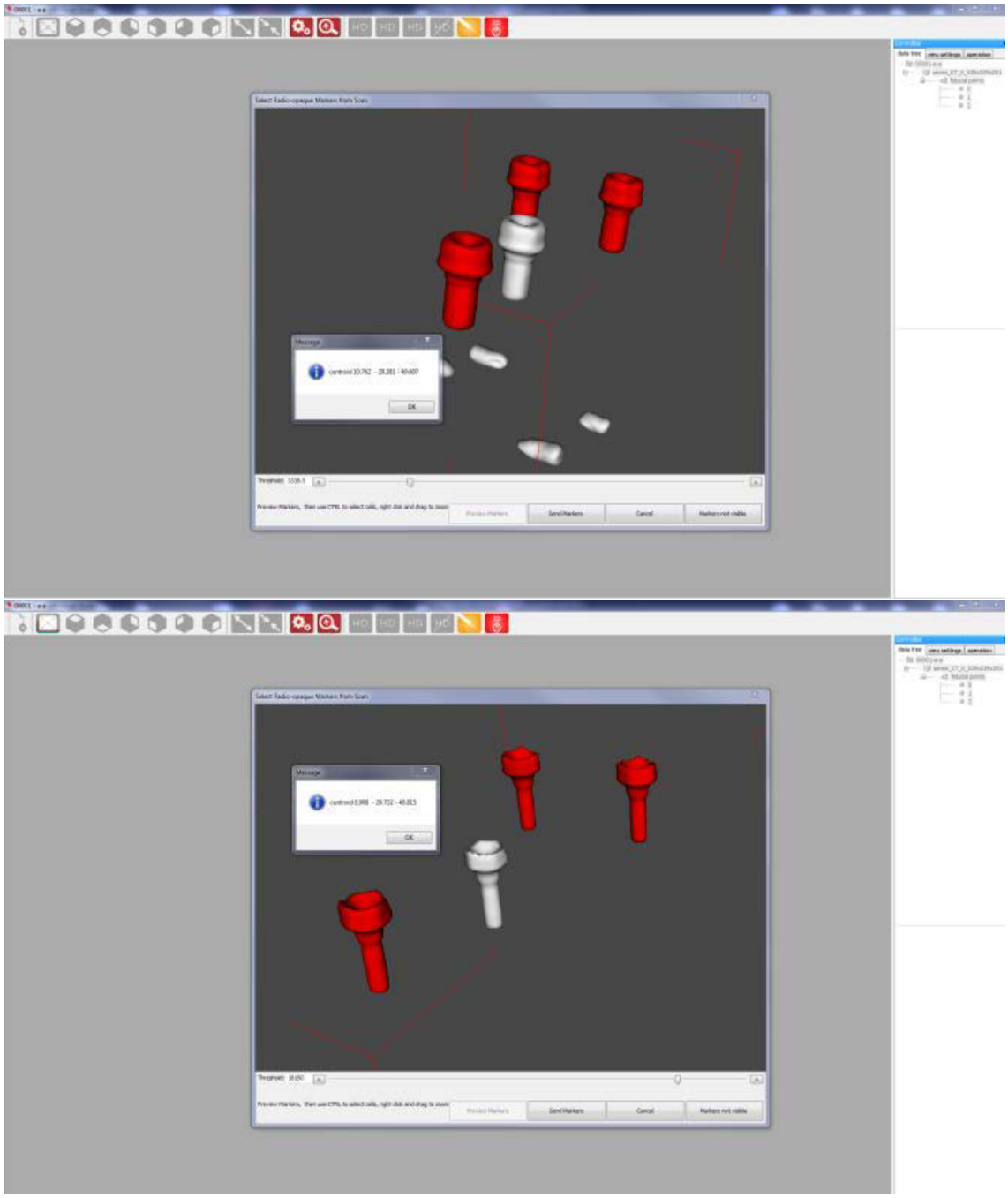

Fig. 6.8 Visualisation of the isosurfaces of the radiopaque markers at different threshold values (top, bottom): irregular surfaces results in variable surface points used by the registration algorithm.

Table 6.1 Calculation of surface points of three Titanium screws fiducial markers in X, Y and Z axis respectively (P1, P2 and P3 isosurfaces): the table shows how for different threshold values **T** different algorithms give in output different surface points with a significant deviation **D**.

Surface Point Calculation by Segmentation Algorithm											
T	$P1_X$	$P1_Y$	$P1_Z$	$P2_X$	$P2_Y$	$P2_Z$	$P3_X$	$P3_Y$	$P3_Z$	**D**	Max **D**
10476	16.46	30.08	48.91	13.45	8.73	50.07	8.65	28.19	49.21	1.13	**1.13**
3338	16.47	31.15	49.28	13.45	9.81	50.45	8.68	29.28	49.60	0.03	
18160	16.49	31.13	49.29	13.49	9.79	50.45	8.68	29.25	49.61	1.11	
Surface Point Calculation by Centroid Offset											
T	$P1_X$	$P1_Y$	$P1_Z$	$P2_X$	$P2_Y$	$P2_Z$	$P3_X$	$P3_Y$	$P3_Z$	**D**	Max **D**
10476	16.70	30.06	48.57	13.70	8.71	49.66	8.91	28.17	48.87	0.11	**0.11**
3338	16.70	30.06	48.46	13.69	8.73	49.58	8.92	28.18	48.76	0.09	
18160	16.72	30.04	48.54	13.72	8.70	49.69	8.91	28.16	48.87	0.04	

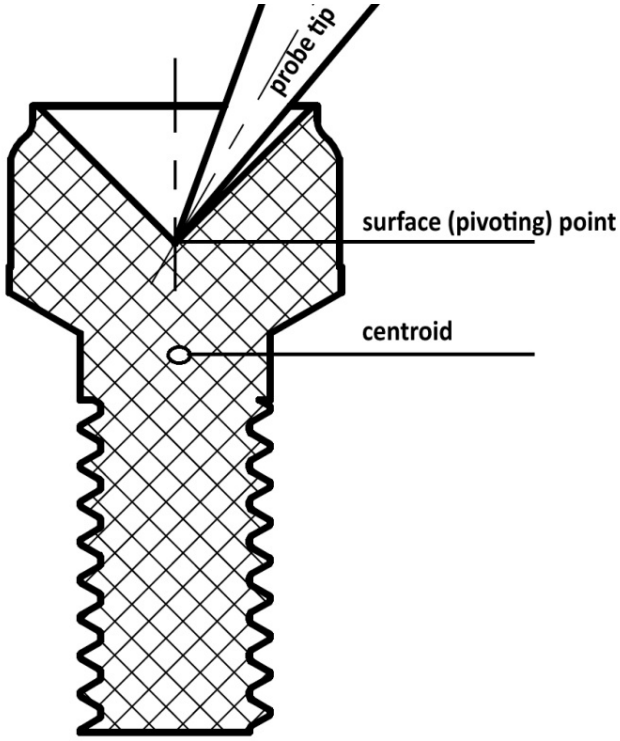

Fig. 6.9 Design of a Titanium screw used as fiducial marker: the distance between the centroid of the screw and the vertex of the sunken cone in the screw head was used in the algorithm which computes the segmented surface point.

the distance between its analytical centroid and the surface point was calculated using the CAD software package Autodesk Inventor (Autodesk Inc., USA). This CAD software was also used to design the engineering model of the Titanium screw. Two sets of coordinates corresponding to a proposed surface point were calculated: one by applying the algorithm to the segmented surface, another by adding to the centroid calculated for the segmented surface the analytical distance measured in the engineering model.

As reported in Table 6.1, when different thresholds were applied, each surface point was calculated with a variance of about 1mm. On the contrary, when the centroids were used, the maximum error was ten times smaller.

Based on these results, the author decided to use the following solutions as tools for the registration of the patient with the tomography scan: small Titanium screws as hardware and an algorithm for calculating the centroids from the screws isosurfaces included in the software application.

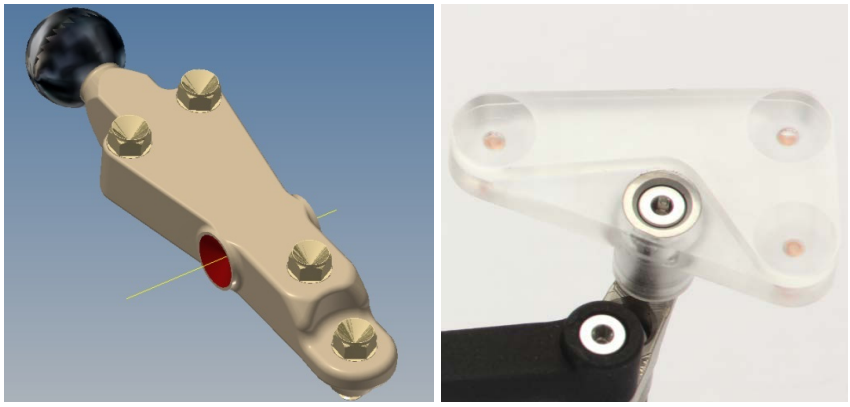

Fig. 6.10 Fiducial markers plate for edentulous patients: original version with pressed Guttapercha cavities (right) and later version with Titanium conical head screws (lelf).

6.3.8 Patient registration: edentulous or partially edentulous case

In case the patient is only partially edentulous (dentured), the registration plate which hosts the fiducial markers was designed to be attached to the teeth by an impression resin. Teeth are then responsible for holding a specifically designed tray in a unique position during the tomographic scan (Figure 6.11). On the day of the surgery the complex profile of the teeth is supposed to relocate the tray in the same position.

The radiopaque screws described in the previous section are fixed on the tray itself which also supports the optical reference tool via a three-dimensional joint. At the moment of the surgery the adapter can be re-located to fit the patient's anatomy with accuracy. The

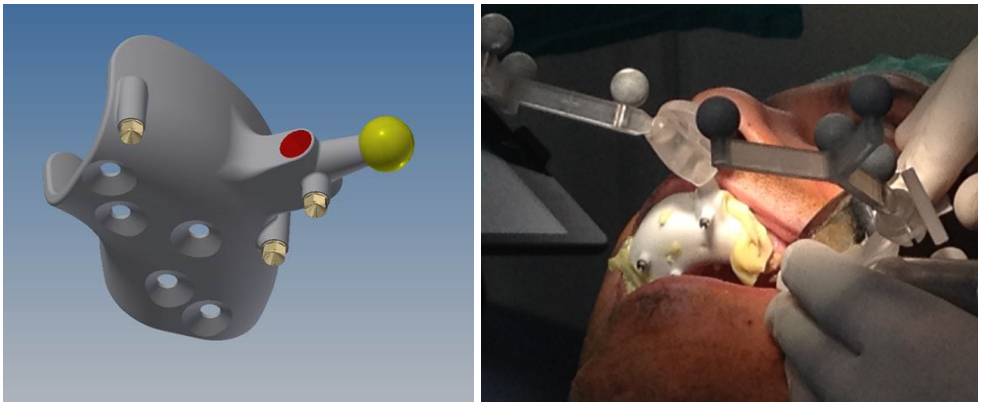

Fig. 6.11 Fiducial markers tray for partially edentulous patients: (left) CAD model and (right) prototype as used during clinical trials; the prototype on the right is fixed via an acrylic resin (Ramitech 3M) and supports the patient's reference tool via a "double-joint".

"double-joint" between the fiducial tray and the reference tool was designed following the guidelines below:

- to preserve the mutual position of the optical reference tool with respect to the fiducial markers during the calibration procedure
- to be able to move the optical reference tool away from the surgical site, although preserving a line-of-sight with the camera sensors.

In case the patient is completely edentulous the radiopaque markers are embedded in a plastic plate which is supported by a temporary implant (Figures 6.10 and 6.14).
The improved mechanical stability achieved by using a bone-supported reference tool and the biomechanical validation of this procedure has been analysed in Chapter 3.
Once a tomographic scan of the patient has been taken, the user can load the digital data for surgery planning and start using the software application in navigation mode.

6.3.9 Calibration procedure: hardware design

The calibration procedure allows the user to track both tip and axis of one of the drill tips or implants from the software application's library.

Calibration of the surgical instrument can be achieved in two steps with the use of the calibration device specifically designed for this function (Figure 6.5) or respectively long and short tip probes (Figure 6.12). The successful completion of the calibration steps is reported within the navigation panel in the software interface and allows to proceeding to the live tracking software module. An initial version of a calibration device that is used

Fig. 6.12 Original design for a calibrating instrument: short and long straight tips are used to pivot around a point fixed in three dimensions with respect to the patient's optical reference tool.

for calibrating the surgical drills was developed so that respectively the tip and axis of the surgical drill could be identified.

This device (Figure 6.12) included a body which hosted the pivoting point of both a long and a short calibration probe and optical markers (as will be explained in the next section) in a fixed configuration.

These markers were used to determine the position and axial orientation in the physical world (oral environment) of the end points of the calibration probes.

A standard calibration procedure was designed for which the user is required to pivot the surgical tool around a point in space in a fixed position with respect to the patient's reference tool. During this movement (shown in Figure 6.12), which is required to last a minimum of five seconds, the software records the positions of the reference tool. Once the movement is complete, the software calculates the average origin of the virtual cone whose base is virtually drawn by a master marker in the reference tool (Figure 6.13). An alternative calibration procedure, referred to as "one-touch calibration", was also imple-

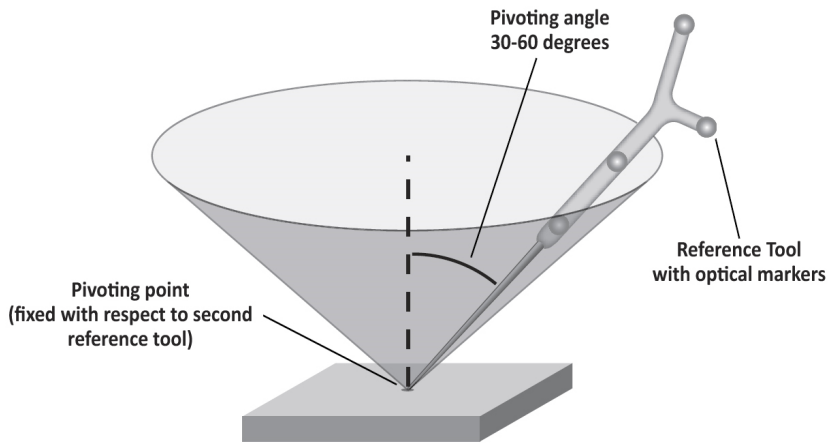

Fig. 6.13 Movement required for drill tip calibration: the optical markers, here illustrated in a simplified geometry, are mounted on a surgical instrument via a rigid support and a "double-joint" to facilitate its orientation towards the tracking device.

mented in the software application.

In the one-touch calibration procedure, the user touches one pre-determined point on the reference tool once it is mounted on a patient. A cross-hair engraved on the reference tool helps locating the tip onto the point.

Differently to the pivoting calibration procedure used in Figure 6.13, the one-touch calibration was considered as a more comfortable solution for the insertion of maxillary implants. In this type of surgery, in fact, the surgical instrument's tip is oriented upwards and if pivoted could interfere with other instruments used during the surgery.

6.3.10 Additional hardware design for live tracking

6.3.10.1 Optical reference supports

In order for the navigation system to accurately track and display surgical instruments in their correct position and axial orientation, the stereoscopic camera is required to identify some plastic spheres coated with reflective paint (manufactured by Ilumark GmbH, Munchen, Germany) used by the device as optical markers. These must be positioned both on the patient's anatomical structure and on the surgical instrument to be tracked (workflow illustrated in details in Appendix B).

The camera system identifies the bright spots in each frame's image capture and computes the coordinates of their geometrical centres. Reciprocal distances calculated between the centres of the spheres are compared with the geometrical configuration of the markers as memorised in the software application for that specific reference tool. If the distances are within a margin of error, the bright spots are identified as optical markers for a specific reference tool and the coordinates the spheres are sent to the computer through the camera's API's.

In force of basic geometric considerations, the error associated with calculating the geometrical centres of spherical objects from a two-dimensional projection (image-capture) is augmented when the plane containing the spheres is not perpendicular to the stereoscopic axis. It is common that this type of misalignment would occur during navigation. Since this error would be directly impacting the accuracy of the instrument tracking, a hardware solution was designed to minimise it.

6.3.10.2 Double-joint

In summary, it has been remarked how the optical markers (reflective balls) must be fixed in specific configurations identified by the camera's firmware. Secondly, the reference tool which supports the markers in that configuration is mounted on the tooth-supported or implant-supported patient reference plate via a specific joint. Thirdly, in the scenario in which the plane hosting the spheres is not perpendicular to the stereoscopic axis, a level of inaccuracy has been noted. This inaccuracy has been quantified to a spatial deviation up to 2.5mm.

The hardware solution designed to help with the three issues specified above is a specific joint able to connect the fiducial markers plate with the reference tool (Figure 6.15) and rotate it in three degrees of freedom. Through housing one ball fixed to the extremities of the reference tool and another to the markers plate, the joint allows to move the reference assembly in three dimensions. This feature gives the user the possibility to position the tool in a direction for which the normal to the plane containing the reflective balls is best aligned with the stereoscopic axis (Figure 6.16).

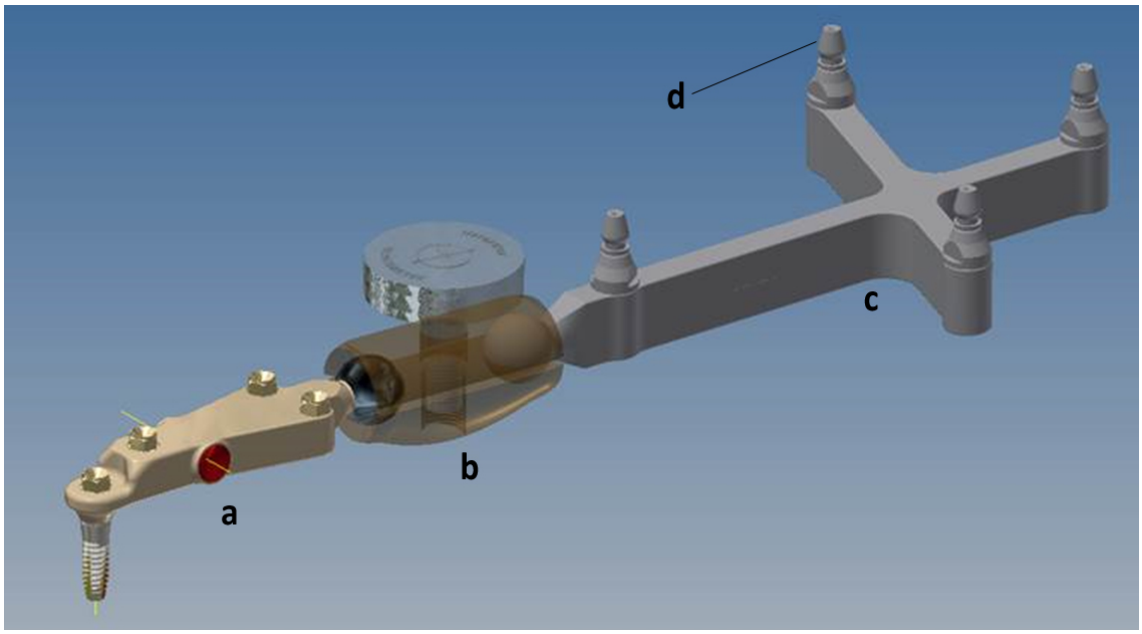

Fig. 6.14 CAD model of the developed reference tool assembly, composed of (a) implant-supported markers reference plate, (b) "double-joint" and (c) rigid reference frame embedding posts (d) for supporting the optical reflective balls.

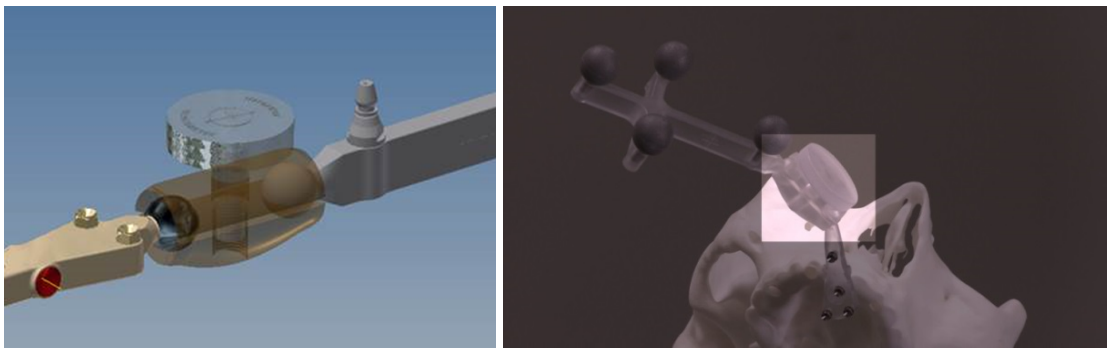

Fig. 6.15 "Double-joint" connecting the fiducial markers holder and the optical reference frame: CAD model (left) and produced prototype (right).

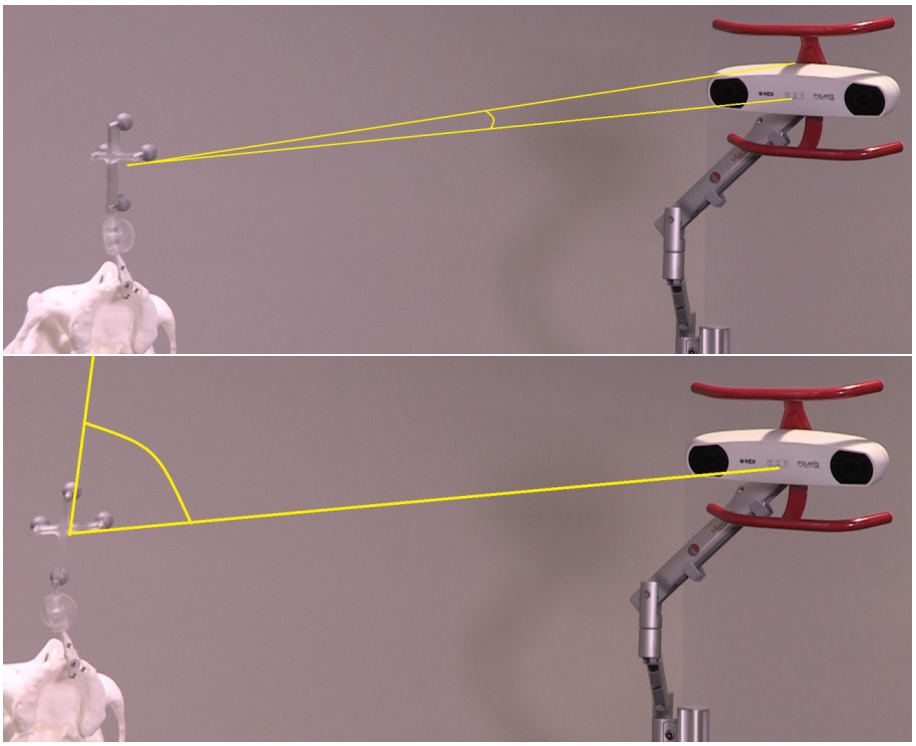

Fig. 6.16 Reference assembly facing the tracking camera (top) and facing away from the camera (bottom): the optimal tracking procedure requires that the plane formed by the reflective balls normally faces the tracking axis. Misalignment (bottom) generates inaccuracy due to the geometrical error made by the stereoscopic camera's firmware in computing the position of the centre of gravity of the reflective balls.

6.3.10.3 Handpiece attachments

For the navigation system to be used in multiple surgical approaches, the attachment for the optical frame which makes the tips trackable was designed be compatible to a variety of surgical or diagnostic instruments, such as contra-angle drills, straight or handpieces for ultrasonic preparation (Figure 6.17).

Each reference system includes a handle support which is a vehicle for supporting the reference tool to the surgical instrument via the three-dimensional joint. The configuration

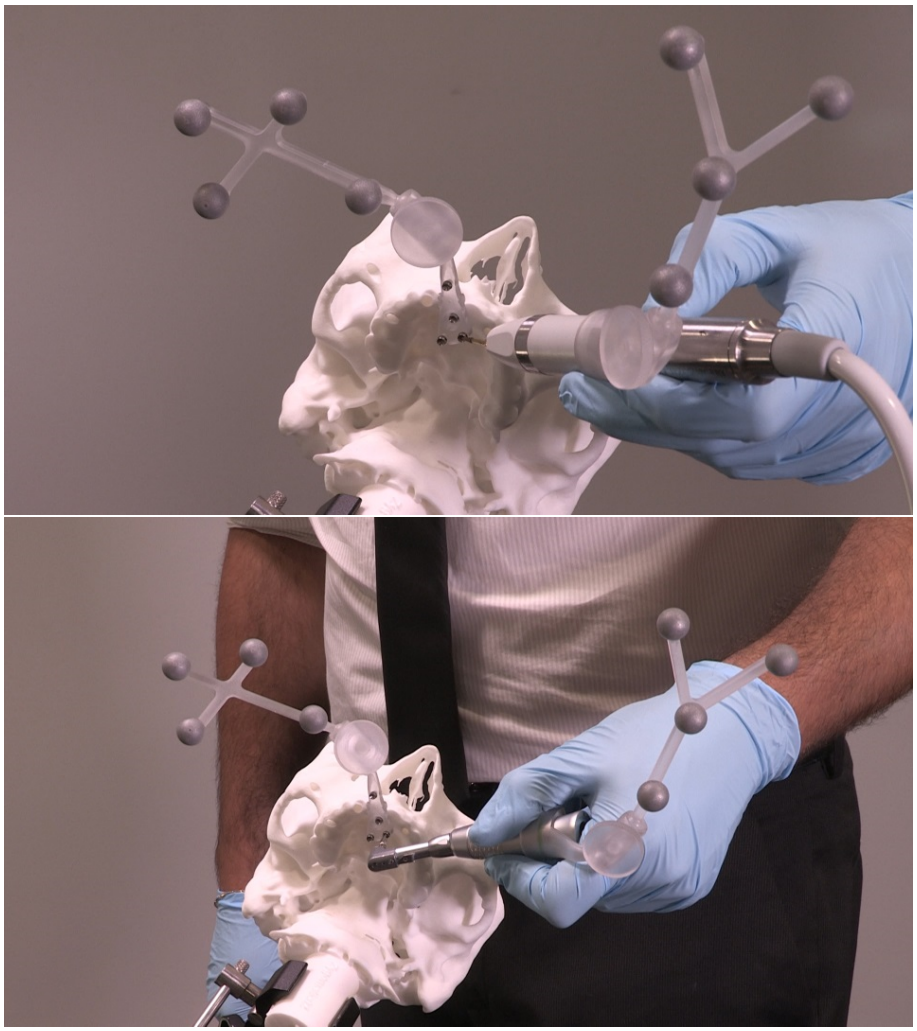

Fig. 6.17 Reference assembly applied to two different surgical techniques: piezoelectric surgery (top) and contra-angle drilling (bottom).

of the reference markers has also been engineered to balance tracking accuracy and user comfort during implant surgery.

6.3.11 GUI Design

Because of the multiple functions to be accessed, two main operations in the software required a complex graphic user interface (GUI): the implant insertion planning and the surgical navigation module.

6.3.11.1 GUI: surgical planning

Because of the multiple functions to be accessed, two main operations in the software required a complex graphic user interface (GUI): the implant insertion planning and the surgical navigation module.
In the virtual planning operation the implant needs to be placed in its ideal position and by inspecting the radiographic sections of the volume along clinically relevant views. This is why the panoramic profile, previously drawn in a separate software operation, was used to move a main vestibulo-lingual volume slice on which the implant insertions points can be picked.

According to these requirements, in the virtual planning operation, illustrated in Figures 6.18 and 6.19, the views displayed in the application frame are updated by sliding bars present in the user interface allowing the following transformations:

- Scrolling perpendicular to the panoramic profile
- Scrolling parallel to the antero-posterior slice
- Scrolling parallel to the axial slice
- Tilt along the main slice axis
- Flip along the main slice axis
- Rotation the panoramic profile around its axis.

According to pre-clinical trials feedback from surgeons from the University of Bologna (Italy), each implant insertion should be guided, in principle, by the prosthetic restoration associated to it. For this reason, in addition to the implantable components, the option to

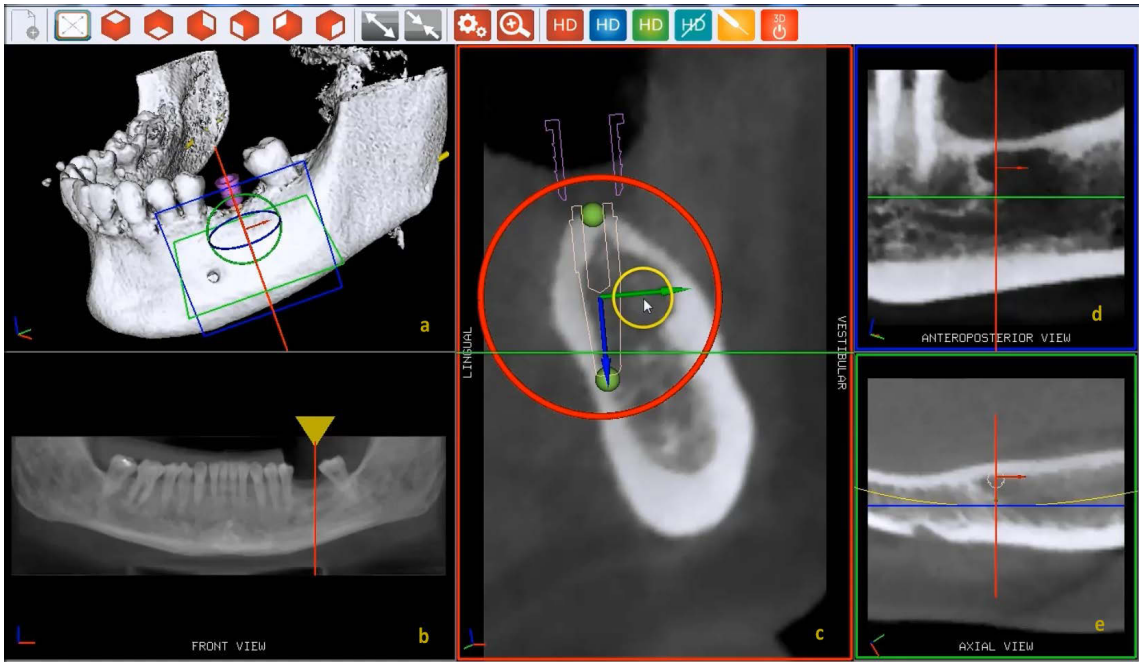

Fig. 6.18 Virtual planning stage in the developed software application: (a) three-dimensional volume rendering; (b) orthopantomographic volume section; (c) vestibulo-lingual volume slice hosting the main implant positioning handles; (d) antero-posterior volume slice; (e) axial volume slice.

pre-visualise implant abutments, virtual teeth and handles to spatially transform virtual prostheses was added both to the volume rendering and to the volume slices sub-windows. The resulting procedure for virtual implant insertion includes:

- Selecting an implant from an implants library
- Designing a customised implant via geometry specifications
- Selecting a volume slice via transformation sliders accessible in the user interface and placing the desired start and end point of the implant
- Moving the implant in 3D via transformation handles
- Pre-visualising an abutment on top of the implant placed
- Pre-visualising, manipulating and spatially transforming a tooth on top of the implant from a teeth library.

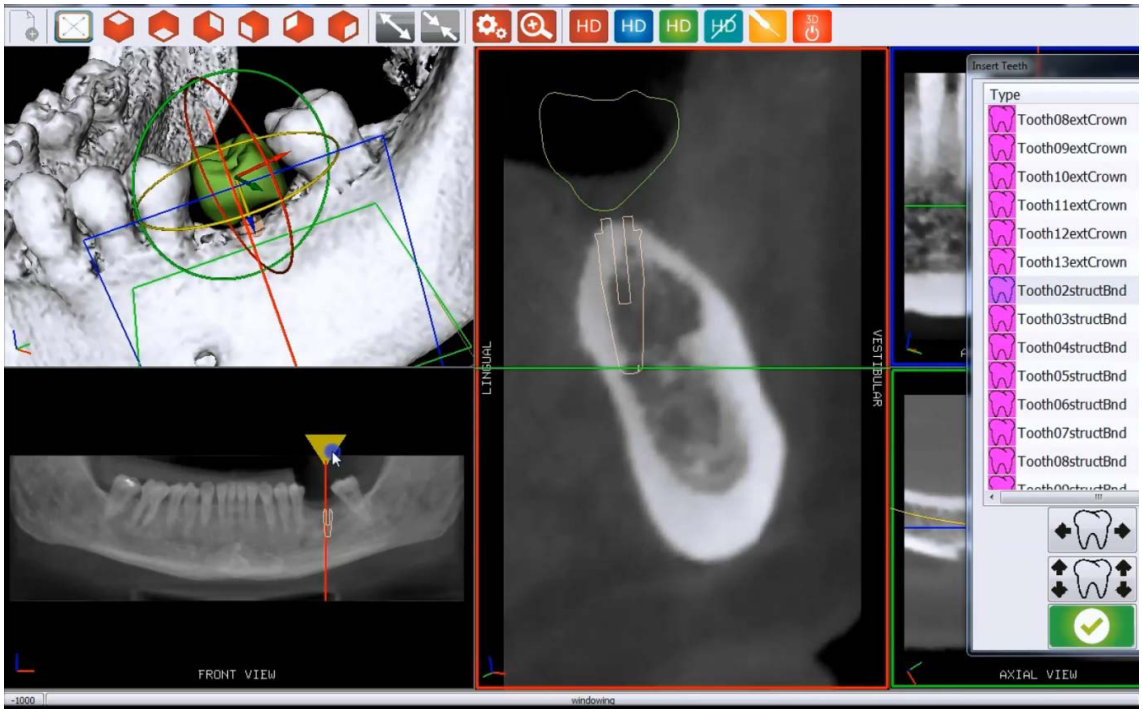

Fig. 6.19 Virtual prosthesis visualisation during implant planning using the protocol developed: the tooth's positions can be transformed in three dimensions; its section can be visualised in the lingual-vestibular volume slice.

6.3.11.2 GUI: surgical navigation

Similarly to the surgical planning operation, the design of a software interface was developed for live tracking to solve a number of significant issues:

- The navigation views should be intuitive for the surgeon to inspect patient's anatomy on radiographic images oriented in preferential directions (anteroposterior, craniocaudal, sagittal, etc.)
- The alignment of the navigation view should be compatible with the symmetry of the planned implants or sockets
- The surgeon or the dentist should be able to inspect, at any time, the quality of the bone using the surgical instrument as a probe

These requirements produced a compound window self-updating at a specific frame rate in which the position of the surgical tip is calculated from the information received from the stereoscopic camera, preferably updating the following views to increase accuracy and efficiency (Figure 6.20):

- Axial two-dimensional volume slice
- Antero-posterior two-dimensional volume slice
- Three-dimensional isosurface of the patient's bone
- Two-dimensional slice perpendicular to the patient's occlusal plane and orthopantomographic profile

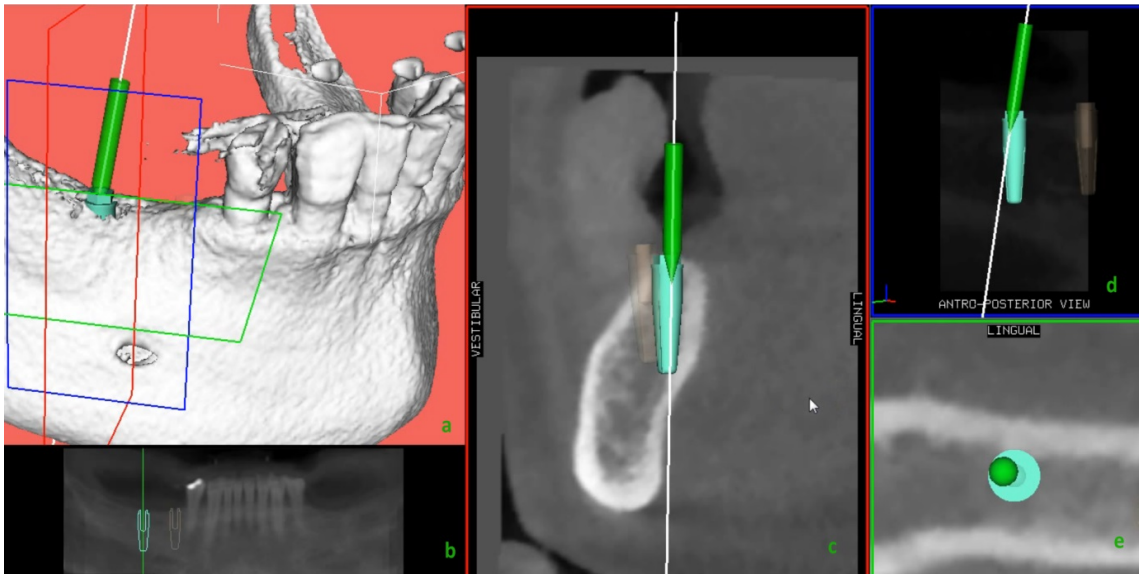

Fig. 6.20 Navigation operation views: (a) three-dimensional volume rendering; (b) orthopantomographic volume section; (c) vestibulo-lingual volume slice; (d) antero-posterior volume slice; (e) axial volume slice; in all views there is present a live representation of tip and axis of the surgical instrument tracked by the stereoscopic camera.

The criteria used for updating the positions of the volumetric slices are based on two navigation modes. In a "free" navigation mode, the slices are intersecting at the transformed three-dimensional position of the drill tip in the current frame. In an "implant-based" navigation mode, the orientation of the volumetric slices is calculated from the axis of the current nearest implant. A dedicated algorithm for the software application was developed to determine which implant is closer to the probe at each frame.

In summary, the software interface has been designed so that the virtual tip can be visualised in the same environment where the surgical plan and the tomographic canvas are present.**As a consequence, the accuracy of the procedure should be maximised when the user aligns the surgical instrument with the virtual implant in all the slice views of the navigation panel.**

6.4 Analysis and verification

In order to test the efficacy and the accuracy of the whole navigation system pre-clinical experiments were undertaken in conjunction with University of Bologna (Italy) and BresMedical Pty Ltd.

A polymeric bone replica was manufactured via Selective Laser Sintering by Advanced Manufacturing Services (Sydney, NSW) on the base of a reverse-engineered model of the mandible obtained segmenting tomographic images of a voluntary 30 years old male. The live tracking technology was tested using a teeth-supported markers tray and an implant-supported markers plate. Both were hosting Titanium screws as radiopaque reference.

Four implants for each model were virtually placed using the navigation software developed. After the calibrating the surgical instrument, the socket was prepared and self-tapping implants (Hex-Ex, Southern Implant, Irene, South Africa) were placed in navigation mode.

A post-operative scan of the models was performed and the implants were segmented from the volume using the Multimode Application Framework (Cineca, Rome, Italy) .The deviation from the planned position was evaluated via a numerical analysis using the 3-matic software package (Materialise, Leuven, Belgium).

Results for the pre-clinical trials showed an average deviation of about 0.9 +/- 0.8 mm from the surgical plan which is comparable to the deviations reported in literature for computer-assisted surgery systems as discussed in Chapter 5. Being these preliminary clinical results encouraging, a clinical protocol was submitted to the ethical committee of the University of Bologna for clinical trials. Currently the clinical trials are being performed at University of Bologna (Italy) in collaboration with BresMedical Pty Ltd (Ingleburn, Australia) to establish the clinical accuracy and efficiency of the system (Figure 6.21 and 6.22). Preliminary results from the clinical trials limited to the application of the navigation system to ultrasonic implant socket preparations are presented in Chapter 7 (Figure 6.23).

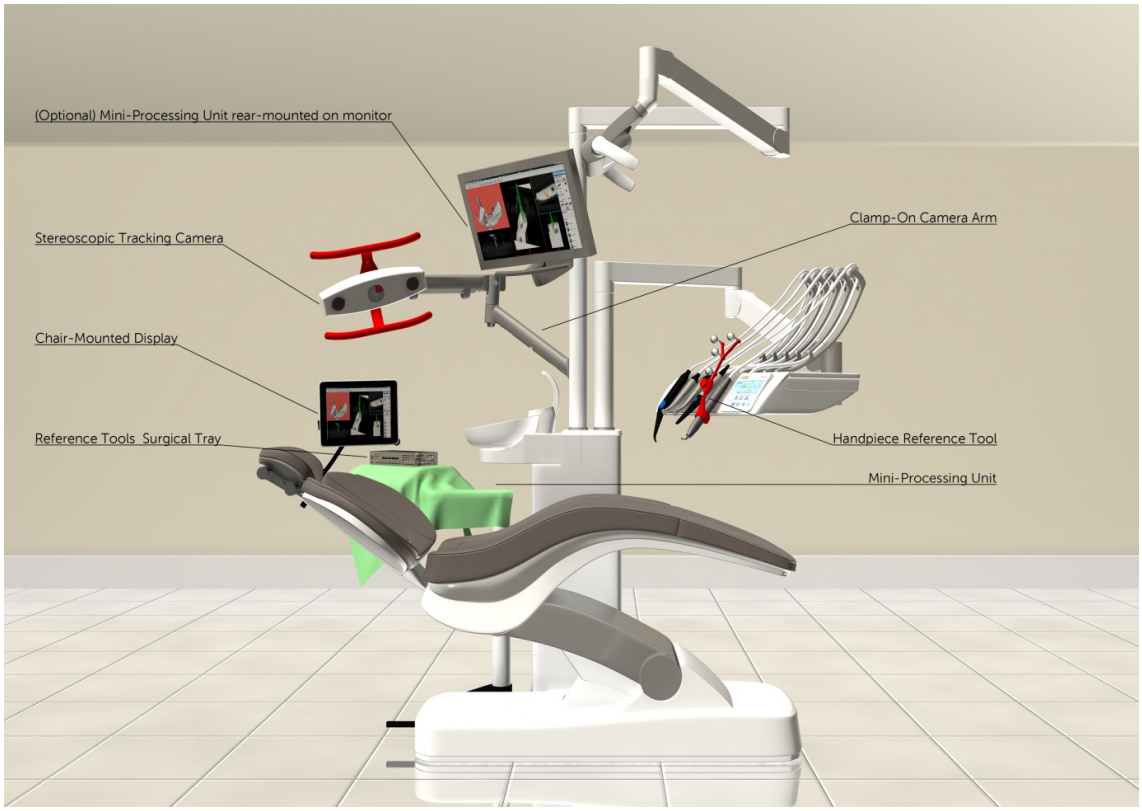

Fig. 6.21 Concept setup of the developed surgical navigation system, including tracking camera and wireless display, as it is being used in current clinical trials.

6.5 Conclusions

Feedback from the clinicians suggests how the pre-visualisation of the final prosthetics can help in the choice of the surgical site and the right angle of the implant insertion. Generally, the combination of guided surgery with a prosthetic plan is obtained through the use of radiographic templates which are then converted into surgical guides after being segmented in the tomographic scan.

The developed surgical navigation system inherits this useful feature from traditional computer-assisted surgery and introduces a number of advantages which promote higher accuracy in implant insertion, improved safety and better patient care.

Using this navigation system, surgeons can look inside the patient's bone accurately, in real time and while inserting an implant, without damaging surrounding nerves and eliminating the need to create a flap as generally required for inspecting bone quality. Differently from the navigation systems reviewed in Chapter 5, the proposed solution has been designed to be clinically relevant.

Fig. 6.22 Display device used to output the information of the navigation system during the in vivo trials performed at University of Bologna (Italy). A monitor was mounted on the dental chair broadcasting live images from the processing unit via a wireless connection.

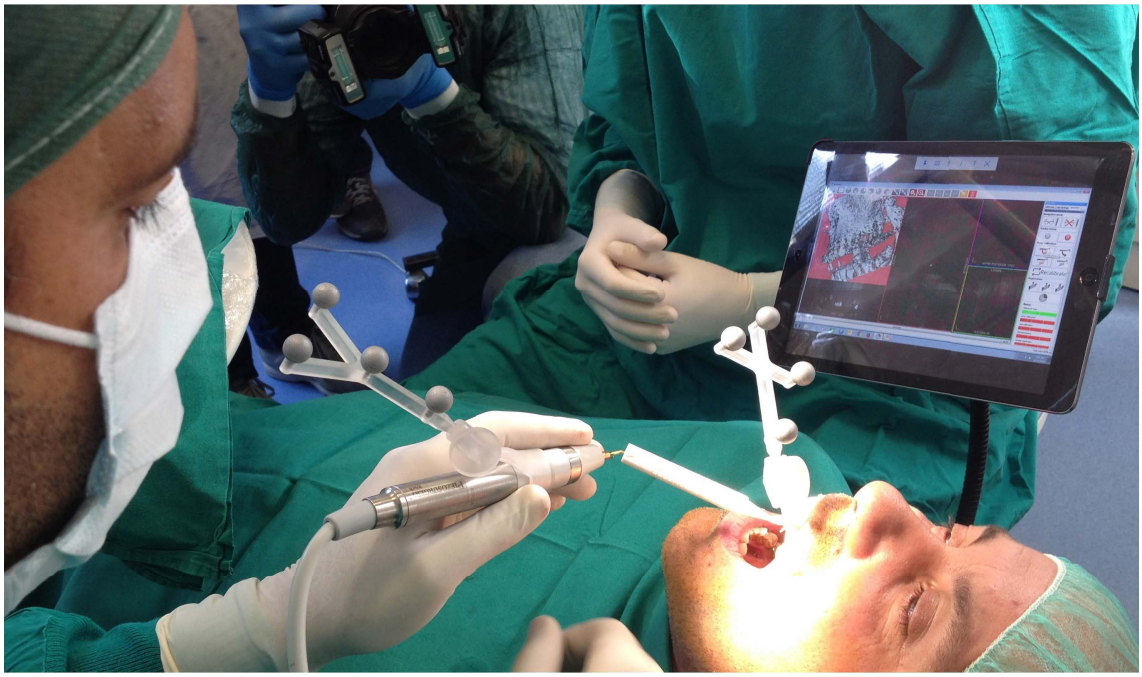

Fig. 6.23 Use of reference tool system on a Piezosurgery® (Mectron S.R.L., Italy) handpiece: the extra rotational degree of freedom offered by the "double-joint" allows moving the reflective balls towards the camera as required for maximising accuracy during tracking and reducing the possible interference with the surgeon's operations.

Most of the hardware components have been engineered to reduce their invasiveness on the patient and to be compatible with the dental surgery equipment the surgeons and dentists are already familiar with. Also the software presents innovative features which are currently not present on any existing device for surgical research or commercial applications for surgery planning.

The developed IGS is extremely easy to use and compatible to multiple surgical techniques, like Piezosurgery® or conventional drilling. Surgeons should be able to use navigation on any patient on a routine basis without having to replace their hardware. In the same appointment, they could make a diagnosis, plan the surgery and perform the implant insertion more accurately than using drill guides.

Because of the efficacy and easiness of use of the tools designed to interface the hardware with the software application, the system can also be used for educational purposes. In practice, the developed navigation and dental drill guide automatic design technology can be applied to bone replicas simulating a surgical procedure for training in a surgical skills laboratory.

Chapter 7

Pre-Clinical trials: application of a new intra-oral navigation system to piezoelectric surgery for three-dimensional implant site preparation

7.1 Introduction

Osseointegration is one of the main indicators of success and secondary stability of a dental implant. Using traditional drills, in which the cutting action is performed by the axial rotation of sharp blurs or flutes usually generates considerable heat which is then dissipated into the surrounding bone (Cordioli and Majzoub 1997; Mishra and Chowdhary 2014).

As stated earlier Piezosurgery® (Mectron S.r.l., Genova, Italy) is a modern surgical technique which allows for selective bone cutting or drilling via different ultrasonic frequencies acting only in hard mineralised tissues (Vercellotti et al. 2004, Pereira et al. 2014). It has been largely applied to osteotomy for alveolar bone crest expansion,

maxillary sinus lifting and dental implant removal which can be performed accurately and safely, providing excellent clinical and biological results. A recent application of Piezosurgery® has been proposed for dental implantology (Vercellotti 2014) specifically based on the availability of a dedicated set of curved inserts (see Figure 6.1). In particular, the differential preparation allows widening of a socket wall by a 3-dimensional cutting action which includes lateral movements.

Clinical studies reported show how, when compared to traditional drilling techniques, ultrasonic implant site preparation results in an increase of implant stability ISQ value with an earlier shifting from a decreasing to an increasing stability pattern (Stacchi, Vercellotti et al. 2013; da Silva Neto, Joly et al. 2014; Gandhi, Baker et al. 2014). This behaviour could be attributed to a more abundant irrigation reducing the generated heat and to the improved access to deeper bone during the socket preparation. It has been reported that as a consequence both primary and secondary stability are improved and the risk of postoperative necrosis is lowered (Jo et al. 2011; Tehemar 1999).

Other studies have examined how ultrasonic drilling can be more accurate when compared with conventional rotary instruments in terms of uniformity of the osteotomy cut (Stacchi et al. 2013, Scarano et al. 2014).

Also mixed traditional and ultrasonic techniques for implant site osteotomy have been clinically evaluated for implant placement, revealing that implant stability might develop faster (Vercellotti 2009, Canullo et al. 2014).

Because of the non-axial action, it is ideal if the implant socket is prepared through live tracking of the Piezosurgery® tip. Although based on ultrasonic vibrations, the Piezosurgery® surgical technique avoids the macrovibrations generated by conventional drilling allowing greater intraoperative control with higher safety in cutting difficult anatomical regions (Schaeren et al 2008, Bertossi et al. 2013).

In this context of reduced vibrations, if applied, a tracking system would facilitate the access to deeper cortical areas of the surgical site guiding the cutting action more accurately without damaging the mandibular nerve or the maxillary sinus.

A preliminary clinical study has been undertaken to evaluate the effect on osseointegration in deploying the surgical navigation system developed (described in Chapter 6) to guide the 3-dimensional socket preparation using a Piezosurgery® technique (Pellegrino et al. 2015).

7.2 Piezoelectric surgery for oral implantology

The piezoelectric effect consists in creating electrical tension on ceramic materials such as quarts when a mechanical pressure ("piezein" in Greek) is applied or vice versa.

Piezoelectric bone surgery is a technique for osteotomy and osteoplasty based on ultrasonic vibrations. This technique was created in response to the need to reach major levels of precision and safety in bone surgery, as compared to that available by the usual manual and motorized instruments. The first piezoelectric surgical instrument able to achieve more precision and safety in bone surgery, as compared to usual rotary instruments, is known as the Mectron Piezosurgery® Device. It is characterized by piezoelectric ultrasonic vibrations of a frequency of 29 kHz within a range of 60/200 Hz. Due to their characteristics, the microvibrations allow for selective cut of only mineralized structures without affecting soft tissues, which remain undamaged even in case of accidental contact. The precision of the cutting action, mostly in anatomically difficult areas, is enhanced by the micrometric vibration of the tips while the physical phenomenon of cavitation reduces the blood loss. Both of these characteristic tend to improve the safety of the surgical procedure (Vercellotti, 2004).

The cutting characteristics of piezoelectric surgery are mainly depending upon the degree of bone mineralization, the design of the insert being used, the pressure being applied on the handpiece and the speed of movement during usage (Yaman et Suer, 2013). Low frequency of vibrations may be chosen in low mineralized bone, while bone with high mineralization can be treated with frequencies up to 30 Hz. In terms of pressure, there are studies (Claire et al., 2013) which observed a reduction in oscillations and therefore in the cutting ability in case an excessive pressure is applied on the insert.

Depending on the shape of the insert being attached to the piezoelectric handpiece, this surgical technique can be used in different applications. Also the degree of irrigation and level of power are adjustable settings that should be set in accordance with the intended procedure (Vercellotti, 2004).

Applications of piezoelectric osteotomy in oral and maxillofacial surgery are multiple. It can be used in dento-alveolar procedures to prevent nerve damage while tooth sectioning is close to important anatomical structures. It can be deployed in sinus bone grafting surgery using a lateral approach which has been proven to minimise sinus perforation rates (Wallace et al., 2007). Piezosurgery® can be used in orthognathic surgery, for example for sagittal split ramus osteotomies, or in a very different specialty like tumour resection, without the risk of damaging delicate surrounding structures.

On the other hand, the use of piezoelectric surgery is not recommended for patients with pacemakers and it extends the duration of the surgical procedure (Yaman & Suer 2013).

In particular, implant site preparation can be performed with a specifically designed set of Piezosurgery® inserts (Figure 6.1) consisting in a cutting tip and an internal canal where irrigation is delivered to the site cooling off the bone during the preparation.

With the “differential ultrasonic socket preparation” (see Figure 6.2) introduced by Vercellotti (2009), piezosurgical site preparation allows for the selective enlargement of only one socket wall.

7.3 Materials and Methods

7.3.1 Surgical plan

Surgical planning is performed within the software application developed (Figure 6.3) for the surgical navigation system on a three-dimensional model reconstructed from a Cone Beam Computed Tomography scan.

The clinician or the dentist is facilitated in positioning the implant in its ideal site by placing landmarks for respectively the entry point and the apical point of the insert in a

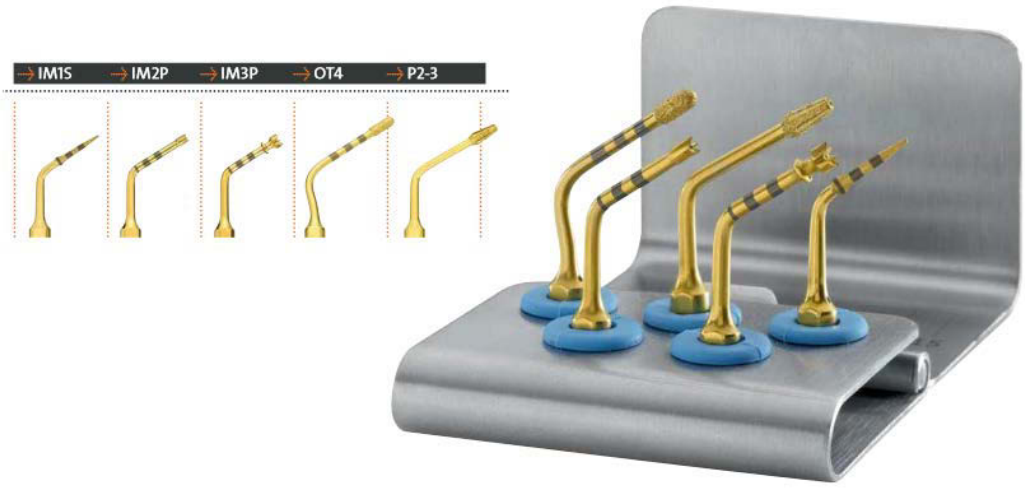

Fig. 7.1 Piezosurgery® kit for dental implantology and relative sequence of utilisation (source: www.dental.mectron.com/)

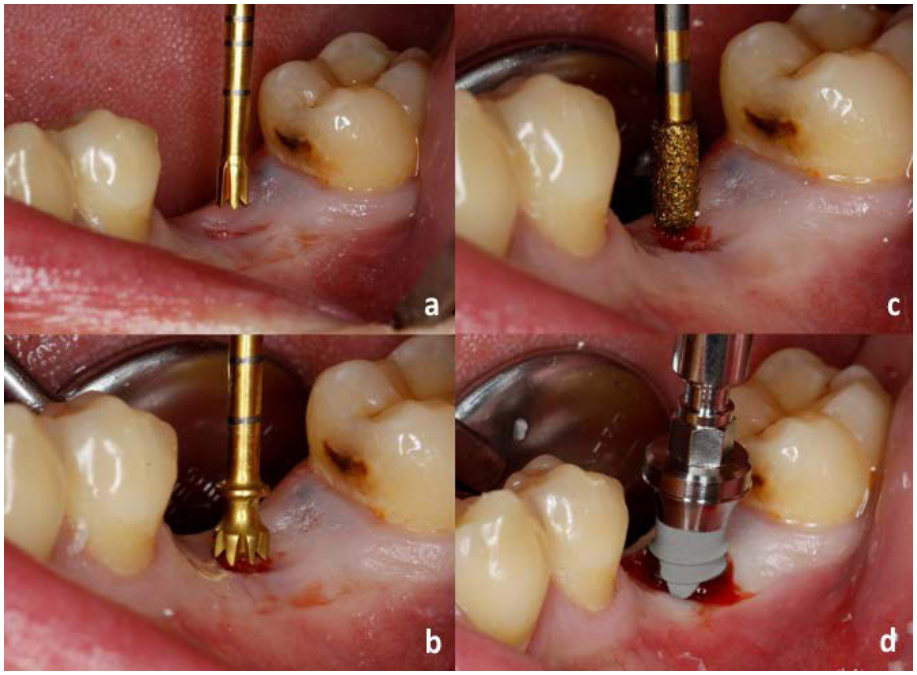

Fig. 7.2 Socket preparation (a,b,c) and implant insertion (d) using Piezosurgery® differential preparation (From Yaman 2013).

vestibulo-lingual volume slice. Then desired insertion and apex point of the implant is picked in the central slice and, as a result, the best fitting implant from the library is pre-visualised in place. The position of the implant can then be refined by the use of "gizmos" (which are handles used for translation and rotational transformations). At this point the user checks the proximity of the implant with the alveolar nerve (in case of mandibular implants) or the sinus floor/walls and the planned implant primary stability by anchorage with deep cortical bone. (Figures 7.3 and 7.4). During the surgical planning stage the

Fig. 7.3 Surgical plan using the developed compound view of the software application, composed of a three-dimensinal view (a), a panoramic view (b), a vestibule-lingual volumetric cut (c), an anteroposterior (d) and an axial (e) slice. The central vestibulo-lingual volume slice (c) is moved perpendicularly to the panoramic profile using the yellow handle in the orthopantomographic view (b). Then desired insertion and apex point of the implant is picked in the central slice and as a result the best fitting implant from the library is pre-visualised in place.

optimal position for the implants is evaluated according the virtual representation of matching prostheses which are loaded from an internal software library and superimposed to the tomographic data.

7.3.2 Calibration

Tips for piezoelectric handpiece are characterized by a curved shape to facilitate the application of a mild pressure by the user.

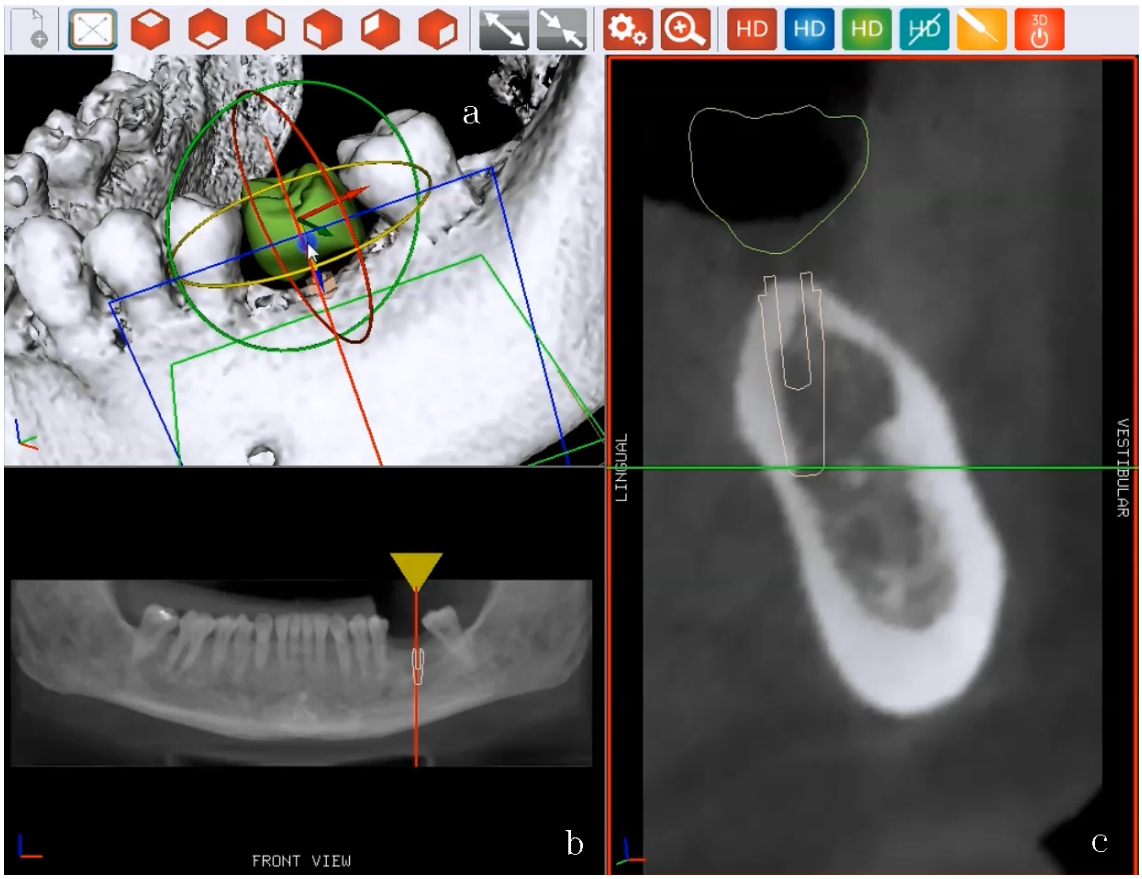

Fig. 7.4 Virtual tooth function: after being selected from a library of prostheses, the virtual tooth is displayed in axis with the planned implant with a default offset in the vestibule-lingual view (c). The user can modify the position of the implant by dragging transformation handles shown in the three-dimensional view (a). The contour of the virtual tooth can also be explored by dragging the yellow handle in the orthopantomographic view (b).

Being the cutting region located in the distal straight section of the tip, calibrating the piezoelectric insert for navigated surgery results in identifying the pivoting point of the tip and the axis of the cutting surface.

Given the multiple axes of symmetry of the Piezosurgery® inserts as opposed to the straight tips for contra-angle handpieces, a special tool has been designed to allow the calibration and therefore the correct virtualisation of the tips into the 3D rendering environment (Figure 7.5). Because of its complex internal design, a prototype for the calibration tool has been manufactured via Selective Laser Sintering using EOS P380 machines by Advanced Manufacturing Services (Sydney, NSW Australia).

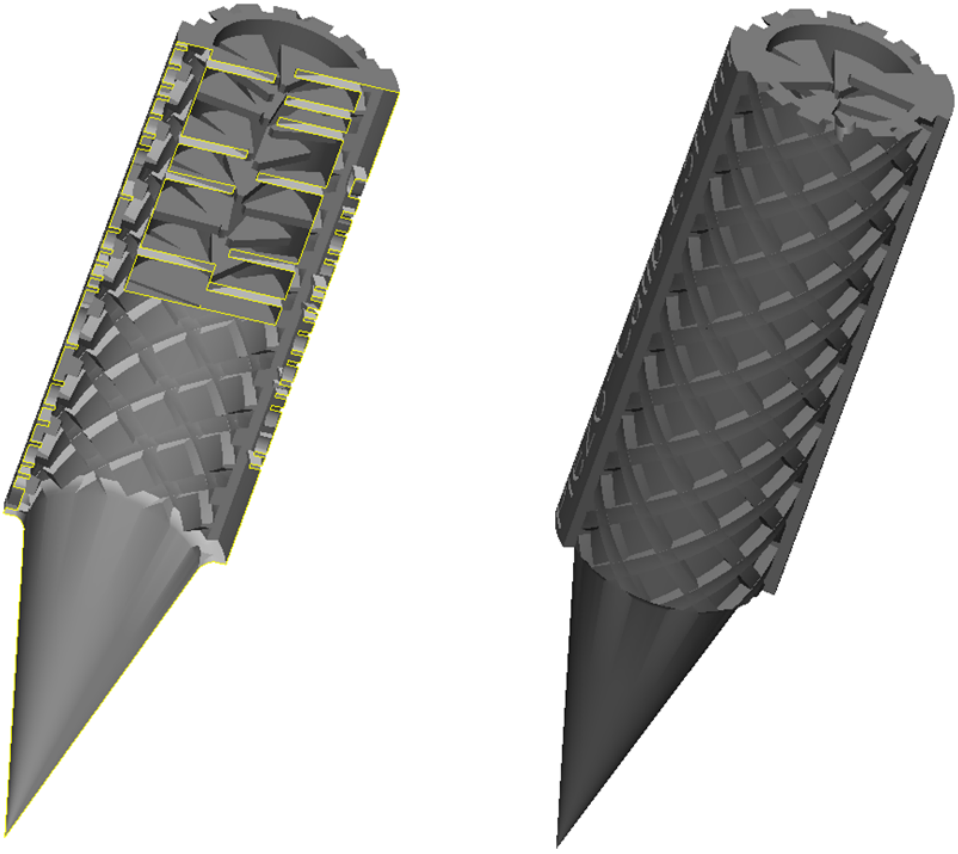

Fig. 7.5 Curved tip calibration device (right) and its section (left) showing the internal spiral teeth structure used to keep the tip in axis with its apical cutting section when inserted.

7.3.3 Patient-scan registration

Following the calibration procedure the position of the implant site is registered with the three-dimensional model used to virtually plan the surgery.

Both the patient and the surgical handpiece are equipped with a minimally invasive optical reference frame (Figure 7.6) supporting markers which are reflecting the infrared light from the stereoscopic camera NDI Polaris Vicra (Northern Digital, Canada). Image-

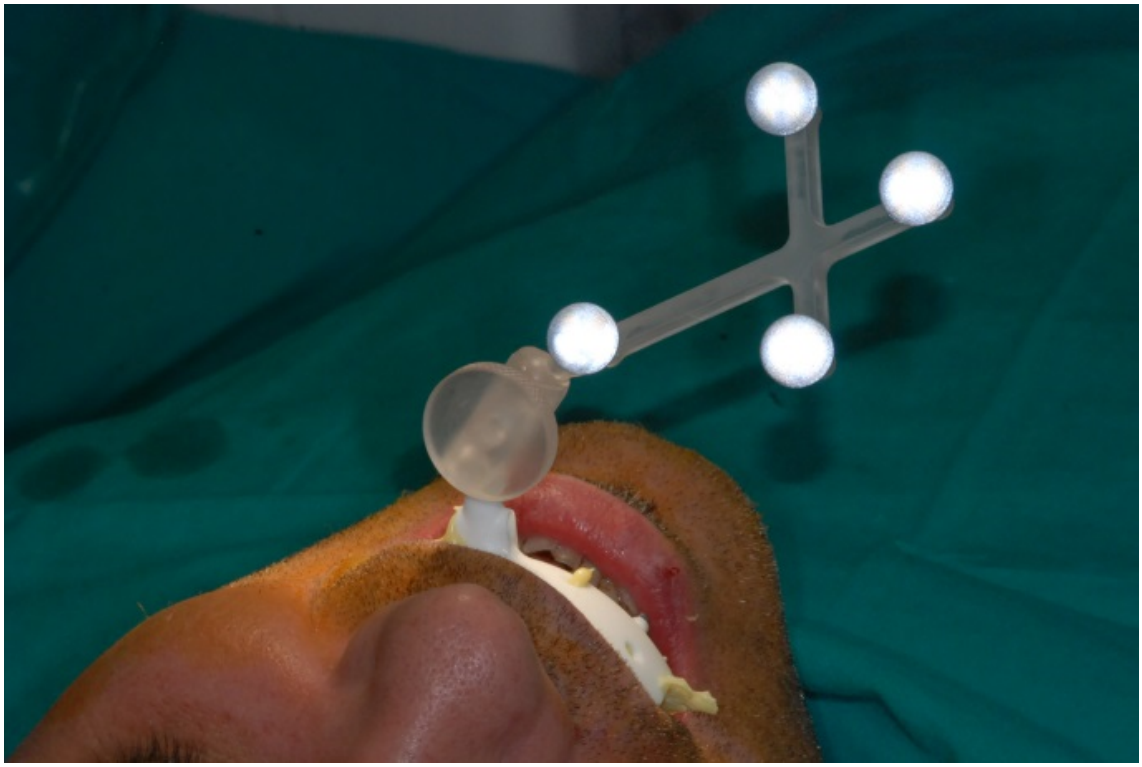

Fig. 7.6 Reference frame supporting the plastic reflective balls tracked by the stereoscopic camera. The frame is linked via a 3D joint to the teeth-supported radiopaque reference plate.

to-world registration is performed using radiopaque Titanium screws whose position as probed by a calibration tip is matched with the surface identified in the software registration operation. The radiopaque references are embedded in the calibration plate which is teeth-supported for the case of partially edentulous patients or bone-supported via a temporary fixture in the case of a fully edentulous patient.

The registration procedure consists of touching three-points with the tip mounted on the handpiece. Because of the curved nature of the tips, axis calibration is performed identifying the axis of the distal end of the ultrasonic tip.

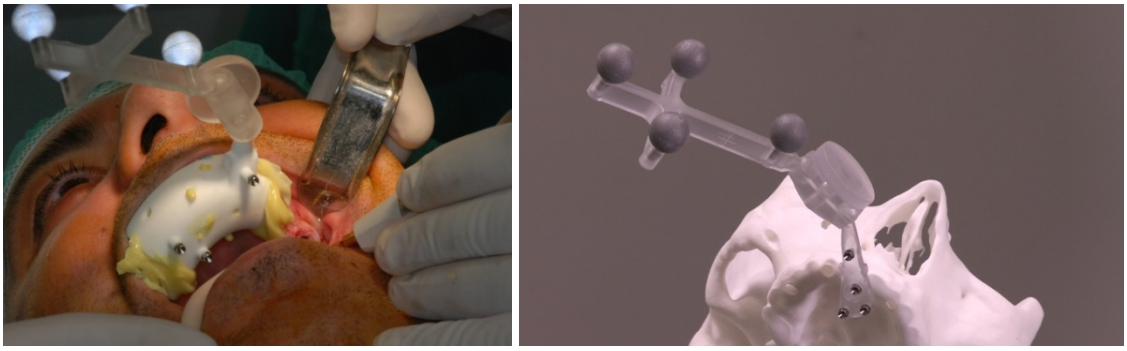

Fig. 7.7 Different reference plates respectively used for partially edentulous patients (left) and totally edentulous patients (here shown on a bone replica on the right).

7.3.4 Surgical technique and cases

The setup described in the previous sections allows the surgeon to follow in real time via LCD display the increasing depth of the cutting action of the surgical tips.

The first preparation on the implant site is performed via the surgical bit IM1S. Differently from straight tips commonly used for implant socket preparation, IM1S presents a very pointy termination (radius < 0.5mm). Because of its sharpness and its vibrating action as opposed to a rotary one, using IM1S allows preparing deep cortical bone without risk of sliding along the cortical wall. Sliding along the inner wall would, in fact, generate a deviation from the planned socket axis (Figure 7.8). Once the socket has reached the desired penetration, using the OT4 insert the surgeon performs a progressive circumferential border preparation until the desired depth. During this action the surgeon shapes the socket as the virtual volume occupied by the planned implant by way of radial extensions according to the feedback from the navigation system. This innovative technique has been deployed in five clinical cases undertaken at University of Bologna as part of the ImplaNav01.14 clinical trials protocol approved by the University Ethical Committee.

In one of the five cases the implant site was a thin crest posterior mandible, where traditional socketing procedures often result in a shifting of the implant due to the contact between the drill tip and the lingual mandibular wall (Figure 7.8 top). In this case with the use of the piezo-navigated technique the surgeon could perform a combined differential preparation (Figure 7.8 bottom) which mainly consisted in a selective preparation of the lingual cortical wall using the IMS1 and IM2P inserts. This procedure proved to be more

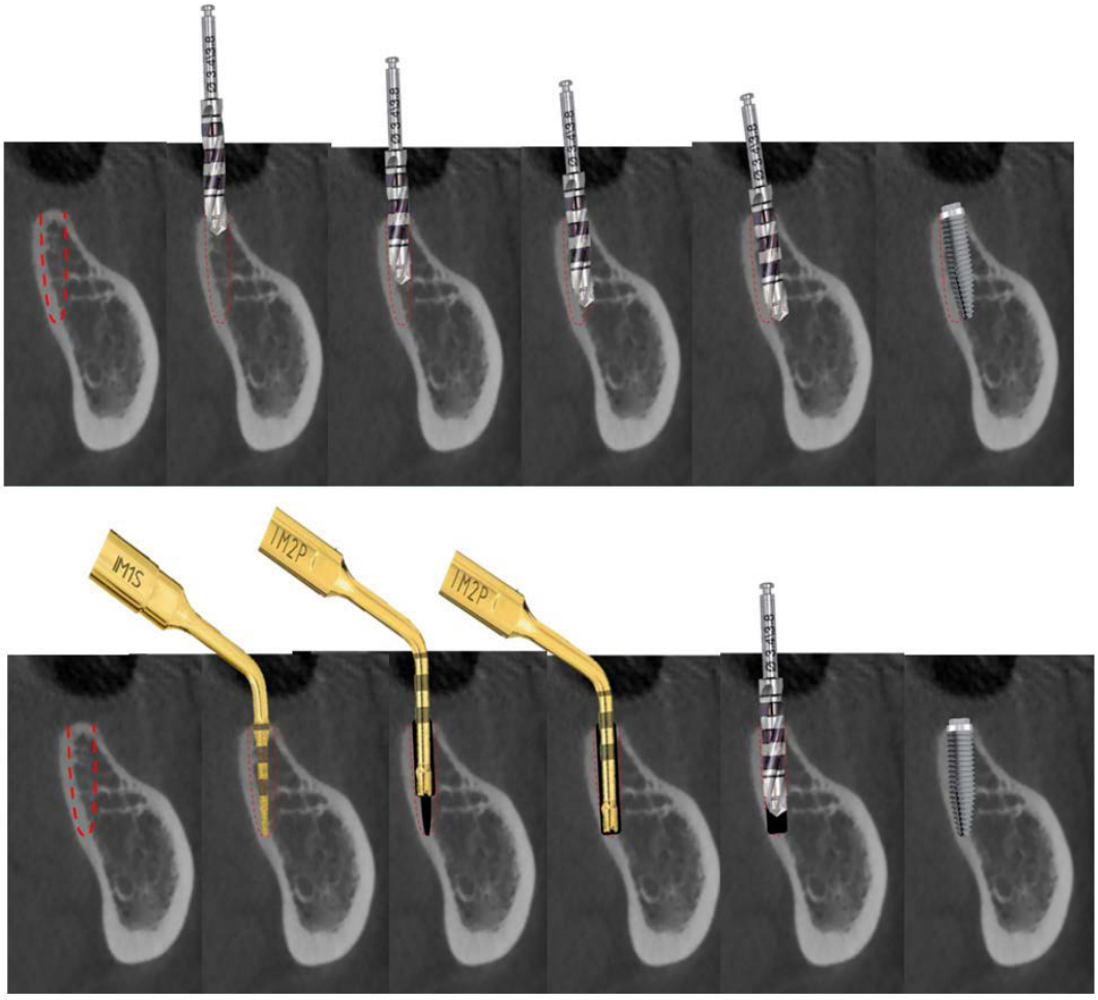

Fig. 7.8 (Top) implant shift due to the contact between the tip and the lingual cortical wall; (bottom) differential preparation using a combined piezoelectric and traditional preparation. The last picture of the right shows the position which the implant would reach with (top) or without shift (bottom).

accurate, safe and agile than the use of rotary instruments which were only utilised as part of the last step to refine the shape of the implant socket.

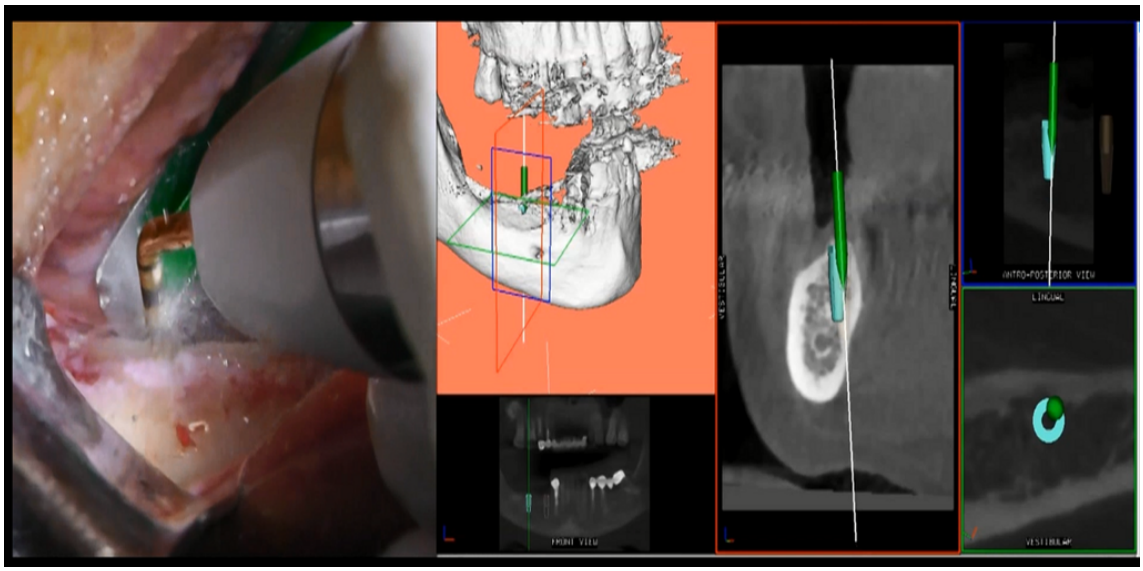

Fig. 7.9 Software interface showing the selective preparation of the lingual cortical wall using the IMS1 and IM2P inserts.

In another case of a flapless posterior mandibular site, the surgeon used a full piezo-navigated preparation. Using only two Piezosurgery® inserts, IMS1 and OT4 (Figures 7.9 and 7.10), the socketing procedure was completed via a three-dimensional approach, by way of visualising the live tracked position of the Piezosurgery® tip and the volume of the virtually planned implant on a wireless digital display mounted near the patient's head.

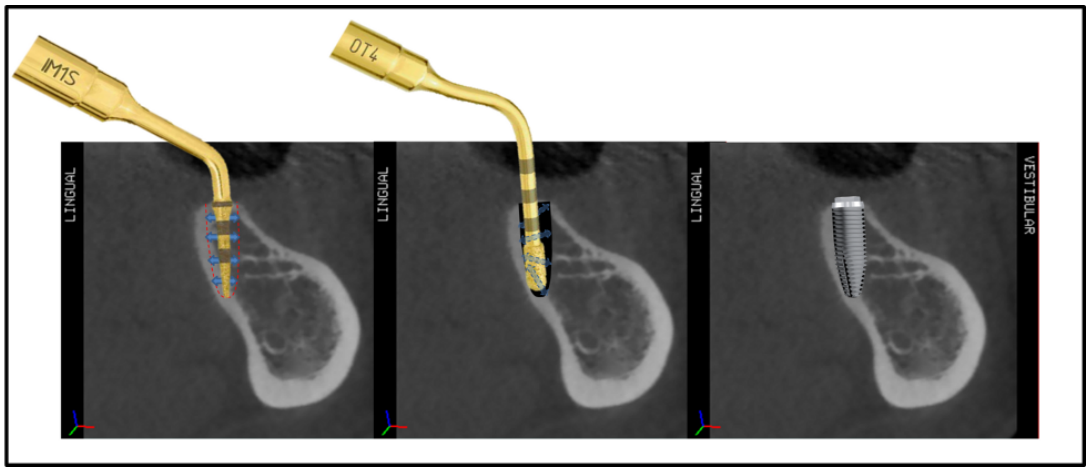

Fig. 7.10 Different steps of a full piezo-navigated implant site preparation using only two Piezosurgery® inserts, IMS1 and OT4, and a three-dimensional approach.

After the socket preparation the implants were positioned via a contra-angle handpiece at

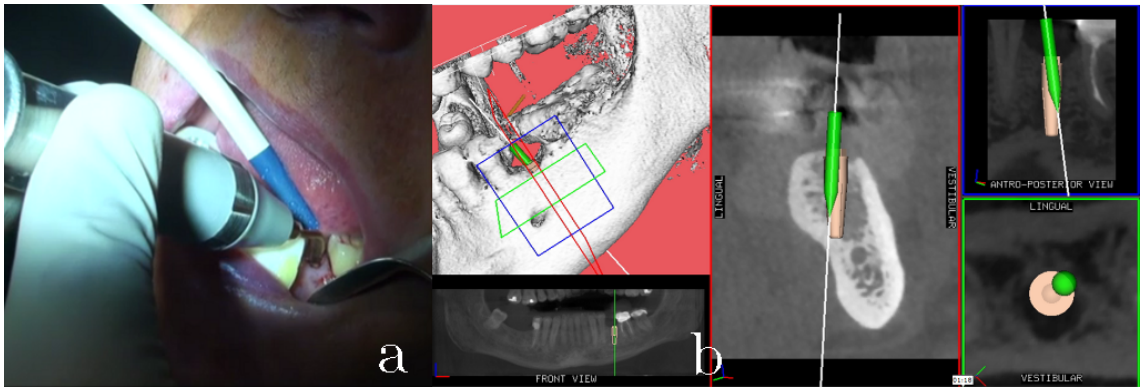

Fig. 7.11 Contextual visualisation on a digital display of the position of the Piezosurgery® tip while tracked live on the patient (a) and the virtually planned implant in the software interface (b).

40rmp with torque exceeding 40Ncm. The depth of the implant insertion could also be tracked on the software against the virtually planned position, as shown in Figures 7.11 and 7.12.

External hexagonal head implants manufactured by Southern Implants (Irene, South Africa) were used for all surgical trials.

Fig. 7.12 Live tracking of implant insertion: the implant is selected from a library within the software application compound view, composed of a three-dimensional view (a), a panoramic view (b), a vestibule-lingual volumetric cut (c), an anteroposterior (d) and an axial (e) slice. The physical position of the implant is updated in real time while being inserted by a driver.

7.3.5 Accuracy evaluation

The accuracy of the procedure was evaluated comparing the software-based surgical plan with post-operative topology derived from the Computed Tomography. The inserted implants were segmented from CT/CBCT scan using the OpenMAF platform (Ansaloni et al. 2007; Viceconti et al. 2002) and the volumes from the pre-operative and post-operative models were aligned using an N-point registration module within the software application.

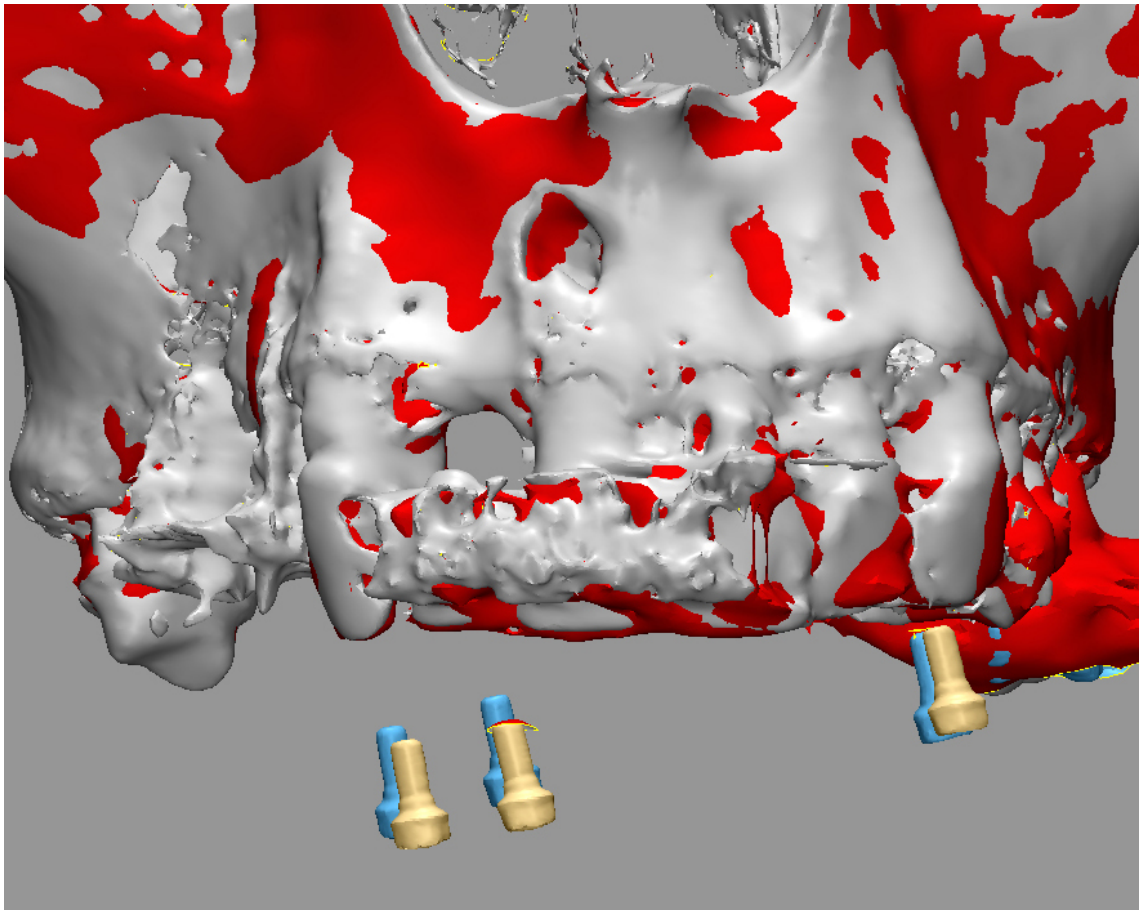

Fig. 7.13 Alignment of the pre-operative scan (canvas of the virtual planning) and the post-operative volume. The radiopaque Titanium screws are used to locate the N-points used by the registration algorithm.

This software module is a modification of the one designed for the image-to-world registration. The clinician is asked to pick three surfaces respectively in the pre-operative scan (on which the surgical plan is performed) and in the post-operative one. Because this software module runs an algorithm which calculates the top surface point of the selected region as an offset from its centre of gravity, the author has chosen to deploy the same

radiopaque Titanium screws used during the patient-registration operation (see Figure 7.13).

At a later stage the deviation of each planned implant with respect to the segmented post-operative implant profiles was evaluated using two methods. The first one is a dedicated function in Geomagic Studio 12.0 (Geomagic, Inc., North Carolina, USA) which computes all point-to-point distances and calculates an average deviation quantity. The additional method is identifying the Euclidean distance between the 3D coordinates of entry position and apical point for each pair of implants.

These two reference points were identified using the OpenMAF software application. A three-dimensional meter module was used to measure the desired distances.

Measures of deviations were repeated using 3-matic (Materialise, Leuven, Belgium). The "N-point Registration" module was used to align the virtual plan with the post-operative volume and measurements were repeated for the entry and apical points of the implants to ensure consistency with the results obtained through the OpenMAF software platform.

7.3.6 Post-operative corrections

In some case the post-operative scan was taken 2 to 5 weeks after the surgical procedure. In the meanwhile a healing screw (WBN, Southern Implants) had been positioned on top of the implant. For this reason the offset generated by the screw in the segmented surfaces had to be corrected to match the length of the implant. This operation was performed in 3-matic using a temporary cutting plane perpendicular to the inertia axis of the implant surface, as shown in Figure 7.14.

7.4 Results and Discussion

A total of 5 dental implants placed in 5 adults were evaluated. Each patient was treated in either his mandibular arch or his maxilla. During postoperative healing all implants

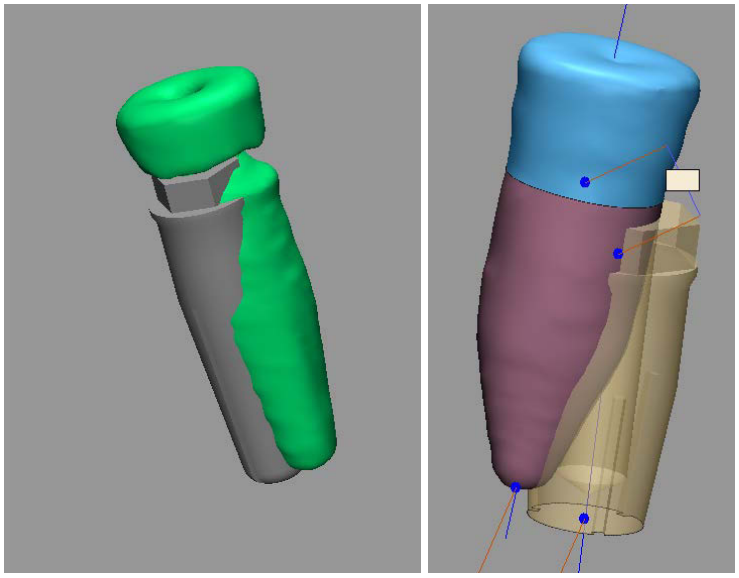

Fig. 7.14 Superposition of post-operative implant with planned implant showing how the segmented surface includes a healing screw (top abutment) which needs to be specifically removed (blue surface on the right) in order to perform a correct deviation evaluation.

osseointegrated successfully without complications. Accuracy evaluations were performed on all the osseointegrated implants.

For the present study, the analysis of the point-to-point distances for the 5 implant insertion on 5 different patients reported an average deviation of 0.90+/-0.07 mm. Results, which are reported in detail in Table 7.1, also show a mean deviation to the implant head (insertion point) of 1.05+/-0.39 mm and 1.26+/-0.30 mm for the implant apex.

Maximum lateral errors were calculated to be 1.51mm for the insertion point and 1.62mm for the apical point.

With respect to the centre of gravity coordinate deviations, the results showed a mean Euclidean deviation of 0.86+/-0.21mm.

A statistical analysis could not be performed due to the small number of patients enrolled in this preliminary study. Results were compared to clinical studies on humans reported by Jung et al. (2009) in their review which covered recent computer technology applications in surgical implant dentistry. In this extensive review Jung analyses 29 different image guidance systems via a selection of 13 clinical and 19 accuracy studies. Among his results, we selected the ones relative clinical cases performed using image-

Table 7.1 Results of the comparison between planned and placed implant position in terms of implant's head and apex lateral deviations (Dx and Dy) and Euclidean distance (3D), obtained by overlapping the pre- and post-operative Computed Tomography scans. Units are **mm**.

		Insertion Point				**Apex Point**				**Barycenter**
Impl. #	Position	**3D**	D_x	D_y	D_z	**3D**	D_x	D_y	D_z	**3D**
1	45	1.8	0.97	0.16	1.51	1.71	1.62	0.07	0.54	1.73
2	36	0.77	0.33	0.56	0.42	0.8	0.64	0.29	0.38	0.9
3	36	0.88	0.28	0.82	0.16	1.29	1.19	0.38	0.31	0.74
4	26	0.75	0.06	0.15	0.73	1.4	0.07	1.1	0.86	1.07
5	26	1.05	0.62	0.85	0.12	1.09	0.78	0.7	0.28	1.29
Mean		**1.05**	0.97	0.85	1.51	**1.26**	1.62	1.10	0.86	**1.15**
SD		**0.39**	0.31	0.31	0.51	**0.30**	0.52	0.36	0.21	**0.34**

Table 7.2 Extracted data on accuracy of two different image-guided surgery systems for oral implantology: the publications are all reporting clinical evaluations undertaken on living human subjects.

					Error entry (mm)			Error apex (mm)		
Study	**Year**	**System**	**Sites**	**Direction**	**Mean**	**SD**	**Max**	**Mean**	**SD**	**Max**
Wittwer et al.	2006	Treon	80	3D	1.2	0.8	3.4	0.8	0.6	2.0
Wagner et al.	2003	VISIT	32	Lingual	1.0	0.5	2.6	1.3	0.9	3.5
				Buccal	0.8	0.3	2.1	1.1	0.9	3.4
Wittwer et al.	2007	VISIT	32	Buccal	1.0	0.5	2.0	0.6	0.2	0.9
				Lingual	0.7	0.3	1.2	0.7	0.3	1.0
		Treon	32	Buccal	1.0	0.5	2.4	0.8	0.6	2.0
				Lingual	1.2	0.8	3.4	0.7	0.5	1.6

guided surgery systems other than surgical templates with pre-drilled sockets in axis with the planned implants. Table 7.2 summarises the results from the selection of cases.

The performance of the developed navigation system seems to align with both the one of the Treon navigation system (Medtronic, Dublin, Ireland) and the VISIT navigation system (University of Vienna, Austria) for navigated implant insertion as per the studies published respectively by Wittwer (2006) and Wagner (2003).

The application of the piezo-navigation technology facilitates the use of a smaller diameter insert for the lateral and vertical preparation of the implant socket, promoting a more abundant and deeper irrigation of the osteotomy area.

Implant site preparation using a navigated piezo-surgery approach might be the key for the improvement of the primary stability of the implant.

In fact, the ability to access lower trabecular regions of the bone would strengthen the deeper implant anchorage while keeping low the pressure acting on the upper implant-cortical bone interface where generally re-absorption phenomena related to the implant buccal-lingual inclination occur (Ramaglia, Toti et al. 2015).

This biomechanical advantage has been proven in Chapter 3 using a comprehensive finite element model of the human mandible during clenching.

If tracked in real time over the tomographic scan, the surgeon can selectively prepare deeper regions of the cortical walls like the mandibular lingual wall or the oblique walls of the maxillary sinus floor while damage to the surrounding soft and neurovascular tissues can be drastically reduced by the use of Piezosurgery® (Schaeren et al 2008, Pereira et al. 2014).

As demonstrated in this work, when navigation is combined with ultrasonic drilling and in particular with a three-dimensional differential preparation, the number of the inserts used for socketing can be easily reduced. If specifically designed, one insert only could be deployed for the whole procedure.

Moreover, the possibility of horizontal movements during a lateral preparation promotes more control over the socket's geometry in case of narrow bone crests and according to the morphology of the vestibulo-lingual walls.

In addition, being able to use an insert which is considerably smaller than the socket in both lateral and vertical movements allows a more generous irrigation of the socket itself up to its floor.

7.5 Conclusions

As per advantages related to the use of an image-guided surgery system specialised in oral implantology, it is reasonable to conclude that surgical navigation allows a deeper and more accurate preparation of the implant site which is performed according to the pre-operative virtual surgery planning.

Differently from the use of surgical drill guides, and because of the live feedback from the tracking procedure, diameter and orientation of the socket can be dynamically changed during surgery with respect to the virtual planning, whether poor bone quality, pathological or anatomical anomalies are exposed.

Because this technique can be used with standard drill tips, it becomes more useable for posterior areas where limited mouth opening might limit the access to the extenders required by drilling through the drill guides.

Lastly, because the surgical planning and the live tracking are performed within the same software application, the surgeon can decide to modify the optimal position of the implants at any time or even use a free-navigation module which allows to inspect the morphology and density of the surgical site below the tracked surgical instrument, dynamically.

More clinical studies are being undertaken to evaluate the long term efficacy of this procedure.

Chapter 8

Major contributions of the thesis to science and knowledge

(A) This is the first **patient-specific biomechanically correct** FEM of the human mandible which derives local material stiffness (Young's modulus) from CT scan data by applying both critically selected and novel relationships between Hounsfield Units, local densities and Elastic Moduli. This includes the introduction of an empirical "inverse approach" discussed in Chapter 2 which is aimed to further improve the realism of the simulation.

(B) This FEA model is unique as the implants are positioned in the mandibular bone according to a clinically validated surgical plan, guided by three main purposes of:

- Selecting the surgical sites according to a dynamic inspection of the bone density from the tomographic data through the developed software application interface
- Minimising the interference with delicate anatomical structures by controlling the virtual implant position in the radiographic images
- **Determining the best surgical technique and clinical approach for a full-arch denture restoration**

(C) In this model the results obtained for stresses and distortion relative to the implants and the adjacent bone tissues are discussed in terms of their biomechanical impact for **implant osseointegration** and therefore success/failure.

(D) This work was directed to design an innovative surgical navigation system with a combined software/hardware solution for dental implantology, which is unique in its applicability to multiple surgical techniques including ultrasonic implant socket preparation.

(E) By applying the developed navigation system and as a result of the reduced invasiveness of piezoelectric drilling, this research supports the use of alternative surgical techniques against previous published studies which includes the use of smaller implants with bi-cortical anchorage as opposed to longer axial implants and the use of angled implants in posterior regions of the mandible as opposed to more anterior implants. The superior biomechanical advantage achieved using these techniques was supported by the results of finite element simulations.

(F) The developed **navigation system** is the first system in the world to propose tools for patient specific anatomy and tomographic scan that are analysed through a dedicated Finite Element Model with the capability to prevent bone damage due to accidental interference during surgery.

(G) The FEA model developed has also identified that a miniaturised component can be used to support the frame without exposing the surrounding bone to additional risk of fracture or tear. A novel clinical procedure has been designed, consisting of the temporary insertion of one mini-implant to support the assembly necessary to provide optical and radiopaque reference to respectively the tracking camera and the registration operation for the intra-surgical navigation system.

(H) The results from the presented FEM of the mandible applied to novel surgical techniques and surgical navigation have contributed to initiate Clinical Trials which are currently being conducted at University of Bologna (Italy).

In conclusion, the research work presented in this thesis has produced an output of a logical and organic union between an accurate and realistic FEM and a revolutionary navigation system for dental implantology. This unique combination has resulted in clinically relevant surgical techniques being developed which are currently being used by dental surgeons to promote surgical accuracy and implant longevity, to reduce operational invasiveness and to improve patient care.

Glossary

Abutment	A connector placed on the top of a dental implant to connect the implant to the replacement tooth
AP	Antero-posterior
API	Application Program Interface, consisting in a set of routines, protocols, and tools for building software applications
Ascii	American Standard Code for Information Interchange: it is a character encoding standard
Bezier curve	Parametric curve frequently used in computer graphics
Bulk Modulus	Relative change in the volume of a body produced by a unit compressive or tensile stress acting uniformly over its surface
CAD	Computer Assisted Design
CAS	Computer Assisted Surgery
CBCT	Cone Beam Computed Tomography
CT	Computed Tomography

CT number	Normalized value of the calculated X−ray absorption coefficient of a pixel in a Computed Tomography scan, expressed in Hounsfield units, where the CT number of air is −1000 and that of water is 0
DICOM	Digital Communication in Medicine
Edentulous	Lacking teeth
FE	Finite Element
FEA	Finite Element Analysis
FEM	Finite Element Model
Fiducial marker	Radiopaque object used for aligning the physical patient position with the reconstructed volume
FMP	Fiducial Markers Plate
FMT	Fiducial Markers Tray
Gizmos	Handles used for translation and rotational transformations in software applications
GUI	Graphic User Interface
HU	See “CT number”
IGES	Initial Graphics Exchange Specification
IGS	Image Guided Surgery
Image-to-world Registration	Software process of aligning the physical patient position with the reconstructed volume
IS	Inferior-superior

Isosurface	Surface that represents points of a constant CT number within the reconstructed volume
ML	Medial-lateral
Non-manifold (geometry)	Essentially geometry which cannot exist in the real world, for example by allowing disjoint lumps to exist in a single logical body
MRI	Magnetic Resonance Imaging
NURBS	Non-uniform rational B-splines
OPRF	Optical Patient Reference Frame
OPRT	Optical Patient Reference Tray
Piezoelectric surgery	Technique used for osteotomy and osteoplasty based on ultrasonic vibrations.
Poisson ratio	Fraction of expansion divided by the fraction of compression for small values of these changes
Radiopaque	Opaque to X-rays
Segmentation	Process of partitioning a radiographic image into multiple segments which are easier to analyse or combine in a three-dimensional object
STEP	CAD file format, usually used to share 3D models between users with different CAD systems
Surgical navigation (dynamic)	Procedure for assisting a surgical intervention by using a computer-based system which tracks in real time the position of a surgical instrument against the patient's anatomical structures

Surgical navigation (static)	Procedure for assisting a surgical intervention by using surgical drill guides (templates)
VME	Node in an OpenMAF software application hierarchical tree which features a procedural core and generates an output data structure storing a pose matrix and a visual dataset
VMEmesh	Volumetric data structure in an OpenMAF software application tree able to store scalars for each voxel in the volume
VMEVolume	Node representing a reconstructed volume in an OpenMAF software application tree
VTK	The Visualisation Toolkit (www.vtk.org)
Young Modulus	Material parameter which describes tensile elasticity, which is the tendency of an object to deform along an axis when opposing forces are applied along that axis; it is defined as the ratio of tensile stress to tensile strain and it is often referred to simply as the elastic modulus

Appendix A

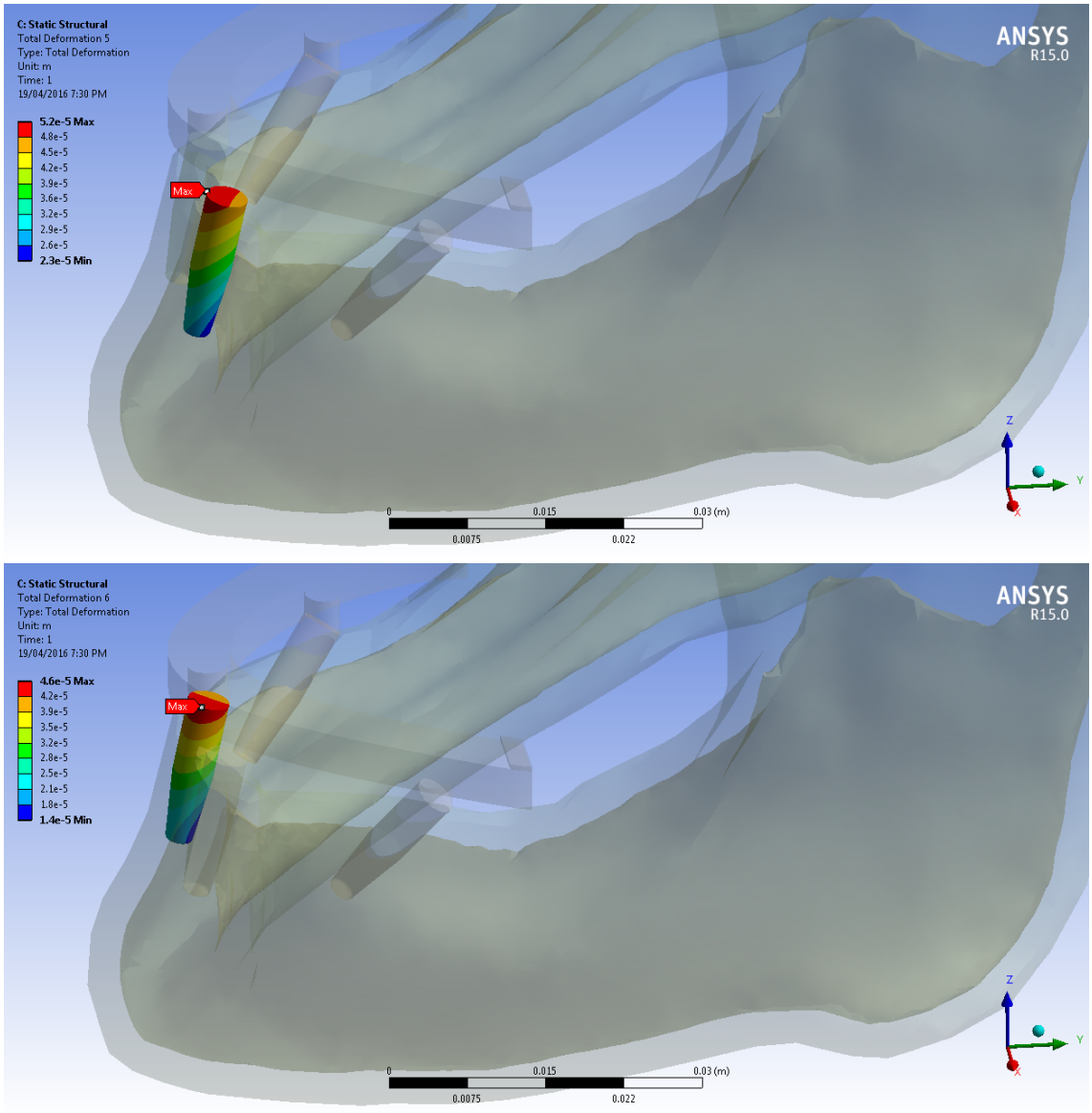

Fig. 1 Model I4: deformation of anterior left (top) and right (bottom) implants in complete muscle load set biomechanical configuration.

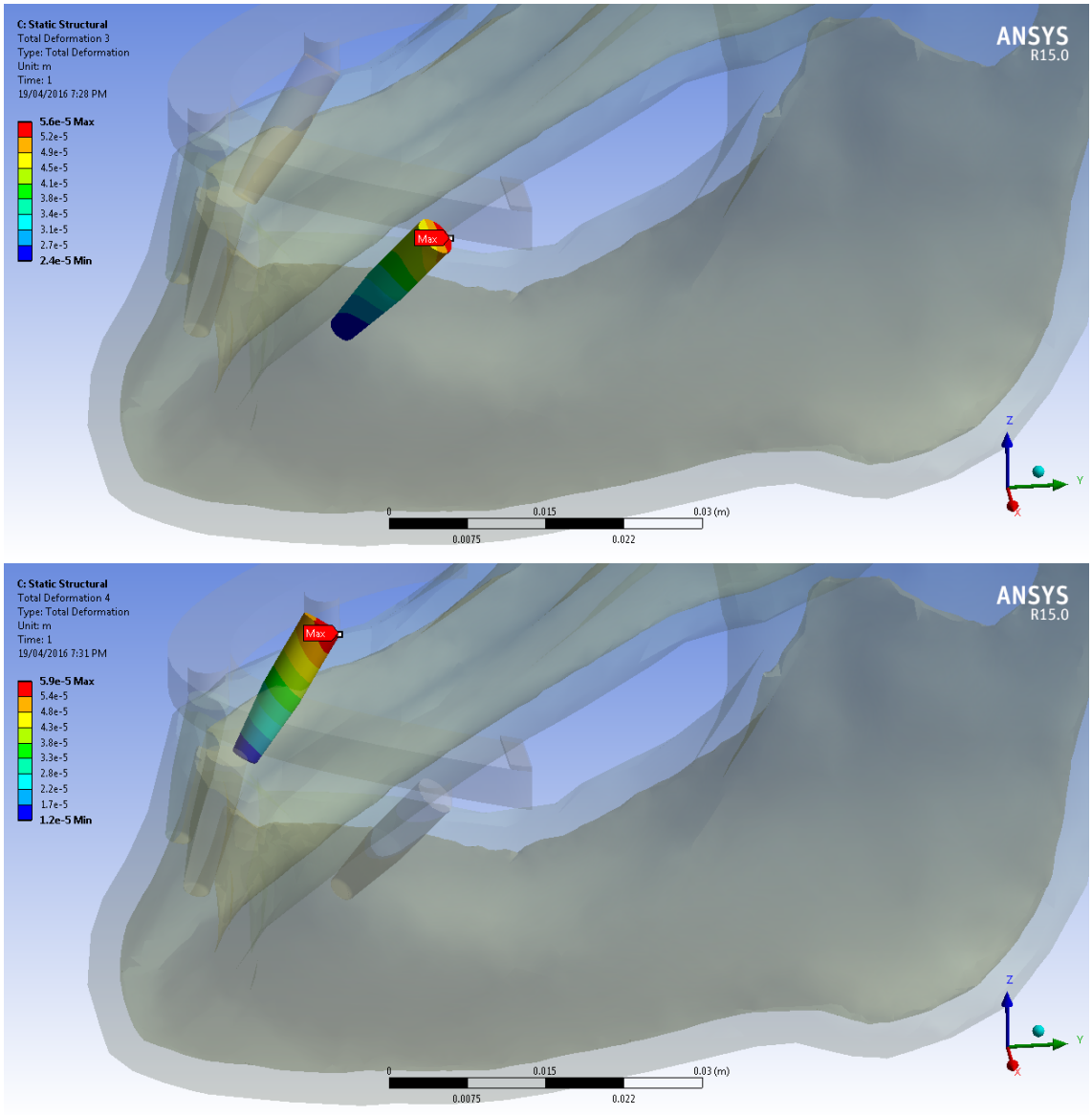

Fig. 2 Model I4: micro-motions of posterior left (top) and right (bottom) implants in complete muscle load set biomechanical configuration.

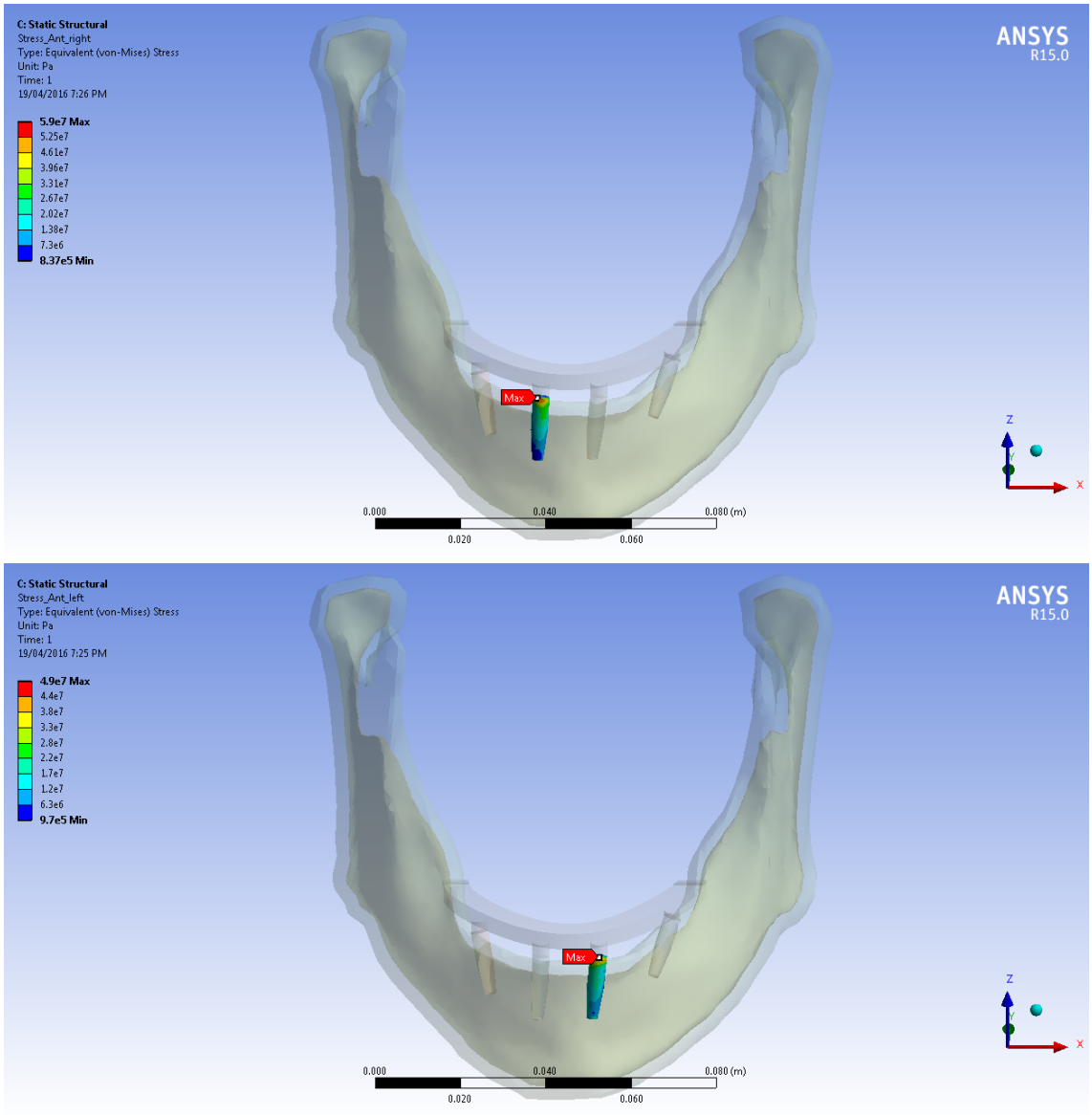

Fig. 3 Model I4: equivalent (von Mises) stress recorded for anterior right (top) and left (bottom) implants in complete muscle load set biomechanical configuration.

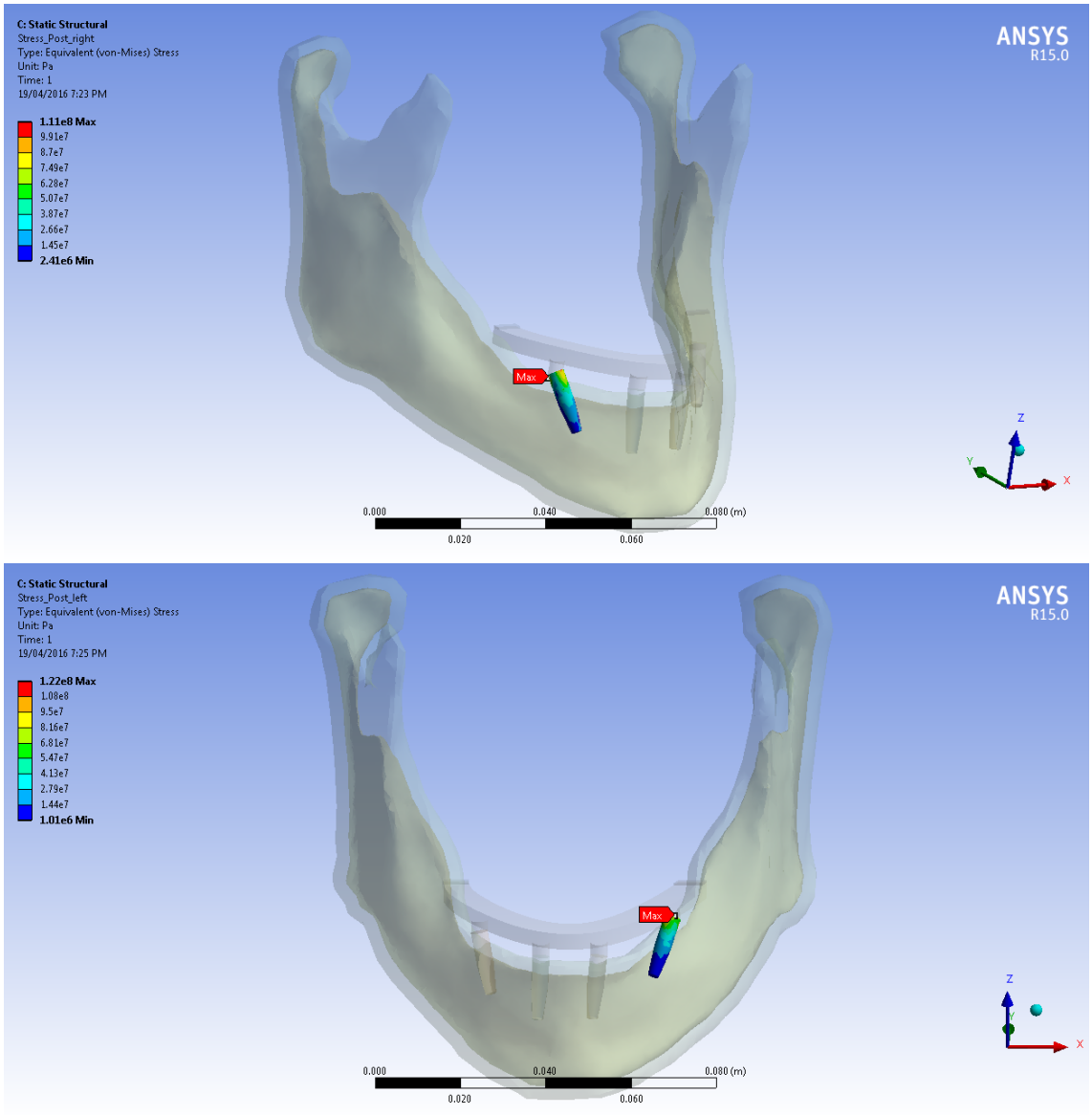

Fig. 4 Model I4: equivalent (von Mises) stress recorded for posterior right (top) and left (bottom) implants in complete muscle load set biomechanical configuration.

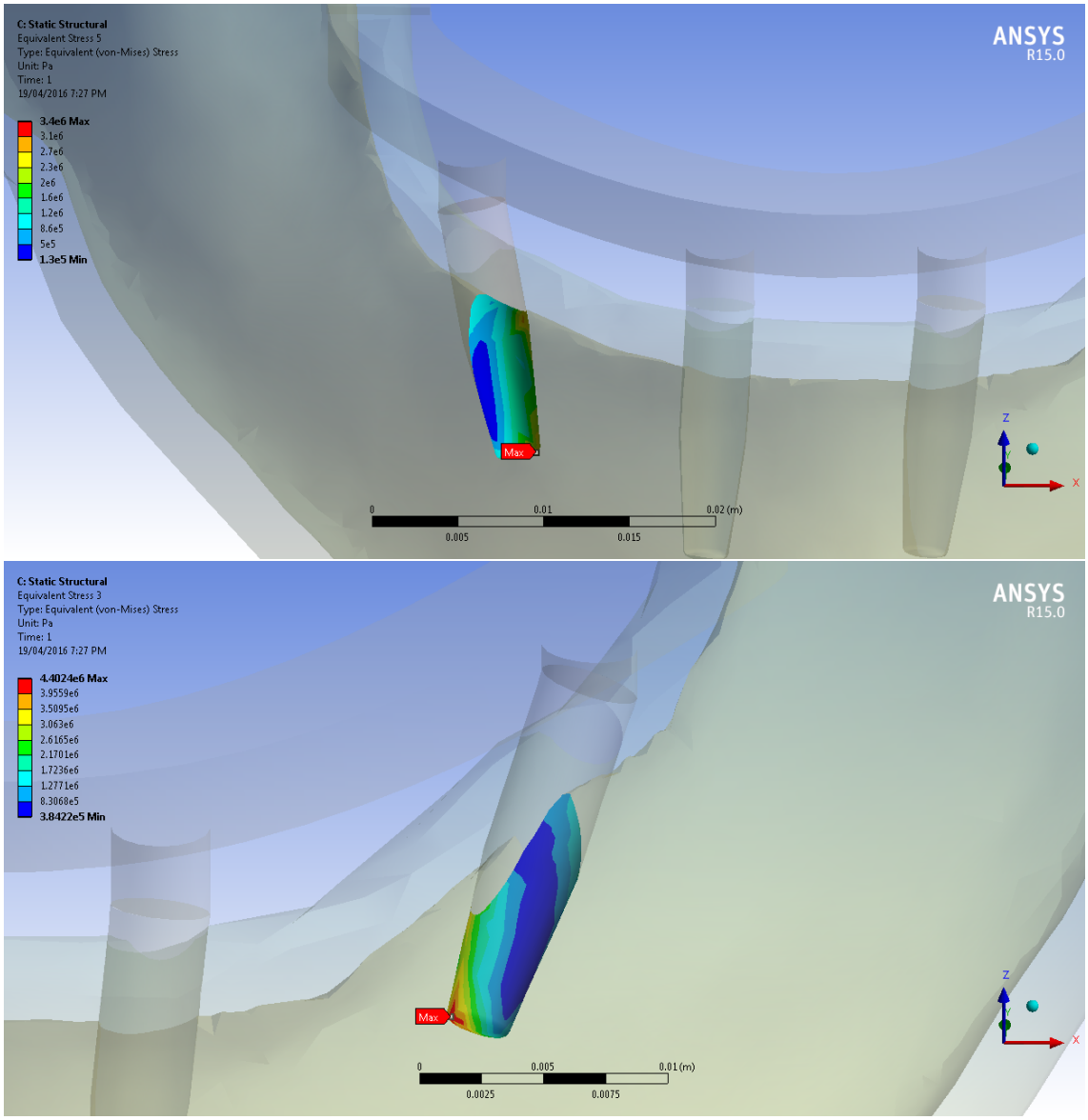

Fig. 5 Model I4: equivalent (von Mises) stress recorded for cancellous bone interface with posterior right (top) and left (bottom) implants in complete muscle load set biomechanical configuration.

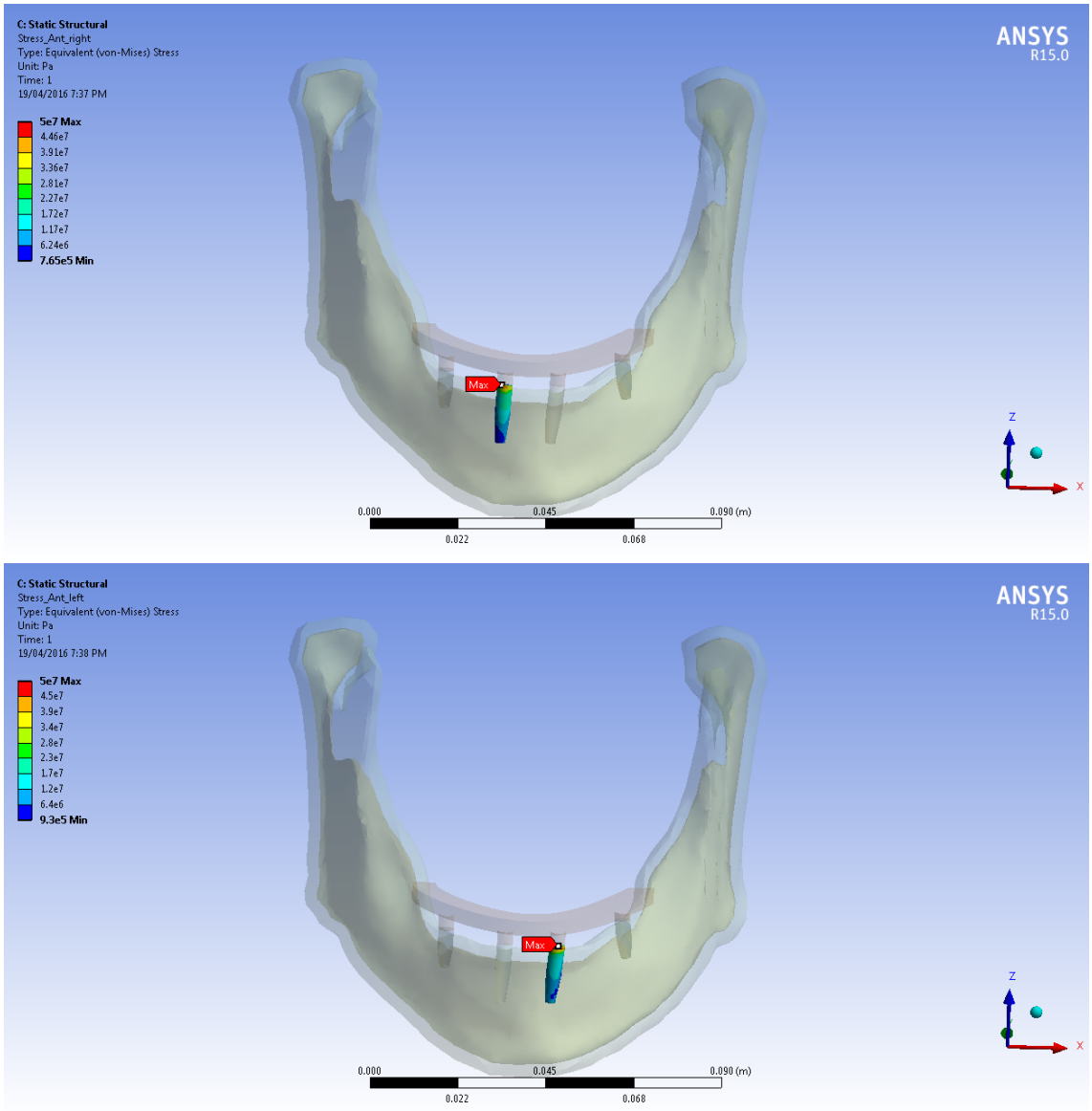

Fig. 6 Model I4c1 (first control group): equivalent (von Mises) stress recorded for anterior right (top) and left (bottom) implants in complete muscle load set biomechanical configuration.

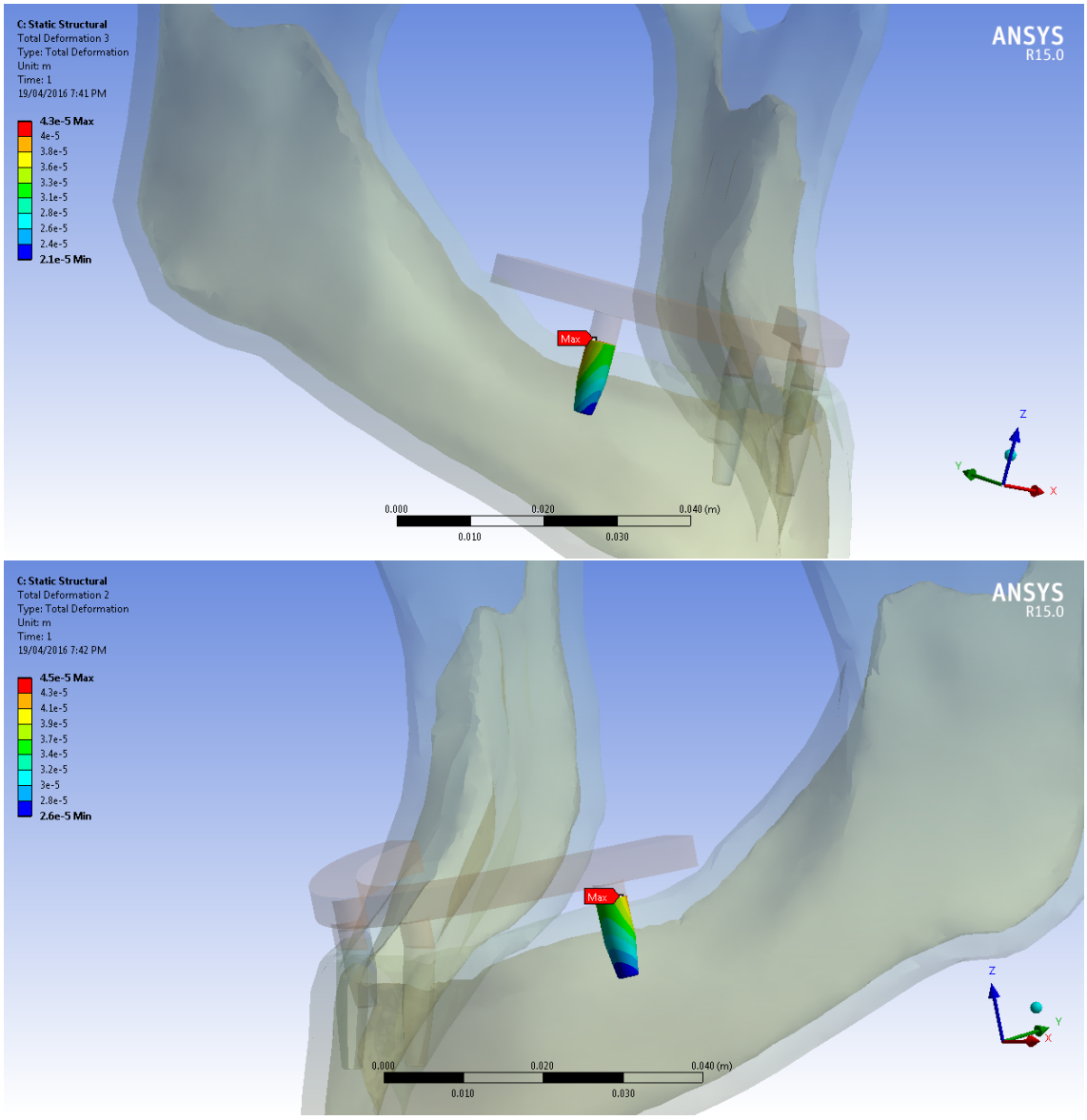

Fig. 7 Model I4c1: micro-motions of posterior right (top) and left (bottom) axial implants in complete muscle load set biomechanical configuration.

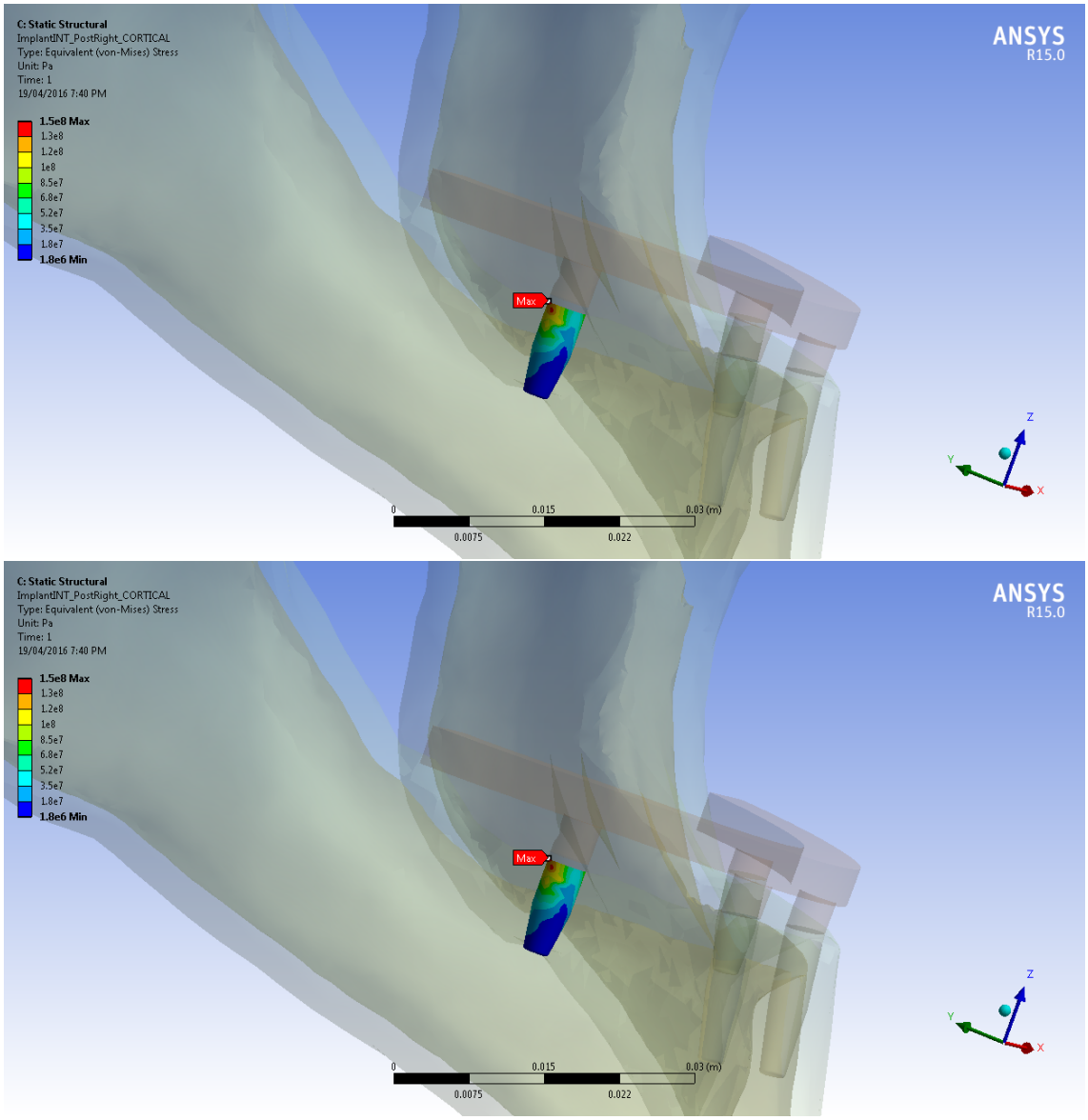

Fig. 8 Model I4c1 (first control group): equivalent (von Mises) stress recorded for posterior right (top) and left (bottom) axial implants in complete muscle load set biomechanical configuration.

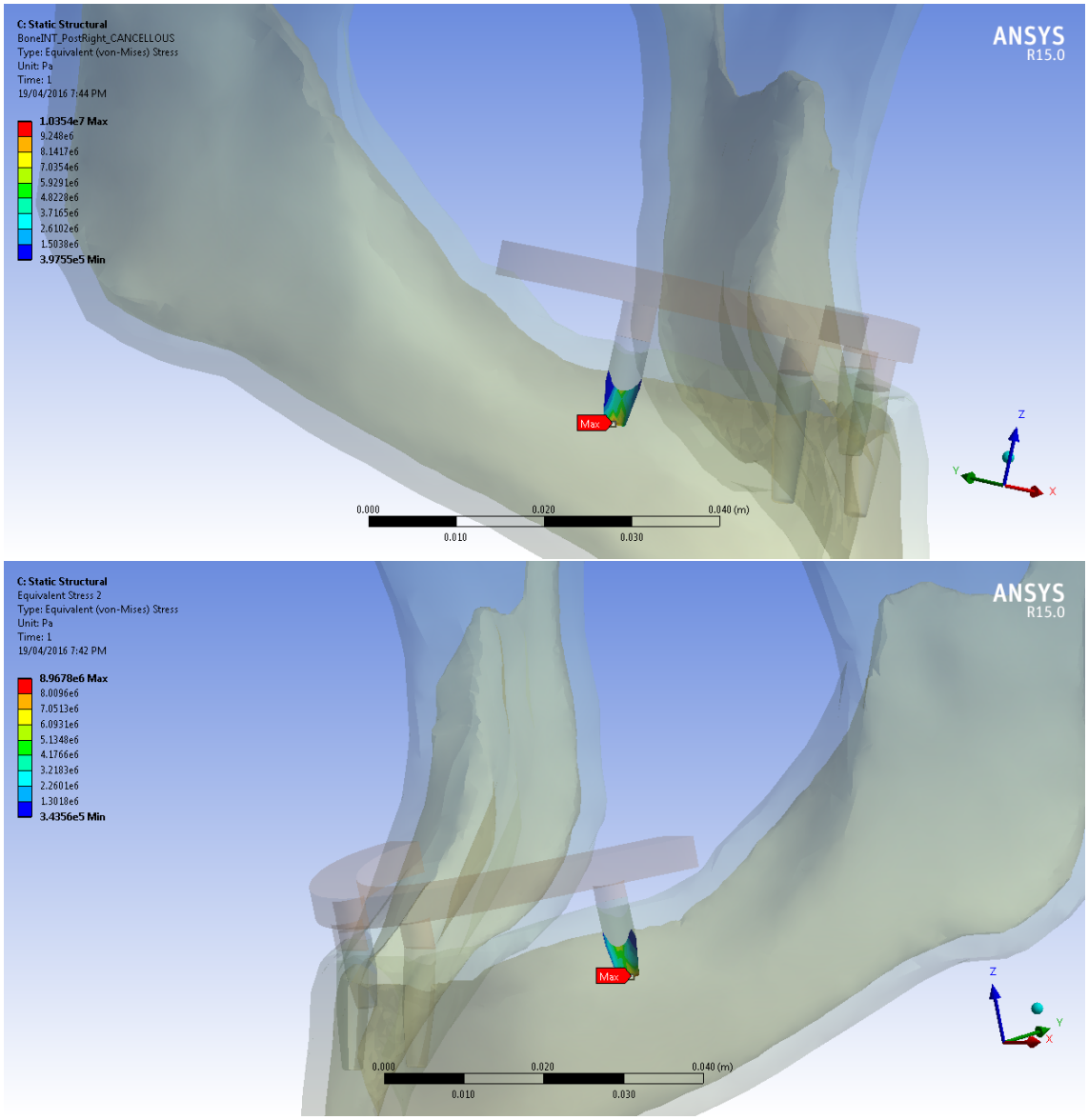

Fig. 9 Model I4c1: equivalent (von Mises) stress recorded for cancellous bone interface with posterior right (top) and left (bottom) implants in complete muscle load set biomechanical configuration.

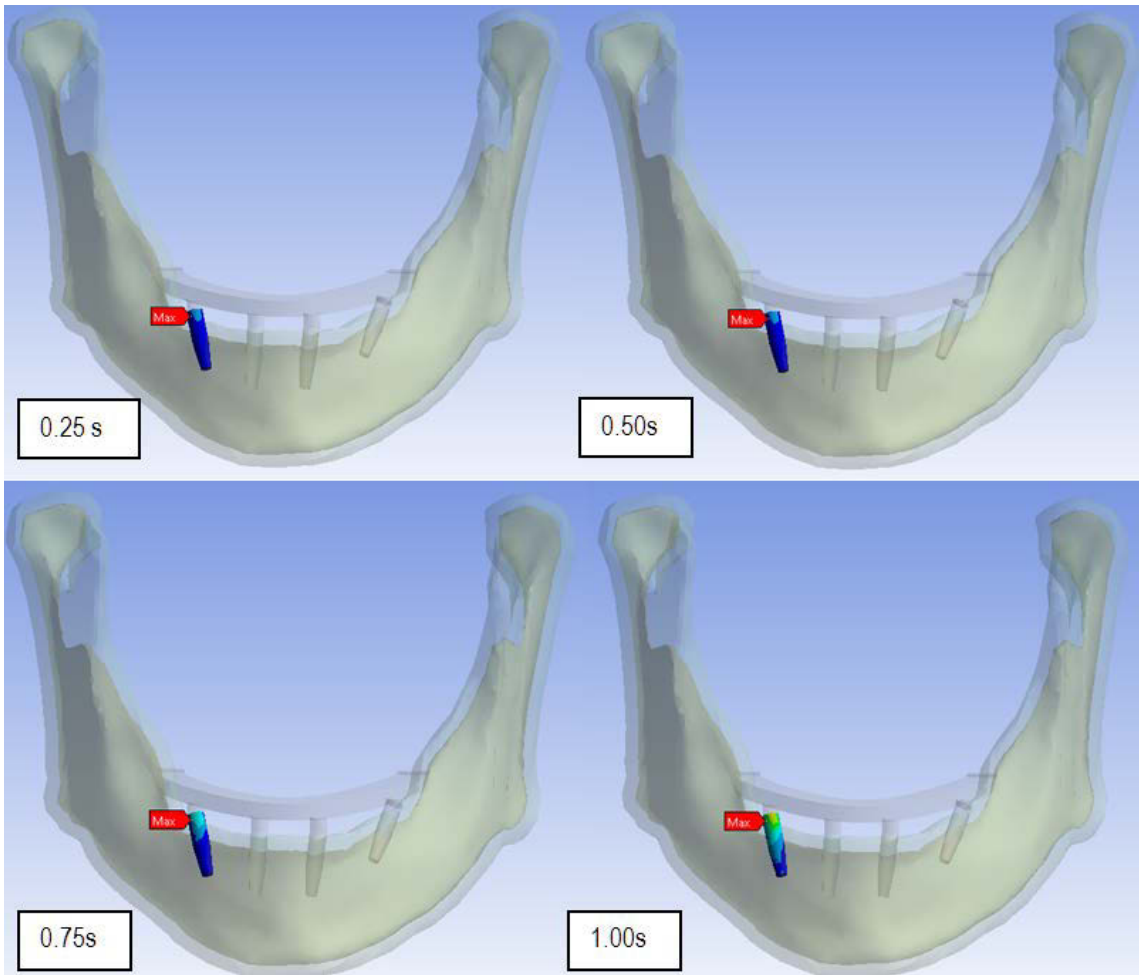

Fig. 10 Model I4: stress patterns on the surface of the posterior right angled implant at different time steps during clenching.

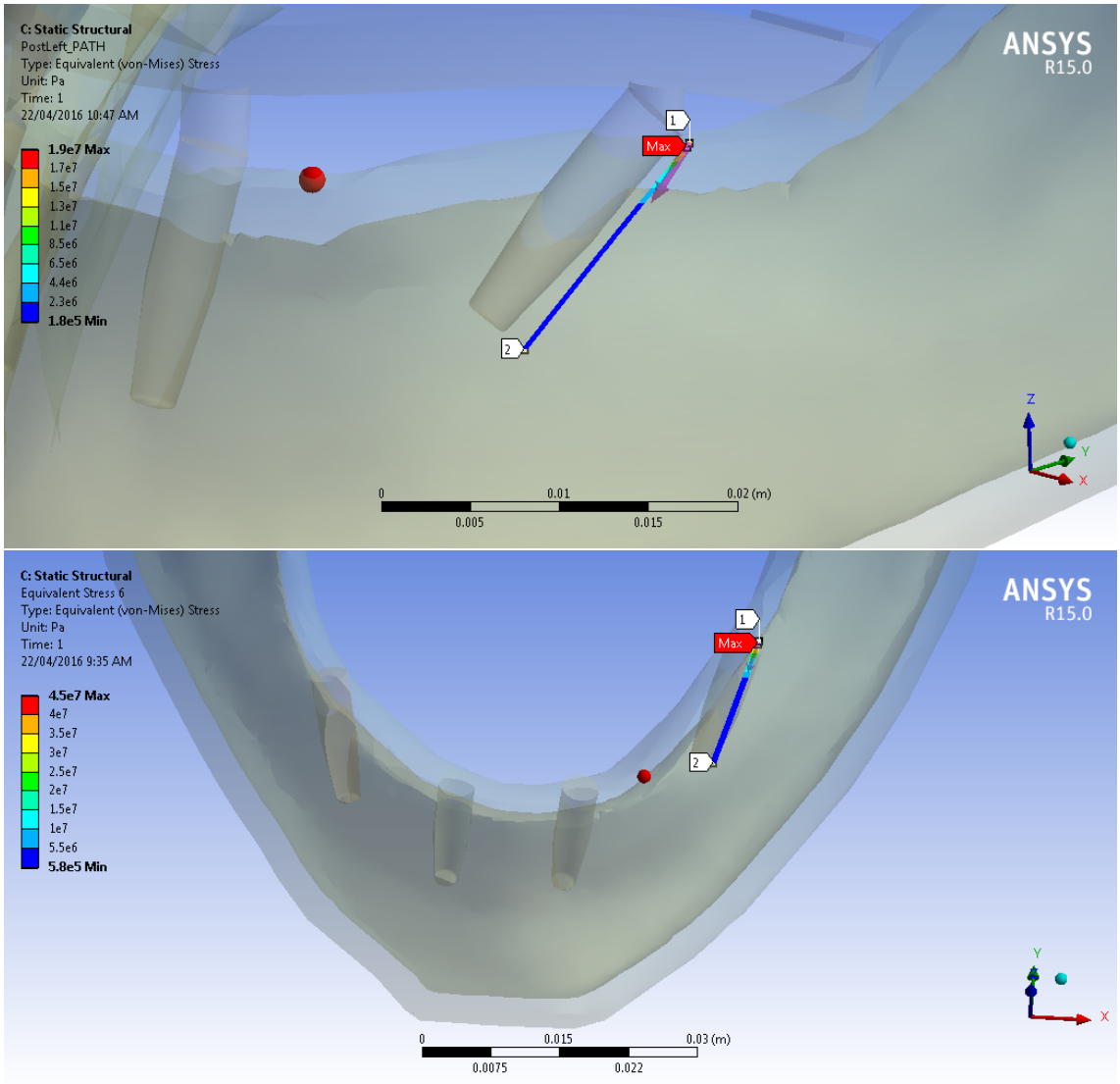

Fig. 11 Model I4: equivalent (von Mises) stress along the implant socket of the posterior left implant in complete muscle load set biomechanical configuration (top) and with fixed constraints at muscle attachment regions (bottom).

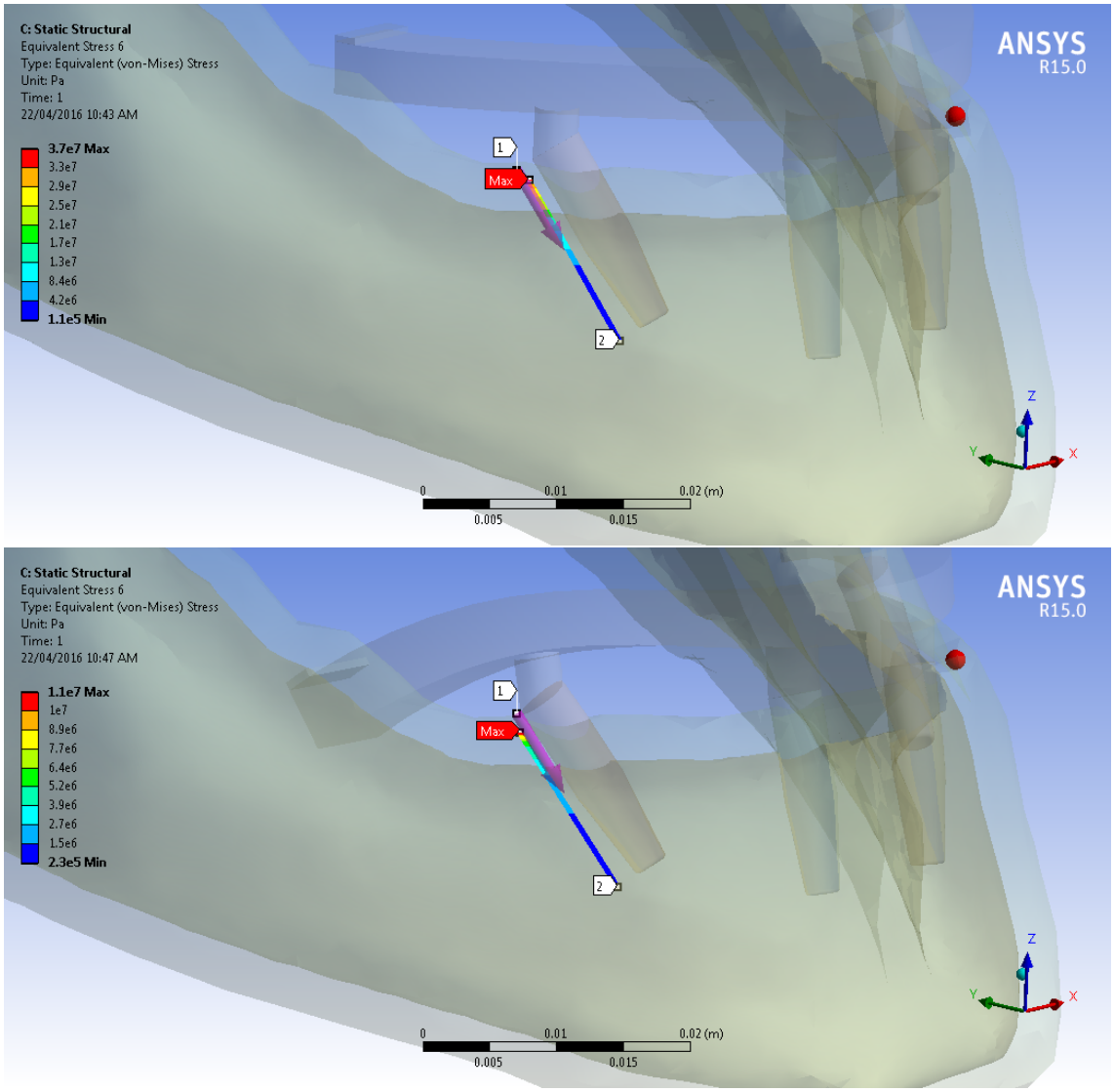

Fig. 12 Model I4: equivalent (von Mises) stress along the implant socket of the posterior right implant in complete muscle load set biomechanical configuration (top) and with fixed constraints at muscle attachment regions (bottom).

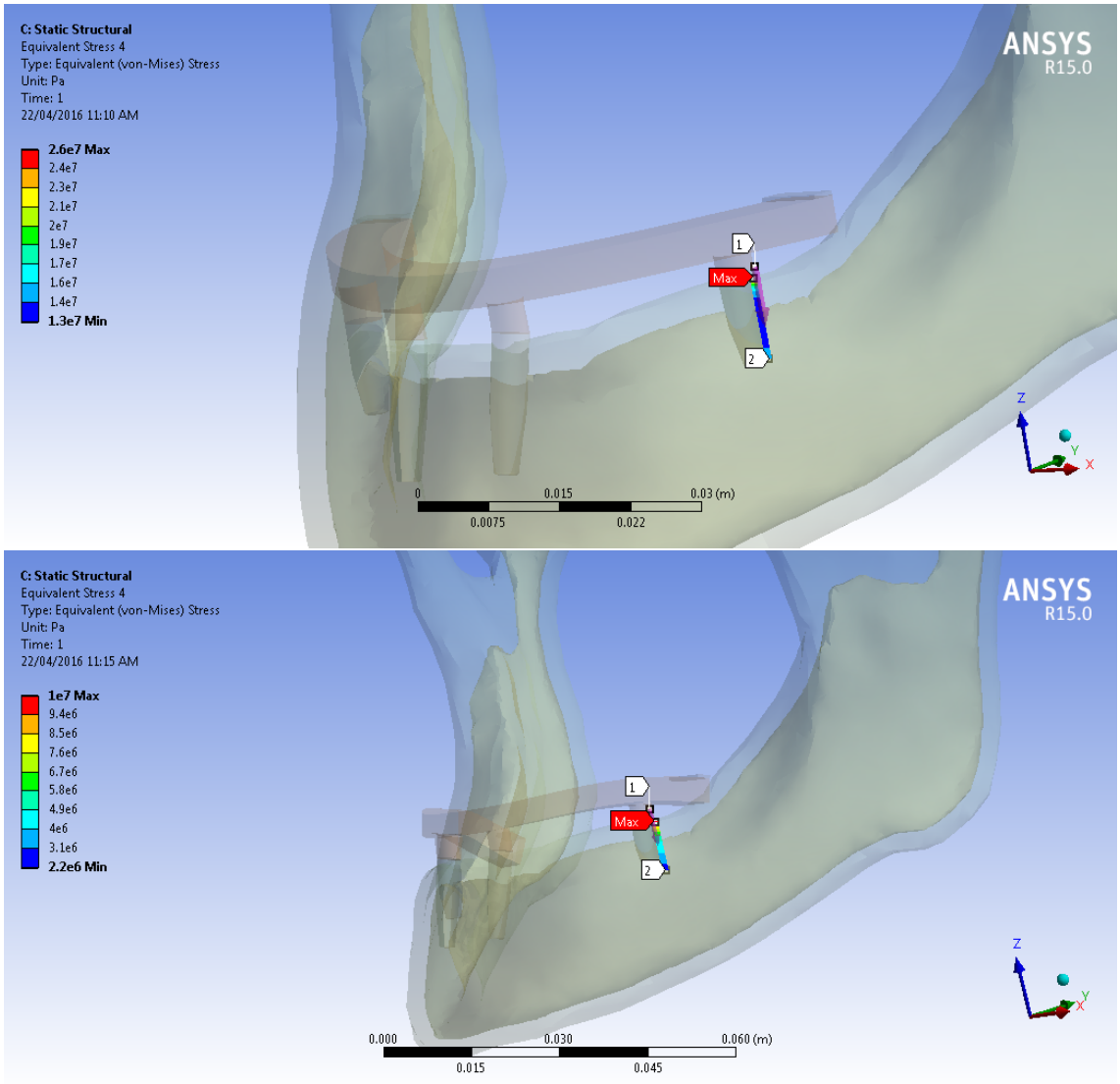

Fig. 13 Model I4c1 (first control group): equivalent (von Mises) stress along the implant socket of the posterior axial left implant in complete muscle load set biomechanical configuration (top) and with fixed constraints at muscle attachment regions (bottom).

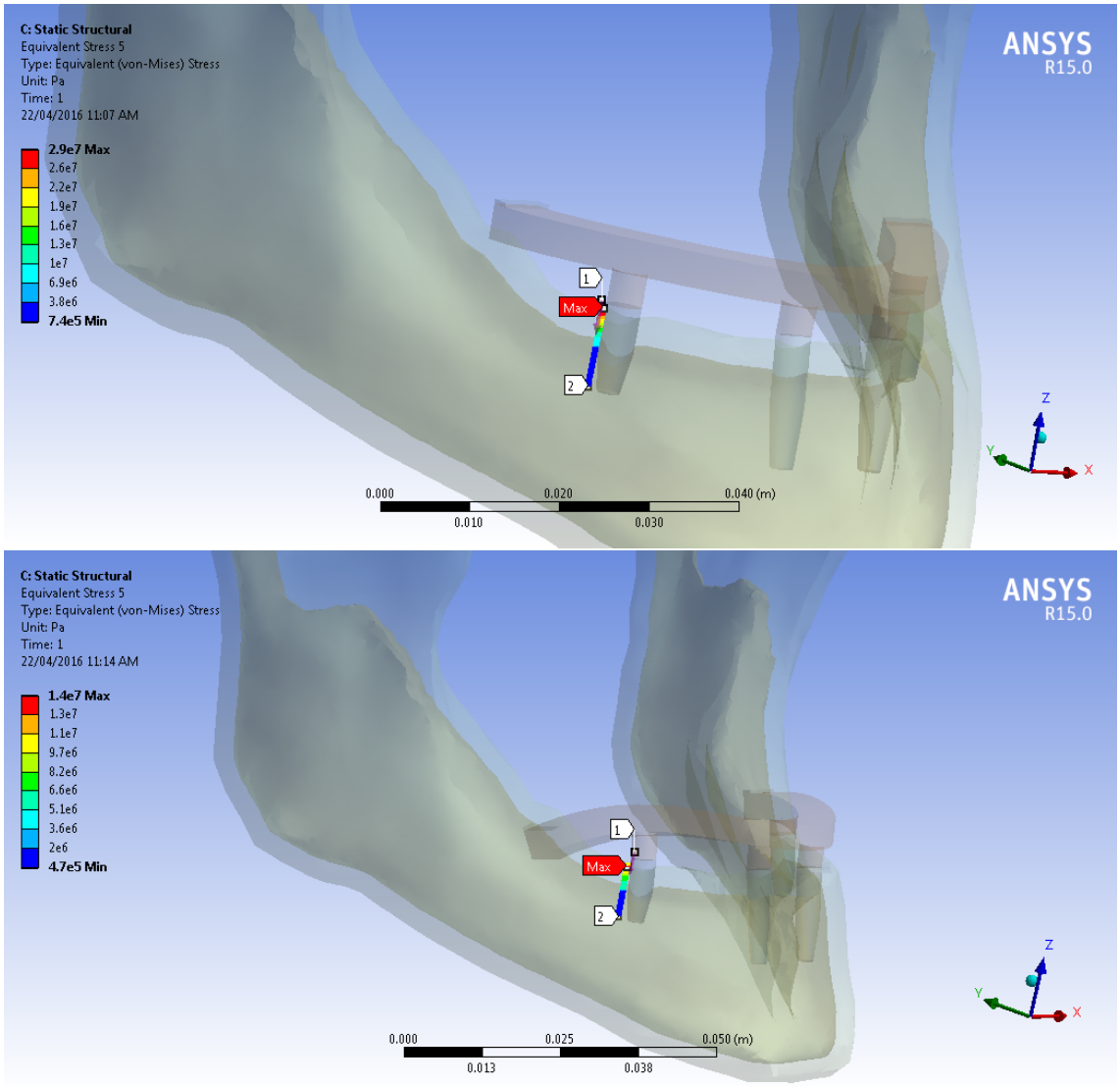

Fig. 14 Model I4c1 (first control group): equivalent (von Mises) stress along the implant socket of the posterior axial right implant in complete muscle load set biomechanical configuration (top) and with fixed constraints at muscle attachment regions (bottom).

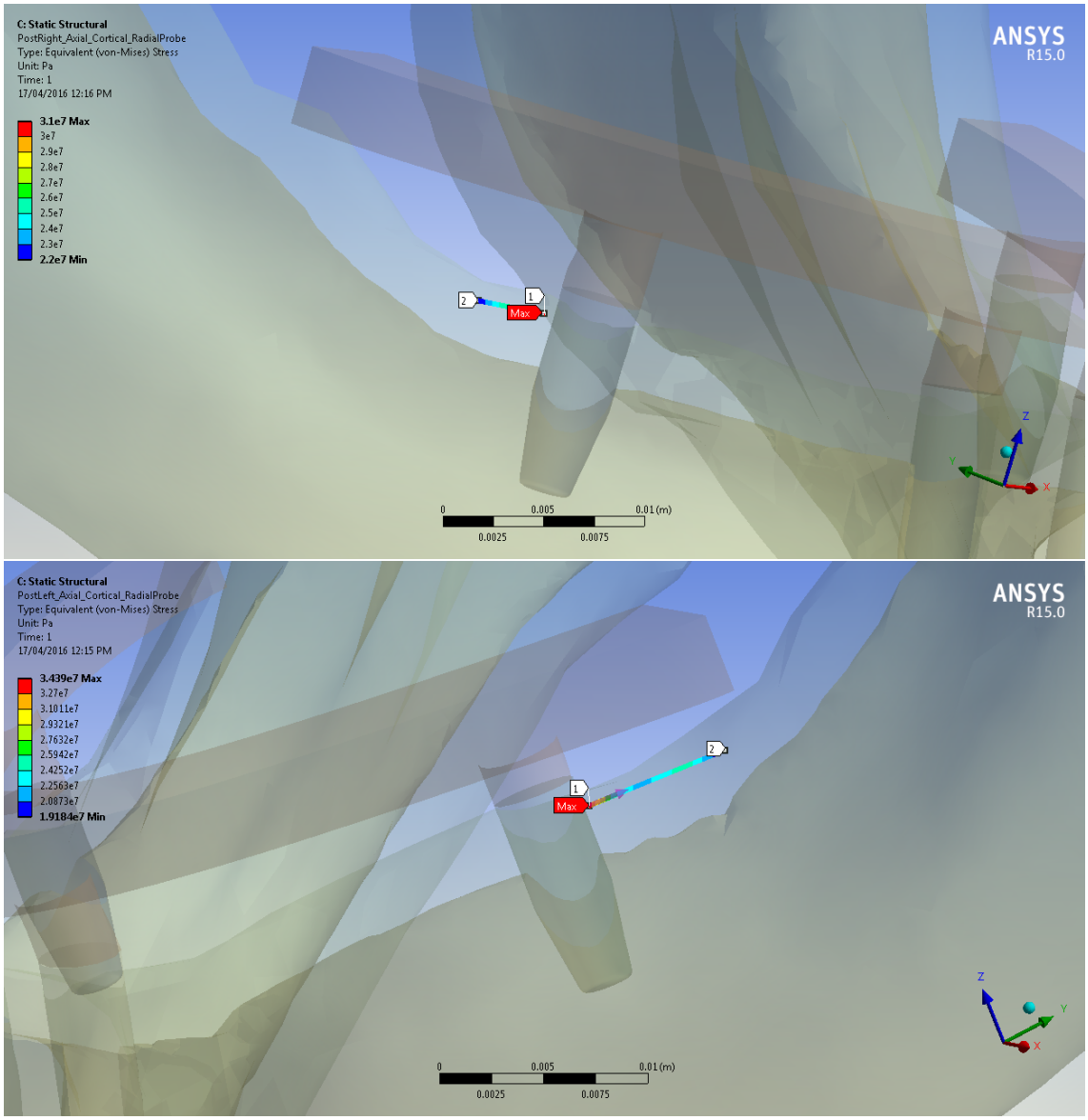

Fig. 15 Model I4c1 (first control group): equivalent (von Mises) stress relative to the cortical bone probed from the posterior axial right (top) and left (bottom) implant in complete muscle load set biomechanical configuration.

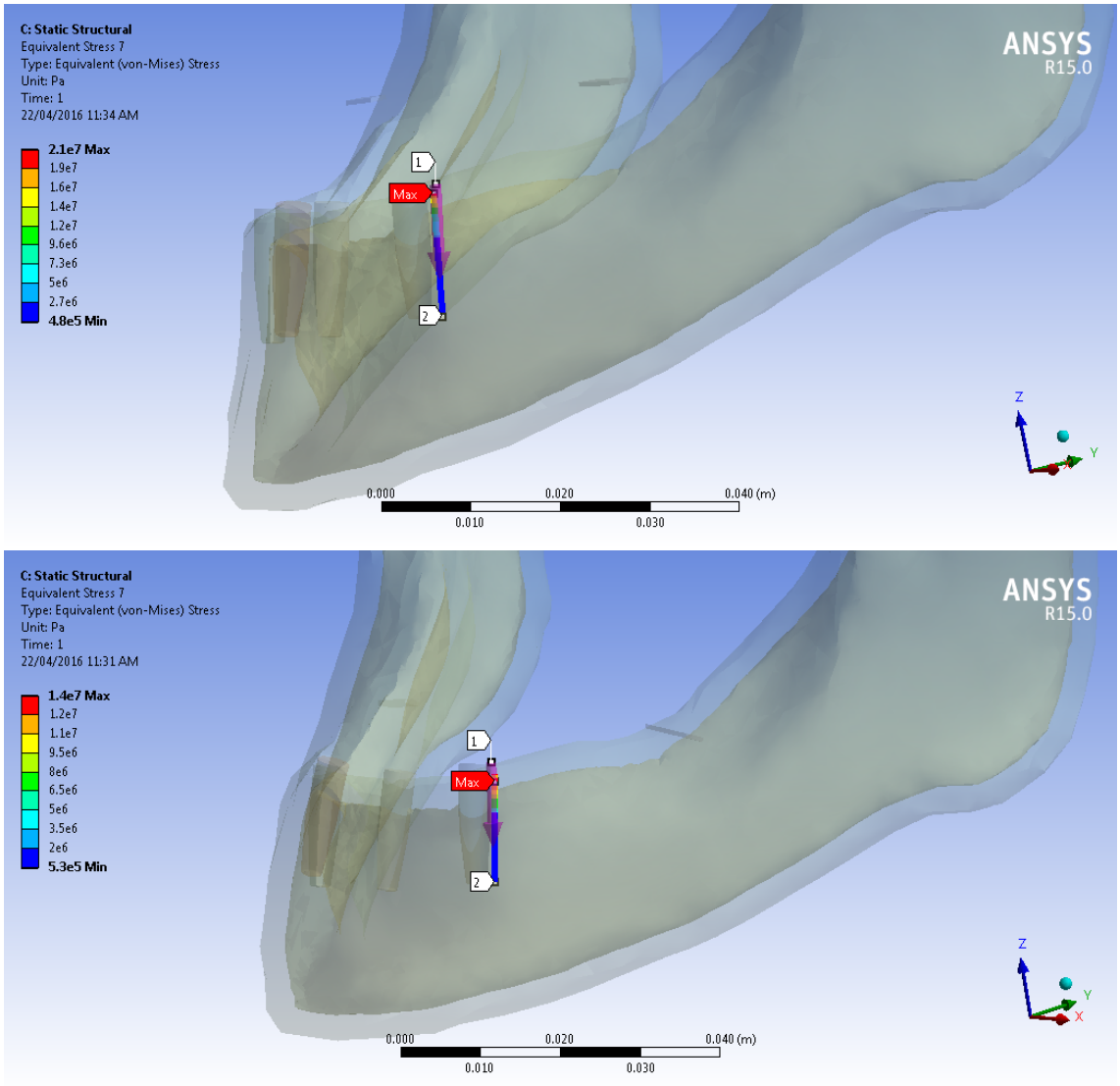

Fig. 16 Model I4c2 (second control group): equivalent (von Mises) stress along the implant socket of the longer posterior axial left implant in complete muscle load set biomechanical configuration (top) and with fixed constraints at muscle attachment regions (bottom).

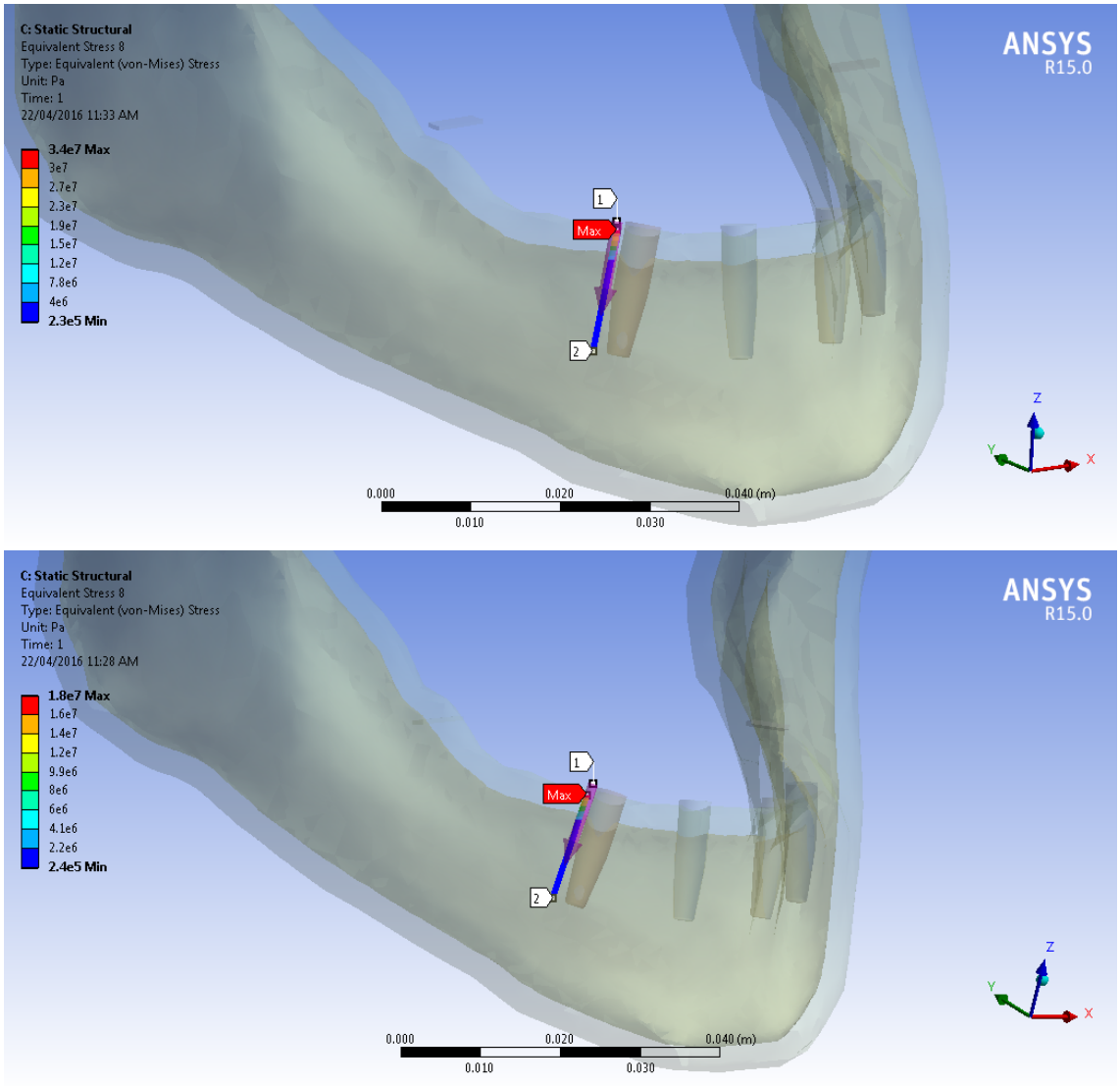

Fig. 17 Model I4c2 (second control group): equivalent (von Mises) stress along the implant socket of the longer posterior axial right implant in complete muscle load set biomechanical configuration (top) and with fixed constraints at muscle attachment regions (bottom).

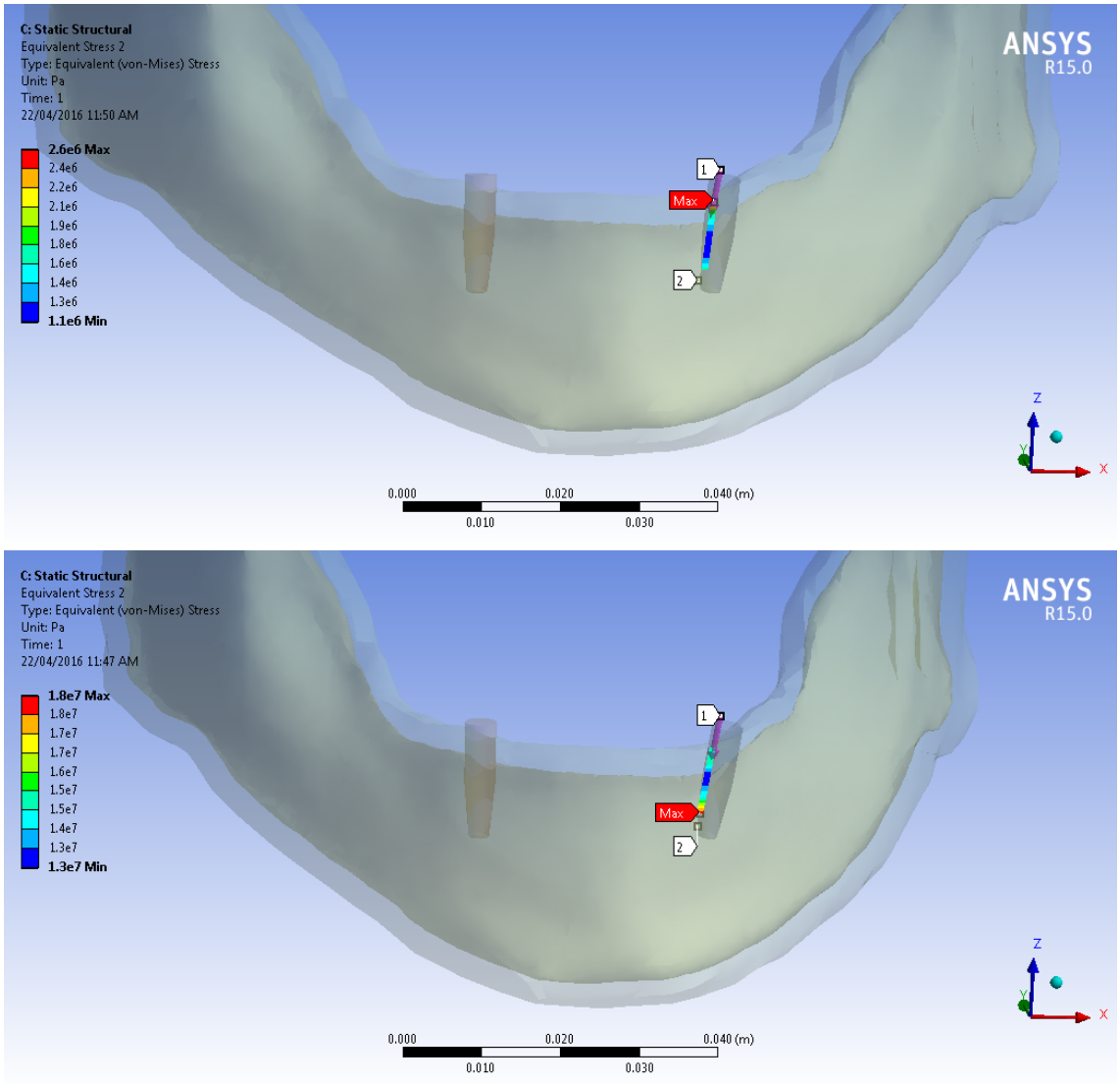

Fig. 18 Model I1: equivalent (von Mises) stress along the implant socket of a deep cortical left implant in complete muscle load set biomechanical configuration (top) and with fixed constraints at muscle attachment regions (bottom).

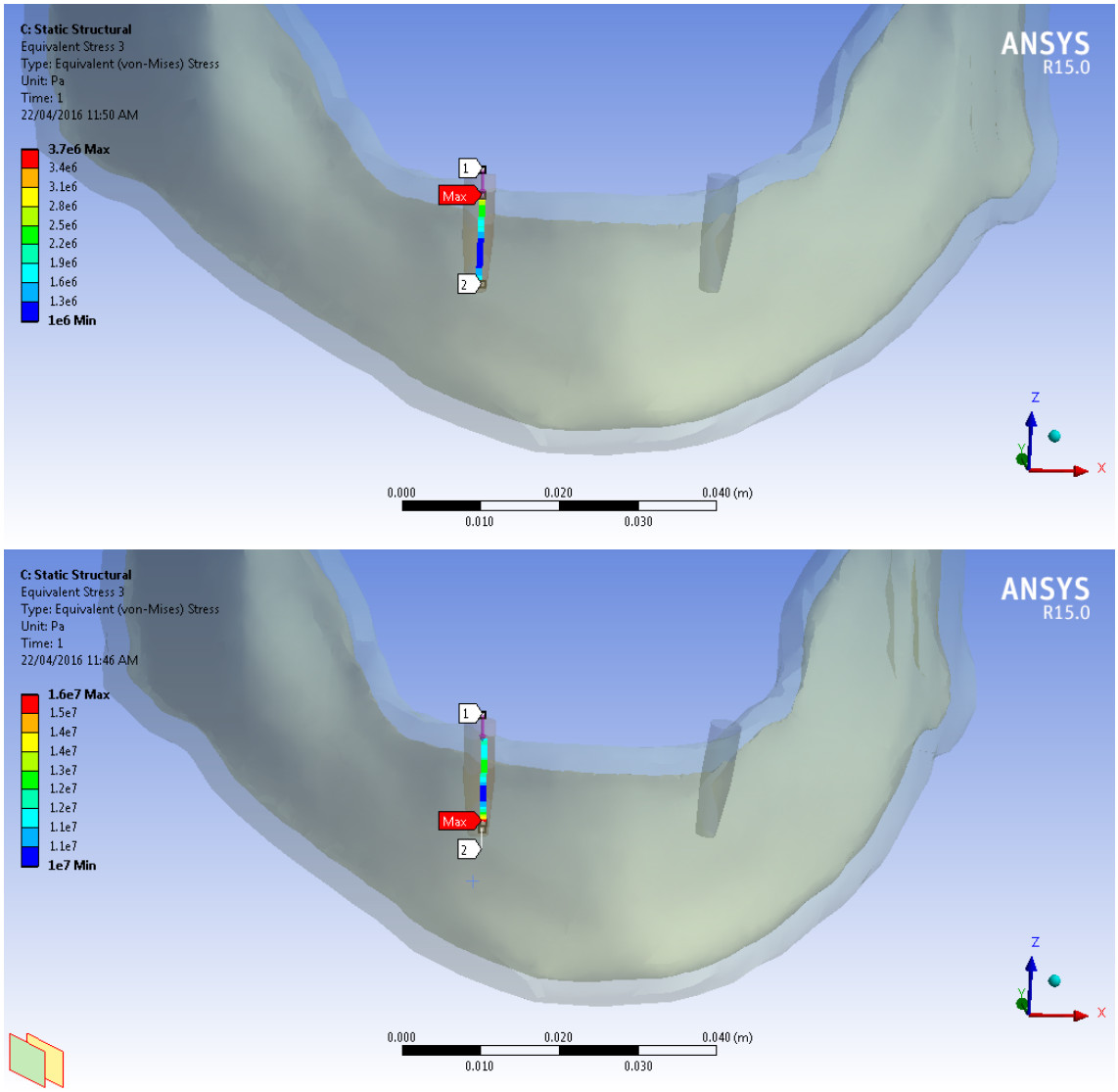

Fig. 19 Model I1: equivalent (von Mises) stress along the implant socket of a deep cortical right implant in complete muscle load set biomechanical configuration (bottom) and with fixed constraints at muscle attachment regions (top).

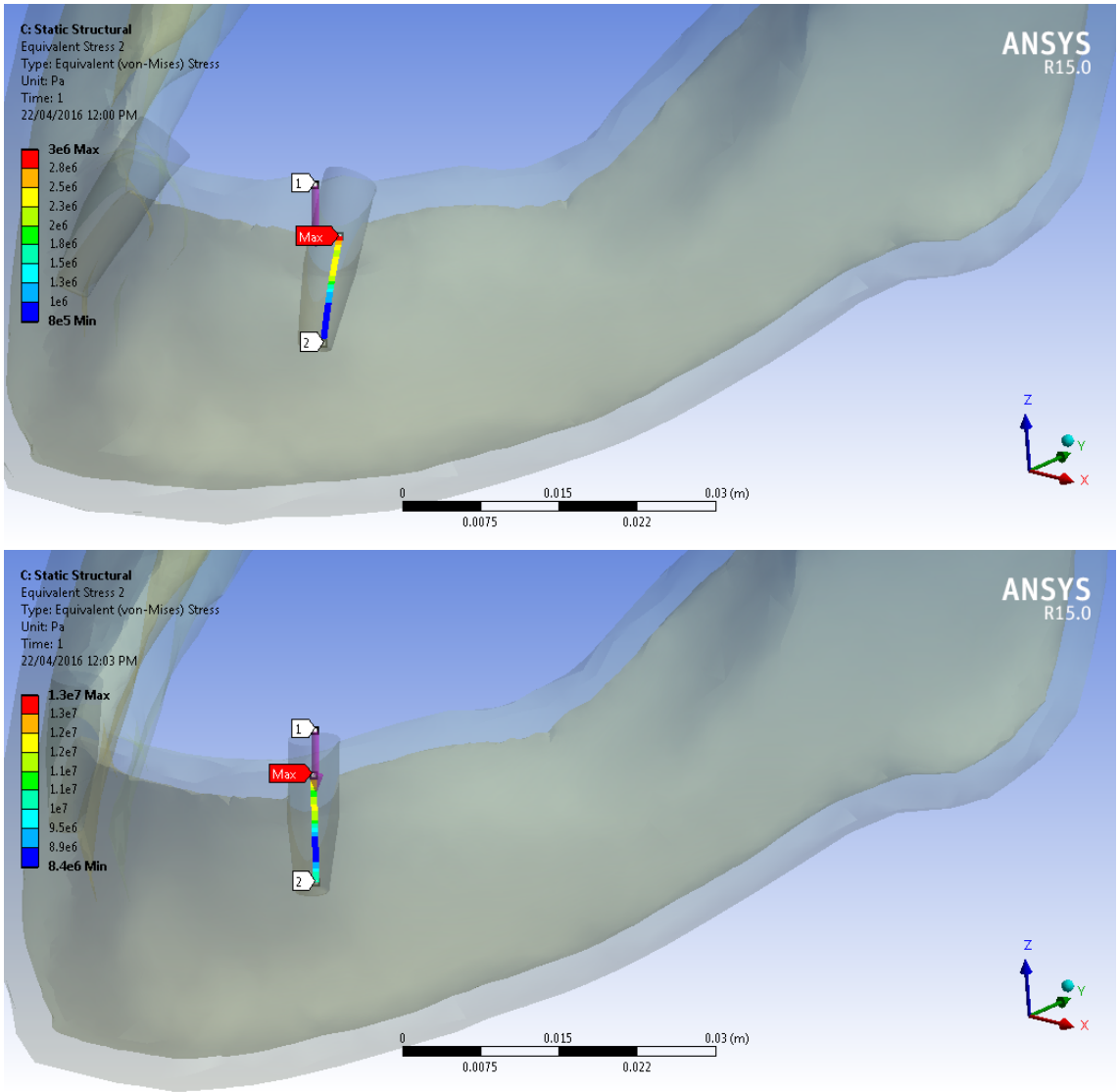

Fig. 20 Model I1c1 (control group): equivalent (von Mises) stress along the implant socket of a mono- cortical left implant in complete muscle load set biomechanical configuration (bottom) and with fixed constraints at muscle attachment regions (top).

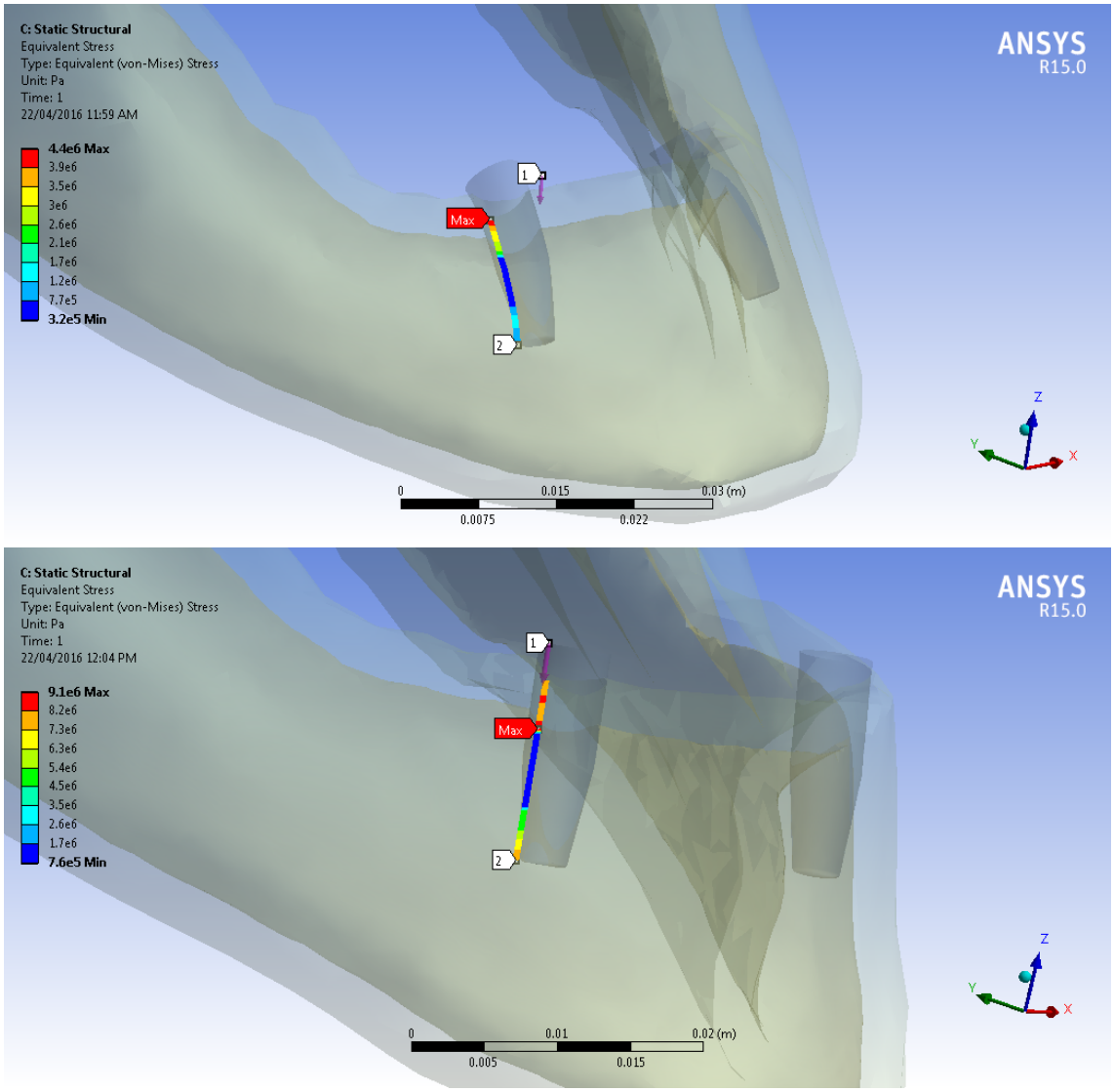

Fig. 21 Model I1c1: equivalent (von Mises) stress along the implant socket of a monocortical right implant in complete muscle load set biomechanical configuration (bottom) and with fixed constraints at muscle attachment regions (top).

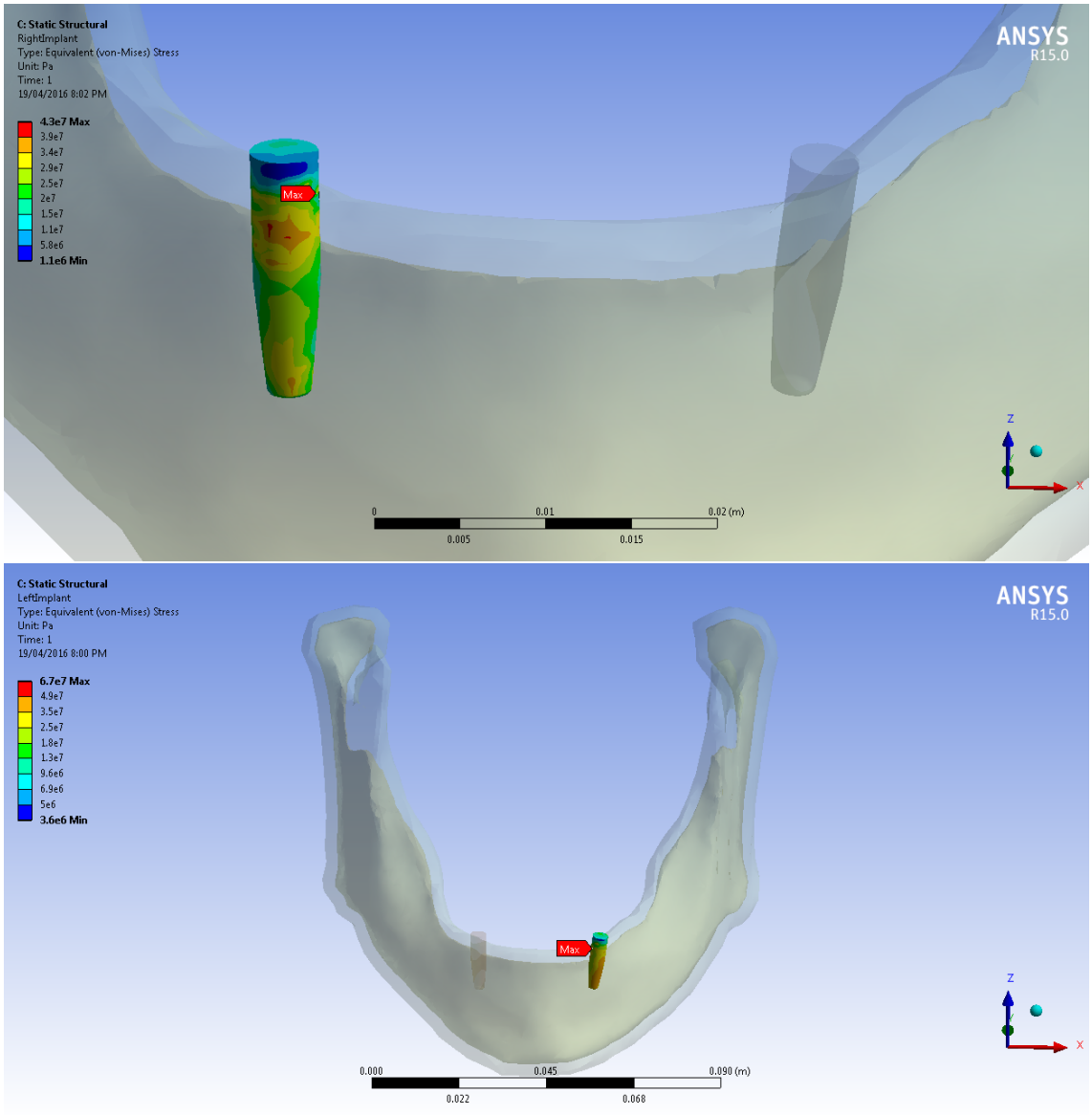

Fig. 22 Model I1: equivalent (von Mises) stress generated on the right (top) and left (bottom) deep cortical implant during clenching.

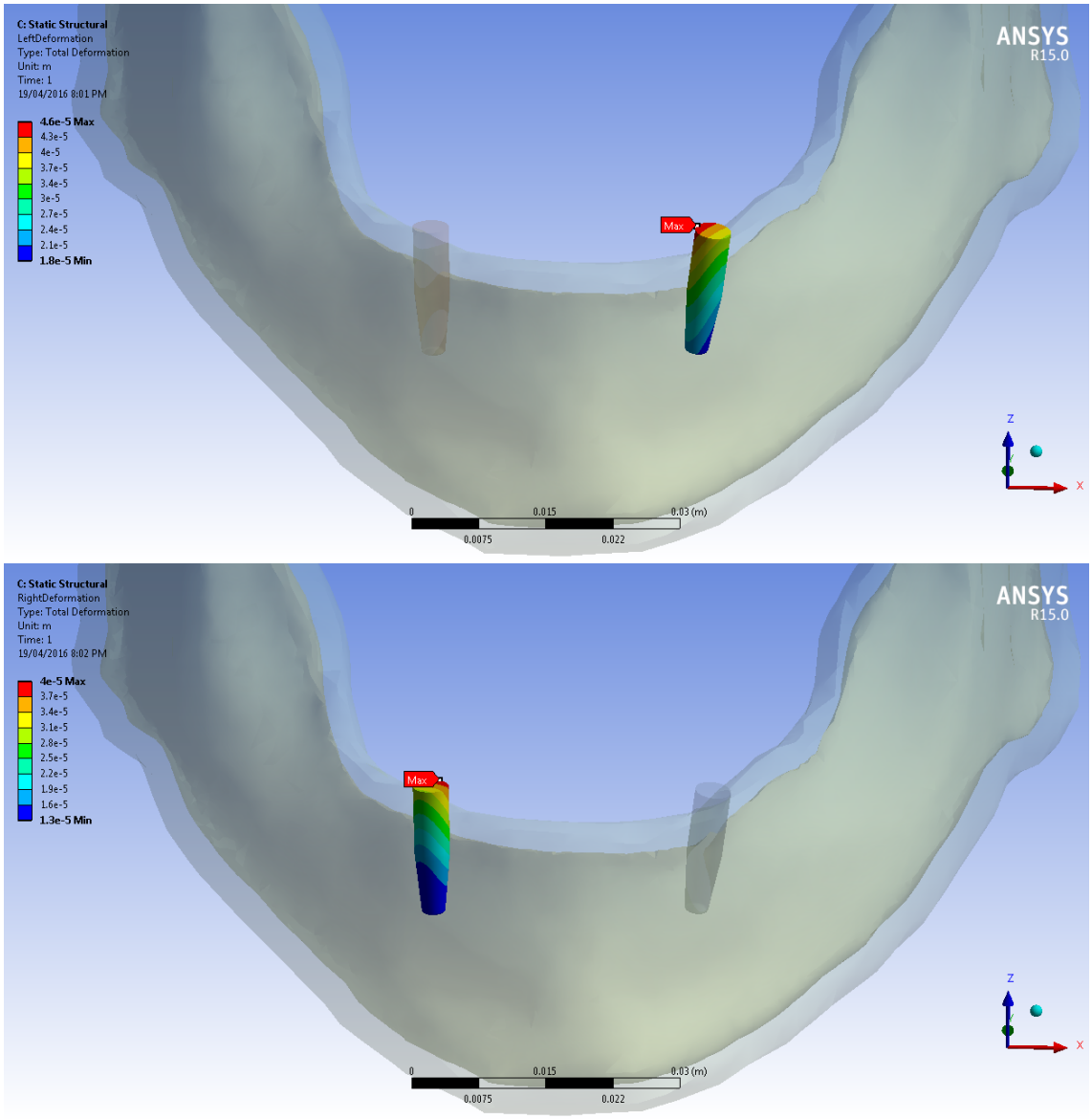

Fig. 23 Model I1: micro-motion generated on the left (top) and right (bottom) deep cortical implant during clenching.

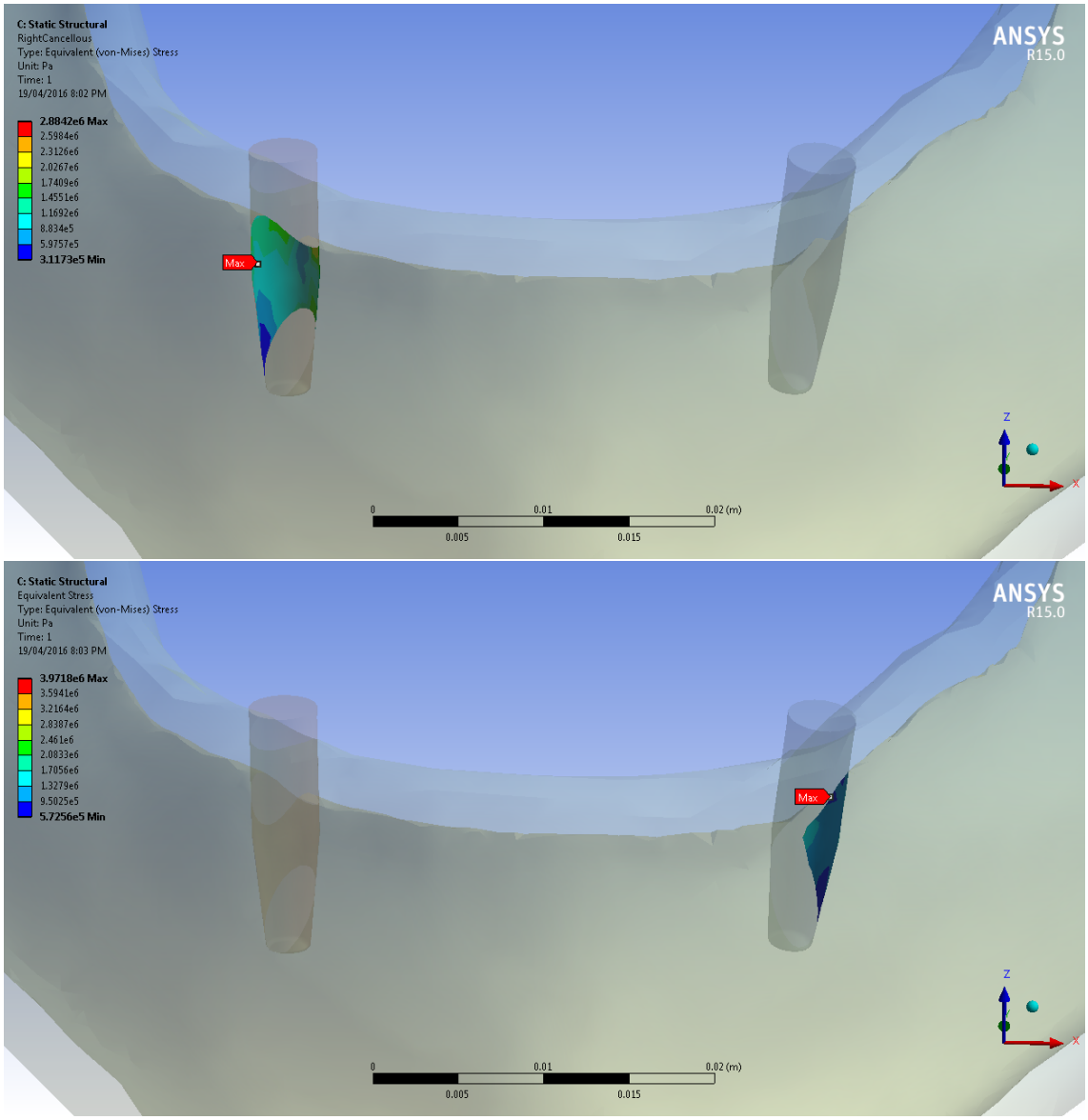

Fig. 24 Model I1: equivalent (von Mises) stress generated on the cancellous bone interface of the right (top) and left (bottom) deep cortical implant during clenching.

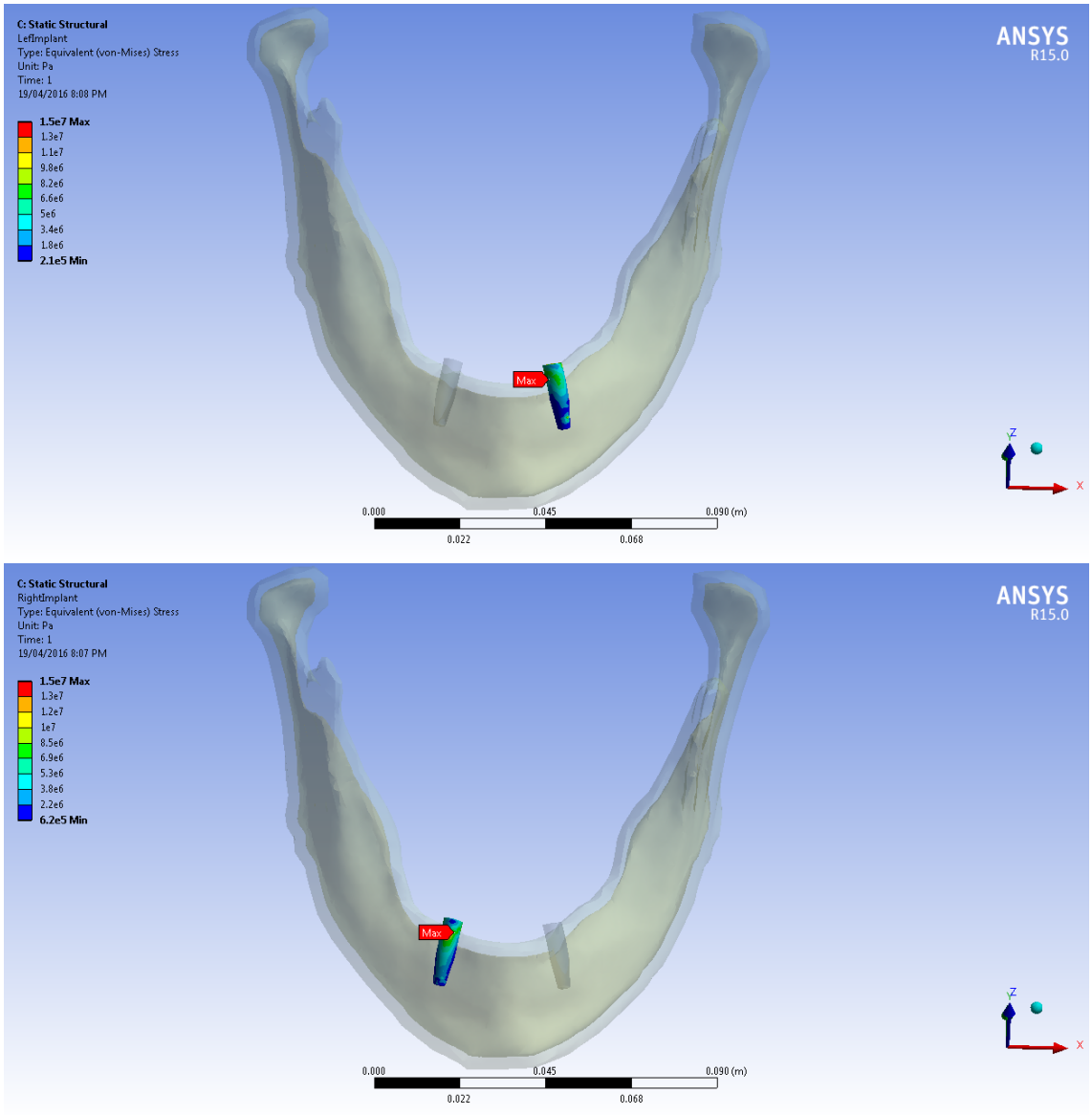

Fig. 25 Model I1c1 (control group): equivalent (von Mises) stress generated on the left (top) and right (bottom) mono-cortical implant during clenching.

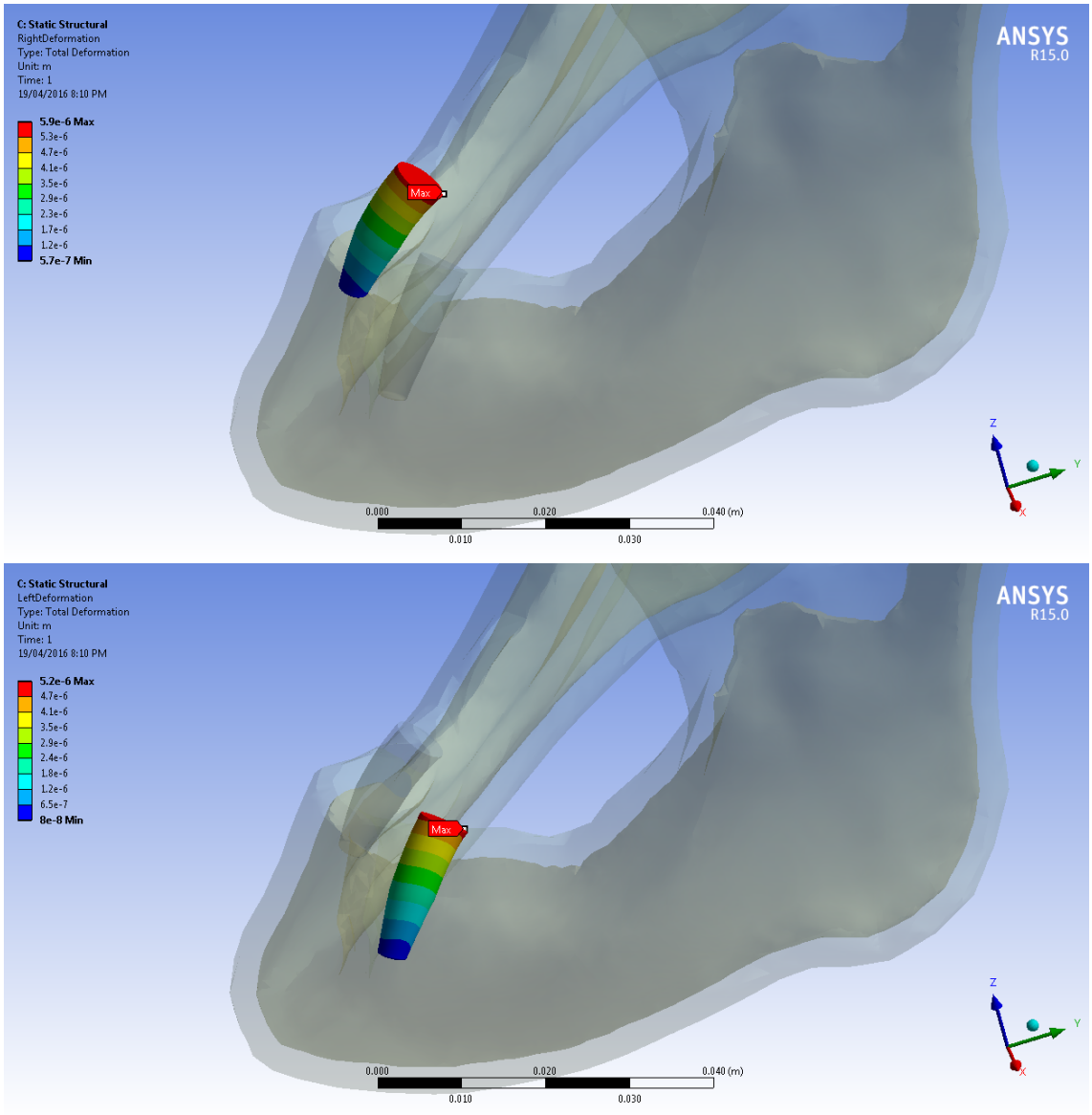

Fig. 26 Model I1c1 (control group): micro-motion generated on the right (top) and left (bottom) mono-cortical implant during clenching.

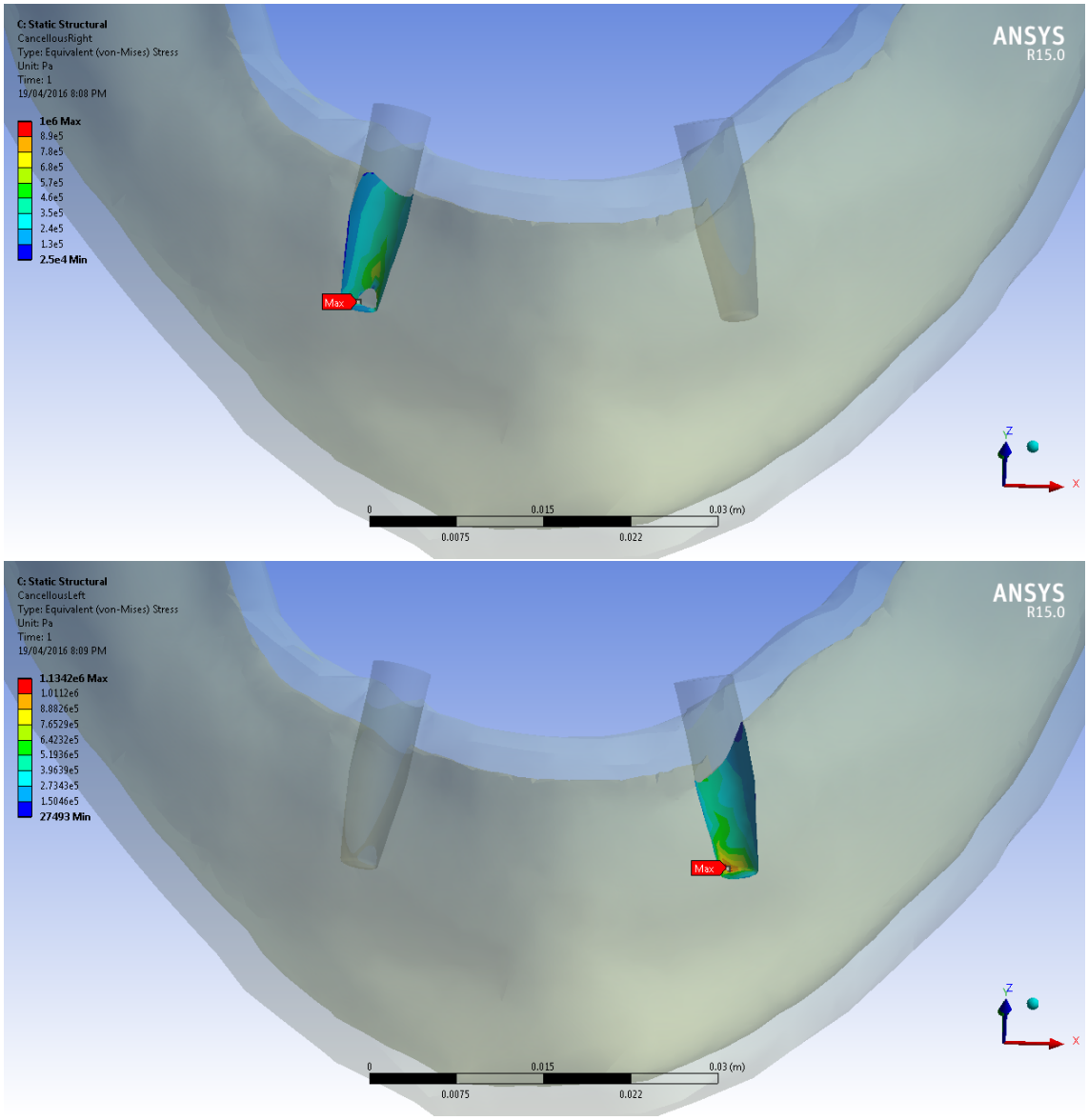

Fig. 27 Model I1c1 (control group): equivalent (von Mises) stress generated on the cancellous bone interface of the right (top) and left (bottom) mono-cortical implant during clenching.

Appendix B

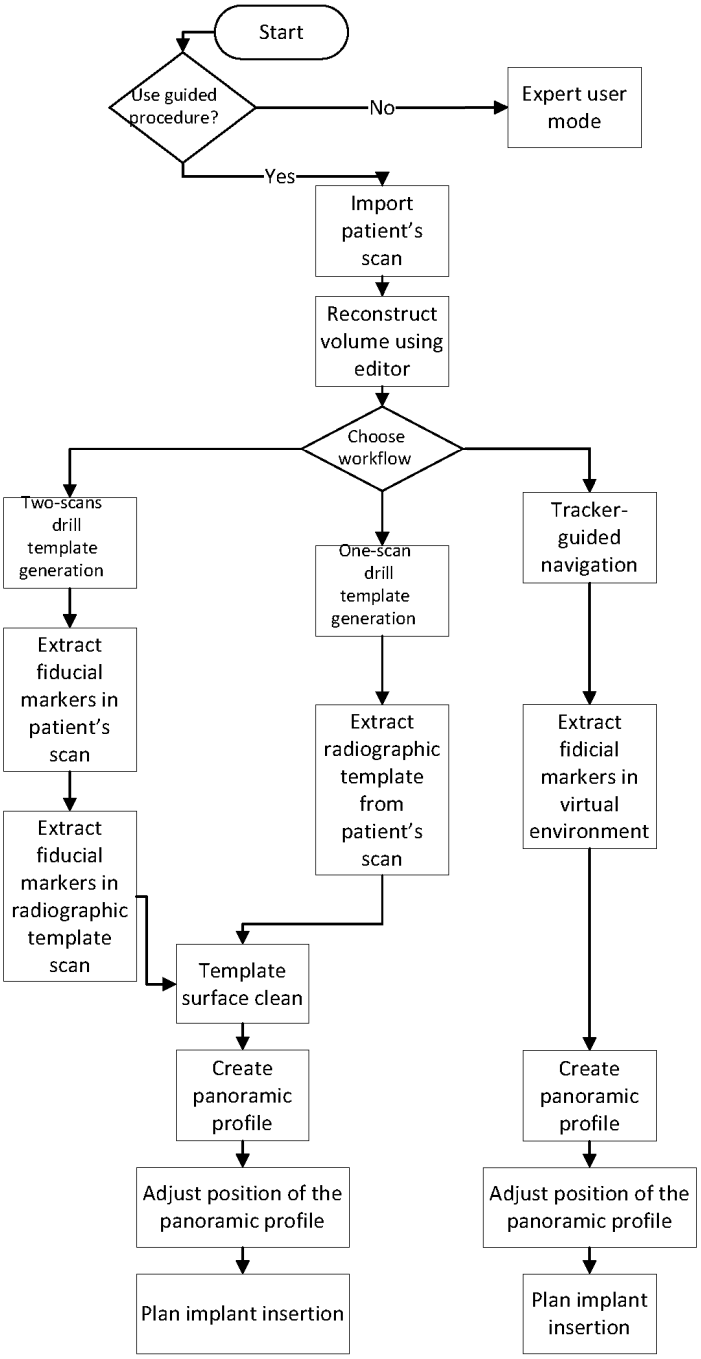

Fig. 28 General workflow for the computer-assisted surgery method, including surgical guide generation and real time tracking option (Part I).

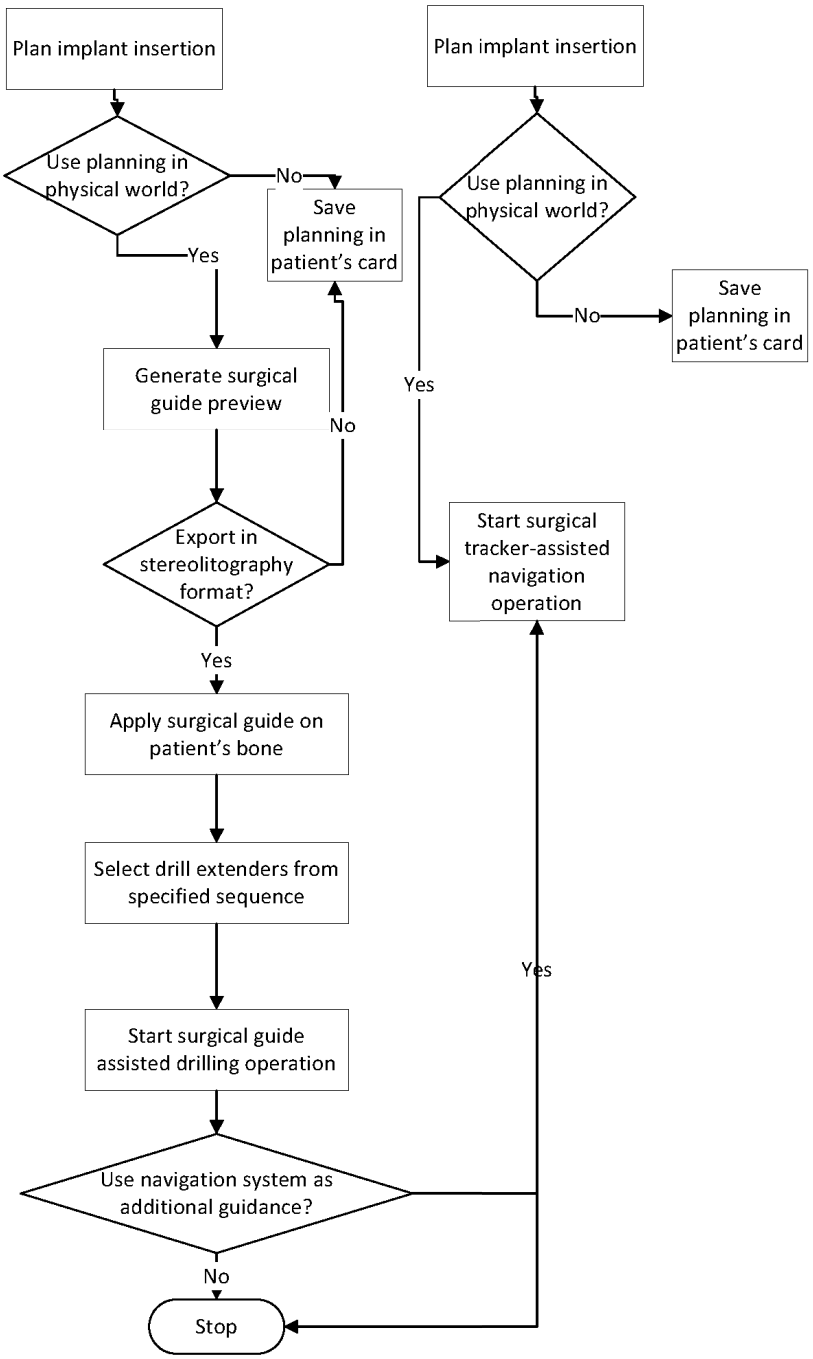

Fig. 29 General workflow for the computer-assisted surgery method, including surgical guide generation and real time tracking option (Part II).

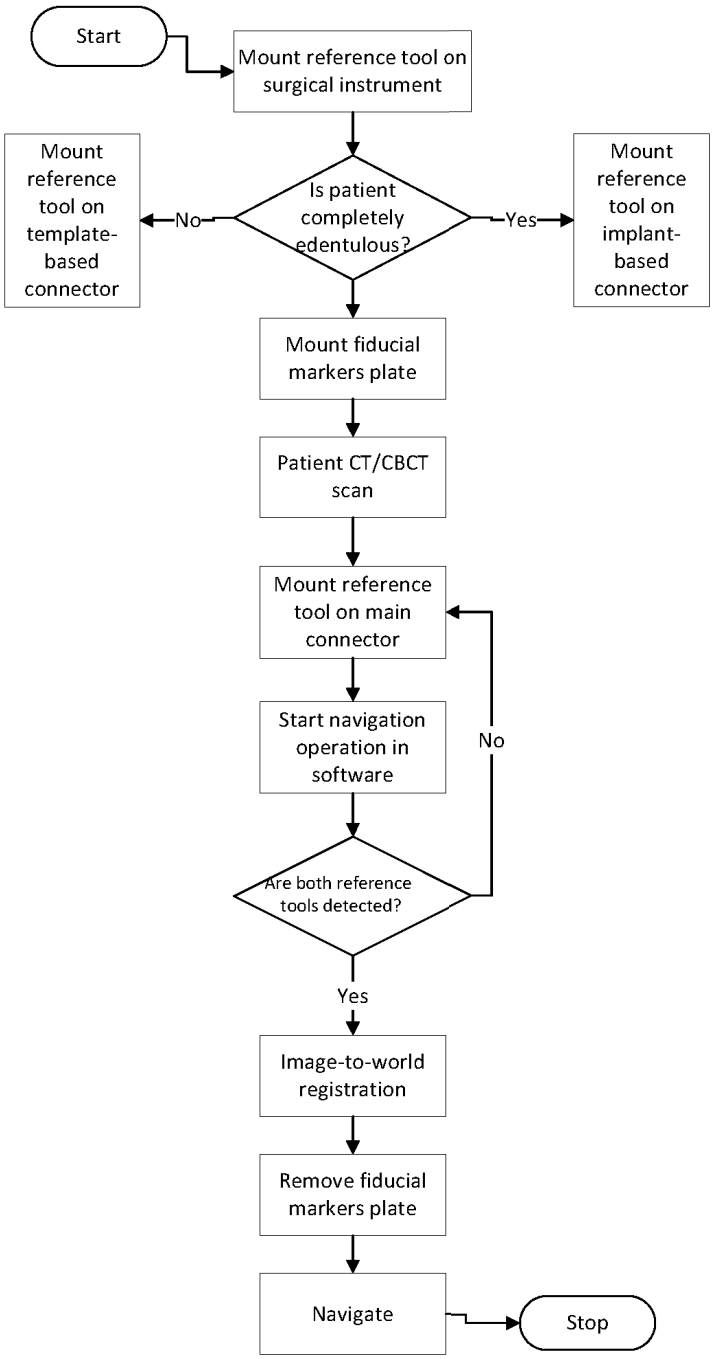

Fig. 30 Surgical navigation workflow including software/hardware interaction.

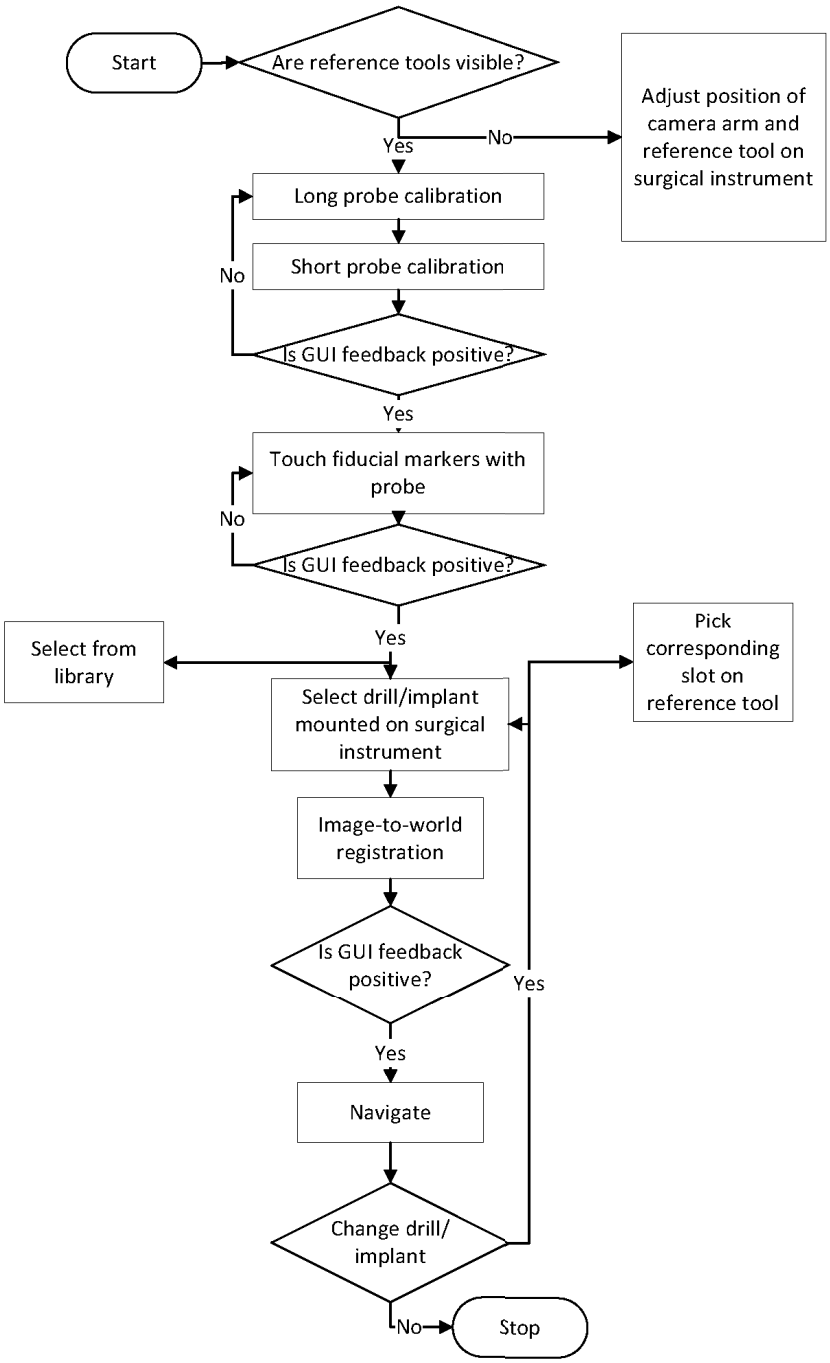

Fig. 31 Software workflow associated to the surgical navigation operation.

References

1. Amis, A. A., D. Dowson and V. Wright. "Elbow Joint Force Predictions for Some Strenuous Isometric Actions." J Biomech 13, no. 9 (1980): 765-75.

2. Ammar, H. H., P. Ngan, R. J. Crout, V. H. Mucino and O. M. Mukdadi. "Three-Dimensional Modeling and Finite Element Analysis in Treatment Planning for Orthodontic Tooth Movement." Am J Orthod Dentofacial Orthop 139, no. 1 (2011): e59-71.

3. Arisan, V., Z. C. Karabuda and T. Ozdemir. "Accuracy of Two Stereolithographic Guide Systems for Computer-Aided Implant Placement: A Computed Tomography-Based Clinical Comparative Study." J Periodontol 81, no. 1 (2010): 43-51.

4. Ashman, R. B., J. D. Corin and C. H. Turner. "Elastic Properties of Cancellous Bone: Measurement by an Ultrasonic Technique." J Biomech 20, no. 10 (1987): 979-86.

5. Ashman, R. B. and J. Y. Rho. "Elastic Modulus of Trabecular Bone Material." J Biomech 21, no. 3 (1988): 177-81.

6. Barao, V. A., W. G. Assuncao, L. F. Tabata, J. A. Delben, E. A. Gomes, E. A. de Sousa and E. P. Rocha. "Finite Element Analysis to Compare Complete Denture and Implant-Retained Overdentures with Different Attachment Systems." J Craniofac Surg 20, no. 4 (2009): 1066-71.

7. Barao, V. A., W. G. Assuncao, L. F. Tabata, J. A. Delben, E. A. Gomes, E. A. de Sousa and E. P. Rocha. "Finite Element Analysis to Compare Complete Denture and Implant-Retained Overdentures with Different Attachment Systems." J Craniofac Surg 20, no. 4 (2009): 1066-71.

8. Barao, V. A., J. A. Delben, J. Lima, T. Cabral and W. G. Assuncao. "Comparison of Different Designs of Implant-Retained Overdentures and Fixed Full-Arch Implant-Supported Prosthesis on Stress Distribution in Edentulous Mandible–a Computed Tomography-Based Three-Dimensional Finite Element Analysis." J Biomech 46, no. 7 (2013): 1312-20.

9. Barbenel, J. C. "The Mechanics of the Temporomandibular Joint–a Theoretical and Electromyographical Study." J Oral Rehabil 1, no. 1 (1974): 19-27.

10. Barbier, L., J. Vander Sloten, G. Krzesinski, E. Schepers and G. Van der Perre. "Finite Element Analysis of Non-Axial Versus Axial Loading of Oral Implants in the Mandible of the Dog." J Oral Rehabil 25, no. 11 (1998): 847-58.

11. Barone, A., U. Covani, R. Cornelini and E. Gherlone. "Radiographic Bone Density around Immediately Loaded Oral Implants." Clin Oral Implants Res 14, no. 5 (2003): 610-5.

12. Bayraktar, H. H., E. F. Morgan, G. L. Niebur, G. E. Morris, E. K. Wong and T. M. Keaveny. "Comparison of the Elastic and Yield Properties of Human Femoral Trabecular and Cortical Bone Tissue." J Biomech 37, no. 1 (2004): 27-35.

13. Bell, R. B. "Computer Planning and Intraoperative Navigation in Cranio-Maxillofacial Surgery." Oral Maxillofac Surg Clin North Am 22, no. 1 (2010): 135-56.

14. Ben-Nissan, B. "Three-Dimensional Modelling and Finite Element Distortion Analysis of the Mandible." Ph.D. Dissertation, University of New South Wales - Australia, 1987.

15. Ben-Nissan, B. ; Svensson, N.L.; Kelly, D.W. and Vajda, T.T. "Computer Aided Three-Dimensional Modelling and Finite Element Analysis of the Mandible. ." In Fifth International Conference in Australia on Finite Element Methods, edited by J.F. Stevens Williams, L.K., 290-294. Melbourne, VIC Australia: University of Melbourne, Faculty of Engineering, in association with The Institution of Engineers, Australia, 1987.

16. Bertossi, D., A. Lucchese, M. Albanese, M. Turra, F. Faccioni, P. Nocini and Y. Baena R. Rodriguez. "Piezosurgery Versus Conventional Osteotomy in Orthognathic Surgery: A Paradigm Shift in Treatment." J Craniofac Surg 24, no. 5 (2013): 1763-6.

17. Bitsakos, C., J. Kerner, I. Fisher and A. A. Amis. "The Effect of Muscle Loading on the Simulation of Bone Remodelling in the Proximal Femur." J Biomech 38, no. 1 (2005): 133-9.

18. Bonnet, A. S., M. Postaire and P. Lipinski. "Biomechanical Study of Mandible Bone Supporting a Four-Implant Retained Bridge: Finite Element Analysis of the Influence of Bone Anisotropy and Foodstuff Position." Med Eng Phys 31, no. 7 (2009): 806-15.

19. Bragger, U., P. Krenander and N. P. Lang. "Economic Aspects of Single-Tooth Replacement." Clin Oral Implants Res 16, no. 3 (2005): 335-41.

20. Branemark, P. I. "Osseointegration and Its Experimental Background." J Prosthet Dent 50, no. 3 (1983): 399-410.

21. Branemark, R., L. O. Ohrnell, P. Nilsson and P. Thomsen. "Biomechanical Characterization of Osseointegration During Healing: An Experimental in Vivo Study in the Rat." Biomaterials 18, no. 14 (1997): 969-78.

22. Brief, J., D. Edinger, S. Hassfeld and G. Eggers. "Accuracy of Image-Guided Implantology." Clin Oral Implants Res 16, no. 4 (2005): 495-501.

23. Brodala, N. "Flapless Surgery and Its Effect on Dental Implant Outcomes." Int J Oral Maxillofac Implants 24 Suppl, (2009): 118-25.

24. Brown, Terry, Lawrence Kohan and Bessim Ben-Nissan. "Hp15: Finite Element Analysis and Surgical Considerations of the Impact of Osteoporosis and Osteoarthritis on Hip Resurfacing." Orthopaedic Proceedings 92-B, no. SUPP I (2010): 184-184.

25. Brunski, J. B. "Biomechanics of Oral Implants: Future Research Directions." J Dent Educ 52, no. 12 (1988): 775-87.

26. Bujtar, P., G. K. Sandor, A. Bojtos, A. Szucs and J. Barabas. "Finite Element Analysis of the Human Mandible at 3 Different Stages of Life." Oral Surg Oral Med Oral Pathol Oral Radiol Endod 110, no. 3 (2010): 301-9.

27. Bujtar, P., G. K. Sandor, A. Bojtos, A. Szucs and J. Barabas. "Finite Element Analysis of the Human Mandible at 3 Different Stages of Life." Oral Surg Oral Med Oral Pathol Oral Radiol Endod 110, no. 3 (2010): 301-9.

28. Bujtar, P., J. Simonovics, G. Zombori, Z. Fejer, A. Szucs, A. Bojtos, W. O. Batista, K. Varadi and G. K. Sandor. "Internal or in-Scan Validation: A Method to Assess Cbct and Msct Gray Scales Using a Human Cadaver." Oral Surg Oral Med Oral Pathol Oral Radiol 117, no. 6 (2014): 768-79.

29. Burstein, A. H., D. T. Reilly and M. Martens. "Aging of Bone Tissue: Mechanical Properties." J Bone Joint Surg Am 58, no. 1 (1976): 82-6.

30. Burstein, A. H., D. T. Reilly and M. Martens. "Aging of Bone Tissue: Mechanical Properties." J Bone Joint Surg Am 58, no. 1 (1976): 82-6.

31. Canullo, L., D. Penarrocha, M. Penarrocha, A. G. Rocio and M. Penarrocha-Diago. "Piezoelectric Vs. Conventional Drilling in Implant Site Preparation: Pilot Controlled Randomized Clinical Trial with Crossover Design." Clin Oral Implants Res 25, no. 12 (2014): 1336-43.

32. Caputo, A. et al. Biomechanics in Clinical Dentistry. Chicago: Quintessence, 1987.

33. Carter, D. R. and W. C. Hayes. "The Compressive Behavior of Bone as a Two-Phase Porous Structure." J Bone Joint Surg Am 59, no. 7 (1977): 954-62.

34. Carter, D. R. and D. M. Spengler. "Mechanical Properties and Composition of Cortical Bone." Clin Orthop Relat Res, no. 135 (1978): 192-217.

35. Casap, N., A. Wexler and R. Eliashar. "Computerized Navigation for Surgery of the Lower Jaw: Comparison of 2 Navigation Systems." J Oral Maxillofac Surg 66, no. 7 (2008): 1467-75.

36. Casap, N., A. Wexler and J. Lustmann. "Image-Guided Navigation System for Placing Dental Implants." Compend Contin Educ Dent 25, no. 10 (2004): 783-4, 786, 788 passim; quiz 794-5.

37. Casap, N., A. Wexler, N. Persky, A. Schneider and J. Lustmann. "Navigation Surgery for Dental Implants: Assessment of Accuracy of the Image Guided Implantology System." J Oral Maxillofac Surg 62, no. 9 Suppl 2 (2004): 116-9.

38. Chen, S. Y., P. E. Lestrel, W. J. Kerr and J. H. McColl. "Describing Shape Changes in the Human Mandible Using Elliptical Fourier Functions." Eur J Orthod 22, no. 3 (2000): 205-16.

39. Chen, X., Y. Lin, C. Wang, G. Shen, S. Zhang and X. Wang. "A Surgical Navigation System for Oral and Maxillofacial Surgery and Its Application in the Treatment of Old Zygomatic Fractures." Int J Med Robot 7, no. 1 (2011): 42-50.

40. Chen, X., Y. Wu and C. Wang. "Application of a Surgical Navigation System in the Rehabilitation of Maxillary Defects Using Zygoma Implants: Report of One Case." Int J Oral Maxillofac Implants 26, no. 5 (2011): e29-34.

41. Choi, A. H., B. Ben-Nissan and R. C. Conway. "Three-Dimensional Modelling and Finite Element Analysis of the Human Mandible During Clenching." Aust Dent J 50, no. 1 (2005): 42-8.

42. Choi, A. H., R. C. Conway and B. Ben-Nissan. "Finite-Element Modeling and Analysis in Nanomedicine and Dentistry." Nanomedicine (Lond) 9, no. 11 (2014): 1681-95.

43. Choi, A. H., J. Matinlinna and B. Ben-Nissan. "Effects of Micromovement on the Changes in Stress Distribution of Partially Stabilized Zirconia (Ps-Zro2) Dental Implants and Bridge During Clenching: A Three-Dimensional Finite Element Analysis." Acta Odontol Scand 71, no. 1 (2013): 72-81.

44. Choi, A. H., J. P. Matinlinna and B. Ben-Nissan. "Finite Element Stress Analysis of Ti-6al-4v and Partially Stabilized Zirconia Dental Implant During Clenching." Acta

Odontol Scand 70, no. 5 (2012): 353-61.

45. Claire, S., S. C. Lea and A. D. Walmsley. "Characterisation of Bone Following Ultrasonic Cutting." Clin Oral Investig 17, no. 3 (2013): 905-12.

46. Cleary, K., H. Zhang, N. Glossop, E. Levy, B. Wood and F. Banovac. "Electromagnetic Tracking for Image-Guided Abdominal Procedures: Overall System and Technical Issues." Conf Proc IEEE Eng Med Biol Soc 7, (2005): 6748-53.

47. Cody, D. D., D. A. McCubbrey, G. W. Divine, G. J. Gross and S. A. Goldstein. "Predictive Value of Proximal Femoral Bone Densitometry in Determining Local Orthogonal Material Properties." J Biomech 29, no. 6 (1996): 753-61.

48. Cordioli, G. and Z. Majzoub. "Heat Generation During Implant Site Preparation: An in Vitro Study." Int J Oral Maxillofac Implants 12, no. 2 (1997): 186-93.

49. Cordioli, G., Z. Majzoub, A. Piattelli and A. Scarano. "Removal Torque and Histomorphometric Investigation of 4 Different Titanium Surfaces: An Experimental Study in the Rabbit Tibia." Int J Oral Maxillofac Implants 15, no. 5 (2000): 668-74.

50. Cowin, S. C. and M. M. Mehrabadi. "Identification of the Elastic Symmetry of Bone and Other Materials." J Biomech 22, no. 6-7 (1989): 503-15.

51. Crowninshield, R. D. "Use of Optimization Techniques to Predict Muscle Forces." Journal of Biomechanical Engineering 100, no. 2 (1978): 88-92.

52. Currey, J. D. "Tensile Yield in Compact Bone Is Determined by Strain, Post-Yield Behaviour by Mineral Content." J Biomech 37, no. 4 (2004): 549-56.

53. da Silva Neto, U. T., J. C. Joly and S. A. Gehrke. "Clinical Analysis of the Stability of Dental Implants after Preparation of the Site by Conventional Drilling or Piezosurgery." Br J Oral Maxillofac Surg 52, no. 2 (2014): 149-53.

54. Dang, H., Y. Otake, S. Schafer, J. W. Stayman, G. Kleinszig and J. H. Siewerdsen. "Robust Methods for Automatic Image-to-World Registration in Cone-Beam Ct Interventional Guidance." Med Phys 39, no. 10 (2012): 6484-98.

55. De Santis, R., F. Mollica, R. Esposito, L. Ambrosio and L. Nicolais. "An Experimental and Theoretical Composite Model of the Human Mandible." J Mater Sci Mater Med 16, no. 12 (2005): 1191-7.

56. Di Giacomo, G. A., P. R. Cury, N. S. de Araujo, W. R. Sendyk and C. L. Sendyk. "Clinical Application of Stereolithographic Surgical Guides for Implant Placement: Preliminary Results." J Periodontol 76, no. 4 (2005): 503-7.

57. Ding, X., X. H. Zhu, S. H. Liao, X. H. Zhang and H. Chen. "Implant-Bone Interface Stress Distribution in Immediately Loaded Implants of Different Diameters: A Three-Dimensional Finite Element Analysis." J Prosthodont 18, no. 5 (2009): 393-402.

58. Eggers, G., E. Patellis and J. Muhling. "Accuracy of Template-Based Dental Implant Placement." Int J Oral Maxillofac Implants 24, no. 3 (2009): 447-54.

59. English, C., O. Bahat, B. Langer and C. G. Sheets. "What Are the Clinical Limitations of Wide-Diameter (4 Mm or Greater) Root-Form Endosseous Implants?" Int J Oral Maxillofac Implants 15, no. 2 (2000): 293-6.

60. Eskitascioglu, G., A. Usumez, M. Sevimay, E. Soykan and E. Unsal. "The Influence of Occlusal Loading Location on Stresses Transferred to Implant-Supported Prostheses and Supporting Bone: A Three-Dimensional Finite Element Study." J Prosthet Dent 91, no. 2 (2004): 144-50.

61. Fazi, G., S. Tellini, D. Vangi and R. Branchi. "Three-Dimensional Finite Element Analysis of Different Implant Configurations for a Mandibular Fixed Prosthesis." Int J Oral Maxillofac Implants 26, no. 4 (2011): 752-9.

62. Fitzpatrick, J. M., J. B. West and C. R. Maurer, Jr. "Predicting Error in Rigid-Body Point-Based Registration." IEEE Trans Med Imaging 17, no. 5 (1998): 694-702.

63. Frank, L. "Muscular Influence on Occlusion as Shown by X-Rays of the Condyle." Dent Dig 56, no. 11 (1950): 484-8.

64. Frost, H. M. "From Wolff's Law to the Utah Paradigm: Insights About Bone Physiology and Its Clinical Applications." Anat Rec 262, no. 4 (2001): 398-419.

65. Futterling, S. et al. "Automated Finite Element Modelling of a Human Mandible with Dental Implants." In Sixth international conference in central Europe on computer graphics and visualisation, edited by University W Bohemia. Plzen, Czech Republic, 1998.

66. Gandhi, S. A., J. A. Baker, L. Bairam, H. I. Kim, E. L. Davis and S. Andreana. "Primary Stability Comparison Using Piezoelectric or Conventional Implant Site Preparation Systems in Cancellous Bone: A Pilot Study." Implant Dent 23, no. 1 (2014): 79-84.

67. Gates, G. N. and J. I. Nicholls. "Evaluation of Mandibular Arch Width Change." J Prosthet Dent 46, no. 4 (1981): 385-92.

68. Geng, J. P., K. B. Tan and G. R. Liu. "Application of Finite Element Analysis in Implant Dentistry: A Review of the Literature." J Prosthet Dent 85, no. 6 (2001):

585-98.

69. Gershenfeld, N. The Nature of Mathematical Modeling: Cambridge University Press, 1999.

70. Gibson, L. J.; Ashby, M.F. Cellular Solids Structure and Properties: Cambridge University Press, 1999.

71. Giesen, E. B. and T. M. van Eijden. "The Three-Dimensional Cancellous Bone Architecture of the Human Mandibular Condyle." J Dent Res 79, no. 4 (2000): 957-63.

72. Gingerich, P. D. Functional Significance of Mandibular Translation in Vertebrate Jaw Mechanics. Peabody Museum of Natural History: Yale University, 1971.

73. Goldstein, S. A. "The Mechanical Properties of Trabecular Bone: Dependence on Anatomic Location and Function." J Biomech 20, no. 11-12 (1987): 1055-61.

74. Gotfredsen, K., T. Berglundh and J. Lindhe. "Anchorage of Titanium Implants with Different Surface Characteristics: An Experimental Study in Rabbits." Clin Implant Dent Relat Res 2, no. 3 (2000): 120-8.

75. Guan, H., R. van Staden, Y. C. Loo, N. Johnson, S. Ivanovski and N. Meredith. "Influence of Bone and Dental Implant Parameters on Stress Distribution in the Mandible: A Finite Element Study." Int J Oral Maxillofac Implants 24, no. 5 (2009): 866-76.

76. Gur, Y. "Additive Manufacturing of Anatomical Models from Computed Tomography Scan Data." Mol Cell Biomech 11, no. 4 (2014): 249-58.

77. Hammerle, C. H., P. Stone, R. E. Jung, T. Kapos and N. Brodala. "Consensus Statements and Recommended Clinical Procedures Regarding Computer-Assisted Implant Dentistry." Int J Oral Maxillofac Implants 24 Suppl, (2009): 126-31.

78. Hara, S., M. Mitsugi, T. Kanno and Y. Tatemoto. "Computer-Aided Design Provisionalization and Implant Insertion Combined with Optical Scanning of Plaster Casts and Computed Tomography Data." Ann Maxillofac Surg 4, no. 1 (2014): 64-9.

79. Hart, R. T., V. V. Hennebel, N. Thongpreda, W. C. Van Buskirk and R. C. Anderson. "Modeling the Biomechanics of the Mandible: A Three-Dimensional Finite Element Study." J Biomech 25, no. 3 (1992): 261-86.

80. Haskell, B., M. Day and J. Tetz. "Computer-Aided Modeling in the Assessment of the Biomechanical Determinants of Diverse Skeletal Patterns." Am J Orthod 89, no. 5 (1986): 363-82.

81. Helgason, B., E. Perilli, E. Schileo, F. Taddei, S. Brynjolfsson and M. Viceconti. "Mathematical Relationships between Bone Density and Mechanical Properties: A Literature Review." Clin Biomech (Bristol, Avon) 23, no. 2 (2008): 135-46.

82. Helgason, B., F. Taddei, H. Palsson, E. Schileo, L. Cristofolini, M. Viceconti and S. Brynjolfsson. "A Modified Method for Assigning Material Properties to Fe Models of Bones." Med Eng Phys 30, no. 4 (2008): 444-53.

83. Himmlova, L., T. Dostalova, A. Kacovsky and S. Konvickova. "Influence of Implant Length and Diameter on Stress Distribution: A Finite Element Analysis." J Prosthet Dent 91, no. 1 (2004): 20-5.

84. Hirabayashi, M., M. Motoyoshi, T. Ishimaru, K. Kasai and S. Namura. "Stresses in Mandibular Cortical Bone During Mastication: Biomechanical Considerations Using a Three-Dimensional Finite Element Method." J Oral Sci 44, no. 1 (2002): 1-6.

85. Hobkirk, J. A. and T. K. Havthoulas. "The Influence of Mandibular Deformation, Implant Numbers, and Loading Position on Detected Forces in Abutments Supporting Fixed Implant Superstructures." J Prosthet Dent 80, no. 2 (1998): 169-74.

86. Hoffmann, B. and A. Sepehrnia. "Taylored Implants for Alloplastic Cranioplasty–Clinical and Surgical Considerations." Acta Neurochir Suppl 93, (2005): 127-9.

87. Hoffmann, J., C. Westendorff, G. Gomez-Roman and S. Reinert. "Accuracy of Navigation-Guided Socket Drilling before Implant Installation Compared to the Conventional Free-Hand Method in a Synthetic Edentulous Lower Jaw Model." Clin Oral Implants Res 16, no. 5 (2005): 609-14.

88. Hsu, C. "Medical Image Processing for Fully Integrated Subject Specific Whole Brain Mesh Generation." Technologies 3, no. 2 (2015): 126-141.

89. Huang, H. L., C. L. Lin, C. C. Ko, C. H. Chang, J. T. Hsu and J. S. Huang. "Stress Analysis of Implant-Supported Partial Prostheses in Anisotropic Mandibular Bone: In-Line Versus Offset Placements of Implants." J Oral Rehabil 33, no. 7 (2006): 501-8.

90. Hultin, M., K. G. Svensson and M. Trulsson. "Clinical Advantages of Computer-Guided Implant Placement: A Systematic Review." Clin Oral Implants Res 23 Suppl 6, (2012): 124-35.

91. Hussein, M. O. and M. E. Rabie. "Three-Dimensional Nonlinear Contact Finite Element Analysis of Mandibular All-on-4 Design." J Oral Implantol 41, no. 2 (2015): e12-8.

92. Hylander, W. L. "The Human Mandible: Lever or Link?" Am J Phys Anthropol 43, no. 2 (1975): 227-42.

93. Hylander, W. L. "Incisal Bite Force Direction in Humans and the Functional Significance of Mammalian Mandibular Translation." Am J Phys Anthropol 48, no. 1 (1978): 1-7.

94. Hylander, W. L. "Stress and Strain in the Mandibular Symphysis of Primates: A Test of Competing Hypotheses." Am J Phys Anthropol 64, no. 1 (1984): 1-46.

95. Hylander, W. L., K. R. Johnson and A. W. Crompton. "Loading Patterns and Jaw Movements During Mastication in Macaca Fascicularis: A Bone-Strain, Electromyographic, and Cineradiographic Analysis." Am J Phys Anthropol 72, no. 3 (1987): 287-314.

96. Jirousek, O. Nanoindentation of Human Trabecular Bone ? Tissue Mechanical Properties Compared to Standard Engineering Test Methods Nanoindentation in Materials Science, edited by Dr. Jiri Nemecek, 2012.

97. Jo KH, Park KS, Bae JH, You KH, Han JH, Shin JM, Baik JS, Jeon IS, Cheong JK. "Thermally Induced Bone Necrosis During Implant Surgery: 3 Case Reports." Journal of Korean Association of Oral and Maxillofacial Surgery 37, no. 5 (2011): 406-414.

98. Jonasson, G., F. Lindberg, A. Jorge, T. Alstad and H. Kashani. "Mandibular Trabecular Bone Structure in Adults with Crohn's Disease." Clin Oral Investig 18, no. 2 (2014): 423-8.

99. Jung, R. E., D. Schneider, J. Ganeles, D. Wismeijer, M. Zwahlen, C. H. Hammerle and A. Tahmaseb. "Computer Technology Applications in Surgical Implant Dentistry: A Systematic Review." Int J Oral Maxillofac Implants 24 Suppl, (2009): 92-109.

100. Kaneko, T. S., M. R. Pejcic, J. Tehranzadeh and J. H. Keyak. "Relationships between Material Properties and Ct Scan Data of Cortical Bone with and without Metastatic Lesions." Med Eng Phys 25, no. 6 (2003): 445-54.

101. Kang, S. H., J. W. Lee, S. H. Lim, Y. H. Kim and M. K. Kim. "Verification of the Usability of a Navigation Method in Dental Implant Surgery: In Vitro Comparison with the Stereolithographic Surgical Guide Template Method." J Craniomaxillofac Surg 42, no. 7 (2014): 1530-5.

102. Katz, A., I. Kaffe, M. Littner, M. Tagger and A. Tamse. "Densitometric Measurement of Radiopacity of Gutta-Percha Cones and Root Dentin." J Endod 16, no. 5 (1990): 211-3.

103. Kavanagh, E. P., C. Frawley, G. Kearns, F. Wallis, T. McGloughlin and J. Jarvis. "Use of Finite Element Analysis in Presurgical Planning: Treatment of Mandibular Fractures." Ir J Med Sci 177, no. 4 (2008): 325-31.

104. Kawahara, H., D. Kawahara, M. Hayakawa, Y. Tamai, T. Kuremoto and S. Matsuda. "Osseointegration under Immediate Loading: Biomechanical Stress-Strain and Bone Formation–Resorption." Implant Dent 12, no. 1 (2003): 61-8.

105. Keaveny, T. M. and W. C. Hayes. "A 20-Year Perspective on the Mechanical Properties of Trabecular Bone." J Biomech Eng 115, no. 4B (1993): 534-42.

106. Keller, T. S. "Predicting the Compressive Mechanical Behavior of Bone." J Biomech 27, no. 9 (1994): 1159-68.

107. Keyak, J. H., M. G. Fourkas, J. M. Meagher and H. B. Skinner. "Validation of an Automated Method of Three-Dimensional Finite Element Modelling of Bone." J Biomed Eng 15, no. 6 (1993): 505-9.

108. Kim, S. G., W. J. Lee, S. S. Lee, M. S. Heo, K. H. Huh, S. C. Choi, T. I. Kim and W. J. Yi. "An Advanced Navigational Surgery System for Dental Implants Completed in a Single Visit: An in Vitro Study." J Craniomaxillofac Surg 43, no. 1 (2015): 117-25.

109. Kim, S. G., W. J. Lee, S. S. Lee, M. S. Heo, K. H. Huh, S. C. Choi, T. I. Kim and W. J. Yi. "An Advanced Navigational Surgery System for Dental Implants Completed in a Single Visit: An in Vitro Study." J Craniomaxillofac Surg 43, no. 1 (2015): 117-25.

110. Kitagawa, T., Y. Tanimoto, K. Nemoto and M. Aida. "Influence of Cortical Bone Quality on Stress Distribution in Bone around Dental Implant." Dent Mater J 24, no. 2 (2005): 219-24.

111. Knoell, A. C. "A Mathematical Model of an in Vitro Human Mandible." J Biomech 10, no. 3 (1977): 159-66.

112. Kollner, H. J. "[the Registration of the Retrusive Closing Phase and Its Effect on the Mandible]." Zahn Mund Kieferheilkd Zentralbl 66, no. 8 (1978): 792-6.

113. Koolstra, J. H. and T. M. van Eijden. "Combined Finite-Element and Rigid-Body Analysis of Human Jaw Joint Dynamics." J Biomech 38, no. 12 (2005): 2431-9.

114. Korioth, T. W., D. P. Romilly and A. G. Hannam. "Three-Dimensional Finite Element Stress Analysis of the Dentate Human Mandible." Am J Phys Anthropol 88, no. 1 (1992): 69-96.

115. Kramer, F. J., C. Baethge, G. Swennen and S. Rosahl. "Navigated Vs. Conventional Implant Insertion for Maxillary Single Tooth Replacement." Clin Oral Implants Res 16, no. 1 (2005): 60-8.

116. Lakatos, L. et al. "Material Properties of the Mandibular Trabecular Bone." Journal of Medical Engineering 2014, (2014): 7.

117. Lange, T., S. Eulenstein, M. Hunerbein and P. M. Schlag. "Vessel-Based Non-Rigid Registration of Mr/Ct and 3d Ultrasound for Navigation in Liver Surgery." Comput Aided Surg 8, no. 5 (2003): 228-40.

118. Lappi, V.G.; King, M.S., LeMay, I. "Determination of Elastic Constants for Human Femurs." Journal of Biomechanical Engineering, no. 101 (1979): 193-197.

119. Lattanzi, R., M. Viceconti, C. Zannoni, P. Quadrani and A. Toni. "Hip-Op: An Innovative Software to Plan Total Hip Replacement Surgery." Med Inform Internet Med 27, no. 2 (2002): 71-83.

120. Lee, J. D., C. H. Huang, S. T. Wang, C. W. Lin and S. T. Lee. "Fast-Micp for Frameless Image-Guided Surgery." Med Phys 37, no. 9 (2010): 4551-9.

121. Lehman, M. L. "Stress-Distribution in the Alveolar Bone." J Biomech 1, no. 2 (1968): 139-45.

122. Lewis, M., K. Reid and A. P. Toms. "Reducing the Effects of Metal Artefact Using High Kev Monoenergetic Reconstruction of Dual Energy Ct (Dect) in Hip Replacements." Skeletal Radiol 42, no. 2 (2013): 275-82.

123. Li, P., Z. Li, W. Tian and W. Tang. "A Strategy for Removal of Foreign Body in Mandible with Navigation System." Int J Oral Maxillofac Surg 44, no. 7 (2015): 885-8.

124. Li, P., Y. Tang, J. Li, L. Shen, W. Tian and W. Tang. "Establishment of Sequential Software Processing for a Biomechanical Model of Mandibular Reconstruction with Custom-Made Plate." Comput Methods Programs Biomed 111, no. 3 (2013): 642-9.

125. Li, T., L. Kong, Y. Wang, K. Hu, L. Song, B. Liu, D. Li, J. Shao and Y. Ding. "Selection of Optimal Dental Implant Diameter and Length in Type Iv Bone: A Three-Dimensional Finite Element Analysis." Int J Oral Maxillofac Surg 38, no. 10 (2009): 1077-83.

126. Li, W., M. V. Swain, Q. Li and G. P. Steven. "Towards Automated 3d Finite Element Modeling of Direct Fiber Reinforced Composite Dental Bridge." J Biomed Mater Res B Appl Biomater 74, no. 1 (2005): 520-8.

127. Lin, D., Q. Li, W. Li and M. Swain. "Dental Implant Induced Bone Remodeling and Associated Algorithms." J Mech Behav Biomed Mater 2, no. 5 (2009): 410-32.

128. Lin, S., S. Shi, R. Z. LeGeros and J. P. LeGeros. "Three-Dimensional Finite Element Analyses of Four Designs of a High-Strength Silicon Nitride Implant." Implant Dent 9, no. 1 (2000): 53-60.

129. Lonner, J. H., J. R. Smith, F. Picard, B. Hamlin, P. J. Rowe and P. E. Riches. "High Degree of Accuracy of a Novel Image-Free Handheld Robot for Unicondylar Knee Arthroplasty in a Cadaveric Study." Clin Orthop Relat Res 473, no. 1 (2015): 206-12.

130. Lozada, J. L., M. F. Abbate, F. A. Pizzarello and R. A. James. "Comparative Three-Dimensional Analysis of Two Finite-Element Endosseous Implant Designs." J Oral Implantol 20, no. 4 (1994): 315-21.

131. Lubbers, H. T., F. Matthews, W. Zemann, K. W. Gratz, J. A. Obwegeser and M. Bredell. "Registration for Computer-Navigated Surgery in Edentulous Patients: A Problem-Based Decision Concept." J Craniomaxillofac Surg 39, no. 6 (2011): 453-8.

132. Luebbers, H. T., P. Messmer, J. A. Obwegeser, R. A. Zwahlen, R. Kikinis, K. W. Graetz and F. Matthews. "Comparison of Different Registration Methods for Surgical Navigation in Cranio-Maxillofacial Surgery." J Craniomaxillofac Surg 36, no. 2 (2008): 109-16.

133. Ma, D., F. Lin and K. C. Chua. "Rapid Prototyping Applications in Medicine. Part 2: Stl File Generation and Case Studies." The International Journal of Advanced Manufacturing Technology 18, no. 2 (2001): 118-127.

134. Marcian, P., L. Borak, J. Valasek, J. Kaiser, Z. Florian and J. Wolff. "Finite Element Analysis of Dental Implant Loading on Atrophic and Non-Atrophic Cancellous and Cortical Mandibular Bone - a Feasibility Study." J Biomech 47, no. 16 (2014): 3830-6.

135. Mariano, LOH et al. "Stresses in Implant-Supported Overdentures with Bone Resorption: A 3-D Finite Element Analysis." Revista Odonto Ciencia Journal Of Dental Science 27, no. 1 (2012).

136. Markiewicz, M. R., E. J. Dierks and R. B. Bell. "Does Intraoperative Navigation Restore Orbital Dimensions in Traumatic and Post-Ablative Defects?" J Craniomaxillofac Surg 40, no. 2 (2012): 142-8.

137. McCalden, R. W., J. A. McGeough, M. B. Barker and C. M. Court-Brown. "Age-Related Changes in the Tensile Properties of Cortical Bone. The Relative Importance of Changes in Porosity, Mineralization, and Microstructure." J Bone Joint Surg Am 75, no. 8 (1993): 1193-205.

138. McClarance, E. "Close to the Edge: Branemark and the Development of Osseointegration." Quintessence Publishing, (2004).

139. Meijer, H. J., F. J. Starmans, W. H. Steen and F. Bosman. "Loading Conditions of Endosseous Implants in an Edentulous Human Mandible: A Three-Dimensional, Finite-Element Study." J Oral Rehabil 23, no. 11 (1996): 757-63.

140. Menicucci, G., A. Mossolov, M. Mozzati, M. Lorenzetti and G. Preti. "Tooth-Implant Connection: Some Biomechanical Aspects Based on Finite Element Analyses." Clin Oral Implants Res 13, no. 3 (2002): 334-41.

141. Meyer, U., U. Joos, J. Mythili, T. Stamm, A. Hohoff, T. Fillies, U. Stratmann and H. P. Wiesmann. "Ultrastructural Characterization of the Implant/Bone Interface of Immediately Loaded Dental Implants." Biomaterials 25, no. 10 (2004): 1959-67.

142. Meyer, U., D. Vollmer, C. Homann, R. Schuon, S. Benthaus, A. Vegh, E. Felszegi, U. Joos and J. Piffko. "Experimental and Finite-Element Models for the Assessment of Mandibular Deformation under Mechanical Loading." Mund-, Kiefer- und Gesichtschirurgie 4, no. 1 (2000): 14-20.

143. Meyer, U., D. Vollmer, C. Runte, C. Bourauel and U. Joos. "Bone Loading Pattern around Implants in Average and Atrophic Edentulous Maxillae: A Finite-Element Analysis." J Craniomaxillofac Surg 29, no. 2 (2001): 100-5.

144. Meyer, U., H. P. Wiesmann, C. Runte, T. Fillies, N. Meier, T. Lueth and U. Joos. "Evaluation of Accuracy of Insertion of Dental Implants and Prosthetic Treatment by Computer-Aided Navigation in Minipigs." Br J Oral Maxillofac Surg 41, no. 2 (2003): 102-8.

145. Mischkowski, R. A., M. J. Zinser, J. Neugebauer, A. C. Kubler and J. E. Zoller. "Comparison of Static and Dynamic Computer-Assisted Guidance Methods in Implantology." Int J Comput Dent 9, no. 1 (2006): 23-35.

146. Mishra, S. K. and R. Chowdhary. "Heat Generated by Dental Implant Drills During Osteotomy-a Review: Heat Generated by Dental Implant Drills." J Indian Prosthodont Soc 14, no. 2 (2014): 131-43.

147. Miyamoto, I., Y. Tsuboi, E. Wada, H. Suwa and T. Iizuka. "Influence of Cortical Bone Thickness and Implant Length on Implant Stability at the Time of Surgery–Clinical, Prospective, Biomechanical, and Imaging Study." Bone 37, no. 6 (2005): 776-80.

148. Mohagheghi, S., A. Ahmadian and S. Yaghoobee. "Accuracy Assessment of a Marker-Free Method for Registration of Ct and Stereo Images Applied in Image-Guided Implantology: A Phantom Study." J Craniomaxillofac Surg 42, no. 8 (2014): 1977-84.

149. Mongini, F., P. M. Calderale and G. Barberi. "Relationship between Structure and the Stress Pattern in the Human Mandible." J Dent Res 58, no. 12 (1979): 2334-7.

150. Morgan, E. F., H. H. Bayraktar, O. C. Yeh, S. Majumdar, A. Burghardt and T. M. Keaveny. "Contribution of Inter-Site Variations in Architecture to Trabecular Bone Apparent Yield Strains." J Biomech 37, no. 9 (2004): 1413-20.

151. Motoyoshi, M., S. Ueno, K. Okazaki and N. Shimizu. "Bone Stress for a Mini-Implant Close to the Roots of Adjacent Teeth–3d Finite Element Analysis." Int J Oral Maxillofac Surg 38, no. 4 (2009): 363-8.

152. Naftulin, J. S., E. Y. Kimchi and S. S. Cash. "Streamlined, Inexpensive 3d Printing of the Brain and Skull." PLoS One 10, no. 8 (2015): e0136198.

153. Nagasue, N., Y. Funama, R. Oniki, A. Segawa, S. Iwatake, T. Kawachino and M. Uetani. "[Combinations of Scan Parameters and Image Quality at C-Arm Ct for Abdominal Imaging]." Nihon Hoshasen Gijutsu Gakkai Zasshi 65, no. 6 (2009): 765-72.

154. Naini, R. B., S. Nokar, H. Borghei and M. Alikhasi. "Tilted or Parallel Implant Placement in the Completely Edentulous Mandible? A Three-Dimensional Finite Element Analysis." Int J Oral Maxillofac Implants 26, no. 4 (2011): 776-81.

155. Natali, A. N., P. G. Pavan and A. L. Ruggero. "Analysis of Bone-Implant Interaction Phenomena by Using a Numerical Approach." Clin Oral Implants Res 17, no. 1 (2006): 67-74.

156. Nickenig, H. J., M. Wichmann, S. Eitner, J. E. Zoller and M. Kreppel. "Lingual Concavities in the Mandible: A Morphological Study Using Cross-Sectional Analysis Determined by Cbct." J Craniomaxillofac Surg 43, no. 2 (2015): 254-9.

157. Niebur, G. L., M. J. Feldstein, J. C. Yuen, T. J. Chen and T. M. Keaveny. "High-Resolution Finite Element Models with Tissue Strength Asymmetry Accurately Predict Failure of Trabecular Bone." J Biomech 33, no. 12 (2000): 1575-83.

158. Nomura, T., E. Gold, M. P. Powers, S. Shingaki and J. L. Katz. "Micromechanics/Structure Relationships in the Human Mandible." Dent Mater 19, no. 3 (2003): 167-73.

159. Novelli, G., G. Tonellini, F. Mazzoleni, A. Bozzetti and D. Sozzi. "Virtual Surgery Simulation in Orbital Wall Reconstruction: Integration of Surgical Navigation and Stereolithographic Models." J Craniomaxillofac Surg 42, no. 8 (2014): 2025-34.

160. Okumura, N., R. Stegaroiu, E. Kitamura, K. Kurokawa and S. Nomura. "Influence of Maxillary Cortical Bone Thickness, Implant Design and Implant Diameter on Stress

around Implants: A Three-Dimensional Finite Element Analysis." J Prosthodont Res 54, no. 3 (2010): 133-42.

161. O'Mahony, A., Q. Bowles, G. Woolsey, S. J. Robinson and P. Spencer. "Stress Distribution in the Single-Unit Osseointegrated Dental Implant: Finite Element Analyses of Axial and Off-Axial Loading." Implant Dent 9, no. 3 (2000): 207-18.

162. O'Mahony, A. M., J. L. Williams, J. O. Katz and P. Spencer. "Anisotropic Elastic Properties of Cancellous Bone from a Human Edentulous Mandible." Clin Oral Implants Res 11, no. 5 (2000): 415-21.

163. O'Mahony, A. M., J. L. Williams and P. Spencer. "Anisotropic Elasticity of Cortical and Cancellous Bone in the Posterior Mandible Increases Peri-Implant Stress and Strain under Oblique Loading." Clin Oral Implants Res 12, no. 6 (2001): 648-57.

164. Ota, T., I. Yamamoto and R. Morita. "Fracture Simulation of the Femoral Bone Using the Finite-Element Method: How a Fracture Initiates and Proceeds." J Bone Miner Metab 17, no. 2 (1999): 108-12.

165. Pellegrino, G. et al. "A New Navigation System for Dental Implantology." Clinical Oral Implants Research 25, no. 10 (2014): 297.

166. Pellegrino, G. et al. "3d Piezo-Navigated Implant Site Preparation." In EAO, edited by Clinical Oral Implant Research, 26. Stockholm, 2015.

167. Pereira, C. C., W. C. Gealh, L. Meorin-Nogueira, I. R. Garcia-Junior and R. Okamoto. "Piezosurgery Applied to Implant Dentistry: Clinical and Biological Aspects." J Oral Implantol 40 Spec No, (2014): 401-8.

168. Perillo-Marcone, A., L. Ryd, K. Johnsson and M. Taylor. "A Combined Rsa and Fe Study of the Implanted Proximal Tibia: Correlation of the Post-Operative Mechanical Environment with Implant Migration." J Biomech 37, no. 8 (2004): 1205-13.

169. Petrie, C. S. and J. L. Williams. "Comparative Evaluation of Implant Designs: Influence of Diameter, Length, and Taper on Strains in the Alveolar Crest. A Three-Dimensional Finite-Element Analysis." Clin Oral Implants Res 16, no. 4 (2005): 486-94.

170. Piegl, L. "Modifying the Shape of Rational B-Splines. Part2: Surfaces." Comput. Aided Des. 21, no. 9 (1989): 538-546.

171. Pilliar, R. M., J. M. Lee and C. Maniatopoulos. "Observations on the Effect of Movement on Bone Ingrowth into Porous-Surfaced Implants." Clin Orthop Relat Res, no. 208 (1986): 108-13.

172. Porter, J. A. and J. A. von Fraunhofer. "Success or Failure of Dental Implants? A Literature Review with Treatment Considerations." Gen Dent 53, no. 6 (2005): 423-32; quiz 433, 446.

173. Preti, G., G. Martinasso, B. Peirone, R. Navone, C. Manzella, G. Muzio, C. Russo, R. A. Canuto and G. Schierano. "Cytokines and Growth Factors Involved in the Osseointegration of Oral Titanium Implants Positioned Using Piezoelectric Bone Surgery Versus a Drill Technique: A Pilot Study in Minipigs." J Periodontol 78, no. 4 (2007): 716-22.

174. Pruim, G. J., J. J. Ten Bosch and H. J. de Jongh. "Jaw Muscle Emg-Activity and Static Loading of the Mandible." J Biomech 11, no. 8-9 (1978): 389-95.

175. Qian, L., M. Todo, Y. Matsushita and K. Koyano. "Effects of Implant Diameter, Insertion Depth, and Loading Angle on Stress/Strain Fields in Implant/Jawbone Systems: Finite Element Analysis." Int J Oral Maxillofac Implants 24, no. 5 (2009): 877-86.

176. Ralph, J. P. and A. A. Caputo. "Analysis of Stress Patterns in the Human Mandible." J Dent Res 54, no. 4 (1975): 814-21.

177. Ramaglia, L., P. Toti, C. Sbordone, F. Guidetti, R. Martuscelli and L. Sbordone. "Implant Angulation: 2-Year Retrospective Analysis on the Influence of Dental Implant Angle Insertion on Marginal Bone Resorption in Maxillary and Mandibular Osseous Onlay Grafts." Clin Oral Investig 19, no. 4 (2015): 769-79.

178. Rangert, B., T. Jemt and L. Jorneus. "Forces and Moments on Branemark Implants." Int J Oral Maxillofac Implants 4, no. 3 (1989): 241-7.

179. Reilly, D. T. and A. H. Burstein. "Review Article. The Mechanical Properties of Cortical Bone." J Bone Joint Surg Am 56, no. 5 (1974): 1001-22.

180. Reilly, D. T. and A. H. Burstein. "The Elastic and Ultimate Properties of Compact Bone Tissue." J Biomech 8, no. 6 (1975): 393-405.

181. Reilly, D. T., A. H. Burstein and V. H. Frankel. "The Elastic Modulus for Bone." J Biomech 7, no. 3 (1974): 271-5.

182. Rho, J. Y. "Ultrasonic Characterisation in Determining Elastic Modulus of Trabecular Bone Material." Med Biol Eng Comput 36, no. 1 (1998): 57-9.

183. Rho, J. Y., R. B. Ashman and C. H. Turner. "Young's Modulus of Trabecular and Cortical Bone Material: Ultrasonic and Microtensile Measurements." J Biomech 26, no. 2 (1993): 111-9.

184. Rho, J. Y., L. Kuhn-Spearing and P. Zioupos. "Mechanical Properties and the Hierarchical Structure of Bone." Med Eng Phys 20, no. 2 (1998): 92-102.

185. Rieger, M. R., M. Mayberry and M. O. Brose. "Finite Element Analysis of Six Endosseous Implants." J Prosthet Dent 63, no. 6 (1990): 671-6.

186. Roberts, D. ; Tattersall, I. "Skull Form and the Mechanics of Mandibular Evolution in Mammals." Am Mus Novit, no. 2536 (1974): 1-9.

187. Rubo, J. H. and E. A. Capello Souza. "Finite-Element Analysis of Stress on Dental Implant Prosthesis." Clin Implant Dent Relat Res 12, no. 2 (2010): 105-13.

188. Ruppin, J., A. Popovic, M. Strauss, E. Spuntrup, A. Steiner and C. Stoll. "Evaluation of the Accuracy of Three Different Computer-Aided Surgery Systems in Dental Implantology: Optical Tracking Vs. Stereolithographic Splint Systems." Clin Oral Implants Res 19, no. 7 (2008): 709-16.

189. Rutkowski, J. L. "Fundamentals of Implant Dentistry: Prosthodontic Principles. Beumer J Iii, Faulkner Rf, Shah Kc, Moy Pk. Hanover Park, Ill: Quintessence Publishing, 2015." J Oral Implantol 41, no. 3 (2015): 343.

190. Scarano, A., G. Iezzi, V. Perrotti, S. Tete, G. Staiti, C. Mortellaro and C. Cappucci. "Ultrasonic Versus Drills Implant Site Preparation: A Histologic Analysis in Bovine Ribs." J Craniofac Surg 25, no. 3 (2014): 814-7.

191. Schaeren, S., C. Jaquiery, M. Heberer, M. Tolnay, T. Vercellotti and I. Martin. "Assessment of Nerve Damage Using a Novel Ultrasonic Device for Bone Cutting." J Oral Maxillofac Surg 66, no. 3 (2008): 593-6.

192. Schileo, E., E. Dall'ara, F. Taddei, A. Malandrino, T. Schotkamp, M. Baleani and M. Viceconti. "An Accurate Estimation of Bone Density Improves the Accuracy of Subject-Specific Finite Element Models." J Biomech 41, no. 11 (2008): 2483-91.

193. Schileo, E., F. Taddei, L. Cristofolini and M. Viceconti. "Subject-Specific Finite Element Models Implementing a Maximum Principal Strain Criterion Are Able to Estimate Failure Risk and Fracture Location on Human Femurs Tested in Vitro." J Biomech 41, no. 2 (2008): 356-67.

194. Schileo, E., F. Taddei, A. Malandrino, L. Cristofolini and M. Viceconti. "Subject-Specific Finite Element Models Can Accurately Predict Strain Levels in Long Bones." J Biomech 40, no. 13 (2007): 2982-9.

195. Schmidt, F., F. Lampe, R. Elfring, S. Nebelung, T. Mumme, S. Andereya, K. Radermacher, F. U. Niethard and R. Muller-Rath. "[Soft-Tissue Management in Primary Knee Arthroplasty: Common Techniques, Navigation and Force-Sensing Devices]."

Z Orthop Unfall 145, no. 5 (2007): 599-607.

196. Schneider, D., F. Schober, P. Grohmann, C. H. Hammerle and R. E. Jung. "In-Vitro Evaluation of the Tolerance of Surgical Instruments in Templates for Computer-Assisted Guided Implantology Produced by 3-D Printing." Clin Oral Implants Res 26, no. 3 (2015): 320-5.

197. Schnitman, P. A., P. S. Wohrle, J. E. Rubenstein, J. D. DaSilva and N. H. Wang. "Ten-Year Results for Branemark Implants Immediately Loaded with Fixed Prostheses at Implant Placement." Int J Oral Maxillofac Implants 12, no. 4 (1997): 495-503.

198. Schuller, S., S. Sawall, K. Stannigel, M. Hulsbusch, J. Ulrici, E. Hell and M. Kachelriess. "Segmentation-Free Empirical Beam Hardening Correction for Ct." Med Phys 42, no. 2 (2015): 794-803.

199. Seo, S. S., J. H. Seo, M. W. Sohn and Y. J. Kim. "Differences in Measurement of Lower Limb Alignment among Different Registration Methods of Navigation and Radiographs in Tka Using the Orthopilot System." Orthopedics 35, no. 10 Suppl (2012): 50-5.

200. Siessegger, M., B. T. Schneider, R. A. Mischkowski, F. Lazar, B. Krug, B. Klesper and J. E. Zoller. "Use of an Image-Guided Navigation System in Dental Implant Surgery in Anatomically Complex Operation Sites." J Craniomaxillofac Surg 29, no. 5 (2001): 276-81.

201. Skalak, R. "Biomechanical Considerations in Osseointegrated Prostheses." J Prosthet Dent 49, no. 6 (1983): 843-8.

202. Somogyi-Ganss, E., H. I. Holmes and A. Jokstad. "Accuracy of a Novel Prototype Dynamic Computer-Assisted Surgery System." Clin Oral Implants Res 26, no. 8 (2015): 882-90.

203. Stacchi, C., T. Vercellotti, L. Torelli, F. Furlan and R. Di Lenarda. "Changes in Implant Stability Using Different Site Preparation Techniques: Twist Drills Versus Piezosurgery. A Single-Blinded, Randomized, Controlled Clinical Trial." Clin Implant Dent Relat Res 15, no. 2 (2013): 188-97.

204. Strong, E. B., A. Rafii, B. Holhweg-Majert, S. C. Fuller and M. C. Metzger. "Comparison of 3 Optical Navigation Systems for Computer-Aided Maxillofacial Surgery." Arch Otolaryngol Head Neck Surg 134, no. 10 (2008): 1080-4.

205. Stubinger, S., J. Kuttenberger, A. Filippi, R. Sader and H. F. Zeilhofer. "Intraoral Piezosurgery: Preliminary Results of a New Technique." J Oral Maxillofac Surg 63, no. 9 (2005): 1283-7.

206. Sun, Y., H. T. Luebbers, J. O. Agbaje, S. Schepers, L. Vrielinck, I. Lambrichts and C. Politis. "Accuracy of Upper Jaw Positioning with Intermediate Splint Fabrication after Virtual Planning in Bimaxillary Orthognathic Surgery." J Craniofac Surg 24, no. 6 (2013): 1871-6.

207. Sun, Y., H. T. Luebbers, J. O. Agbaje, S. Schepers, L. Vrielinck, I. Lambrichts and C. Politis. "Evaluation of 3 Different Registration Techniques in Image-Guided Bimaxillary Surgery." J Craniofac Surg 24, no. 4 (2013): 1095-9.

208. Sun, Y., H. T. Luebbers, J. O. Agbaje, S. Schepers, L. Vrielinck, I. Lambrichts and C. Politis. "Validation of Anatomical Landmarks-Based Registration for Image-Guided Surgery: An in-Vitro Study." J Craniomaxillofac Surg 41, no. 6 (2013): 522-6.

209. Szmukler-Moncler, S., A. Piattelli, G. A. Favero and J. H. Dubruille. "Considerations Preliminary to the Application of Early and Immediate Loading Protocols in Dental Implantology." Clin Oral Implants Res 11, no. 1 (2000): 12-25.

210. Tada, S., R. Stegaroiu, E. Kitamura, O. Miyakawa and H. Kusakari. "Influence of Implant Design and Bone Quality on Stress/Strain Distribution in Bone around Implants: A 3-Dimensional Finite Element Analysis." Int J Oral Maxillofac Implants 18, no. 3 (2003): 357-68.

211. Taddei, F., M. Ansaloni, D. Testi and M. Viceconti. "Virtual Palpation of Skeletal Landmarks with Multimodal Display Interfaces." Med Inform Internet Med 32, no. 3 (2007): 191-8.

212. Taddei, F., A. Pancanti and M. Viceconti. "An Improved Method for the Automatic Mapping of Computed Tomography Numbers onto Finite Element Models." Med Eng Phys 26, no. 1 (2004): 61-9.

213. Taddei, F., E. Schileo, B. Helgason, L. Cristofolini and M. Viceconti. "The Material Mapping Strategy Influences the Accuracy of Ct-Based Finite Element Models of Bones: An Evaluation against Experimental Measurements." Med Eng Phys 29, no. 9 (2007): 973-9.

214. Takahashi, T., I. Shimamura and K. Sakurai. "Influence of Number and Inclination Angle of Implants on Stress Distribution in Mandibular Cortical Bone with All-on-4 Concept." J Prosthodont Res 54, no. 4 (2010): 179-84.

215. Taraschi, V. "Computed Tomography Based Patient-Matched Modelling and Finite Element Analysis of the Human Mandible." Proceedings of ISACB International Conference ISACB Abstract Book, (2010).

216. Tarnow, D. P., S. Emtiaz and A. Classi. "Immediate Loading of Threaded Implants at Stage 1 Surgery in Edentulous Arches: Ten Consecutive Case Reports with 1- to 5-Year Data." Int J Oral Maxillofac Implants 12, no. 3 (1997): 319-24.

217. Taylor, T. D. and J. R. Agar. "Twenty Years of Progress in Implant Prosthodontics." J Prosthet Dent 88, no. 1 (2002): 89-95.

218. Tehemar, S. H. "Factors Affecting Heat Generation During Implant Site Preparation: A Review of Biologic Observations and Future Considerations." Int J Oral Maxillofac Implants 14, no. 1 (1999): 127-36.

219. Tepper, G., R. Haas, W. Zechner, W. Krach and G. Watzek. "Three-Dimensional Finite Element Analysis of Implant Stability in the Atrophic Posterior Maxilla: A Mathematical Study of the Sinus Floor Augmentation." Clin Oral Implants Res 13, no. 6 (2002): 657-65.

220. Throckmorton, G. S. and L. S. Throckmorton. "Quantitative Calculations of Temporomandibular Joint Reaction Forces–I. The Importance of the Magnitude of the Jaw Muscle Forces." J Biomech 18, no. 6 (1985): 445-52.

221. Topkaya, T. and M. Y. Solmaz. "The Effect of Implant Number and Position on the Stress Behavior of Mandibular Implant Retained Overdentures: A Three-Dimensional Finite Element Analysis." J Biomech 48, no. 10 (2015): 2102-9.

222. Tsukrov, Igor, Judson C. DeCew, Kenneth Baldwin, Regina Campbell-Malone and Michael J. Moore. "Mechanics of the Right Whale Mandible: Full Scale Testing and Finite Element Analysis." Journal of Experimental Marine Biology and Ecology 374, no. 2 (2009): 93-103.

223. Van Staden, R. C., H. Guan and Y. C. Loo. "Application of the Finite Element Method in Dental Implant Research." Comput Methods Biomech Biomed Engin 9, no. 4 (2006): 257-70.

224. van Steenberghe, D., M. Quirynen, B. Svensson and P. I. Branemark. "Clinical Examples of What Can Be Achieved with Osseointegration in Anatomically Severely Compromised Patients." Periodontol 2000 33, (2003): 90-104.

225. van Zyl, P. P., N. L. Grundling, C. H. Jooste and E. Terblanche. "Three-Dimensional Finite Element Model of a Human Mandible Incorporating Six Osseointegrated Implants for Stress Analysis of Mandibular Cantilever Prostheses." Int J Oral Maxillofac Implants 10, no. 1 (1995): 51-7.

226. Ventola, C. L. "Medical Applications for 3d Printing: Current and Projected Uses." P T 39, no. 10 (2014): 704-11.

227. Vercellotti, T. "Technological Characteristics and Clinical Indications of Piezoelectric Bone Surgery." Minerva Stomatol 53, no. 5 (2004): 207-14.

228. Vercellotti, T. Essentials in Piezosurgery: Clinical Advantages in Dentistry: Quintessence, 2009.

229. Vercellotti, T., C. Stacchi, C. Russo, A. Rebaudi, G. Vincenzi, U. Pratella, D. Baldi, M. Mozzati, C. Monagheddu, R. Sentineri, T. Cuneo, L. Di Alberti, S. Carossa and G. Schierano. "Ultrasonic Implant Site Preparation Using Piezosurgery: A Multicenter Case Series Study Analyzing 3,579 Implants with a 1- to 3-Year Follow-Up." Int J Periodontics Restorative Dent 34, no. 1 (2014): 11-8.

230. Viceconti, M., G. Clapworthy, D. Testi, F. Taddei and N. McFarlane. "Multimodal Fusion of Biomedical Data at Different Temporal and Dimensional Scales." Comput Methods Programs Biomed 102, no. 3 (2011): 227-37.

231. Viceconti, M., C. Zannoni, D. Testi, M. Petrone, S. Perticoni, P. Quadrani, F. Taddei, S. Imboden and G. Clapworthy. "The Multimod Application Framework: A Rapid Application Development Tool for Computer Aided Medicine." Comput Methods Programs Biomed 85, no. 2 (2007): 138-51.

232. Vollmer, D., U. Meyer, U. Joos, A. Vegh and J. Piffko. "Experimental and Finite Element Study of a Human Mandible." J Craniomaxillofac Surg 28, no. 2 (2000): 91-6.

233. Vrielinck, L., C. Politis, S. Schepers, M. Pauwels and I. Naert. "Image-Based Planning and Clinical Validation of Zygoma and Pterygoid Implant Placement in Patients with Severe Bone Atrophy Using Customized Drill Guides. Preliminary Results from a Prospective Clinical Follow-up Study." Int J Oral Maxillofac Surg 32, no. 1 (2003): 7-14.

234. Wagner, A., F. Wanschitz, W. Birkfellner, K. Zauza, C. Klug, K. Schicho, F. Kainberger, C. Czerny, H. Bergmann and R. Ewers. "Computer-Aided Placement of Endosseous Oral Implants in Patients after Ablative Tumour Surgery: Assessment of Accuracy." Clin Oral Implants Res 14, no. 3 (2003): 340-8.

235. Wallace, S. S., Z. Mazor, S. J. Froum, S. C. Cho and D. P. Tarnow. "Schneiderian Membrane Perforation Rate During Sinus Elevation Using Piezosurgery: Clinical Results of 100 Consecutive Cases." Int J Periodontics Restorative Dent 27, no. 5 (2007): 413-9.

236. Weinans, H., D. R. Sumner, R. Igloria and R. N. Natarajan. "Sensitivity of Periprosthetic Stress-Shielding to Load and the Bone Density-Modulus Relationship in Subject-Specific Finite Element Models." J Biomech 33, no. 7 (2000): 809-17.

237. Winkler, S., J. Piermatti, A. Rothman and G. Siamos. "An Overview of the O-Ring Implant Overdenture Attachment: Clinical Reports." J Oral Implantol 28, no. 2 (2002): 82-6.

238. Wittmann, W., T. Wenger, B. Zaminer and T. C. Lueth. "Automatic Correction of Registration Errors in Surgical Navigation Systems." IEEE Trans Biomed Eng 58, no. 10 (2011): 2922-30.

239. Wittwer, G., W. L. Adeyemo, K. Schicho, W. Birkfellner and G. Enislidis. "Prospective Randomized Clinical Comparison of 2 Dental Implant Navigation Systems." Int J Oral Maxillofac Implants 22, no. 5 (2007): 785-90.

240. Wittwer, G., W. L. Adeyemo, K. Schicho, N. Gigovic, D. Turhani and G. Enislidis. "Computer-Guided Flapless Transmucosal Implant Placement in the Mandible: A New Combination of Two Innovative Techniques." Oral Surg Oral Med Oral Pathol Oral Radiol Endod 101, no. 6 (2006): 718-23.

241. Wong, A. S., A. M. New, G. Isaacs and M. Taylor. "Effect of Bone Material Properties on the Initial Stability of a Cementless Hip Stem: A Finite Element Study." Proc Inst Mech Eng H 219, no. 4 (2005): 265-75.

242. Xiaojun, C., Y. Ming, L. Yanping, W. Yiqun and W. Chengtao. "Image Guided Oral Implantology and Its Application in the Placement of Zygoma Implants." Comput Methods Programs Biomed 93, no. 2 (2009): 162-73.

243. Yaman, Z. "Piezoelectric Surgery in Oral and Maxillofacial Surgery." Annals of Oral & Maxillofacial Surgery 1, no. 1 (2013): 5.

244. Zannoni, C., R. Mantovani and M. Viceconti. "Material Properties Assignment to Finite Element Models of Bone Structures: A New Method." Med Eng Phys 20, no. 10 (1998): 735-40.

245. Zhang, H., F. Banovac, R. Lin, N. Glossop, B. J. Wood, D. Lindisch, E. Levy and K. Cleary. "Electromagnetic Tracking for Abdominal Interventions in Computer Aided Surgery." Comput Aided Surg 11, no. 3 (2006): 127-36.